National Technical University of Athens
School of Civil Engineering
Geotechnical Division

Delft University of Technology
Faculty of Civil Engineering & Geosciences
Section of Geo-Engineering

Diploma Thesis by

BOUZONI ELENI

Supervised by

Assistant Professor N. Gerolymos

Associate Professor R.B.J. Brinkgreve

NUMERICAL MODELING OF THE DYNAMIC LATERAL RESPONSE OF CAISSON FOUNDATIONS

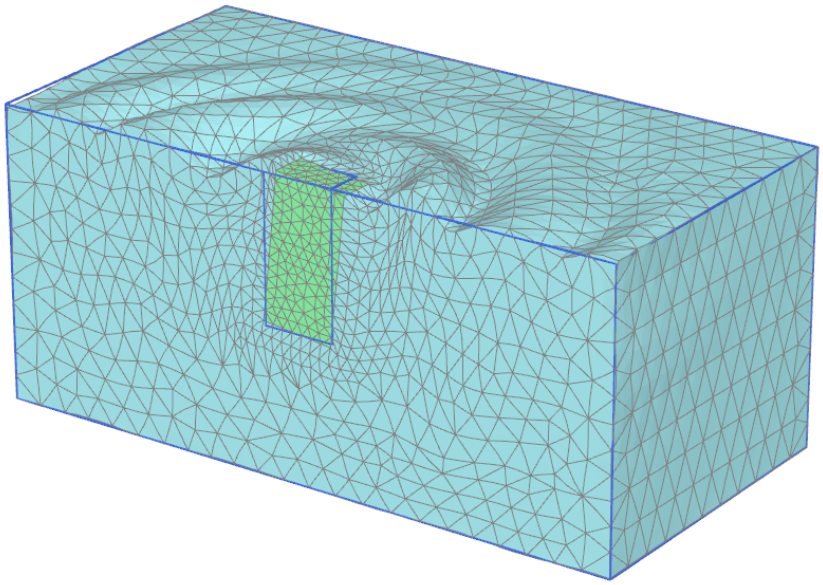

Athens, March 2013

PLAXIS

Education and Culture
Lifelong Learning Programme
ERASMUS

Preface

This diploma thesis finalizes my studies in Civil Engineering, with specialization on Geotechnical Engineering at National Technical University of Athens. Partial of the fulfillment of the requirements for this thesis was conducted at the Technical University of Delft under the auspices of Erasmus Lifelong Learning Program.

Upon completing my diploma thesis, I feel the need to thank the people that supported and encouraged me throughout my work.

First of all, I would like to express my deepest appreciation and gratitude to Professor G. Gazetas, for his valuable guidance throughout my studies. He has been an endless source of inspiration and has greatly contributed to the love that I have developed towards Engineering in general and Geotechnical Engineering in particular.

This thesis would not have been possible without the guidance, help and patience of my supervisors, Dr N. Gerolymos (NTUA) and Dr R.B.J. Brinkgreve (TU Delft and PLAXIS B.V.), to whom I owe my respectful gratitude. Their contribution to solving the challenging obstacles that arised throughout this thesis was considerable.

I would also like to express my gratitude to PLAXIS B.V. for offering me the opportunity to perform my research at a pleasant workplace. This includes all the colleagues at PAXIS, who contributed to this pleasant working environment. Special thanks goes to Dr Richard Witasse, for his help and guidance through the whole process.

Finally, above all, I feel the need to thank my family for their consistent support and encouragement all these years of my studies.

Table of Contents

1 Introduction

Traditionally, soil-structure interaction effects were ignored in seismic design of structures, since they were believed to have favorable effects. The lengthening of the period shifts the structure response to the spectral branch of lower accelerations which implies a reduction of inertia forces in the structure. However, along modern performance based design principles soil-structure interaction effects are recognized to not necessarily have beneficial but even may have very detrimental effects for the response of the superstructure. Considering this fact, proper consideration of soil-structure interaction is a critical factor in design. The effects of soil-structure interaction have been subjective to research for about half a century, but are still under discussion. The general methods to quantify soil structure interaction effects are direct approach and substructure approach.

In the direct approach, the soil and structure are simultaneously accounted for in the mathematical model and analyzed in a single step. Typically, the soil is discretized with solid finite elements and the structure with finite beam elements. Since assumptions of superposition are not required, true nonlinear analyses are possible in this case. Nonetheless, the analyses remain quite expensive from a computational standpoint. Hence, direct SSI analyses are more commonly performed for structures of very high importance and are not employed for the design of regular structures. Another additional problem considering direct approach is that nowadays code provisions relating to soil-structure interaction are still very limited and straightforward procedures to fully account for SSI effects in design and are not included in most practicing codes. Hence, even though the research activities at the universities all over the world are already ahead, providing a variety of knowledge in this field, the connection with engineering practice appears to be still limited.

In the substructure approach, the SSI problem is decomposed into three distinct parts, namely the soil, the foundation and the superstructure, which are combined to formulate the complete solution. In this approach the terms kinematic interaction and inertial interaction are introduced. The former refers to the effects of the incident seismic waves to the massless system while the latter refers to the response

of the complete system to excitation by D' Alembert forces associated with the acceleration of the superstructure due to kinematic interaction. Inertial interaction is conducted in two steps: computing the foundation dynamic impedance (i.e. springs and dashpots) associated with each mode of vibration, and determining the response of structure and foundation supported by these springs and dashpots and subjected to kinematic motion of the base. Thus, the complete solution is estimated by applying the superposition principle. The principal advantage of the substructure approach is the associated numerical flexibility. Because each step is independent of the others, it is easy to focus resources on the most significant aspects of the problem. This is the main reason of its wide implementation in research as well as in engineering practice.

Following the substructure approach this thesis dealt with the problem of caissons. Caissons is a type of embedded foundations that compared to other types of foundations have attracted less attention by the researchers. Different computation methods of the dynamic impedance of caissons are compared for elastic conditions. The study is extended to the more realistic inelastic behavior of the caisson and qualitatively comparisons are made between nonlinear inelastic behavior and equivalent elastic behavior of the caisson under dynamic loading. An alternative Winkler-type approach is developed where the foundation is supported by a series of distributed independent vertical, rotational and horizontal springs and dashpots along the soil-footing interface, which correspond to the vibration modes, namely the oscillation pattern imposed by the external load (swaying, rocking etc.). The study is focused on the horizontal mode where a special connection of nonlinear and linear springs and dashpots is suggested for the real inelastic dynamic response. A methodology for the calibration of this system is proposed and proper validation is performed with nonlinear numerical analyses.

1.1 Project description

This study exists of four main parts:

The first part is a literature study of different aspects of geotechnical earthquake engineering with focus on embedded foundations and elastic as well as inelastic conditions. This study is based on research papers, seismic engineering texts and books. Beginning from general principles that concern the vibrations, definitions and descriptions of fundamental phenomena are reported. Some general approaches for soil-structure interaction problems are presented while focus is given on the response of foundations and especially on impedance and its components. The Finite Element Method is introduced with emphasis on the element-size and domain-dimensions which are one of the main concerns of this project. A presentation of the Finite Element Code that has been used for the performed analyses for the needs of this study follows. Initially general information about the use and the development of the program are provided while special focus is given on the dynamic mode and its features. More details are given about the choices that the software provides about the criteria of the selection of the parameters that have been used in this study.

Finally the last section of the first part addresses to the kind of foundation that has been studied herein which is caissons. Introduction about the caisson as a type of foundation has been conducted at the beginning while general description of their design methodologies follows. At this part an attempt to understand the difficulties of the embedded foundation has been performed by describing the mechanisms and the physics of the caisson. Special focus has been given on the coupling mode of the rotation and the lateral displacement as well as the reference point that has been chosen and its importance.

The second part is related to the elastic response of the caisson and the corresponding elastic dynamic impedance. First sensitivity analyses considering the finite element size (mesh discretization) and the domain dimensions of the numerical simulation, have performed in order to set the numerical model. After this optimization, the design methodology and the elastic formulas that have been used are presented more extensively and comparison is made between them and the

numerical results after the proper process of the results in order to be comparable. The impedance of the concerning caisson is investigated with the addition of artificial damping (Rayleigh damping) and comparisons are made considering the dynamic response where conclusions and remarks are formulated.

The third phase addresses to the inelastic response of the caisson. The methodology that has been followed is described, considering the bearing capacity of caisson in lateral loading, the meaning of the coupling impedance in inelastic conditions and the different aspects of the dashpot which now consists of two different parts, the radiation damping and the material damping. Two different cases have been selected considering the conditions at the interface of the soil-foundation, namely the bonded interfaces where full contact conditions have assumed and the nonlinear interfaces where sliding and gapping are allowed to occur.

Finally, a different approach for the inelastic behavior of embedded foundations is being studied. Numerical analyses under plain strain conditions are performed in order to investigate and evaluate the local horizontal mode of the shaft of the caisson. A nonlinear Winkler model with springs, dashpots and masses is suggested. The suggested calibration of the distributed nonlinear springs and dashpots that arised from the physics of the dynamic behavior of the foundation is validated with the previous numerical analyses.

The fourth part of this thesis consists of a case study of a suction caisson. Here a comparison is made between some field trials that performed at the Bothkennar test site for a large diameter suction caisson and numerical analyses using the PLAXIS 3D code. Some interesting conclusions and remarks are presented considering this comparison.

Finally, some general concluding remarks are presented. Except for conclusions, suggestions for further research work are also recommended.

1.2 Research objectives

The main research objective of this diploma thesis is to investigate the dynamic behavior of caissons in terms of the impedance that computed by the Finite Element Method using the PLAXIS 3D code. A comparison is made with available solutions from the literature for the elastic response of a caisson with a specific embeddedment ratio. Considering the inelastic response numerical analyses are performed using the PLAXIS 3D code in order to conduct useful conclusions. As the PLAXIS 3D dynamics program (3D12) released quite recently in 2012, it is very interesting to evaluate its possibilities and limitations considering that it is a worldwide-used finite element program for engineers that expands rapidly. In order to achieve this goal the following additional objectives are defined:

CAISSON:

- Evaluate the dependency of the mesh discretization density (Finite Element size).
- Evaluate the influence to the response of the distance of the boundaries of the numerical model.
- Evaluate the response in static loading.
- Evaluate the frequency-dependent dynamic impedance in dynamic loading in elastic conditions.
- Evaluate the behavior in dynamic loading in inelastic conditions first with full bonded conditions and afterwards by taking into consideration the interfaces between the structure and the soil.
- Study the possibilities of a generalized Winkler model for the proper simulation of the soil-foundation interaction in the horizontal mode of the shaft.
- Investigate and compare a real case study of a suction caisson with numerical simulation.

2 Theoretical background

2.1 Vibrations

Motion characterizes everything in the world. The study of kinematic systems begins from the first existence of humans with very simple observations and early conclusions. In Civil Engineering concepts like motion, movement, oscillation and displacement are fundamental. The research in vibrating systems arises from the need to understand and explain the behavior of structures under dynamic loading in real life in order to improve the safety of structures.

2.1.1 Earthquakes

Because of their huge impact on humans' lives earthquakes and seismic activity have always been a hot issue for Science that needs constant investigation. The fact that new earthquakes are about to come is a motivation for civil engineers to keep on the research for safer structures, in order to minimize their catastrophic results. Hence, understanding the way that earthquakes occur is a first fundamental step. The Earth's surface consists of six continental-sized tectonic plates and many micro plates which move constantly but with an uncertain way. This movement is the result of natural processes in the internal of the Earth. Convection cause the semimolten rock to move slowly, forcing in this way the plates to move with respect to each other. According to the elastic rebound theory, this relative deformation between the faults planes that separate the plates, stores elastic strain energy in the rocks with the gradual building up of shear stresses. When the shear stresses reach the shear strength of the rock, energy releases. This release of energy occurs either quite slowly so the movement characterized aseismically or suddenly and abruptly causing the rupture of new or preexisting geological faults, so earthquakes are born. Earthquakes are generated mostly by this sudden release of strain energy but there are also other causes of earthquakes such as volcanic activity, landslides, mine blasts, and nuclear tests.

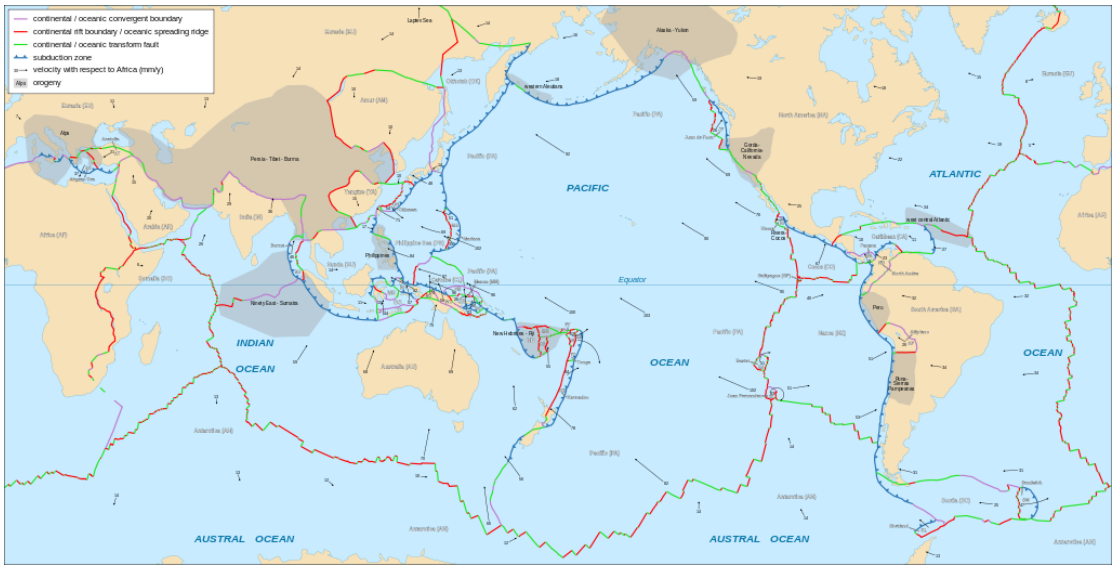

Figure 2-1: Global Tectonic Plates. The rows indicate the movement of plates.

2.1.2 Foundation Vibrations

When seismic waves arrive through ground to foundations, they excite their support causing oscillations. However, foundations are excited also by dynamic forces imposed directly or indirectly on their top. Such excitations can be result of operating machines, ocean waves and vehicle movement on the top of the structure. In this project vibrating foundations have been studied. In addition to being directly applicable to machine loaded foundations, much of the results can be used in assessing the dynamic soil-foundation-structure interaction during seismic or any other ground shaking. In such cases the loading arises from inertial (D' Alembert) forces developing in the oscillating superstructure.

2.2 Soil waves

The seismic energy that releases during the generation of a vibration has kinematic characteristics and radiates outward in all directions in the form of waves. This wave propagation can be described through solids theory (Kramer, 1996).

In general seismic waves can be considered elastic. However the soil is a very complex material, inhomogeneous and anisotropic with elastoplastic nonlinear behavior. So the assumption that the soil reacts to local disturbance as an elastic solid can be considered simplified. However the theory of the elastic waves is the base of the geotechnical earthquake engineering, not only for understanding the behavior of soil materials and structures during an earthquake (or any vibration) but also for configuring the seismic design methods for all kinds of structures.

The seismic waves can be divided into two main categories: body waves and surface waves. The former have such small energies that are mostly not threatening while the latter arrive last at a given distance from the epicenter with all of their damaging energies and are predominantly noticed by people.

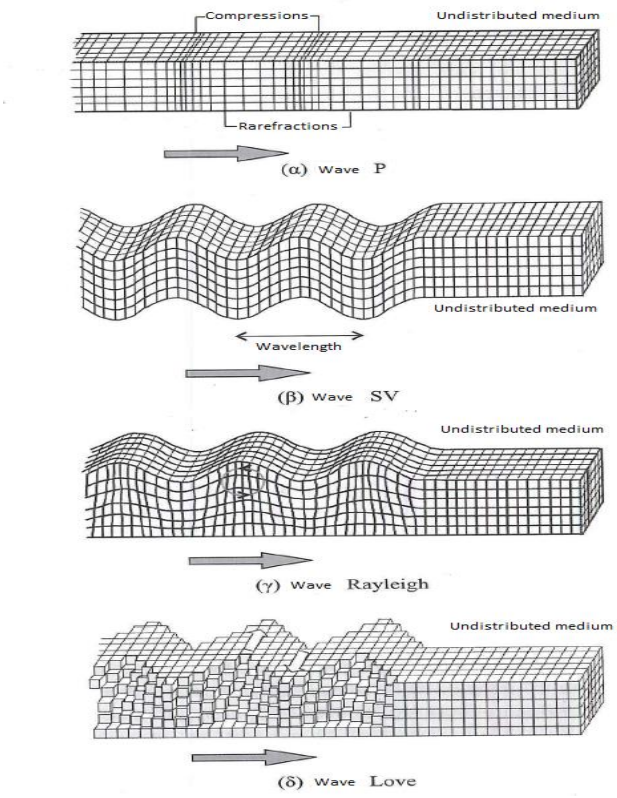

Figure 2-2: Deformations that are caused by body waves (a) P and (b) S and by surface waves (c) Rayleigh and (d) Love.

The body waves consists of two types of waves, first the compressional, or longitudinal waves which are called P-waves by the word primary, because they

travel faster and they are the first to be recorded, and second the shear, or transverse waves which are called S-waves by the word secondary as they arrive after the P-waves because their velocity is lower. P-waves can travel not only through solids but also through fluids. The deformations that cause are always parallel to the direction that they travel. In contrast, S-waves can travel only through solids because liquids as it is known, do not have shear stiffness. S-waves cause shearing deformations and depending on the direction of the plane movement can be divided into vertical S-waves (SV-waves) and horizontal S-waves (SH-waves). It should be mentioned that the common engineering approach representing the seismic load is by vertically propagating shear waves only. As the speed of waves varies with the stiffness of the materials, P-waves travel faster because geological materials are stiffer in compression. The relations that provide the velocities of the various waves are presented in the Table 2-1. It must be noted that the velocities of the waves depend mostly on the properties of the mean that they are propagating.

Table 2-1: Velocities of different kinds of soil waves

TYPE OF WAVE	VELOCITY
Primary wave	$V_P = \sqrt{\frac{D}{\rho}}$
Secondary wave	$V_S = \sqrt{\frac{G}{\rho}}$
Rayleigh wave	$V_R \cong 0.94 V_s \; for \; 0.25 < v < 0.50$

Surface waves are generated by the interaction of P-waves and S-waves at the interfaces of geological or soil layers and especially at the surface of the Earth. They play a significant role since they can be the most destructive category of seismic waves. The two most important types of surface waves are the Rayleigh-waves, which are generated by the interaction of P-waves and SV-waves, and the Love-waves which are generated by the interaction of P-waves and SH-waves. Rayleigh-waves exist near the surface of homogeneous elastic half-space and decrease exponentially in amplitude as distance from the surface increases. Most of the shaking felt from an

earthquake is due to the Rayleigh-waves, which can be much larger than the other waves. Love-waves are observed only when there is a low velocity layer overlying a high velocity layer so they do not exist in a homogeneous elastic half-space. They travel with a slower velocity than P- or S- waves, but faster than Rayleigh-waves.

2.2.1 Site amplification effects

The features of the bedrock motion depends on the fault characteristics and the wave propagation phenomena. Instead, the features of the ground motion that civil engineers use in order to design the structures, depends among others on site amplification effects. In general site effects can be defined as the influence to the characteristics (intensity, duration, frequency content) of the incoming seismic wave, caused by the special geologic, soil properties, geometric parameters of the soil layers and the local surface conditions. These phenomena can strengthen the incident seismic motion and increase the consequences on structures and buildings. Since this local amplification of the seismic motion is often very large, seismic site effects is a major issue in the field of geotechnical earthquake engineering.

The influence of site effects can be described as enhancement or reduction of the amplitude of ground motion at all frequencies. Of course, there are many parameters that define the phenomenon such as the relative density (D_r), the plasticity index (PI), the wave velocities V_S, V_P, the shear modulus G and its relation to the deformations, the non-linear constitutive behavior of soil and many others (Pitilakis, 2010).

The site amplification effects are characterized by the natural frequencies of the soil deposit. Natural frequencies are the frequencies that a system responds to a periodic driving force with maximum amplitude. When the driving force has the same frequency as one of the natural frequencies, resonance occurs. Vibrating systems have a number of possible natural frequencies. The lowest is called the fundamental frequency. The other frequencies are at values which are multiples of the fundamental. Consequently, the soil deposit can be made to resonate at more than one frequency.

The resonant frequency is a function of soil stiffness, geometry and boundary conditions. For a homogeneous deposit, natural frequencies can be estimated (Gazetas, 1982) based on the constant soil shear wave velocity, V_s, and the soil deposit height, H:

$$f_n = \frac{V_s}{4H}(2n-1), n = 1,2,3,\ldots \quad (2.1)$$

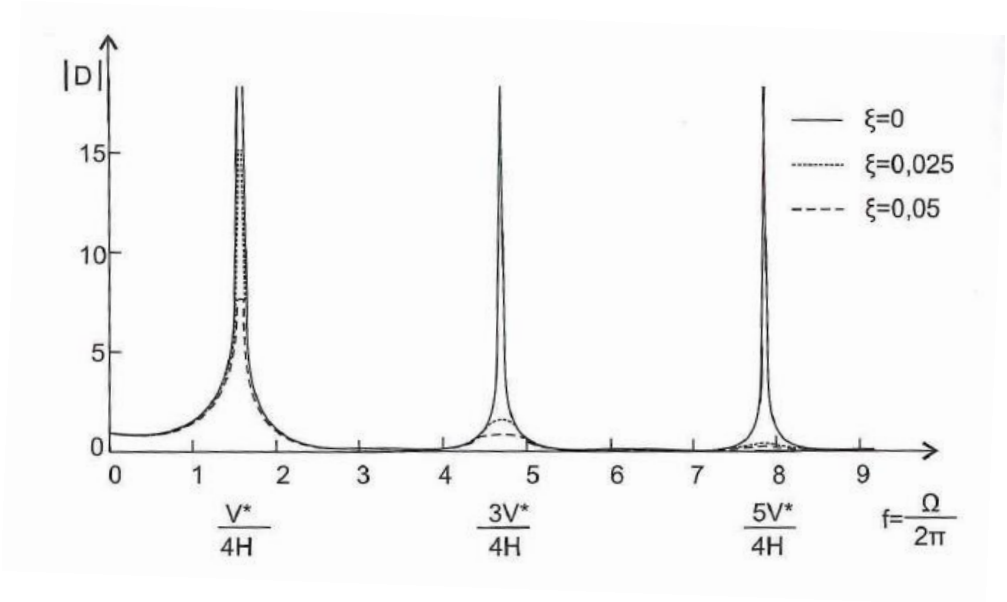

Figure 2-3: Dynamic amplification of soil deposit with different damping ratios ξ.

Vertical one-dimensional propagation of shear waves in a visco-elastic homogeneous layer that lies on rigid bedrock can be described in the frequency domain by its amplification function. The amplification function is defined as the modulus of the transfer function which is the ratio of the Fourier spectrum of the free surface motion to the corresponding component of the bedrock motion. Therefore, for a given visco-elastic stratum and a given seismic motion acting at the rigid bedrock, the motion at the free surface can be easily obtained by this function. First, the Fourier spectrum of the input signal is computed. Then, this spectrum is multiplied by the amplification function and after that, the motion is given by the inverse Fourier transform of the previous product. If the properties of the medium (density ρ or total unit weight of soil γ, shear wave velocity Vs and material damping ξ) and its

geometry (layer thickness H) are known, the amplification function is uniquely defined by Roesset's simplified function:

$$A(f) = \frac{1}{\sqrt{cos^2\left(2\pi f \frac{H}{V_s}\right) + \left(2\pi f \frac{H}{V_s}\xi\right)}} \quad (2.2)$$

The maximum amplification ratio of the layer that corresponds to the natural frequencies can be computed by means of the following approximated relationship:

$$A_{max,n} = \frac{2}{(2n-1)\pi\xi} = \frac{V_s}{H\xi\omega_n}, n = 1,2,3,\ldots \quad (2.3)$$

If a soil is homogeneous or close to homogeneous and ground motion levels are not very high, then this approximation is considered to derive good estimation of actual site response. However these conditions are hard to be satisfied because are not often met in practice.

2.3 Soil structure interaction

Soil-structure interaction is the mechanism that accounts for the flexibility of the foundation support beneath the structure and potential variations between foundation and free-field motions. It determines the actual loading experienced by the structure-foundation-soil system resulting from the free-field seismic ground motions (Varun, 2006)

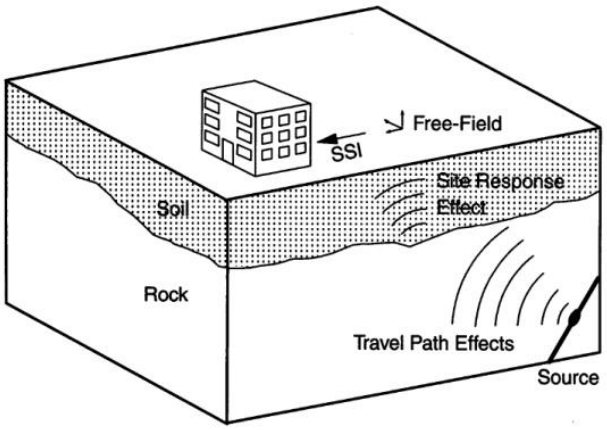

Figure 2-4: Context of system interaction in engineering assessment of seismic loading for a structure

The structure, the foundation and the geologic media of soil and rock are three linked systems that interact and affect the deformations of a structure during dynamic loading. The mechanisms of this interaction can be described by two physical phenomena:

- Inertial interaction: which refers to excitation by D' Alembert forces due to acceleration of the super structure.
- Kinematic interaction: which sets the mass of structure as zero (no inertial effects) and takes into account the deviation of the foundation motion with respect to the corresponding free-field soil motion.

The effect of kinematic interaction is generally captured by complex-valued transfer functions, namely functions that relate the free-field motion to foundation response. In the case of linear elastic soil-foundations systems (or moderately nonlinear), inertial interaction analysis can conveniently be performed in two steps as shown in Figure 2-5: Schematic representation of two-step inertial interaction analysis.

(a) Compute the foundation dynamic impedances (springs and dashpots) associated with each mode of vibration

(b) Determine the seismic response of structure and foundation supported by these springs and dashpots and subjected to the kinematic accelerations of the base.

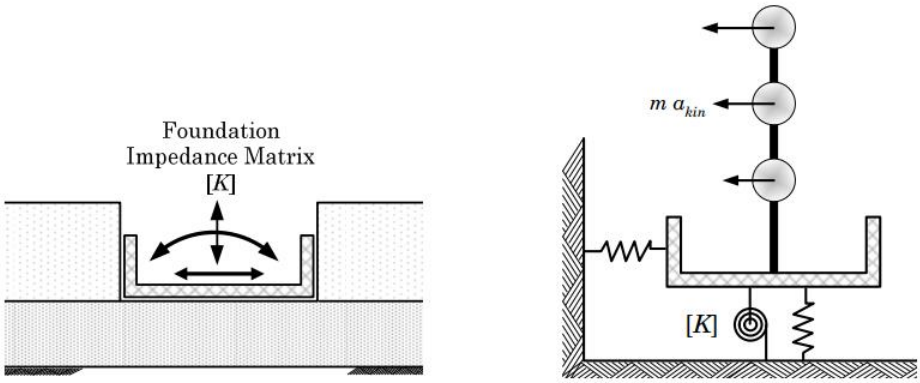

Figure 2-5: Schematic representation of two-step inertial interaction analysis (after (Varun, et al., 2009))

2.4 Dynamic impedance

When a rigid block foundation is subjected to a steady-state harmonic excitation F(t) the respondent displacement u(t) of the foundation is also harmonic with the same frequency ω. In order to determine this response the key step is to estimate the dynamic impedance. Considering the inertia (D' Alembert) forces, the foundation actions on the soil generate equal and opposite reactions, distributed in some unknown resultant P(t). The dynamic impedance can be defined (Gazetas, 1991) as the force-displacement ratio:

$$\widetilde{K} = \frac{P(t)}{u(t)} = \frac{\bar{P}}{\bar{u}} = complex\ number$$

which may be written in the more elegant form:

$$\widetilde{K} = K + i\omega C$$

in which both K and C are functions of the frequency ω. The real component K, termed "dynamic stiffness", reflects the stiffness and inertia of the supporting soil. Its dependence on frequency is attributed solely to the influence that frequency exerts on inertia, since soil properties can considered frequency-independent. The imaginary component ωC, is the product of circular frequency times the "dashpot coefficient" c, which reflects the two types of damping –radiation and material– generated in the system, the former due to energy carried by waves spreading away from the foundation, and the latter due to energy dissipated in the soil due to hysteretic action.

There are six modes of dynamic impedances for rigid foundations as there are six degrees of freedom, three translational and three rotational. Moreover in embedded foundations and piles, which are the main concern of this study, horizontal forces along principal axes induce rotational in addition to translational oscillations. Hence, two more cross coupling horizontal-rotational impedances exist. For caissons with great depth of embedment their effects may become appreciable, owing to the moments about the base axes produced by horizontal soil reactions against the

sidewalls. In piles the cross coupling impedances are as important as the direct impedances.

The equation of dynamic equilibrium in matrix notation assigned to the structure degrees of freedoms is:

$$[M]\ddot{u}(t) + [C]\dot{u}(t) + [K]u(t) = F(t) \quad (2.4)$$

Where

$[M]$: mass matrix

$[C]$: damping matrix

$[K]$: stiffness matrix

$\ddot{u}(t), \dot{u}(t), u(t)$: acceleration, velocity, displacement vectors

$F(t)$: external force vector

In case of an earthquake the foundation is excited at its base with forced displacement $u_g(t)$ so the total displacement of the structure consists of the ground displacement $u_g(t)$ plus the response $u(t)$ of the structure itself. In this case the dynamic equilibrium becomes:

$$[M]\{\ddot{u}(t) + \ddot{u}_g(t)\} + [C]\dot{u}(t) + [K]u(t) = 0 \Rightarrow$$

$$[M]\ddot{u}(t) + [C]\dot{u}(t) + [K]u(t) = -M\ddot{u}_g(t) \quad (2.5)$$

so the external force becomes $F(t) = -M\ddot{u}_g(t)$

Of course this excitation varies way far from a harmonic oscillation. But as it is already known all nonharmonic forces can be decomposed into a large number of sinusoids through Fourier analysis. For a particular excitation frequency ω, once all the dynamic impedances have been determined, the steady-state response of a rigid foundation to arbitrary harmonic external forces can be computed analytically by application of Newton's laws (Gazetas, 1991).

Also analytically, one can derive the steady-state response of a flexible structure possessing natural modes and subjected to harmonic external forces and to harmonic base motion. The procedure is iterative: first the dynamic impedance function is calculated by geotechnical analysis, then the fundamental frequencies of the structure based on these springs and dashpots are computed by structural analysis. For these fundamental frequencies the dynamic impedance is recalculated and for the obtained values of springs and dashpots a new structural analysis will provide new fundamental frequencies etc. When the final fundamental frequencies are estimated the seismic forces can be calculated.

2.4.1 Computation of dynamic impedance

The computation of the dynamic impedances, or equivalents the spring and dashpot coefficients, can be proceeded with various methods and computational codes. The accuracy that the specific project requires will define the choice among these methods, taking also into account the special features that characterize the soil-foundation system of the project. These features are mainly the shape and the type of the foundation as well the soil profile.

The methods of computing the dynamic impedance can be divided into four main groups:

- Analytical and semi-analytical methods
- Dynamic finite-element methods
- Combined analytical-numerical methods (boundary element methods)
- Approximate techniques

Each one of these groups has its own limitations and simplifications of physics (Gazetas, 1991), hence they cannot be applied to every engineering problem.

In the recent years, the rising development of the computers have made the computer codes much more efficient and easier to use. In this way the dynamic finite-element methods have gained ground and today they are the most dominant computing method that offer rigorous solutions for modern engineering problems.

Of course because still finite element analyses can be very time consuming for making parametrically investigations, the user should be very careful when deciding the model features. The results of a finite element analysis should be evaluated and compared with other alternative available methods. In this study the results of the upcoming PLAXIS code are going to be compared with available from the literature solutions.

2.5 Damping

The dashpot coefficient, which was mentioned before, refers to damping of the system. Damping is a general term that can divided into many subcategories depending on its kind and source of causing. An attempt to understand the physical meaning of all different dampings has been made below.

In a homogeneous linear elastic material, stress waves travel indefinitely without change in amplitude, if the effects of scattering are neglected. The conservation of elastic wave energy requires that the flow of energy (energy flux,$\rho V s \dot{u}^2$) to be constant. This type of behavior, however, cannot occur in real materials. The amplitudes of stress waves in real materials, such as those that comprise the earth, attenuate with distance. The attenuation can be attributed to two sources, one of which involves the materials through which the waves travel and the other the geometry of the wave propagation problem (Kramer, 1996). The latter form of damping concerns the first part of this study where linear elastic model has been considered for the soil constitutive behavior. A brief description of different kinds of damping will be presented for a complete understanding of damping mechanisms which are used in the inelastic part of this research.

2.5.1 Material damping

- Soil damping:

The material damping in the soil is divided into two components, hysteretic damping and viscous damping.

i) Hysteretic damping in the soil skeleton (frequency independent):

This kind of damping refers to dry soils and is due to the heat that develops by the friction forces which are caused by the vibration of grains. Some authors (Iwasaki, et al., 1978) have remarked on the absence of frequency dependency for this kind of damping leading them to purpose that soils can be treated not as viscous, but as hysteretic-absorbing energy solely as a function of cycling strain. According to (Bolton & Wilson, 1990) a body of hysteretic material is found to be very sensitive only to the frequencies of excitation just below resonance.

ii) Viscous damping in the pore fluid (frequency dependent):

For saturated permeable soils the heat energy is generated by pore fluid motion through the soil skeleton. This approach treats soils as a truly viscous frequency dependent and draw a parallel between dynamic damping and long term creep (Abbiss, 1986)

Dynamic analyses of soil usually assume that it can be treated as a visco-elastic material. To represent Viscoelastic damping three models are used, Kelvin-Voigt model, Maxwel model and Standard linear solid model. The former is the most widespread model as it is the most accurate for practical purposes. It defines an equivalent viscosity $\eta = 2G\xi/\omega$ using a constant complex shear modulus. By this trick the soil damping is considered frequency independent.

- Structure damping:

Structural damping can be separated into material damping which comes from the micro-scale material straining, and friction damping which is due to rubbing friction or contact among different elements in a structure. The former is related to heat

production in the materials due to vibrations and depends on the kind of materials. The latter is caused by Coulomb friction at structural joints and it depends on many factors such as joint forces or surface properties.

The total viscous structural damping parameter is usually estimated by the area of the global hysteresis loop which represents the energy dissipated in a cycle. It is very common to express this damping as percentage of the maximum potential energy in the system during a cycle.

2.5.2 Interface damping

Increased soil material damping in the region surrounding the soil-structure interface is observed. Due to the relatively high deformation levels extreme hysteresis behavior is locally present, resulting from high local soil strain levels and plastic shearing at the soil-structure interface. In the soil-structure system three general types of interface nonlinearities are recognized:

- Sliding at the interface of soil and foundation when the applied force at the interface exceeds the friction limit. Because of the cyclic character of the load this nonlinear behavior does not lead certainly to failure.
- Gapping and uplifting of the foundation, when the seismic moment exceeds the ultimate moment of the system. These vibrations might have positive effect to the response of the system.
- Plastic failure of the soil in the region of the interface because of the worse quality soil at this area due to the construction of the foundation.

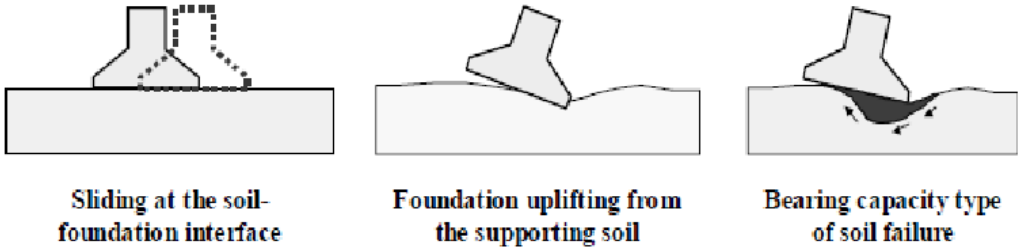

Figure 2-6: Different mechanisms of nonlinear response of the soil-foundation system (after (Gazetas & Apostolou, 2004))

2.5.3 Geometric damping

The consequent gradual reduction of the amplitude of the oscillation comes except for material damping, from another form of damping as well which is due the geometry. It is called geometric or radiation damping/attenuation. This kind of damping is not an internal property of the soil material. The physical meaning of this radiation or geometric damping can easily be explained by the law of conservation of energy. If material damping is neglected then the wave energy should remain constant. However, as the distance from the source increases the spherical area in which energy is included increases too, so the same amount of energy spreads to a larger area. This results the attenuation of energy and consequently the reduction of the amplitude of the oscillation.

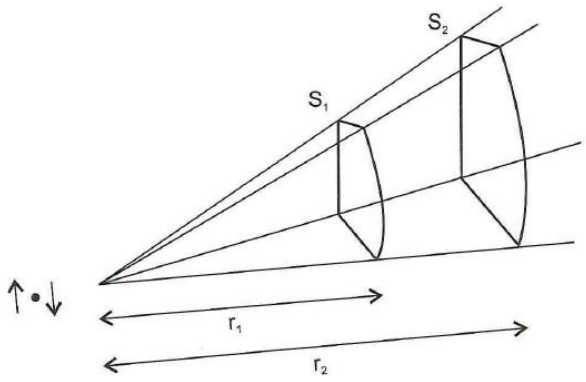

Figure 2-7: Geometrical attenuation

Geometric attenuation for body waves causes the amplitude to decrease at a rate of $\frac{1}{r}$ while for surface waves at a rate of essentially $\frac{1}{\sqrt{r}}$ meaning the latter attenuate geometrically much more slowly than the former. This fact can explain the greater proportion of surface wave motion at large epicentral distances (Kramer, 1996)

The first necessary condition for radiation damping to occur is for the fundamental frequency of soil to be less than or equal to the effective fundamental frequency of the structure:

$$f_{soil} = \frac{V_s}{4H} \leq f_{struct} \quad (2.6)$$

where H is the depth of the soil layer and V_s is the shear wave velocity of the underlying soil (Celebi, 2000).

One of the limitations that geotechnical finite element analyses have is the limited mesh size. Because the boundaries of the model cannot be expanded towards infinity in order to represent the reality of the indefinite travelling of radiation waves, they should be set up in a way to absorb the incoming energy of the waves without reflecting them. In order to achieve this in numerical analyses, artificial Rayleigh material damping in combination with viscous boundaries are used to provide the actual attenuation of stress waves by radiation damping.

2.5.4 Rayleigh damping

One good analysis method that can address nonlinearities, whether geometric or material, in dynamic analysis is direct time integration with Rayleigh damping. This format of damping is one of the most computationally convenient measures of dumping that lumps the damping effect within the mass and stiffness matrices of the system as it meets orthogonally properties of the damping matrix. However its physical background lacks. The material damping matrix for the system is described by the following equation:

$$[C] = \alpha[M] + \beta[K] \quad (2.7)$$

$[C]$: damping matrix

$[M]$: mass matrix

$[K]$: stiffness matrix

α, β: damping constants

Rayleigh alpha is the parameter that determines the influence of the mass in the damping of the system. As alpha increases the lower frequencies are damped more. Rayleigh beta determines the influence of the stiffness in the damping of the system and the higher it is the higher frequencies are damped more. In order to calculate from the following equation, α and β, a pair of damping ratio ξ that correspond to two frequencies of vibration ω is required. The damping ratios for each frequency, (ξ_1, ω_1) and (ξ_2, ω_2), can be obtained experimentally by means of the resonant column test (Das, 1995).

$$\alpha + \beta\omega^2 = 2\omega\xi \qquad (2.8)$$

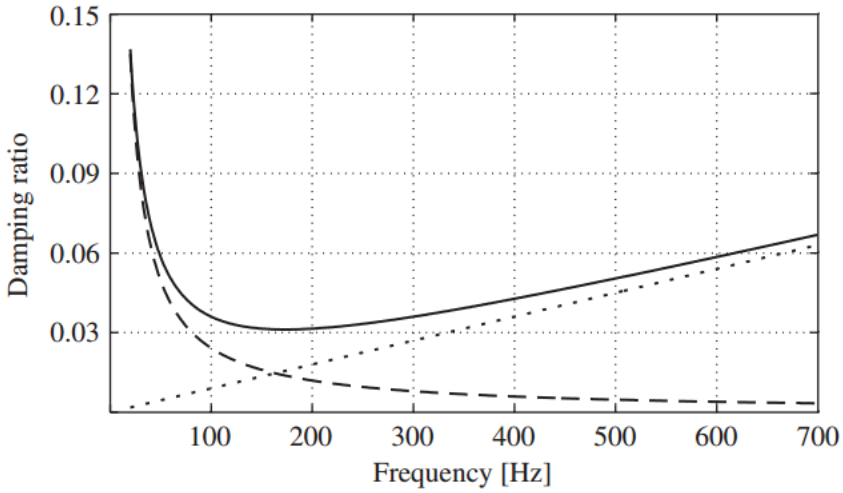

Figure 2-8: Influence of the mass and stiffness matrix on the damping ratio for the proportional Rayleigh damping model: mass-proportional damping (- - -), stiffness-proportional damping (····), both mass proportional damping (—)

In this study because of the assumption of linear elastic constitutive model, there is no material damping for the soil, so the Rayleigh parameters for the main dynamic analyses have been set equal to zero, $\alpha = 0 \; and \; \beta = 0$.

2.5.5 Numerical damping

Numerical damping has no relation with any physical process in structural/soil dynamics and may result from a certain numerical time integration scheme applied in time domain analysis. The time integration scheme applied, affects the stability and accuracy of results causing energy dissipation for certain frequency ranges. Explicit and implicit integration are two commonly used time integration schemes. Newmark family methods and the central difference method are employed in almost totality of structural dynamic analysis problems. The simplicity is a great advantage of these, implicit and explicit respectively, schemes. With Newmark algorithm, which is the method that concerns this study as it is implemented in PLAXIS, the displacement and the velocity at the point in time t+Δt are expressed respectively as:

$$u^{t+\Delta t} = u^t + \dot{u}^t \Delta t + \left[\left(\frac{1}{2} - \beta_N\right)\ddot{u}^t + \beta_N \ddot{u}^{t+\Delta t}\right]\Delta t^2 \quad (2.9)$$

$$\dot{u}^{t+\Delta t} = \dot{u}^t + [(1-\gamma_N)\ddot{u}^t + \gamma_N \ddot{u}^{t+\Delta t}]\Delta t \quad (2.10)$$

β_N, γ_N are the coefficients that affect the stability and the accuracy of this method.

Hilbert, Hughes and Taylor (HHT)-α method is a generalized modification of the initial Newmark β-method. In this method a new parameter, α, is presented in order to introduce numerical energy dissipation. This energy dissipation, however, cannot be predicted as damping ratio. The new Newmark parameters are expressed as function of the parameter α:

$\beta_N = \frac{(1+a)^2}{4}$, $\gamma_N = \frac{1}{2} + \alpha$, where $0 \leq \alpha \leq \frac{1}{3}$

In case that $\alpha=0$, the modified method coincides with the original method but with constant average acceleration during the stepping interval, a condition that has been added to the HHT α-method. Another condition which leads to stable condition that only the modified method satisfy, is:

$$\beta_N \geq \frac{1}{4}\left(\frac{1}{2} + \gamma_N\right)$$

Thus, HHT-α method leads to unconditionally stable integration scheme, a feature that should generally be preferred in the selection of the time integration method because otherwise much smaller time step would be required. Smaller time steps would make the method inconvenient and much more computationally time consuming.

Some typical values for the mentioning parameters that have been suggested are presented in the Table 2-2: Time integration schemes.

Table 2-2: Time integration schemes

Integration scheme	Parameters	Stability	Numerical damping
Linear acceleration method	$\beta_N = \frac{1}{6}, \quad \gamma_N = \frac{1}{2}$	Conditionally stable	No numerical damping
Constant average acceleration method (by default in PLAXIS)	$\beta_N = \frac{1}{4}, \quad \gamma_N = \frac{1}{2}$	Unconditionally stable	No numerical damping
Newmark, HHT-α modification	$\alpha = 0{,}1 \rightarrow$ $\beta_N = 0.3025$ $\gamma_N = 0.60$	Unconditionally stable	Numerical damping by numerical dissipation parameter α

In case of an undamped dynamic analysis, meaning no material and no numerical damping, all the coefficients –Rayleigh and Newmark– should set equal to zero ($\beta_N=\gamma_N=\alpha_R=\beta_R=0$). Then the model is expected to reach the resonant conditions at the natural frequencies of the system with corresponding theoretically infinite amplification ratio. Generally when α increases, the peaks of amplification at the natural frequencies of the layer decrease. However, the shape of amplification function is not essentially modified.

Conclusion

As implied by the aforementioned descriptions of damping one can easily conclude that the total damping in a soil-structure system is very complicated term that is difficult to be modeled mathematically. The reasons are not only because still the mechanism of each damping contribution and its physical meaning is not fully clarified but also because such a model would demand scientific elaborate knowledge and effort, and great computational cost. So such an approach wouldn't be possible for practical reasons.

2.6 Finite Element Method (FEM)

Finite Element Method is, as mentioned before, a very useful and effective approach to engineering applications. First it should be noted that in order to use the Finite Element Method for geotechnical problems special knowledge is required not only for understanding the soil mechanics and finite element theory but also for understanding the limitations and restrictions of the software that is being used to perform the finite element analysis.

A full numerical analysis can provide information on all design requirements which can be divided into the following four fundamental conditions:

- Equilibrium
- Compatibility
- Material constitutive behavior
- Boundary conditions

The Finite Element Method in order to satisfy the above conditions involves the following steps (Potts & Zdravkovic, 1999):

Element discretization: this is the process of modelling the geometry of the problem by small regions, named finite elements.

Primary variable approximation: a primary variable should be selected (most commonly for geotechnical problems the displacement) and rules as to how it should vary over a finite element established.

Element equations: use of an appropriate variational principle to derive element equations

Global equations: combine element equations to form global equations

Boundary conditions: formulate boundary conditions and modify global equations.

Solution of global equations: obtain the displacements at all nodes and then evaluate secondary quantities such as stresses and strains.

2.6.1 Mesh– finite element-size

It is widely accepted that the element size in element-based computations should be related to the wavelength. Often, the element size is measured in a certain (fixed) number of elements per wavelength. This number of elements per wavelength varies between four and ten. Obviously, this number is closely related to a certain desired accuracy. The error is of an acceptable magnitude which depends on the user and which meets certain technical requirements.

(Kuhlemeyer & Lysmer, 1973) showed that for accurate representation of wave transmission through a model, the spatial element size, Δl, of a linear element must be smaller than approximately one-eighth of the wavelength associated with the highest frequency component of the input wave:

$$\Delta l \leq \frac{\lambda}{8} \qquad (2.11)$$

Where λ is the wavelength associated with the highest frequency component that contains appreciable energy.

It is worth mentioning here that this ratio depends also on the type of element (linear, quadratic etc.). Hence, the guideline for Δl developed by (Kuhlemeyer & Lysmer, 1973) is not a universal one owing to its development and use. In this study

the influence of the mesh density (element-size) has been investigated, through sensitivity analysis that has performed for the maximum frequency of interest. Once the maximum element-size has been found for one frequency the density of the mesh can be also applied to lower frequencies -as it would improve the accuracy- but not the other way around.

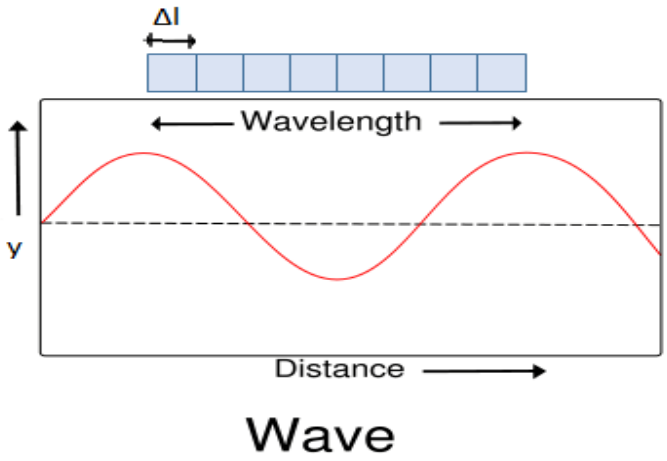

Figure 2-9: Wavelength associated with the finite element-size

2.6.2 Boundary conditions

In the case of a static deformation analysis, prescribed boundary displacements are introduced at the boundaries of a finite element model. The boundaries can be completely free or fixities can be applied in one or two directions. Particularly the vertical boundaries of a mesh are often non-physical (synthetic) boundaries that have been chosen so that they do not actually influence the deformation behavior of the construction to be modelled. This means that the boundaries are “far away”. For dynamic calculations, the boundaries should be in principle much further away than those for static calculations, because otherwise stress waves will be reflected leading to distortions in the computed results. However, locating the boundaries far away requires many extra elements and therefore a lot of extra memory and calculating time.

To counteract reflections, special measures are needed at the boundaries, namely silent or absorbent boundaries. Various methods are used to create these boundaries, which include:

- Use of half-infinite elements (boundary elements).
- Adaption of the material properties of elements at the boundary (low stiffness, high viscosity).
- Use of viscous boundaries (dampers)

All of these methods have their advantages and disadvantages and are problem dependent. For all the implementation of dynamic effects in PLAXIS the absorbent boundaries are created with the last method (viscous boundaries) and more details on the way this method works are described in chapter 3.

2.6.3 Finite dimensions of the numerical domain

As one can conclude from the aforementioned, the boundaries of the numerical model affect the obtained results when shear waves are involved. The waves transmit and reflect at the boundaries of the model so it is imperative to keep the region that will be under observation to study and interpret the results, as far as possible from any reflecting boundary. This should help minimizing the influence of the boundaries but will increase exceedingly the computational cost. Hence, finding the optimum dimensions of the finite model is a key factor to every dynamic analysis.

In this current project in order to determine the optimum domain width for the model, sensitivity analysis has been performed. Considering the depth of the numerical model no clear indications exist in literature. In order to set the depth of the domain so that to have negligible influence on the response, sensitivity analysis has been also performed in the same way as for the width of the domain.

2.7 PLAXIS 3D

PLAXIS 3D is a three-dimensional finite element program, developed for the analysis of deformation, stability and groundwater flow in geotechnical engineering. PLAXIS began its development in 1987 at Delft University of Technology as an easy-to-use 2D finite element program focusing on geotechnical applications. The 3D code first introduced in 2001 when the 3DTunnel program released for the first time. In 2004 the second three dimensional program released, 3DFoundations. However, in neither of these two programs was it possible to define arbitrary 3D geometries because of their geometrical limitations, hence the need of a new full three dimensional program lead to the development of the PLAXIS 3D code which combines an easy-to-use interface with full 3D modelling facilities. The PLAXIS 3D program firstly released in 2010.

The main problem of the most finite element codes is that they are very complicated for an engineer who is not familiar with computer programming. This problem gets more complicated when 3D geometry has to be considered. The main advantage of PLAXIS 3D program is that it can be used by geotechnical engineers who are not necessarily numerical specialists. It is a practical tool for geotechnical applications that provide finite element computations in an easy and not complicated way. As a result, many practical engineers world-wide have adopted this product and use it for engineering purposes. Furthermore PLAXIS 3D is used more and more lately by researchers in universities all over the world in the field of geo-mechanics and numerical methods. Important conclusions have been made by researchers using the PLAXIS code.

This user-friendly interface hides however some risks especially when the program is used by engineers who have not much experience to filter and judge the out coming results. These risks refer not only to PLAXIS but also to all finite element codes that are available. Above all, the simulation of reality by a computer program remains an approximation which implicitly involves some inevitable numerical and modelling errors. Moreover the accuracy at which reality is approximated depends highly on the expertise of the user regarding the modelling of the problem, the understanding of the soil models and their limitations, the selection of model parameters, and the

ability to judge the reliability of the computational results. In conclusion, proper attention should always be paid and the results should be compared, even crudely, with other solutions, simplified or not.

In this thesis, PLAXIS 3D has been used for the performance of the numerical elastic and inelastic analyses and the results have been compared with either solutions from the literature or real facts from field trials (case study). In the following some details of the program that were used in this thesis are given, in order the reader to be able to understand the numerical analyses that performed. Most of the information that follow are given in the PLAXIS manuals.

2.7.1 Constitutive models

Hardening Soil model (HS)

In the Mohr-Coulomb model, material yielding only is a function of the stress tensor. However, for many materials this actually will not be the case. As a result of plastic straining history, the yield function may develop, instead of being fixed in the principal stress space. This phenomena is called hardening, for which generally two types are distinguished, being strain hardening and kinematic hardening. Strain hardening is included in the HS model and can be subdivided in compression hardening and shear hardening. Material models including hardening/softening conceptually better represent actual soil behavior when implemented in soil finite element calculations. It is however noted that real soil hardening behavior is very complex and most models account for this in a very simplified way.

Initially the Hardening Soil Model was first introduced in the Plaxis program as an extension of the Mohr Coulomb model. Then in Plaxis Version 7, an additional cap was added to the model to allow for the pre-consolidation pressure to be taken into account, at this point the soil model name was changed to Hardening Soil Model. The change indicates that the model has the capacity to be used for softer soils, including soft clay, with the aid of Mobilized Friction Function.

Indeed, Hardening Soil model has developed under the framework of the theory of plasticity. In the model, the total strains are calculated using a stress-dependent stiffness, which is different for both loading and unloading/reloading. Hardening is assumed to be isotropic, depending on the plastic shear and volumetric strains. A non-associated flow rule is adopted when related to frictional hardening and an associated flow rule is assumed for the cap hardening. This soil constitutive model including hardening has been developed by Schanz and Vermeer (1998) and it has been implemented in the Plaxis finite element code. Provided a proper parameter selection, the HS model is known to represent soil constitutive behavior reasonably accurate for both soft and stiffer soil types, which is related to its features of stress dependent stiffness, different for both virgin loading and unloading/reloading as it is also observed for real soils.

In fact the HS model allows for hardening related to material effective stresses, but on top of it a Mohr-Coulomb model is applied based on ultimate strength parameters (c' and ϕ') governing the ultimate failure state of the material. This is schematically represented in Figure 2-10. Plaxis offers the possibility to input effective strength/stiffness parameters for both drained and undrained analysis, where undrained material behavior then is governed by effective parameters and excess pore pressure generation based on the water bulk modulus (Undrained calculation method A). Alternatively one may input effective stiffness parameters with undrained shear strength (Undrained calculation method B), which however removes the stress dependent stiffness feature from the constitutive model (ϕ' is set to zero). More details about these methods are presented in 2.7.2.

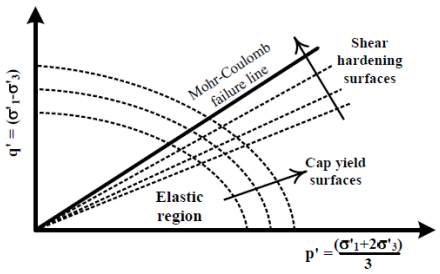

Figure 2-10: Expansion of the Mohr-Coulomb yield surface in the HS model for increasing effective stresses.

In the hardening soil model, stiffness develops as a function of the stress/strain state. Three types of soil stiffness (E_{50}, E_{oed}, E_{ur}) can be inputted independently for three typical loading conditions being triaxial loading, oedometer loading and unloading/reloading respectively. The figure below represents the physical meaning of these three stiffness parameters.

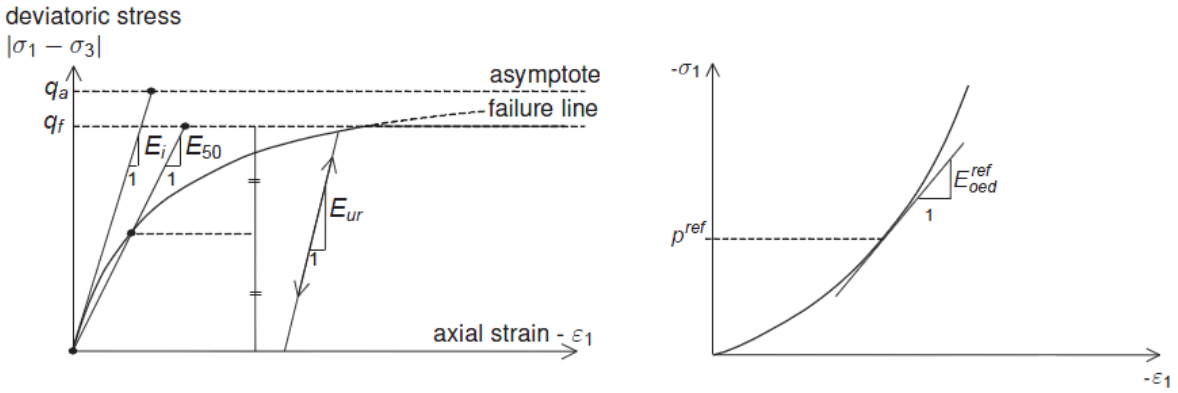

Figure 2-11: Definition of the three types of stiffness parameters in the HS model. Left triaxial testing, right oedometer testing.

Expansion of the yield surface cone is related to shear strains and stiffness parameter E_{50} where on the other hand the expansion of the yield cap (see Figure 2-10 and Figure 2-12) is governed by E_{oed} and the isotropic stress/strain state. The shape of the cap closing the elastic region is determined indirectly by K_0^{NC} and E_{oed}. E_{ur} governs elastic behavior within the yield contour resulting from previous ultimate stress/strain state.

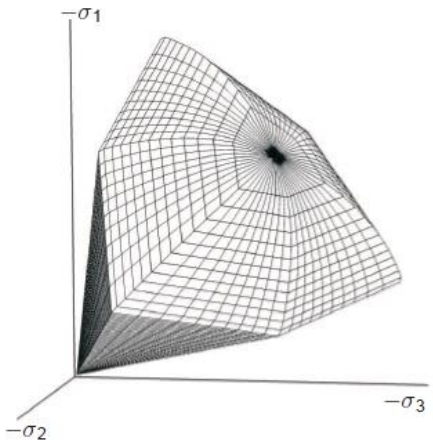

Figure 2-12: The closed HS model yield surface including the yield cap.

Stiffness parameters as mentioned before depend on stress conditions, which would imply that a specific stiffness needs to be inputted based on local assumed stress state. Within the Plaxis Hardening Soil Model this cumbersome selection of input parameters is not required. Instead, the user has to input a reference soil stiffness for a fixed stress level of p_{ref}=100 kPa, and the program automatically adapts stiffness as a function of local stress conditions, the soil ultimate strength properties and a factor representing the level of stiffness stress dependency.

Hardening Soil model with small-strain stiffness (HSsmall)

As explained in the previous section, unloading/reloading within the yield surface is assumed to be linear elastic in the original Hardening Soil model. However truly elastic unloading/reloading behavior for soils is only observed in the very small strain range, where stiffness is high. When strains grow, the unloading/reloading stiffness has a nonlinear dependency on strain amplitude, as indicated in Figure 2-13.

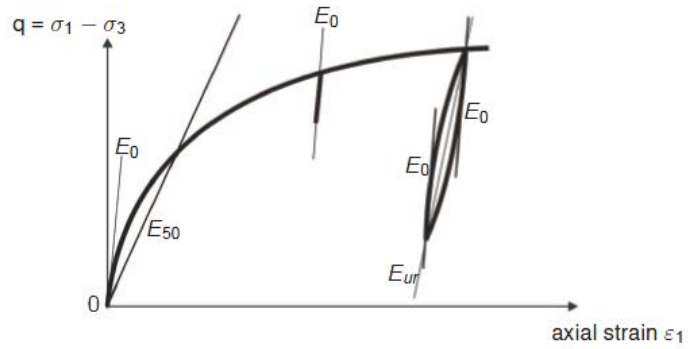

Figure 2-13: HSsmall stress dependent stiffness for triaxial loading conditions.

A small strain overlay model including this phenomena, has been developed for the HS model by Benz (2006). Since the HSsmall model in Plaxis is only an extension of the conventional HS model, it needs only two additional parameters to be defined, i.e. the very small-strain shear modulus G_0 and the shear strain level $\gamma_{0.7}$ at which the secant shear modulus G_s is reduced to 72.2% of G_0. From various test data, it is found

that the stress-strain curve for small strains can be approximately be described by a simple hyperbolic law. The basic characteristic of this hyperbolic relation (Hardin & Drnevich, 1972) is a decrease of stiffness, with increasing strains due to loss of intermolecular and surface forces within the soil skeleton. As a result, actual soil stiffness also for unloading/reloading depends on the small strain loading history, which in the HSsmall model is in accordance to Figure 2-14 taken into account by:

$$\frac{G_s}{G_0} = \frac{1}{1 + a\left|\frac{\gamma}{\gamma_{0,7}}\right|}$$

Where α=0.385, $\gamma_{0,7}$ is the reference strain input parameter as discussed before and γ is a function of the strain history, determined to be a scalar quantity by Benz (2006). Subsequently the HSsmall model constitutive soil relation in the small strain range is easily found from the secant shear modulus G_s as determined by the aforementioned equation, differentiation with respect to strain then results a tangent expression which can be used on time integration procedures.

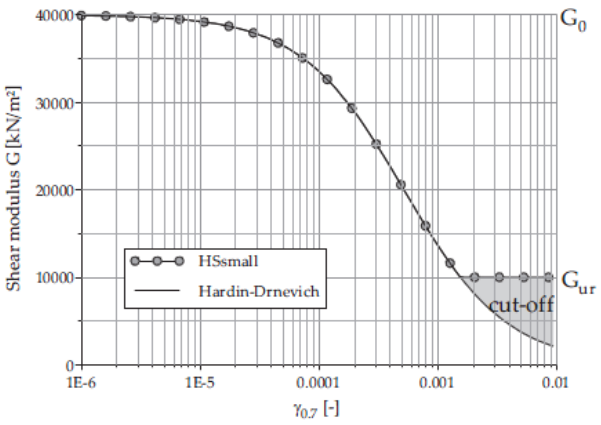

Figure 2-14: Small strain stiffness reduction according to the HSsmall model

As indicated only two additional parameters G_0^{ref}, $\gamma_{0.7}$ need to be defined for the HSsmall model compared to the HS model. The former parameter may (just as for the HS model) be inputted related to a reference stress level and many correlations are presented in literature. A good correlation to void ratio for many soils was presented by (Hardin & Black, 1969) or to unload/reload stiffness as empirically defined by (Alpan, 1970). The latter reference strain level may be related to the soil

plasticity index, or can be defined by using the original Hardin-Drnevich relationship and the Mohr-Coulomb failure criterion.

Under dynamic loading, unloading/reloading loops as included in the HSsmall model, introduce a hysteretic damping component. According to the Hardin-Drnevich relationship for G/G_0 as a function of shear strain, this damping will be negligibly small for small motion amplitudes, which appears to be unrealistic compared to actual soil behavior. Therefore it is recommended (Bringreve, et al., 2007) to introduce additionally a small amount of Rayleigh damping in the model. Fir this Rayleigh damping 1-2% of critical damping may be assumed to be reasonable. On the contrary, the same study shows the hysteretic damping at higher shear strain levels resulting from the HSsmall model to be overestimating actual clay material damping, which can be solved by setting G_0 closer to G_{ur}.

Except for the aforementioned constitutive models that mainly have adapted for this study PLAXIS offers a variety of other constitutive models each one of which is appropriate for different applications. Below are presented in a very brief way the available models.

2.7.2 Drained and undrained modelling

Numerical analyses of undrained materials are complex and therefore, require an understanding in calculation methods and constitutive models. Advantages and limitations of available undrained analysis methods in Plaxis software are summarized and discussed herein.

In conduction a finite element analysis, care must be taken to the drained and undrained behavior of the modelled soils. In case of high permeability material such as sand, appropriate type of analysis is drained analyses. There is no complication in carrying out drained analysis for drained material due to the fact that only effective strength and stiffness parameters should be adopted in conjunction with drained material setting. This drained analysis is applicable for both basic Mohr Coulomb

model (MC) and advanced models, such as the Hardening Soil model (HS) and others. Modelling of undrained material, i.e. clayey types of soil, is on the other hand more complex. Brief summary of drained and undrained analyses is given below.

Drained analysis:

- Applicable for modelling the behavior of high permeability (sandy) materials or low permeability (clayey) materials in case of low rate of loading.
- Short term behavior is not of interest for the problem considered.
- No excess pore pressure is generated.

Undrained analysis:

- Applicable only for modelling the behavior of low permeability (clayey) materials with a high rate of loading.
- Short term behavior is to be accessed.
- Excess pore pressure is fully generated.

Various FE analysis methods are available for undrained behavior modelling. Selection of effective and total stress parameters should be made together with the type of soil model used prior to the modelling process. Basically, there are three methods available in Plaxis, namely Method A, B and C. Method A is used in combination with basic models, Linear Elastic (LE), Mohr Coulomb (MC) as well as advanced models, Hardening Soil (HS), Hardening Soil with small-strain stiffness (HS small), Soft Soil (SS), Soft Soil Creep (SSC) and Modified Cam Clay (MCC) soil models. Method B is used in combination with MC, HS and HS small models while method C is only used for the basic models, LE and MC. Details of each method are given in the following.

When material type is set to “undrained” (Methods A, B and C), Plaxis automatically adds bulk modulus of water, K_w/n ($n=e_0/(1+e_0)$: soil porosity), to the bulk modulus of soil skeleton, K’, and distinguishes between total stresses, effective stresses and excess pore pressures:

Total stress: $\Delta\sigma = K_u \Delta\varepsilon_v$

Effective stress: $\Delta\sigma' = (1 - B)\Delta\sigma = K'\Delta\varepsilon_v$

Excess pore pressure: $\Delta u = B\Delta\sigma = \frac{K_w}{n}\Delta\varepsilon_v$

Excess pore pressure (triaxial): $\Delta u = B(\Delta\sigma_3 + A(\Delta\sigma_1 - \Delta\sigma_3)$

Where Δσ, Δσ' and Δu are changes in total stress effective stress and pore pressure respectively. A and B are the Skempton's parameters. Skempton A-parameter is not a soil parameter, in fact its value depends on calculated stress path resulting from constitutive model used. K_u is the total undrained bulk modulus:

$$K_u = K' + \frac{K_w}{n}$$

$$K_u = \frac{E_u}{3(1 - 2v_u)} = \frac{2G(1 + v_u)}{3(1 - 2v_u)} = \frac{E'(1 + v_u)}{3(1 - 2v_u)(1 + v')}$$

Where E_u and E' are undrained and drained elastic moduli, G is shear modulus, v_u and v' are undrained and drained Poisson's ratios. Calculation of effective stress and excess pore pressure involves Skempton B-parameter which can be approximated by:

$$B = \frac{1}{1 + \frac{n}{K_w}K'}$$

According to this equation, Skempton B-parameter approaches unity when bulk modulus of water, K_w/n is very high compare to the bulk modulus of soil skeleton, K'. In reality, a high realistic bulk modulus of water may cause numerical problems in the calculation, therefore Plaxis utilizes slightly lower number of bulk modulus of water as calculated by the following process. First bulk modulus of soil skeleton, K' is estimated from the input drained elastic modulus, E':

$$K' = \frac{E'}{3(1 - 2v')}$$

Then, estimates total (undrained) bulk modulus, K_u. Note that Plaxis uses value of 0.495 for undrained Poisson's ratio as default setting. Finally, Skempton B-parameter is obtained. Following this process, Skempton B-parameter will depend only on the

value of drained Poisson's ratio. For undrained behavior, drained Poisson's ratio should be smaller than 0.35, as using higher values would lead to an unrealistically low Skempton B-parameter.

Figure 2-15 illustrates typical total stress path (TSP) and effective stress paths (ESP) resulting from isotropically consolidated undrained triaxial test of normally consolidated clay. Stress paths OA, OB, OC and OD in figure (a to d) are the calculated results of Method A, B, C and B respectively. Details of each method are summarized in the following.

Method A:

Method A utilizes both effective stress and stiffness parameters to model undrained behavior of soils. The constitutive model used is Mohr-Coulomb model. As shown in figure (a), effective stress path (ESP) predicted by MC model rose up vertically until failure envelope is reached (stress path OA). This stress path is unlikely to be identical to the real stress path especially in case of normally consolidated clay. As a result, calculated pore water pressure is also unlikely to be correct. Furthermore, undrained shear strength predicted by method A (Point A) may exceed the undrained shear strength as followed by triaxial effective stress path. Due to the unreliability of both soil strength and pore water pressure calculation, this method should generally be avoided.

Method B:

Similar to Method A effective stiffness parameters are used in Method B. However, the failure criterion is governed by an input total strength parameter, i.e. $\phi_u=0$ and $c=S_u$. Calculated stress path from Method B is identical to that of from Method A (stress path OB) for the Mohr Coulomb model, therefore calculated pore water pressure should be ignored. For this reason, Method B should not be followed by consolidation analyses.

It should be note that if Hardening Soil or Hardening Soil small models are selected in Method B, the stiffness moduli will be no longer stress-dependent and the model exhibits no compression hardening. Conversely, the model retains its separation of loading and unloading-reloading moduli and shear hardening. Stress path OD in Figure (d) utilizes a more sophisticated advanced model (such as HS model). Undrained shear strength computed from this method depends on the accuracy of effective stress path as obtained from the advanced model used.

Method C:

Method C is a total stress approach. It adopts both undrained strength and undrained stiffness parameters. Material type of Method C is set to “Undrained C” or “Non-porous” which means neither initial nor excess pore pressure will be taken into account. The disadvantage of this approach is that no distinction is made between effective stress and pore water pressure. Hence, all calculated stresses are total stress and pore water pressures are equal to zero. In Plaxis it is possible to perform a total stress analysis with undrained parameters if the Mohr Coulomb model or the NGI-ADP model is used.

It should be noted that a direct input of undrained shear strength does not automatically give the increase of shear strength with consolidation. In fact, it does not make sense to perform a consolidation analysis since there are no pore pressures to consolidate.

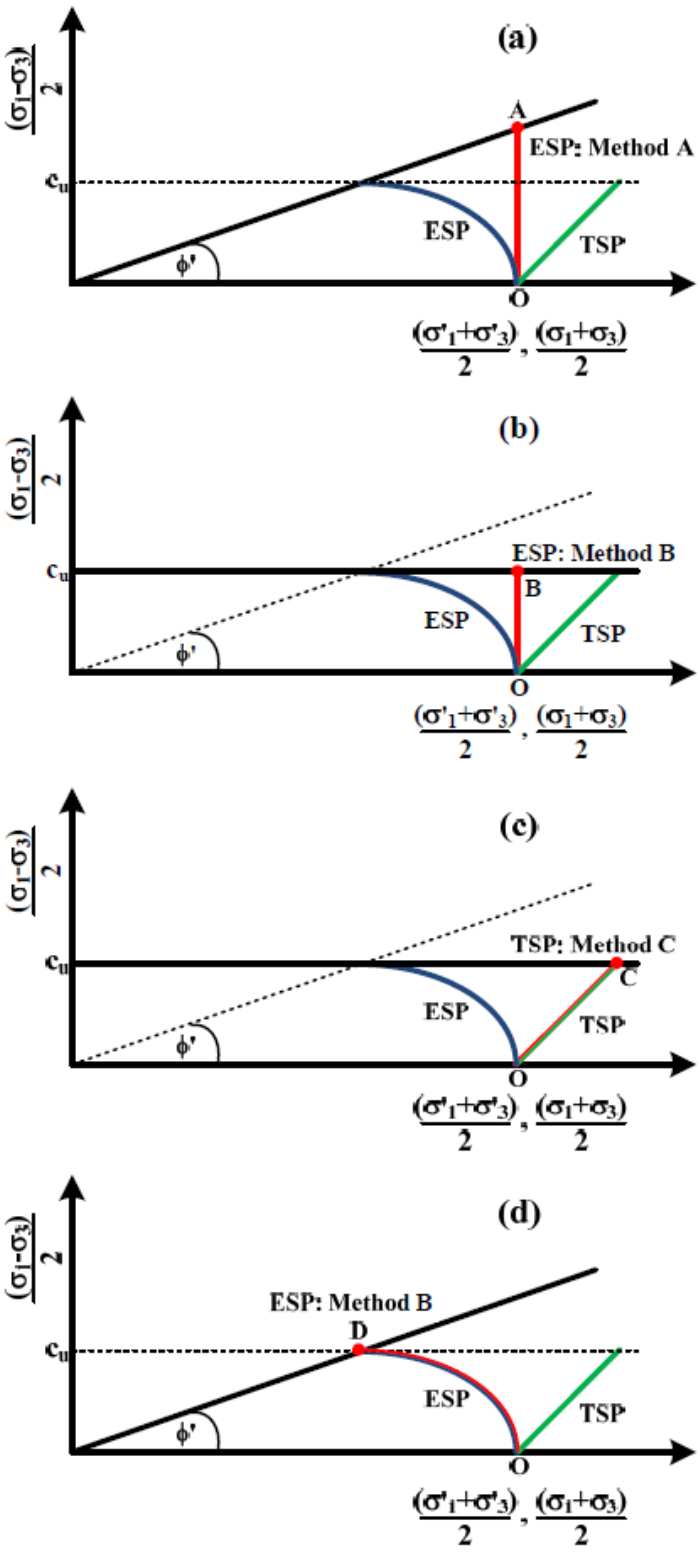

Figure 2-15: Calculated stress paths resulting from methods A, B, C. (a), (b), and (c): Mohr Coulomb model (d): Hardening Soil model

2.7.3 Element type

The soil formation is simulated using 3D continuum soil elements. These 10-node tetrahedral elements provide a second-order interpolation of displacements. There are three local coordinates (ξ, η and ζ) as it can been seen in Figure 2-16. The soil elements have three degrees of freedom per node.

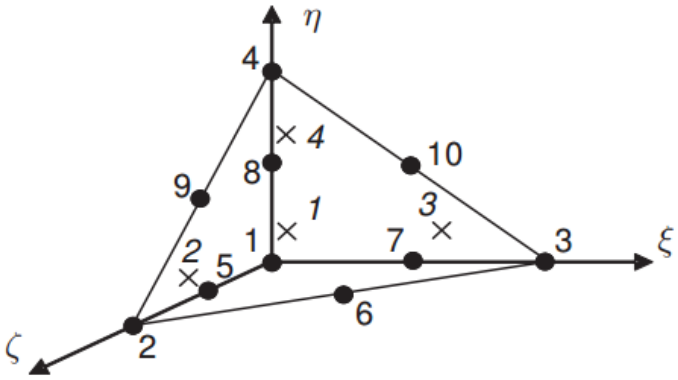

Figure 2-16: Nodes (•) and integration points (x) of a 10-node tetrahedral element (after (PLAXIS3D, 2012) p41)

The numerical integration over volumes can be formulated as:

$$\iiint F(\xi,\eta,\zeta)\, d\xi\, d\eta\, d\zeta \approx \sum_{i=1}^{k} F(\xi_i,\eta_i,\zeta_i)\, w_i$$

Where w_i are the weight factors. The sum of the weight factors is equal to 1/6.

The PLAXIS program uses Gaussian integration within tetrahedral elements and is based on 4 sample points. For more details the reader is referred to (PLAXIS3D, 2012, pp. 40-48)

In addition to the soil elements, special types of elements are used to model structural behavior. For beams. 3-node line elements are used, which are compatible with the 3-node edges of a soil element. In addition, 6-node plate and geogrid elements are used to simulate the behavior of plates and geogrids respectively. Moreover, 12-node interface elements are used to simulate soil-structure interaction behavior.

2.7.4 Interfaces

Interfaces are used when modeling soil structure interaction. Interfaces will be required to simulate the finite frictional resistance between the structure such as the caisson and adjacent soil. It allows relative displacement and separation between the structure and soil mass. When using 6-node elements for soil, the corresponding interface elements are defined by three pairs of nodes, whereas for 15-node soil elements the corresponding interface elements are defined by five pairs of nodes.

The stiffness matrix for interface elements is obtained using Newton-Cotes integration points. The position of these integration points coincides with the position of the node pairs. The 6-node interface elements use a 3-point Newton-Cotes integration, whereas the 10-node interface elements use 5-point Newton-Cotes integration.

The basic property of an interface element is the associated material data set for soil and interfaces. Interface element models the interaction between the foundation and the soil, which is intermediate between smooth and fully rough. The roughness of the interaction is modeled by choosing a suitable value for the strength reduction factor in the interface (R_{inter}). This factor relates the interface strength (structure surface friction and adhesion) to the soil strength (friction angle and cohesion). Furthermore a new material with different strength and stiffness parameters than the surrounding soil can be set for the interface elements. An elastic-plastic model is used to describe the behavior of interfaces for the modeling of soil-structure interaction. The Coulomb criterion is used to distinguish between elastic behavior, where small displacements can occur within the interface, and plastic interface behavior when permanent slip may occur.

2.7.5 Absorbent boundaries

As mentioned in the previous chapters the boundaries of the numerical model play a very important role especially for the dynamic analyses. In this thesis absorbent boundaries are applied for the dynamic numerical analyses of caisson.

In opting for absorbent boundaries, a damper is used instead of applying fixities in a certain direction. The damper ensures that an increase in stress on the boundary is absorbed without rebounding. The boundary then starts to move.

The use of absorbent boundaries in PLAXIS is based on the method described by (Lysmer & Kuhlmeyer, 1969).

The normal and shear stress components absorbed by a damper in x-direction are:

$$\sigma_n = -C_1 \rho V_p \dot{u}_x$$

$$\tau = -C_2 \rho V_s \dot{u}_y$$

Here, ρ is the density of the materials, V_p and V_s are the pressure wave velocity and the shear wave velocity, respectively. C_1 and C_2 are relaxation coefficients that have been introduced in order to improve the effect of the absorption. When pressure waves only strike the boundary perpendicular, relaxation is redundant (C_1=C_2=1).

In the presence of shear waves, the damping effect of the absorbent boundaries is not sufficient without relaxation. The effect can be improved by adapting the second coefficient in particular. The experience gained until now shows that the use of C_1=1 and C_2=0.25 results in a reasonable absorption of waves at the boundary. However, it is not possible state that shear waves are fully absorbed so that in the presence of shear waves a limited boundary effect is noticeable. Additional research is therefore necessary on this point, but the method described will be sufficient for practical applications.

For an inclined boundary, an adjusted formulation based on the equations mentioned above is used that takes place the angle of the boundary into account.

(PLAXIS3D, 2012, p. 57)

2.7.6 Mesh properties

To perform finite element calculations, the geometry has to be divided into elements. A composition of finite elements is called a finite element mesh. 3D finite element calculations are very time-consuming. The time consumption highly

depends on the number of elements used in the analysis. Moreover, when using a large number of 3D elements, the model may be too large to fit in the computer's RAM. Hence care should be taken when generating 3D finite element meshes.

On the other hand, a certain number of elements is required to obtain sufficiently accurate deformations. An even finer mesh is needed when accurate failure loads, bearing capacities or structural forces are to be calculated. When judging the accuracy of 3D finite elements meshes it must be taken into account that the 3D elements have quadratic interpolation functions. Hence, they are more accurate than linear elements, but not as accurate as the 15-node elements in 2D PLAXIS versions.

PLAXIS allows for a fully automatic generation of finite element mesh. The mesh generation process takes into account the soil stratigraphy as well as all structural objects, loads and boundary conditions. The generation of the mesh is based on a robust triangulation procedure, which results in "unstructured" meshes. These meshes may look disorderly, but the numerical performance of such meshes may yield better results than for regular structured meshes.

The mesh generator requires a general meshing parameter which represents the average element size, Δl, computed based on the outer geometry dimensions (x_{min}, x_{max}, y_{min}, y_{max}, z_{min}, z_{max}) using the following relationship:

$$\Delta l = \frac{r_e}{20}\sqrt{(x_{max} - x_{min})^2 (y_{max} - y_{min})^2 (z_{max} - z_{min})^2}$$

Where r_e = 2.0 (very coarse mesh)
= 1.5 (coarse mesh)
= 1.0 (medium mesh)
= 0.7 (fine mesh)
= 0.5 (very fine mesh)

The relative element size factor (r_e) can be modified by the user defining the desirable element distribution. Moreover the user has the option to make the mesh finer or coarser at certain regions, for example in areas where large stress concentrations or large deformation gradients are to be expected or when the geometry model includes edges or corners of structural objects finer finite element mesh needs to be applied.

2.8 Caissons

2.8.1 Introduction

The term caisson is derived from the French word, “caisson” meaning a chest or box. In civil engineering pier or drilled shafts are other terms that are commonly used instead of caisson. All these terms refer to permanent substructures or foundation elements which are either prefabricated or sunk into position providing massive foundation for heavy loads and high horizontal thrusts. The drilled shafts –bored piles, large-diameter piles, foundation piers, sub-piers or drilled caissons are also commonly references– are structural members of relatively large-diameter massive struts constructed and placed in a pre-excavated hole. Caissons or well foundations are structural boxes or chambers that are sunk in place through the ground or water by systematically excavation. The majority of the caissons are made of concrete and always require steel reinforcement. Occasionally they comprise a steel casing or jacket. Other materials that are being used are timber and masonry.

The total volume of caissons is quite large compared to other kinds of foundation. In Figure 2-17 a crude typical classification of foundation elements is presented according to the geometric characteristics of slenderness or depth of embedment. Caissons’ embedment depth is larger than the corresponding depth of shallow embedded foundations, and lower than typical values of pile foundations. Moreover caissons can be classified further depending on their depth (deep or shallow), their diameter (small or large) and the shape of their plan (Figure 2-18). Typical dimensions for caissons are diameters on the order of 0.60–4.00 meters and depth to diameter ratios in the range of 0.60–4.50 meters.

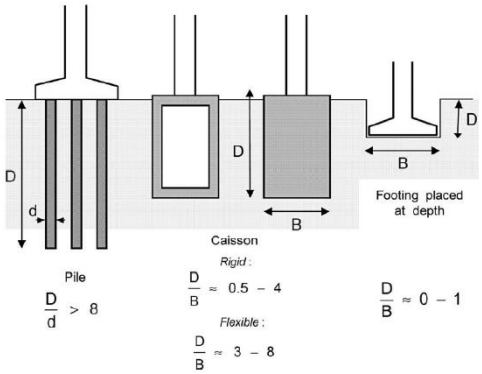

Figure 2-17: Crude classification of foundations (after (Gerolymos & Gazetas, 2006))

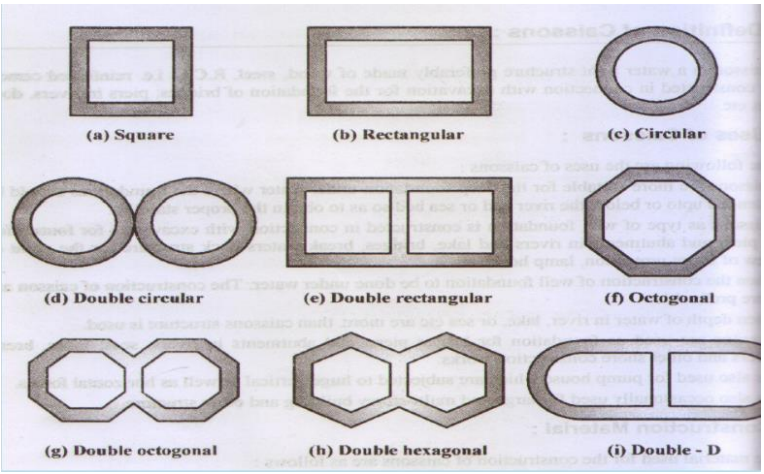

Figure 2-18: Various shapes of plan views of caissons

In general, a caisson foundation is recommended and found to be advantageous when large-size boulders are encountered and a massive sub-structure is required to withstand large lateral stresses. Caissons are more suitable for deep foundations under water where the foundation should be extended up to or below the river bed in order to obtain the proper stability. In this case caissons are more cost effective than piles. Caisson are also suitable as foundation for bridge piers, and abutments in rivers, seas, lakes, break waters and other shore construction works. They are also used for large pump houses which are subjected to heavy vertical as well as horizontal forces. Occasionally caissons are used for large and multistory building and other structures but generally, caissons are used for major foundation works because of the high construction cost.

2.8.2 Historic examples

The purpose of the caissons is protecting walls against water pressure and soil collapse or supporting major superstructures. Traditionally caissons are selected as the most practical method of founding long span bridges which impose heavy loads, in deep water environments. Many examples of these massive constructions can be found in real life. The Tagus Bridge in Portugal is supported on one of the tallest caisson in the world reaching the height of 88 meters. The San Francisco-Oakland bay bridge is founded on a 75 m high caisson. The Williamsburg and Verrazano Narrows

bridges in New York as well as the Port Island and Nishinomiya-ko bridges in Japan are also supported on massive caissons. The well-known longest suspension bridge, Akashi-Kaikyo, shown in Figure 2-19, is founded on huge caissons. In South Africa also, caissons have been successfully used in situations where the designs were best served by rigid support systems founded on dense sands or rock at depths ranging from about 20 m to 30 m in both land and water environments.

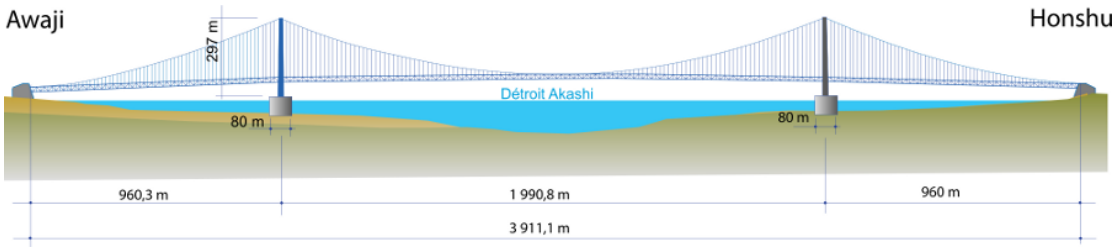

Figure 2-19: Akashi Kaikyo bridge in Japan, the longest suspension bridge in the world. The foundation consists of major caissons.

2.8.3 Construction methods

According to the construction process and their use, caissons can be classified into three major types:

a) Open caissons
b) Box caissons
c) Pneumatic caissons

The first category refer to box type structures which remain open both at the top and at the bottom during construction. Open caisson is the main foundation type of constructing deep foundation and underground structures and is extensively used. They are normally used on sandy soils or soft bearing stratum and where no firm bed is available at a higher depth. According to the shape of caissons, open caissons can be divided into three types: single wall, cylindrical open caisson and open caissons with dredging wells. Monoliths is a special type of open caissons which are much larger than others and are often found in quay walls, where resistance to impact from ships is required. Their heavy weight is favorable for resisting these lateral and impact forces. In order to construct open caissons firstly an open reinforced concrete tube body is made on the ground. Then, when it achieves a certain strength, soil is excavated and transported. With soil level gradually reduced, caisson constantly sink and finally take its place with its own gravity overcoming the friction resistance.

Box caissons are similar to open caissons but with the only difference that they are closed at the bottom. Box caissons are cast and cured properly on ground and then they are launched in water by filling sand, gravel or concrete in the empty spaces. Mostly reinforced concrete is used for making box caissons. A box caisson during floating should be sufficiently safe against the danger of tipping or capsizing. The stability of a floating caisson can be analyzed using the principles of hydrostatics. Box caissons can also be floated in horizontal or inverted positions and placed at the required location in normal position. They can be founded on dredged gravel or rock formation, on crushed rock blanket over rock surface, or on piled raft. Box caissons are not suitable in sites where erosion can undermine the foundations.

Pneumatic caissons are open at the bottom and close at the top. This type of caisson is specially used at situations where it is not possible to construct the well because the soil flow into the excavated area is faster than it can be removed. It is suitable for depth of water more than 12 m as for shallower depths their cost make them inappropriate. In the construction of pneumatic caisson, compressed air is used to remove water from the working chamber and the foundation work is carried out in dry condition. This type of caisson has several advantages compared over open or box-type caissons. Excavations can be carried out by hand in a dry working chamber, soil condition at the foundation level can be inspected as insitu soil tests are possible to determine the bearing capacity, foundation concrete can be placed under ideal conditions as it is known the concrete gain more strength due to dry conditions. Also for major projects, greater depths in bed rocks can be possible and there is no danger of settlement of adjoining structures because of no lowering of ground water table. However, despite the aforementioned advantages, pneumatic caissons have some disadvantages. Their construction is much more expensive compared to open caissons. There are more chances of caisson diseases to workmen working under high pressure. This is why during the whole operation the air pressure should be properly controlled, otherwise fatal accidents are possible. Compared to open caissons, the process of sinking is slower and needs elaborate equipment. Last but not least, the maximum depth below water table is limited to 30 to 40 meters as beyond 40 meters the construction is not possible.

Figure 2-20: Caisson during construction

2.8.4 Advantages - Disadvantages

In general, caissons as an alternative foundation method, are more cost-effective comparing to other regular design methodologies and this is the main reason that are chosen to found constructions. Basically caisson-foundation is more or less similar in form to pile foundation but installed using different way as described before. However, compared to pile or shallow foundations the main advantage is the high axial and lateral load carrying capacity. The construction process generates less noise and vibration, both of which are especially important when working near existing buildings. Moreover, engineers can observe and classify the soils excavated during drilling and compare them with the anticipated soil conditions. Designers can easily change the diameter or length of the shaft during construction to compensate for unanticipated soil conditions. Considering the drilled shafts, the foundation can penetrate through soils with cobbles or boulders, especially when the shaft diameter is large. It is also possible to penetrate many types of bedrocks including residual soils, karstic formations, soft soils and marine sites. When caisson foundations are selected instead of using pile groups, the structural columns may be directly connected to the foundation, thus eliminating the need for a pile cap. Of course in order to select this kind of foundation, structure and site conditions should be properly investigated.

However there are also some disadvantages considering caisson-foundations. Successful construction is very much dependent on contractor's skills. Poor workmanship can produce a weak foundation that may not be able to support the design load. Furthermore, shaft construction removes soil from the ground causing in this way reduction of lateral soil pressure and consequently reducing skin friction. The shaft construction loosens the soil beneath the tip thus giving a lower end bearing. Finally it should be mentioned that full-scale load tests are usually very expensive so the design is based more on theoretical and empirical aspects than experimental.

2.8.5 The influence of the embedment

In general, the embedment ratio has an influence not only to the kinematic interaction but also to the inertial interaction of the caisson.

Considering the kinematic interaction, the embedment causes reduction of the lateral displacement in comparison to the free field while it also introduces a rotation angle. In general as the embedment ratio arises, the lateral displacement decreases while the rotation increases. The rotation is a very important part of the movement of the foundation. If it is been neglected and simultaneously the lateral displacement is considered reduced this might lead to non-conservative results. In many cases it is easy and practical to consider as excitation of the system soil-foundation the free field movement. For the surface foundation under vertical transmitted shear waves it has been proved that this consideration is correct. Even at small embedment ratios ignoring the kinematic interaction leads many times to conservative results (Gazetas, 1983) (Aviles & Perez-Rocha, 1998). However, tall structures that are founded in great depths are subjected to important rotation at their base with direct effects on their response. Ignoring the kinematic interaction at these occasions is not correct since it might lead to unsafety.

Considering the inertial interaction, embedment in general increases the complex impedance of the soil-structure system. The contact between the sidewalls of the foundation and the surrounding soil increase not only the stiffness but also the damping of the system. However the real area of the “good” contact of the sidewalls with surrounding soil is many times less than the total geometric area. Ignoring this might lead to wrong calculation of the impedance which way far of the reality. Furthermore the lateral excitation of the caisson cause not only lateral vibration but also rotational vibration. In this way the coupling impedance is introduced. For shallow embedded foundation this coupling might be ignored but for greater depths its influence is very important.

A general conclusion that can be made is that the embedment increases the strength of the foundation as well as the stiffness for any type of loading. An explanation of this statement holds on the below reasons which are schematically presented in Figure 2-21:

a) The base of the foundation lies not at the free surface of the soil but at a certain depth (trench effect)
b) The influence of the lateral walls that a surface foundation does not have (sidewall effect)

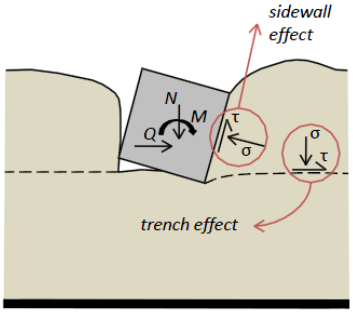

Figure 2-21: The influence of the embedment on the bearing capacity and the stiffness of a caisson (after (Dritsos '12).

2.8.6 Design methodologies

For many years deep foundations have been an interesting subject that has concerned many famous studiers. Especially for the lateral and seismic response of such foundations many different methods have been developed and used. However, almost all the methods that were applied for caissons follow the same semi-empirical approach as used for flexible pile foundations and so they are not directly deal with caisson physics. Another design approach for caissons came up from the observation that pier foundations are more likely to behave as rigid embedded elements rather than as flexible piles. Thus, analytical solutions for shallow embedded surface foundations have been used for providing the response of caissons to lateral loading. These solutions however, are restricted to low embedment depths and do not deal with the soil-structure interaction effects of caisson foundation. In a brief review (Gerolymos & Gazetas, 2006) and (Varun, et al., 2009) present in chronological order a partial list of such designing methods for caissons. In these methods algebraic expressions have been developed that account for arbitrary foundation shape and degree of embedment, and for a variety of soil conditions for the estimation of the dynamic impedance of footings.

Based on the aforementioned methods, more recently, dynamic Winkler models have been developed and modified for the direct application to caissons. Being perhaps the most popular approaches used in practice, these models account properly the soil resistance mechanisms mobilized at the base and the circumference of laterally loaded piers as shown in Figure 2-22. The foundation in these methods is supported by a series of independent vertical, rotational and horizontal springs and dashpots along the soil-footing interface which correspond to the vibration modes.

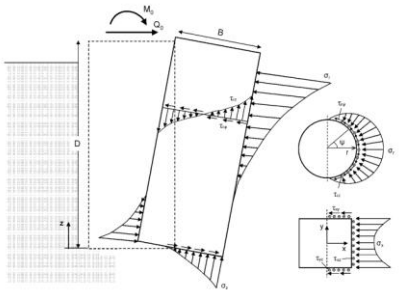

Figure 2-22: Stresses at caisson-soil interface with circular, or square plan shape (after (Gerolymos & Gazetas, 2006))

Continuum model solutions like the widely available commercial 3D finite-element methods can provide more sophisticated solutions that can treat soil nonlinearities and interface issues. However, the use of such programs for the design of non-critical facilities is still limited because of requirements such as computational cost, associated site investigation cost and also user expertise knowledge and experience. Nevertheless, the rising development of the 3D finite element codes have made the use of such methods more practical by limiting these requirements with more and more efficient algorithms and much more user-friendly interface. Thus, taking into account this rising usage of the 3D Finite Element Codes, the need of evaluating the results of such codes and comparing them with other already known solutions has derived.

One of the main objective of this study arises by this need. A direct comparison of elastic solutions has been performed, between a very famous and upcoming Finite Element Program, PLAXIS 3D Dynamics (2012) and a well-established and widely used method (Gazetas, 1991).

3 Elastic response

In this part of the thesis the elastic response of a caisson has been studied. The results of numerical analyses have been used in order to calculate the dynamic impedance of the caisson and a direct comparison has been made with solutions from the literature. The formulations of the literature that have been used as well as the computation method from the numerical analyses are described in the following chapters.

3.1 Gazetas elastodynamic formulations

(Gazetas & Tassoulas, 1987) and (Fotopoulou, et al., 1989) have published a comprehensive series of studies on the static and dynamic response of embedded rigid foundations having various plan shapes. Among others they developed closed-form semi-analytical expressions and charts for stiffness and damping of horizontally and rotationally loaded arbitrarily-shaped rigid foundations embedded in homogeneous soil. These expressions are based on some simple physical models calibrated with the results of rigorous and efficient boundary-element and finite-element elastodynamic formulations as well as with numerous results from the published literature. To derive these expressions, incomplete contact between the foundation vertical walls and the surrounding soil were taken into account in a crude way. (Gadre & Dobry, 1998) provided through centrifuge modeling sufficient confirmation of the basic validity of some of the main concepts and results of these expressions.

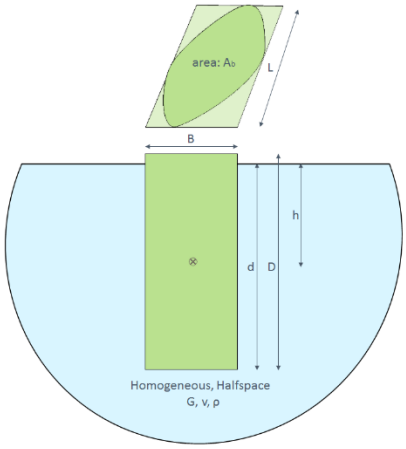

Figure 3-1: Geometry of a rigid foundation embedded in a homogeneous elastic halfspace

The problem that will be studied in this project is that of a square plan rigid caisson embedded in homogeneous elastic halfspace, subjected to lateral dynamic excitation. In general, for arbitrarily shaped foundation in plan view, circumscribed by a rectangle of width B and length L (Figure 3-1), Gazetas and co-workers expressed the dynamic impedances, with respect to the center of the base mat in the form:

$$\widetilde{K} = k + i\omega c$$

- k is the dynamic spring coefficient and is equal to:

$$k = k_{emb,static}\chi_{emb}$$

where $k_{emb,static}$ is the static stiffness and χ_{emb} is the dynamic coefficient which is frequency-dependent, $\chi_{emb}(\omega)$. Consequently the dynamic spring coefficient is also frequency-dependent, $k(\omega)$.

- c is the frequency-dependent total damping coefficient, $c(\omega)$.

This coefficient includes radiation and material damping. It should be noted that the damping coefficients that are extracted from Gazetas relations do not include the soil hysteretic damping ξ. To incorporate such damping, simply the corresponding material dashpot coefficient $2k\xi/\omega$ should be added to the radiation damping $c_{radiation}$ which can be obtained from the relations presented in the following:

$$c_{total} = c_{radiation} + \frac{2k}{\omega}\xi \qquad (3.1)$$

Considering that for the lateral oscillation of rigid embedded foundations there are four modes of dynamic impedances, the complex dynamic impedance matrix of the caisson is 2x2 in size.

$$\widetilde{K} = \begin{bmatrix} \widetilde{K_{hh}} & \widetilde{K_{hr}} \\ \widetilde{K_{rh}} & \widetilde{K_{rr}} \end{bmatrix}$$

where $\widetilde{K_{hh}} = k_{hh} + i\omega c_{hh}$

$\widetilde{K_{hr}} = k_{hr} + i\omega c_{hr}$

$\widetilde{K_{rr}} = k_{rr} + i\omega c_{rr}$

$\widetilde{K_{rh}} = k_{rh} + i\omega c_{rh}$

$\widetilde{K_{hh}}$: is the dynamic horizontal impedance

$\widetilde{K_{hr}}$: is the dynamic cross coupling horizontal-rotational impedance

$\widetilde{K_{rr}}$: is the dynamic rotational impedance

$\widetilde{K_{rh}}$: is the dynamic cross coupling rotational-horizontal impedance

k_{ij} and c_{ij} are the stiffness and damping coefficients for each mode respectively.

In order to compute the aforementioned four complex impedances, meaning equivalently the eight stiffness and damping coefficients, the values of the parameters that should be known are:

- G_s: shear modulus
  E_s: modulus of elasticity
  v: Poison's ratio
  V_s: shear wave velocity
  V_{La}: "Lysmer's analog" wave velocity

  It should be noted that only two of these parameters should be known in order to determine all other, (G or E and v) or (V_s and V_{La}).

- ω: the circular frequency of the applied force (in radians/sec)
  or equally the dimensionless frequency α_0
  α_0: the dimensionless frequency $\alpha_0 = \frac{\omega B}{2V_s}$

- B: width of plan view
  L: length of plan view
  D: depth of embedment

d: depth of sidewall that is in contact with the surrounding soil

- A_b: area of plan view
  I_b: moment of inertia about the longitudinal or transverse axes
  h: distance of the centroid of the effective sidewall from the ground surface

- A_w: total area of the actual sidewall-soil contact surface
- $A_{w,s}$: the sum of the projection of all the sidewall areas in direction parallel to loading, subjected to shear type of soil reaction

  $A_{w,ce}$: the sum of the projection of all the sidewall areas in direction perpendicular to loading, subjected to compression-extension type of soil reaction

- J_{ws}: the sum of the polar moments of inertia about the off-plane axis rotation of all surfaces actually shearing the soil

  I_{wce}: the sum of moments of inertia of all surfaces actually compressing the soil about their base axes parallel to the axis of rotation

- Δ_i: the distance of surface $A_{wce,I}$ from the longitudinal axis

The developed formulae that provide the stiffness and damping coefficients of a caisson are the following:

- For the longitudinal axis the dynamic horizontal impedance is:

$$\widetilde{K_{hh}} = k_{hh} + i\omega c_{hh}$$

where the dynamic stiffness is:

$$k_{hh} = k_{h,static}^{emb} \chi_{emb}$$

$$k_{h,static}^{emb} \approx k_{h,static}^{surf} \left(1 + 0.15\sqrt{\frac{2D}{B}}\right)\left[1 + 0.52\left(\frac{8hA_w}{BL^2}\right)^{0.4}\right]$$

where $k_{h,static}^{surf}$ is the static stiffness of the caisson base, taken as that of a surface foundation on halfspace which is equal to:

$$k_{h,static}^{surf} \approx \frac{2GL}{2-v}\left[2 + 2.5\left(\frac{A_b}{4L^2}\right)^{0.86}\right] - \frac{0.2}{0.75-v}GL\left(1-\frac{B}{L}\right)$$

χ_{emb}: obtained from Graph a (Figure 3-2).

and the horizontal dashpot coefficient is:

$$c_{hh} = c_h^{surf} + \rho V_s A_{ws} + \rho V_{La} A_{wce}$$

where c_h^{surf} is the damping coefficient of the caisson base, taken as that of a surface foundation on halfspace:

$$c_h^{surf} = \rho V_s A_b c_{surf}$$

c_{surf}: obtained from Graph d (Figure 3-2).

- For the dynamic coupled swaying-rocking complex impedance:

$$\widetilde{K_{hr}} = k_{hr} + i\omega c_{hr}$$

$$\widetilde{K_{rh}} = k_{rh} + i\omega c_{rh}$$

The approximate formulae are:

$$k_{hr} = k_{rh} \approx \frac{1}{3} d k_{hh}$$

and

$$c_{hr} = c_{rh} \approx \frac{1}{3} d c_{hh}$$

- For the dynamic rocking impedance the complex form is:

$$\widetilde{K_{rr}} = k_{rr} + i\omega c_{rr}$$

where the dynamic stiffness is:

$$k_{rr} = k_{r,static}^{emb}(1 - 0.30\alpha_0)$$

$$k_{r,static}^{emb} \approx k_{r,static}^{surf}\left[1+0.92\left(\frac{2d}{L}\right)^{0.6}\right]\left[1.5+\left(\frac{2d}{L}\right)^{1.9}\left(\frac{d}{D}\right)^{-0.6}\right]$$

where $k_{r,static}^{surf}$ is the static rocking stiffness of the caisson base, taken as that of a surface foundation on halfspace which is equal to:

$$k_{r,static}^{surf} \approx \frac{G}{1-\nu} I_b^{0.75}\left[3\left(\frac{L}{B}\right)^{0.15}\right]$$

and the rocking dashpot coefficient is:

$$c_{rr} = c_r^{surf} + \rho V_{La} A_{wce} c_{emb} + \rho V_s \left[J_{ws} + \sum_i (A_{wce}\Delta_i^2)\right] c_{emb}$$

where c_r^{surf} is the damping coefficient of the caisson base, taken as that of a surface foundation on halfspace:

$$c_r^{surf} = \rho V_{La} I_b c_{surf}$$

c_{surf}: obtained from Graph f (Figure 3-2).

$$c_{emb} \approx 0.25 + 0.65\sqrt{\alpha_0}\left(\frac{d}{D}\right)^{-\alpha_0/2}\left(\frac{2D}{B}\right)^{-0.25}$$

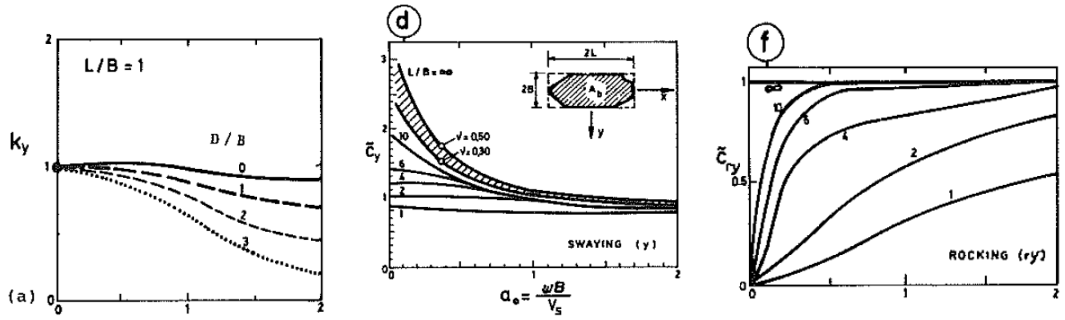

Figure 3-2: Graph (a): χ_{emb}, Graph (d): $c_{h\,surf}$, Graph (f): $c_{r\,surf}$

In this project the caisson that is being studied is square in plan view and fully embedded. This means that $B=L$ and $D=d$. With these observations the formulae can be simplified. For more details on the simplified solutions the reader is referred to Appendix A. From the presented formulae the dynamic impedances for each mode are calculated for every frequency and are compared with the corresponding results of PLAXIS.

3.2 Reference point

The reference point plays a very important role when it comes for the embedded foundations. Traditionally for the surface foundations the reference point is taken at the center of the base of the foundation. However for the embedded foundations there is not a clear suggestion in the literature. Different researchers take different reference points, in the terms of different points where they measure the loads, the displacements and rotations. The different points will lead to different shapes of failure envelopes. The most common reference points that are used are, the center of the base, the center of the mass and the center of the top of the caisson.

As it can be seen from Figure 3-3 below, the role of the applied load is different for different reference points. When the reference point is taken at the base the positive lateral force has competitive role comparing to the positive rotation moment. However when the reference point is at the top the positive lateral force has response (i.e. displacement and rotation) with the same direction as the positive rotation moment. In order to have the competitive response the rotation moment should be negative as it is shown in the figure.

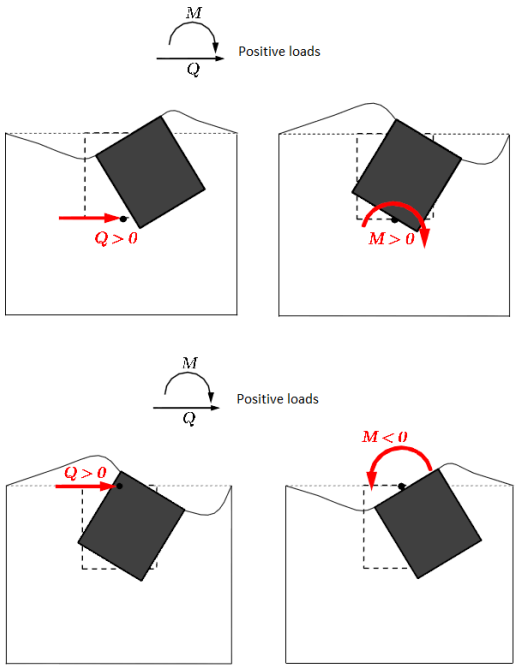

Figure 3-3: Competitive roles of the lateral force and the overturning moment. Above: reference point at the center of the base, below: reference point at the center of the top (after Souliotis '12).

The formulas that presented in the previous chapter are referred at the base of the caisson. In this thesis the reference point has been taken at the top of the caisson. The reason for that is because by engineering point of view the springs and the dashpots that are calculated in order to be applied at the superstructure are easier to be understood and capture their physical meaning when the reference is at the base of the superstructure which is the top of the foundation.

Thus, in order the dynamic impedances that derive from the numerical analyses (reference point at the top) to be comparable with the dynamic impedances of the aforementioned relations (reference point at the base) a proper transformation should be applied. The coordinate transformation is according to the following matrix.

$$A = \begin{bmatrix} 1 & -D \\ 0 & 1 \end{bmatrix}$$

$$\widetilde{K_{TOP}} = A^T \widetilde{K_{BASE}} A = \begin{bmatrix} \widetilde{K_{hh}} & \widetilde{K_{hr}} - D\widetilde{K_{hh}} \\ \widetilde{K_{rh}} - D\widetilde{K_{hh}} & \widetilde{K_{rr}} - 2D\widetilde{K_{hr}} + D^2\widetilde{K_{hh}} \end{bmatrix}$$

For more details about the coordinate transformation the reader is referred to the Appendix B.

3.3 Influence of mass

As described before the general equilibrium equation of the movement of the caisson takes into account except for the stiffness and the damping also the mass. For more details the reader is referred to 3.6.

At the numerical analyses that have been performed the mass of the caisson has been taken into account. The matrix of the mass that is referred at the base is by (Gerolymos & Gazetas, 2006):

$$M_{base} = \begin{bmatrix} m & m\frac{D}{2} \\ m\frac{D}{2} & (J_c + m\frac{D^2}{4}) \end{bmatrix}$$

Where

m: mass, D: depth of embedment, J_c: mass moment of inertia about the center of gravity $J_c = \frac{1}{12}m(B^2 + D^2)$

Of course the proper coordinate transformation as described before for the matrix of impedance should also be applied at this matrix:

$$A = \begin{bmatrix} 1 & -D \\ 0 & 1 \end{bmatrix}$$

$$M_{top} = A^T M_{base} A$$

This transformation results the following matrix which is referred at the top:

$$M_{top} = \begin{bmatrix} m & -m\frac{D}{2} \\ -m\frac{D}{2} & (J_c + m\frac{D^2}{4}) \end{bmatrix}$$

3.4 Numerical model

In this study three dimensional finite element simulations have been conducted for the evaluation of the springs and dashpots coefficients of the caisson. The

simulations are performed using the FEM software package PLAXIS 3D version 2012 which was presented in chapter 2.7.

3.4.1 Geometry

The caisson that is being studied in this project is square plan with width B=10m. The caisson is considered to be fully embedded with depth D=20m. Thus, the ratio depth of embedment to width is D/B=2. It should be noted that because of the symmetric problem of the square plan caisson, only half of the numerical domain is simulated. In this way, taking advantage of the symmetry, considerable computational effort has been saved.

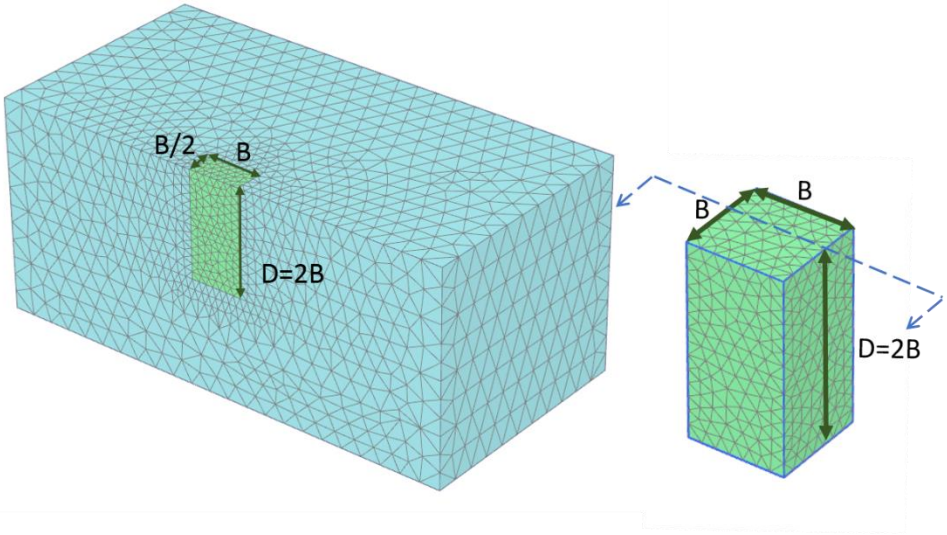

Figure 3-4: Geometric features of the square plan caisson. Left half of the model that was used for the numerical analyses, right the dimensions of the full caisson.

3.4.2 Simulation of caisson

The soil formation was simulated using 3D continuum soil-elements. For the caisson two different types of elements were compared. In model A the caisson was simulated by volume-elements (with different material parameters than the surrounding soil) and in model B the caisson was simulated with plate-elements (with equivalent parameters with model A). The results obtained from the two models found to be almost exact the same (Figure 3-5). The dynamic analyses that

will be presented in the following were performed using model A: volume-elements for the simulation of the caisson.

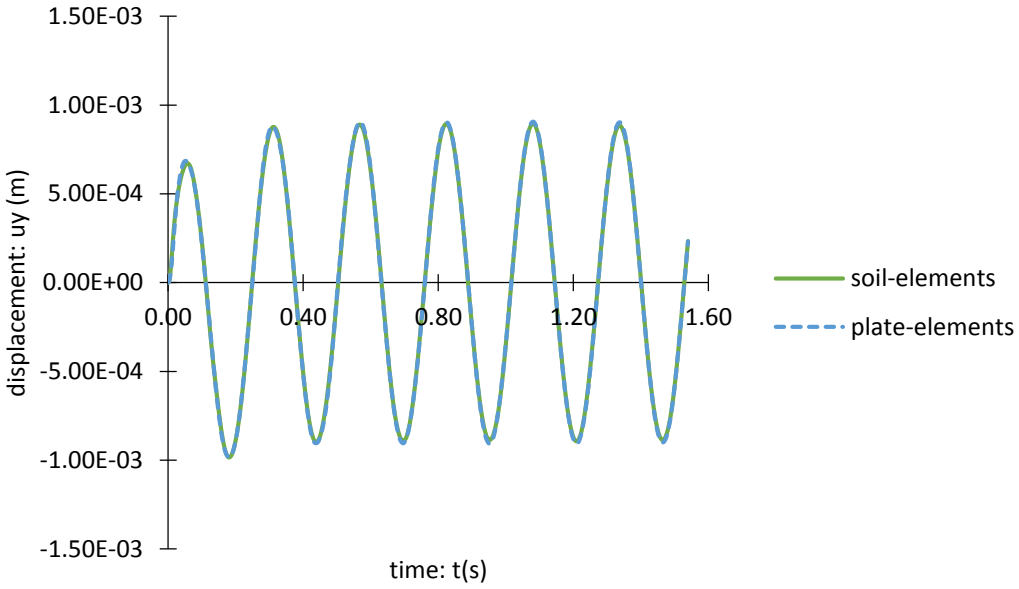

Figure 3-5: Lateral displacement of the center of the top of the caisson for dynamic lateral loading for the two different models.

The reason for choosing the volume elements is that the plates appeared to be a bit deformable so the caisson did not behave as a full rigid body. Although this effect could be considered negligible by comparing the response of the two models, model A considered to be more trustworthy for the analyses that follow.

3.4.3 Material models

Both for soil and caisson elements the material-models have been considered linear elastic at this part. No special interface elements have been adapted because of the assumption of perfect bonding at the soil-structure interface. This means that no separation between the caisson and the surrounding soil is performed, not even under tensile stress. Figure 3-4 depicts the geometry of the caisson while Table 3-1 presents the selected parameters for the material models.

Table 3-1: Material properties

Parameter	*Name*	*Soil*	*Caisson*	*Unit*
General				
Material model	Model	Linear elastic	Linear elastic	
Drainage type	Type	Dry	Non-porous	
Unit weight	γ	20	25	kN/m^3
Parameters				
Young's modulus (constant)	E	$20*10^3$	$100*10^6$	kN/m^2
Poisson's ratio	v	0.30	0.20	
Shear modulus	G	7692	$4{,}17*10^7$	kN/m^2
Shear wave velocity	V_s	61.39	4041	m/s
Primary wave velocity	V_p	114.9	6600	m/s

The values of moduli of elasticity of the soil and the caisson have been selected in such way that the caisson to behave as rigid block. The ratio $E_{caisson}/E_{soil}$ (= 5000) is selected so big to ensure this condition.

3.4.4 Absorbent boundaries

For the implementation of dynamic effects, absorbent boundaries are created with the use of viscous boundaries (dampers). The damper at the boundary element ensures that an increase in stress on the boundary is absorbed without rebounding. When pressure waves strike the boundary perpendicular, relaxation is redundant. However, in the presence of shear waves, the damping effect of the absorbent boundaries is not sufficient without relaxation so shear waves cannot be fully absorbed and a limited boundary effect is noticeable. For more details the reader is referred to (PLAXIS3D, 2012, p. 57)

3.5 Optimization of the model

At this part of the study sensitivity analyses have been performed considering the size of the finite element (mesh fineness) and the dimensions of the numerical domain.

3.5.1 Mesh discretization

For a dynamic analysis, meshing plays a key role in obtaining a realistic result, if not for a simple geometry, but definitely for a complex one. A too coarse meshing fails to capture the subtle changes in the stresses generated in different parts of the medium, especially at the points where stress concentrations are expected. On the other hand, a too fine mesh renders the execution time to be very long, which is uneconomic. Hence, a trade-off is required to obtain an approximately accurate solution in a reasonable time.

In order to determine the mesh density that has been used for the dynamic analyses in this project, sensitivity analysis for the maximum element size was initially performed. At this stage of the study different mesh densities have been applied for the analysis of the maximum frequency of interest which is $f_{max} = 3.9\ Hz$ (or $a_0 = 2$). The caisson is excited at its top with harmonic lateral uniformly distributed load of $10kN/m^2$. The obtained results about the mesh size have also been adapted to lower frequencies. For this sensitivity analysis the far field, namely the viscous boundaries of the numerical domain, are placed at a distance equal to 4 times the diameter (B) of the caisson at both directions. The soil stratum reaches $20\ meters$ deeper (=2B) from the caisson base in order to neglect the influence on the response. The width of the domain as well as its height, have also been investigated by sensitivity analysis (3.5.2).

The main purpose of this sensitivity investigation is to evaluate the relation between the maximum element size (Δl) of the mesh and the wavelength (λ) of the input signal:

$$\Delta l \leq \frac{\lambda}{k}, \qquad where\ \lambda = V_S T = \frac{V_S}{f}$$

Different values of k have been used for generating the global mesh while for the maximum dimension (Δl) of each element, estimations were made in three different ways. In the first way the total volume of the model was divided by the total number of elements (n) and then assuming that the element has a simplified geometry of a normal tetrahedral the maximum dimension was calculated.

$$V_{element} = V_{total}/n$$

$$V_{element} = \Delta l^3 \frac{\sqrt{2}}{12}$$

In the second way the dimension of the element is defined by PLAXIS when generating the mesh by dividing the diagonal of the model by a certain number (n_c) which is called relative element size and can be modified by the user. When the mesh has been generated PLAXIS provides the real average element size (AES) which is usually smaller because of the local refinements. This is the third way. The role of the local refinement at the region of the caisson was investigated too. The results are presented below.

Results

First the influence of the global mesh size was investigated by generating the global mesh by different values of k. Table 3-2 below presents the different mesh discretization that were used without local refinement at the region of the caisson.

Table 3-2: Mesh description and parameters without local refinement at the region of the caisson

mesh description	n	Δl (m)			k=Vs/(Δl*f)		
	number of elements	simplified geometry (1)	PLAXIS definition (2)	PLAXIS AES (3)	k(1)	k(2)	k(3)
very coarse	820	11.88	10.83	14.06	1.3	1.5	1.1
coarse	1753	9.22	8.12	9.61	1.7	1.9	1.6
medium	5842	6.17	5.41	5.26	2.6	2.9	3.0
fine	19781	4.11	3.79	2.86	3.8	4.2	5.5
very fine	51177	3.00	2.71	1.78	5.2	5.8	8.8

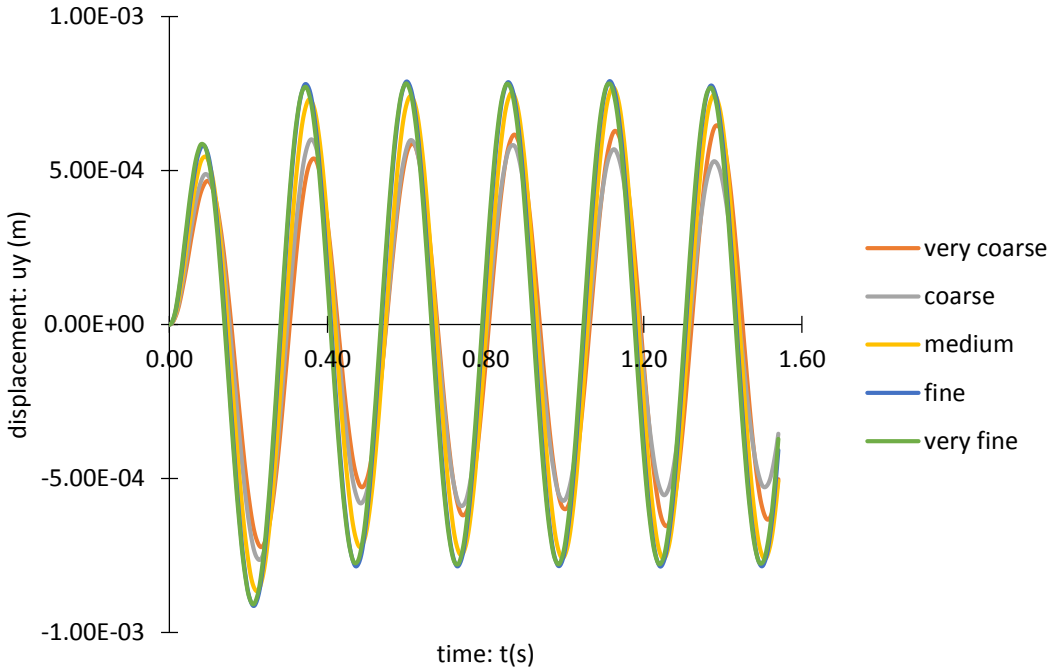

Figure 3-6: Sensitivity of lateral displacement to element size for 3.9 Hz harmonic excitation at the top of the caisson without local refinement at the region of the caisson

From the figure above it can be concluded that very coarse and coarse meshes are not suitable for the analyses as the response deviates enough from the finer meshes. Fine and very fine meshes have the almost exact same response while medium mesh presents a very small deviation from the finer meshes.

In order to optimize the mesh size, local refinement at the region of the caisson was tested for the different mesh densities (very coarse – very fine). Different local refinements at the region of the caisson were used (lr0 – lr4) with lr4 being the densest refinement and lr0 the coarsest. The results for the different mesh densities are given in the figures below.

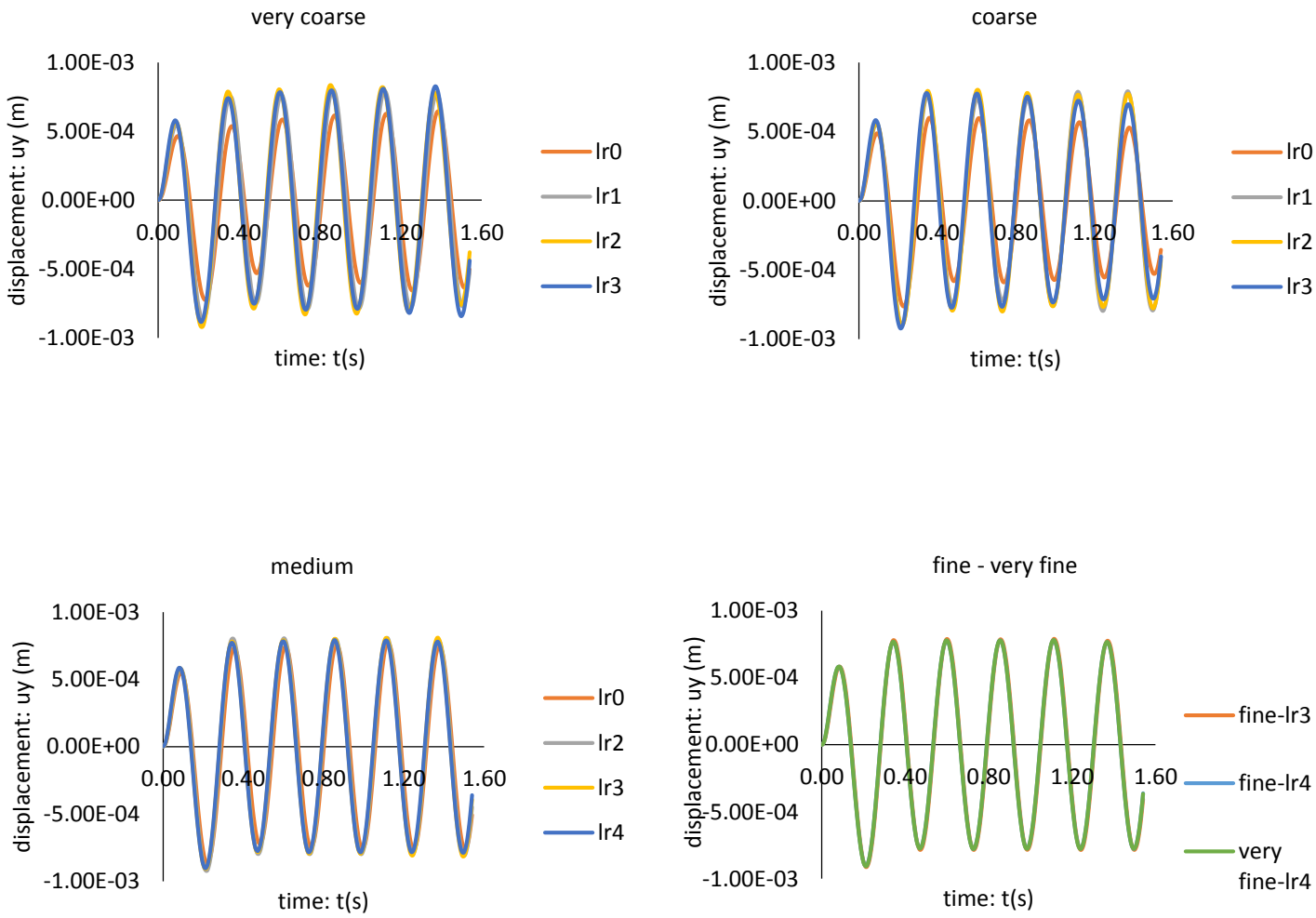

Figure 3-7: Sensitivity of lateral displacement to local refinement (lr) at the region of the caisson for different global meshes (very coarse – very fine)

From Figure 3-7 can be concluded that the densest local refinement at the region of the caisson is suitable for the analyses. For this refinement a comparison has been made for the different global meshes.

Table 3-3 below presents the different mesh discretization that were used including the densest local refinement (lr4) at the region of the caisson. The results are presented in the following figure while conclusions about the final model and discussion on the validity of the guiding from the literature relation about the wavelength is discussed in the following.

Table 3-3: Mesh description and parameters including the densest local refinement at the region of the caisson

mesh description	n	Δl (m)			k=Vs/(Δl*f)		
	number of elements	simplified geometry (1)	PLAXIS definition (2)	PLAXIS AES (3)	k(1)	k(2)	k(3)
very coarse*	2337	8,38	10,83	8,33	1,9	1,5	1,9
coarse*	3325	7,45	8,12	6,98	2,1	1,9	2,3
medium*	17337	4,30	9,22	3,06	3,7	1,7	5,1
fine*	27941	3,66	6,17	2,93	4,3	2,6	5,4
very fine*	123391	2,23	2,71	1,15	7,0	5,8	13,7

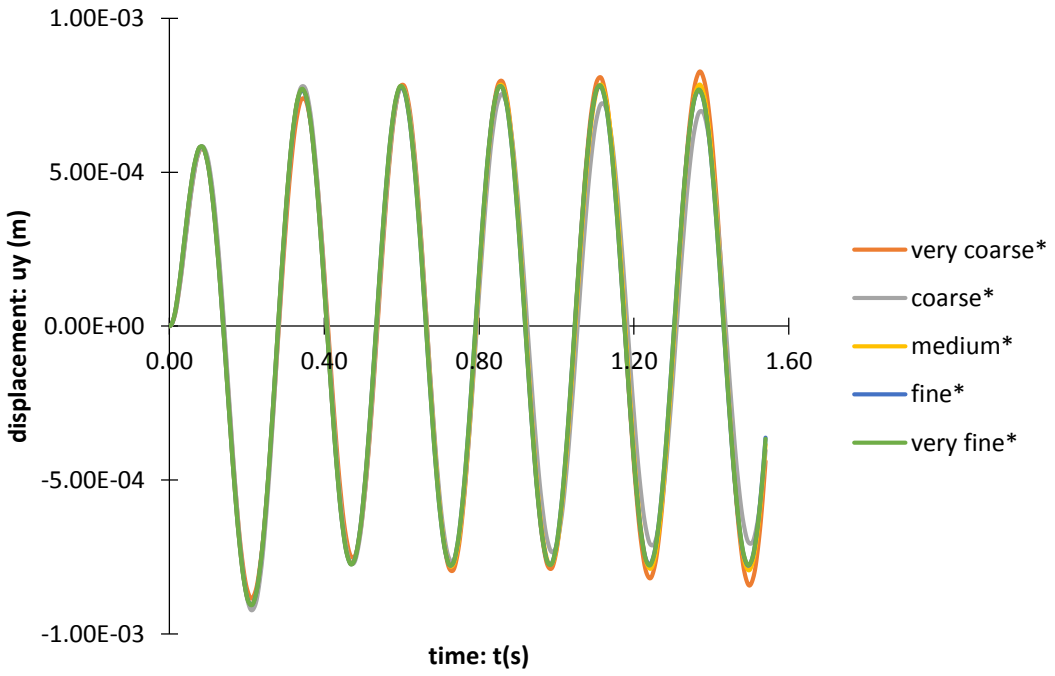

Figure 3-8: Sensitivity of lateral displacement to element size for 3.9 Hz harmonic excitation at the top of the caisson with local refinement (lr4) at the region of the caisson

From Figure 3-8 above, it can be clearly seen that very coarse and coarse meshes have improved but still are not appropriate for the analyses. Medium mesh could be used as global meshing since the deviation is small enough but fine and very fine meshes give almost identical results with negligible deviation with each other. Subsequently the fine global mesh with dense local refinement at the region of the caisson was selected for the dynamic analyses that follow.

Conclusions

With respect to computational requirement lowering the number of elements is always a very important issue which can become critical for dynamic 3D analyses .The main purpose of this sensitivity investigation was to evaluate the relation between the maximum element size (Δl) of the mesh and the wavelength (λ) of the input signal:

$$\Delta l \leq \frac{\lambda}{k}$$

In literature the values that are proposed for k range between 4 and 10. (Kuhlemeyer & Lysmer, 1973) propose the value 8 as guideline for generating mesh but indicate the importance of investigating the influence of the element size. This value is most commonly used for dynamic analyses in case of no initial sensitivity analysis has performed. For more details the reader is referred to 2.6.1.

The results presented above show the clear effects mesh coarsening can have. $k \approx 4$ resulted to be critical as greater values of k have negligible influence to the response. The reason that this value is smaller than the guiding from the literature value is because the volume elements implemented here are 10-node tetrahedral elements while the guiding value has derived from linear elements. Hence lower value of k was expected to be resulted because tetrahedral elements interpolate more nodes than linear elements.

The mesh density that came up from the sensitivity analysis can be applied to lower frequencies because as the wavelength increases the maximum element requirement decreases. Thus, keeping the same fine mesh for lower frequencies the

accuracy increases. Instead applying the same mesh for higher frequencies is not recommended because the wavelength decreases and so more elements are required in order to obtain reliable results. In this study the mesh that has been resulted from the higher frequency of interest has been adapted to the lower frequencies for the rest dynamic analyses.

3.5.2 Domain dimensions

The infinite domain represented by finite element models needs to be truncated at some finite boundary. Because optimization of the computational efficiency requires the boundary to be as close as possible to the finite structure, in this part of the study the influence of the domain dimensions have been investigated. Figure 3-9 below shows the width (*W*) and the height (*H*) of the model as well as the dimensions of the caisson.

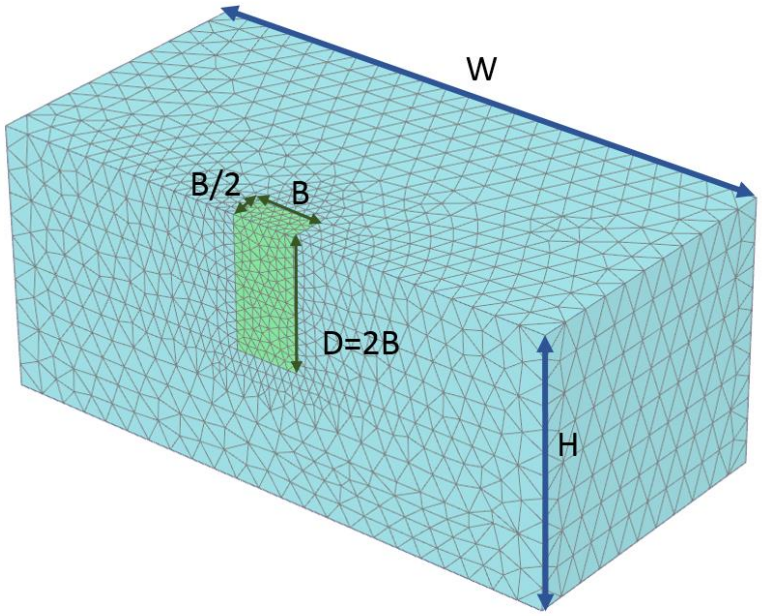

Figure 3-9: Domain (blue) and caisson (green) dimensions.

3.5.2.1 Model width

Since dynamic models involving the study of shear waves are largely affected by the waves transmitted and reflected from the boundaries of the model, it is imperative

to keep the region of interest (the region that will be under observation to study and interpret the results) as far as possible from any reflecting boundary. In general, the width of such dynamic models is chosen much larger than the corresponding static models.

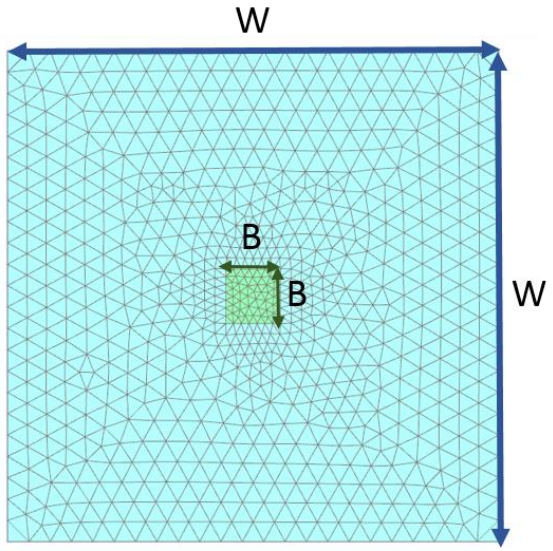

Figure 3-10: Plan view of the caisson and the model domain. W is the width of the domain, B (=10m) is the side of the caisson.

In order to determine the optimum domain width for the problem, different W/B (W is the width of the domain and $B = 10m$ is the side of the caisson) ratios for the soil medium have been considered. Figure 3-10 depicts these dimensions. The primary objective of this sensitivity analysis is to determine the optimum width of the domain, beyond which the soil is simulated as a semi-infinite medium.

Dynamic analyses have been performed for a specific frequency $f = 1.5\ Hz$ (or $a_0 = 0.77$). Smaller frequency than the maximum frequency of interest was selected in order to improve the accuracy of the results considering the mesh element size. The mesh has been derived from the results of the previous sensitivity analysis. The caisson was excited at its top with harmonic lateral uniformly distributed load of $10kN/m^2$. To simulate the semi-infinite domain the soil stratum has been set at depth equal to 2 times the depth (*D=2B*) of embedment of the caisson (*H=2D=4B*).

Results

In order to investigate the influence of the lateral boundaries the width of the model was changed performing the same analysis while the height of the model was kept steady. The dimensions of the caisson were also kept the same. Table 3-4 below shows the different values of W/B that were used and the corresponding results while Figure 3-11 and Figure 3-12 that follow depict the results.

Table 3-4: Different values of W/B that were analyzed and the corresponding results. The first two columns present the distance measured between the lateral side of the caisson and the lateral boundary of the domain. The fifth column shows the deviation of the maximum response from the model with the wider width.

distance of lateral boundaries from the sides of the caisson		W/D	number of elements	u_{max}	deviation
[m]	D			[mm]	
1.00	0.050	0.60	832	1.83	18%
2.50	0.125	0.75	935	1.62	27%
5.00	0.250	1.00	1036	1.59	29%
7.50	0.375	1.25	1709	1.69	24%
10.00	0.500	1.50	2239	1.88	16%
12.50	0.625	1.75	2441	2.09	6%
15.00	0.750	2.00	3063	2.29	-3%
17.50	0.875	2.25	4753	2.39	-7%
20.00	1.000	2.50	5008	2.40	-8%
25.00	1.250	3.00	6961	2.30	-3%
27.50	1.375	3.25	9089	2.23	0%
30.00	1.500	3.50	10566	2.17	3%
35.00	1.750	4.00	14193	2.14	4%
40.00	**2.000**	**4.50**	**27928**	**2.16**	**3%**
50.00	2.500	5.50	36256	2.22	0%
65.00	3.250	7.00	41698	2.17	3%
80.00	4.000	8.50	55693	2.18	2%
90.00	4.500	9.50	68847	2.23	0%

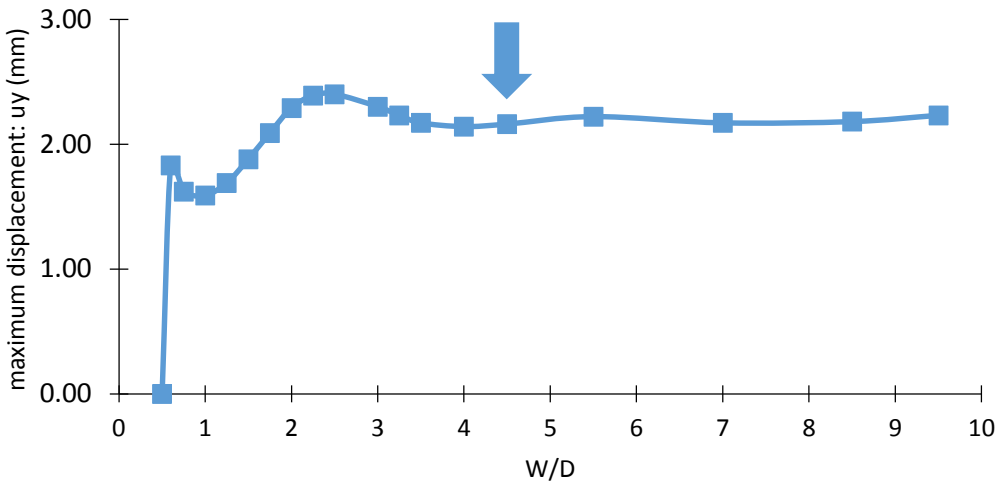

Figure 3-11: Effect of domain width on the maximum lateral response at the top of the caisson due to lateral harmonic excitation. The arrow indicates the selected width beyond which the soil domain is considered to successfully represent semi-infinite medium.

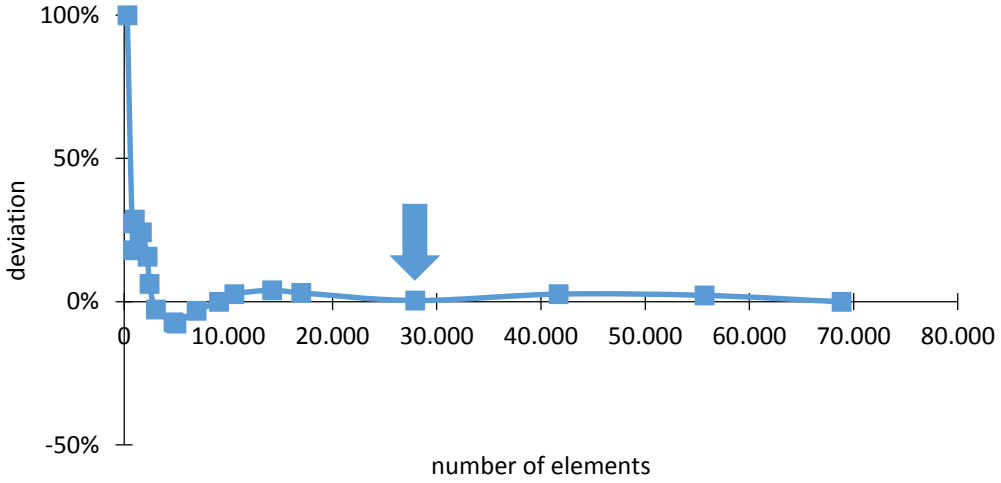

Figure 3-12: Effect of domain width expressed in total number of elements on the deviation of the maximum lateral response of the caisson due to lateral harmonic load of the wider model from the corresponding values of the other ratios. The arrow indicates the selected width beyond which the soil domain is considered to successfully represent semi-infinite medium.

Conclusions

Figure 3-11 reveals the effect of W/D in terms of the maximum displacement of the input excitation measured at the surface of the caisson and at the middle of its width. As it can be concluded the increase of width after the value of $4.5D$ provide

very small deviation. From Figure 3-12 can be observed that after the value of $4.5D$ which is indicated by the arrow, the increase of the total number of finite elements that constitute the model, increases very much making the model inefficient by computational view. By these two observations the optimum width of the domain is determined to be $4.5D$.

3.5.2.2 Model height

The height of the model is another parameter that needs to be investigated since the boundary at the bottom of the model influences the results as well. In order to determine the optimum height of the soil that will represent the halfspace, sensitivity analysis has been performed. The mesh discretization size and the width domain were determined from the previous sensitivity analyses. The excitation (frequency-load) has been the same as the previous analyses for the width. The only parameter that was varied here is the height of the domain.

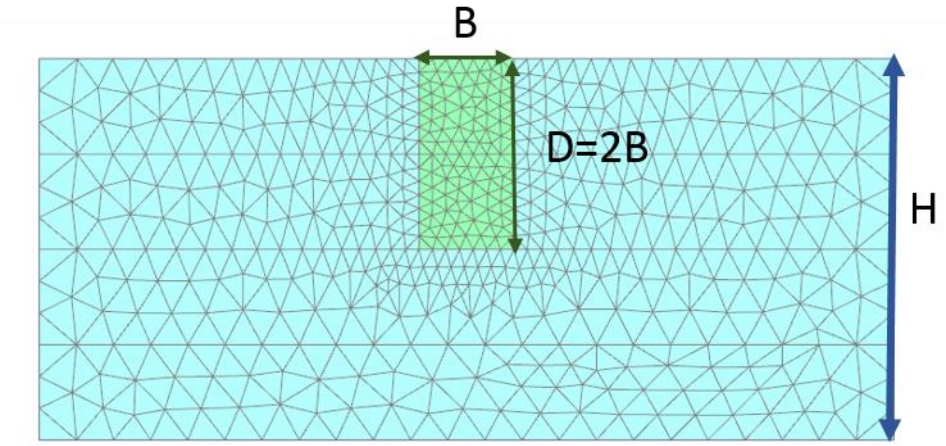

Figure 3-13: Cross section of the model. H is the height of the domain, B (=10m) is the side of the caisson and D (=20m) is the embedment of the caisson.

Results

Table 3-4 below shows the different values of H/B that were used and the corresponding results while Figure 3-11 and Figure 3-12 that follow depict the results.

Table 3-5: Different values of H/B that were analyzed and the corresponding results. The first two columns present the distance measured between the base of the caisson and the bottom boundary of the domain. The fifth column shows the deviation of the maximum response from the model with the deeper height (last row).

distance of bottom boundary from the bottom side of the caisson		H/B	number of elements	u_{max}	deviation
[m]	B			[mm]	
0.00	0.00	2.00	9743	1.25	42%
1.00	0.10	2.10	10053	2.18	-2%
2.00	0.20	2.20	10053	2.17	-1%
5.00	0.50	2.50	10693	2.06	4%
10.00	1.00	3.00	13339	2.08	3%
20.00	**2.00**	**4.00**	**27941**	**2.16**	**-1%**
50.00	5.00	7.00	38623	2.14	0%

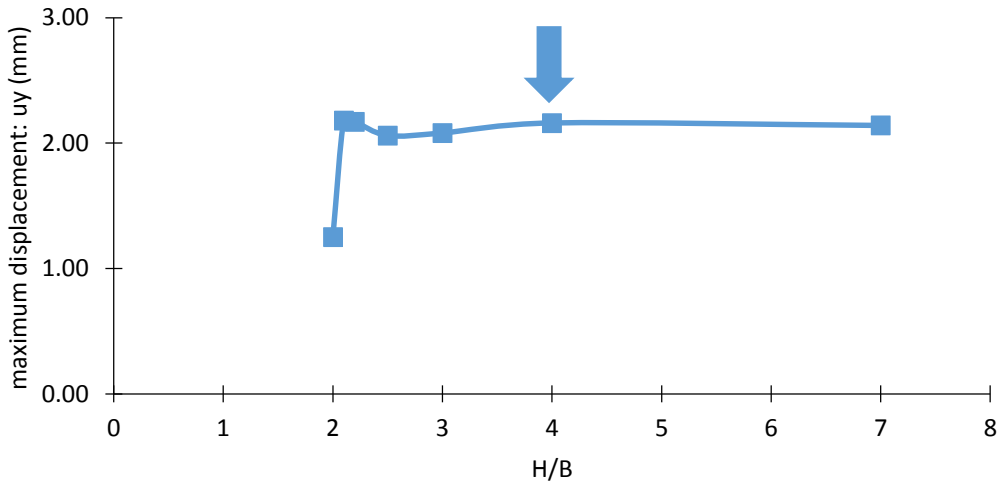

Figure 3-14: Effect of domain height on the maximum lateral response at the top of the caisson due to lateral harmonic excitation. The arrow indicates the selected height beyond which the soil domain is considered to successfully represent semi-infinite medium.

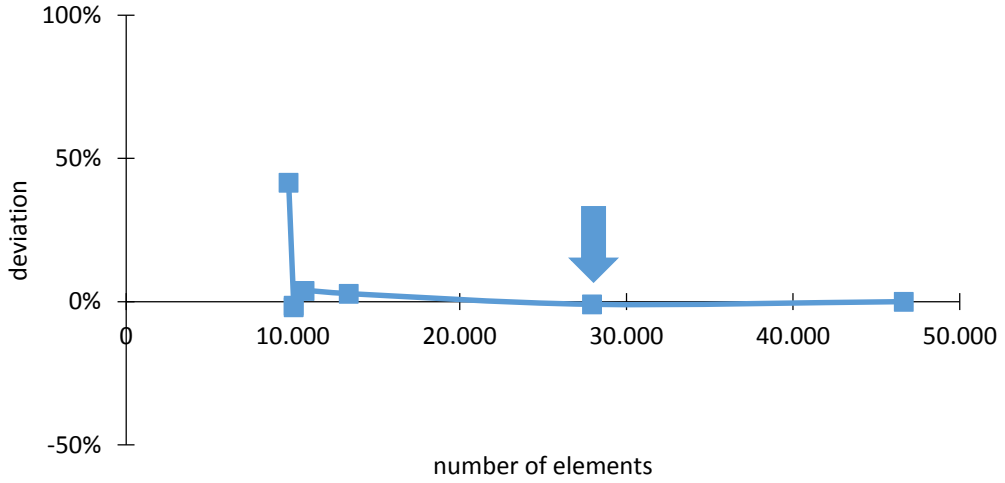

Figure 3-15: Effect of domain height expressed in total number of elements on the deviation of the maximum lateral response of the caisson due to lateral harmonic of the deeper model from the corresponding of the other ratios. The arrow indicates the selected height beyond which the soil domain is consider to successfully represent the halfspace.

Conclusions

Figure 3-14 reveals the effect of H/B in terms of the maximum displacement of the input excitation measured at the surface of the caisson and at the middle of its width. As it can be concluded the increase of width after the value of $4B$ provides

very small deviation for the response. From Figure 3-15 can be observed that after the value of $4B$ which is indicated by the arrow the increase of the total number of finite elements that constitute the model, increases very much making the model inefficient by computational view. By these two observations the optimum height of the domain is determined to be $4B$.

3.6 Formulation of impedance matrix

Directly stemming from the fact that the elasticity modulus of concrete (25 GPa) is significantly higher than that of soil (2-5 MPa in general), the caisson foundation investigated in this study, namely foundation elements of intermediate depth-to-diameter ratio (D/B=2), is here assumed to respond as a rigid body without significant loss of accuracy of the solution. As a result, application of a lateral force *(Q)* and an overturning moment *(M)* at the top will result in a net lateral displacement and a rotation of the caisson as shown in Figure 2-1. Based on the aforementioned assumption, the consequent response of the foundation is adequately described in terms of the displacement at the top *(u),* and the rotation angle of the rigid caisson *(φ).*

Given these quantities, the horizontal displacement at any point is given by:

$$u(z) = u - \varphi z \tag{3.2}$$

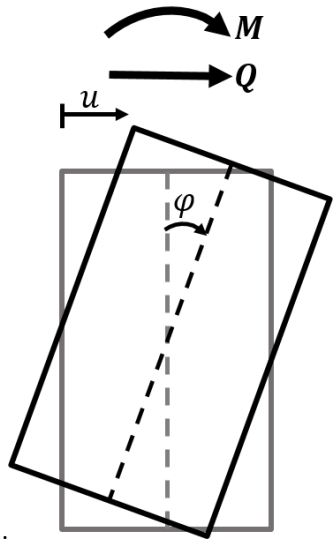

Figure 3-16: Response of caisson upon application of lateral load and overturning moment.

As described before in chapter 2.4, the response of the caisson is related to the forced excitation by the following equation of dynamic equilibrium in matrix notation assigned to the caisson's degrees of freedom:

$$[M]\ddot{u}(t) + [C]\dot{u}(t) + [K]u(t) = F(t) \quad (3.3)$$

Where

$[M]$: mass matrix

$[C]$: damping matrix

$[K]$: stiffness matrix

$\ddot{u}(t), \dot{u}(t), u(t)$: acceleration, velocity, displacement vectors

$F(t)$: external force vector

For harmonic excitation of a lateral force, Q(t), and an overturning moment, M(t), the external vector becomes:

$$[F] = \begin{bmatrix} Q(t) \\ M(t) \end{bmatrix} \quad (3.4)$$

Where

$$Q(t) = Qsin(\omega t)$$

$$M(t) = Msin(\omega t)$$

Q, M are the maximum values of the forced vibration:

$$[F]_{max} = \begin{bmatrix} Q \\ M \end{bmatrix}$$

The response of the caisson, namely the displacement u and the rotation angle ϕ, is also harmonic and are given in matrix form as:

$$[X] = \begin{bmatrix} u(t) \\ \varphi(t) \end{bmatrix}$$

where, displacements, velocities and accelerations are related by the following equations:

$$u(t) = u\sin(\omega t + d_u) \quad (3.5)$$

$$\dot{u}(t) = \dot{u}\sin(\omega t + d_u) = \omega u \sin\left(\omega t + d_u + \frac{\pi}{2}\right) \quad (3.6)$$

$$\ddot{u}(t) = \ddot{u}\sin(\omega t + d_u) = \omega^2 u \sin(\omega t + d_u + \pi) \quad (3.7)$$
$$= -\omega^2 u \sin(\omega t + d_u)$$

For the rotation angle the corresponding equations are the following:

$$\varphi(t) = \varphi\sin(\omega t + d_\varphi) \quad (3.8)$$

$$\dot{\varphi}(t) = \dot{\varphi}\sin(\omega t + d_\varphi) = \omega\varphi\sin(\omega t + d_\varphi + \pi/2) \quad (3.9)$$

$$\ddot{\varphi}(t) = \ddot{\varphi}\sin(\omega t + d_\varphi) = \omega^2\varphi\sin(\omega t + d_\varphi + \pi) = -\omega^2\varphi\sin(\omega t + d_\varphi) \quad (3.10)$$

u, φ are the maximum values of the response of the caisson:

$$[X]_{max} = \begin{bmatrix} u \\ \varphi \end{bmatrix} \quad (3.11)$$

And d_u, d_φ are the differenct phase angles due to the time lag between the displacement and the load or the rotation and the load respectively.

Replacing the terms in equations (3.5)-(3.10) and (3.4) ,(3.11) to equation (3.3) the latter becomes:

$$[F] = \{[K] - [M]\omega^2\}[X]_{max}\sin(\omega t) + [C]\omega[X]_{max}\sin(\omega t + \pi/2)$$

Which can be written in a more elegant way in the form of a complex number:

$$[F] = \{[K] - [M]\omega^2 + i\omega[C]\}[X]$$

$$[F] = \left[\tilde{K}\right][\tilde{X}] \quad (3.12)$$

Where $\left[\tilde{K}\right]$and $[\tilde{X}]$ are complex matrices.

The left-hand side of the equation represents the forcing function $[F]$applied at the top of the foundation, and the right-hand side corresponds to the product of the so-called impedance matrix $\left[\tilde{K}\right]$ of the soil-foundation system as interpreted from the foundation top to the response vector $[\tilde{X}]$, namely the displacement and rotation of the caisson.

It is very important to be noted here that all the matrices above refer to the top of the caisson. In case of another reference system a coordinate transformation needs

to be applied for each matrix separately. Of course the dynamic equilibrium is still valid.

The main purpose of this part of the study is to quantify the matrix $[\widetilde{K}]$for caissons. As it was defined before this matrix is equal to:

$$[\widetilde{K}] = [K] - [M]\omega^2 + i\omega[C]$$

Where $[K]$is the springs matrix, $[C]$ the dashpots matrix and $[M]$the mass matrix.

The mass matrix referred to the top of the caisson, after the proper coordinate transformation that has already been described, is equal to:

$$[M] = \begin{bmatrix} m & -m\frac{D}{2} \\ -m\frac{D}{2} & J_c + m\frac{D^2}{4} \end{bmatrix} \quad (3.13)$$

Subsequently in order to determine the global impedance matrix $[\widetilde{K}]$, the spring-matrix $[K]$ and the dashpot-matrix $[C]$ need to be estimated.

Considering the matrix formulation of the equation of equilibrium of externally applied forces and soil reactions evaluated in Equation (4.12), this expression can also be written as:

$$\begin{bmatrix} u \\ \varphi \end{bmatrix} = \begin{bmatrix} \widetilde{K}_{hh} & \widetilde{K}_{hr} \\ \widetilde{K}_{rh} & \widetilde{K}_{rr} \end{bmatrix}^{-1} \begin{bmatrix} Q \\ M \end{bmatrix}$$

In particular for the case of two different load cases at the top of the caisson, externally applied lateral force combined with no moment and externally applied moment combined with no force the relation can be written as:

$$\begin{bmatrix} u_Q & u_M \\ \varphi_Q & \varphi_M \end{bmatrix} = \begin{bmatrix} \widetilde{K}_{hh} & \widetilde{K}_{hr} \\ \widetilde{K}_{rh} & \widetilde{K}_{rr} \end{bmatrix}^{-1} \begin{bmatrix} Q & 0 \\ 0 & M \end{bmatrix} \quad (3.14)$$

where the displacement components on the right-hand side of the equation are:

u_Q : displacement at top upon the application of a unit force

ϕ_Q : rotation of the rigid body upon the application of a unit force

u_M : displacement at top upon the application of a unit moment

ϕ_M : rotation upon the application of a unit moment

$\widetilde{K}_{ij}$ are the dynamic impedances.

The indicators ij stand for:

hh: horizontal

hr: coupling horizontal-rotational

rr: rotational

rh: coupling rotational-horizontal

As a result, the stiffness matrix can be evaluated by simply computing the displacements at top and rotations of caisson due to the application of a lateral force and a overturning moment separately and inverting the matrix in Equation (3.14). This method is typically referred to as the flexibility approach and is extensively applied in the field of structural mechanics. It should be noted here that because of the calculations involve complex number the computation is quite complicated if performed by hand. Special software (Mathcad v.14) has been used in this thesis in order to calculate the real and imaginary parts of all the impedances.

3.6.1 Static impedance

The methodology that described before can be applied also to evaluate the static impedance. The difference is that the impedance matrix $\left[\widetilde{K}\right]$ instead of complex numbers consists now by real numbers $[K]$ as the imaginary part of the impedance is zero.

The following Table 3-6 presents the different values of static stiffness evaluated by the numerical model and Gazetas formulations that are given below. For Gazetas formulations the proper coordinate modifications due to the different reference point have been applied as described previously in order to be comparable with the results calculated by PLAXIS.

$$K_{hh} \approx \frac{9GB}{2-v}\left(1+0.15\sqrt{\frac{2D}{B}}\right)\left[1+1.58\left(\frac{D}{B}\right)^{2.4}\right]$$

$$K_{hr} = K_{rh} \approx \frac{1}{3}DK_{hh}$$

$$K_{rr} \approx \frac{3.6GB^3}{1-v}\left[1+0.92\left(\frac{2D}{B}\right)^{0.6}\right]\left[1.5+\left(\frac{2D}{B}\right)^{1.9}\right]$$

Table 3-6: Comparison between static impedances and static response calculated by PLAXIS and GAZETAS formulations.

STATIC IMPEDANCE			
$\lvert K_{ij} \rvert$	PLAXIS	GAZETAS	deviation
hh	1.11E+06	9.91E+05	-12%
rr	2.72E+08	2.98E+08	9%
hr	-1.31E+07	-1.32E+07	1%

STATIC RESPONSE			
u/ϕ	PLAXIS	GAZETAS	deviation
u_Q	2.13E-03	2.46E-03	14%
ϕ_Q	1.03E-04	1.09E-04	6%
u_M	1.71E-04	1.82E-04	6%
ϕ_M	1.44E-05	1.36E-05	-6%

As can be clearly seen the deviation between the two methods of calculation of static impedance is quite small (<15%) for all modes. This deviation is acceptable since Gazetas formulations have developed by simplicity, without any serious compromise in accuracy. In general, errors that may result from the use of these formulations are within an acceptable 15%. Use of the approximation symbol (≈) at the formulas, however, implies a slightly inferior accuracy. The deviation is greater for the horizontal mode as the lateral displacement for the applied lateral force is estimated smaller than the corresponding value of Gazetas formulation.

3.6.2 Dynamic impedance

3.6.2.1 Methodology

The problem that has been studied herein is that of a square plan caisson (10x10 m^2) embedded in homogeneous elastic soil and subjected to lateral dynamic excitation at its top: Q(t) and M(t) as shown in Figure 3-17.

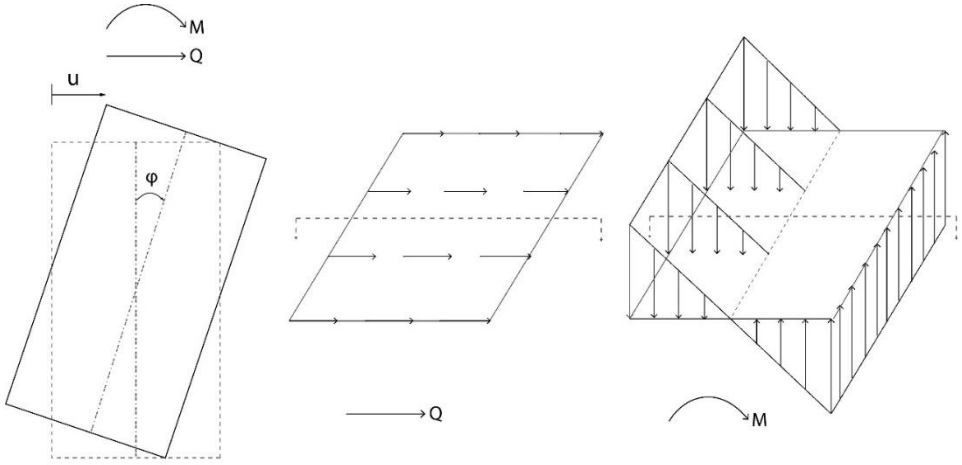

Figure 3-17: Driving excitation atop (right) and response of the caisson (left)

The range of frequencies that has been studied is [0–3.9Hz] or equally in dimensionless frequency terms, α_o [0-2] where $\alpha_0=\omega B/2V_s$. For each frequency two dynamic analyses have been performed. The four dynamic impedances have been calculated using the results of this pair of analyses:

1) input: $Q(t) = 1000sin(\omega t + \pi/2)$ [kN] and $M(t) = 0$
   output: $u_Q(t)$ and $\varphi_Q(t)$
   The equations between the input and output quantities are:

$$Q_{max} = \tilde{K}_{hh}\tilde{u}_Q + \tilde{K}_{hr}\tilde{\varphi}_Q \quad (3.15)$$

$$0 = \tilde{K}_{rh}\tilde{u}_Q + \tilde{K}_{rr}\tilde{\varphi}_Q \quad (3.16)$$

2) input: $M(t) = 1667sin(\omega t + \pi/2)$ [kN] and $Q(t) = 0$

output: $u_M(t)$ and $\varphi_M(t)$

The equations between the input and output quantities are:

$$0 = \tilde{K}_{hh}\tilde{u}_M + \tilde{K}_{hr}\tilde{\varphi}_M \quad (3.17)$$

$$M_{max} = \tilde{K}_{rh}\tilde{u}_M + \tilde{K}_{rr}\tilde{\varphi}_M \quad (3.18)$$

where $\tilde{K}_{ij}$ are the global dynamic impedances, $Q_{max} = 1000\ kN$, $M_{max} = 1667\ kNm$ and u, φ are the corresponding complex response for each analysis respectively Q-0 or 0-M.

The complex values of the response have obtained by taking into account the different lag angle between the load and the response, i.e. Q(t)-u_Q(t) and Q(t)-ϕ_Q(t) or M(t)-u_M(t) and M(t)-ϕ_M(t) respectively. The lag angle for each mode of the response has been calculated by the time lag as shown in Figure 3-18 and it is equal to:

$$d_{ij} = \omega \Delta t_{ij}$$

Where ω is the angular frequency and Δt_{ij} is the time lag between the response and the load. The indicators i,j stand for:

i: the lateral displacement u or the rotation angle ϕ

j: the lateral force Q or the rotation moment M

Thus the real and imaginary parts of the response can be written as:

$$Re(\tilde{u}_Q) = u_Q \cos(d_{uQ})$$

$$Im(\tilde{u}_Q) = u_Q \sin(d_{uQ})$$

, where u_Q is the amplitude of the response. With the same procedure all the modes of the response can be obtained, $\tilde{u}_Q, \tilde{\varphi}_Q$ and $\tilde{u}_M, \tilde{\varphi}_M$.

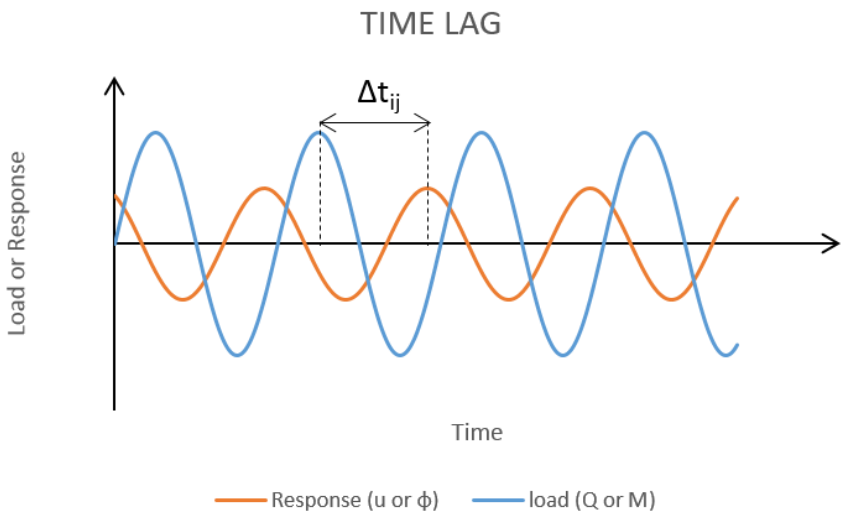

Figure 3-18: Schematic illustration of the time lag between the applied load and the out coming response.

By the four complex equations (3.15)-(3.18) using the methodology that described before, the four unknown global impedances can be calculated. Thus, the global impedance matrix has been calculated.

$$[\tilde{K}] = \begin{bmatrix} \tilde{K}_{hh} & \tilde{K}_{hr} \\ \tilde{K}_{rh} & \tilde{K}_{rr} \end{bmatrix}$$

A first comparison has been performed between the maximum values of the response and their corresponding lag angles derived from PLAXIS analyses, and the values of the corresponding relations from 3.1 Gazetas elastodynamic formulations, after the proper modification in order to be comparable as described there. Furthermore, comparisons have been performed between the values of the norm of each mode of the global impedance calculated by the two methods. The results followed by remarks and conclusions are presented in the following.

Results

In order to present the results of the numerical analyses the response of the caisson has been normalized to the corresponding static values. In this way the results can be generalized. The different lag angles are presented in radians. The dimensionless frequency $\alpha_0 = \frac{\omega B}{2V_s}$ is used in all graphs.

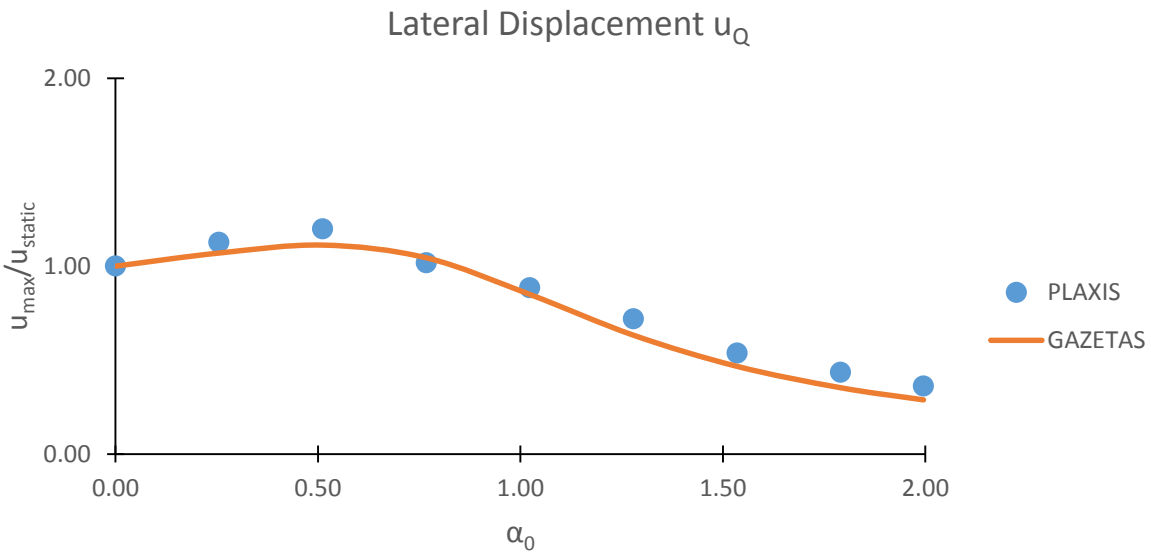

Figure 3-19: Normalized lateral maximum displacement at the center of the top of caisson resulted by lateral dynamic load: Q(t)=1000sin(ωt+π/2) and M(t)=0.

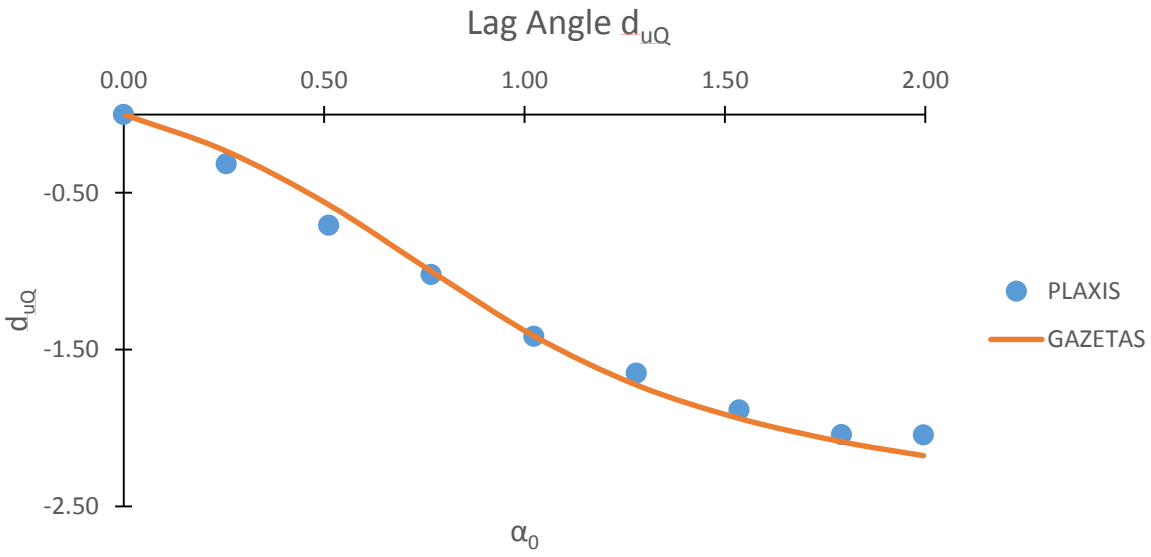

Figure 3-20: Increasing absolute value of the lag angle between the load Q(t) and the lateral displacement u_Q.

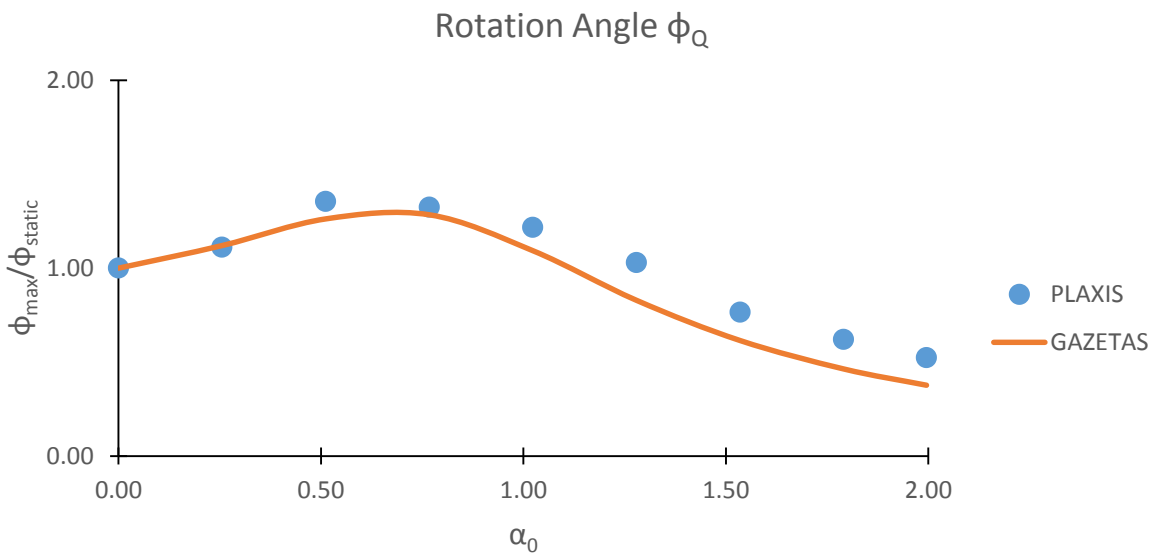

Figure 3-21: Normalized lateral maximum rotation angle of caisson resulted be lateral dynamic load: Q(t)=1000sin(ωt+π/2) and M(t)=0.

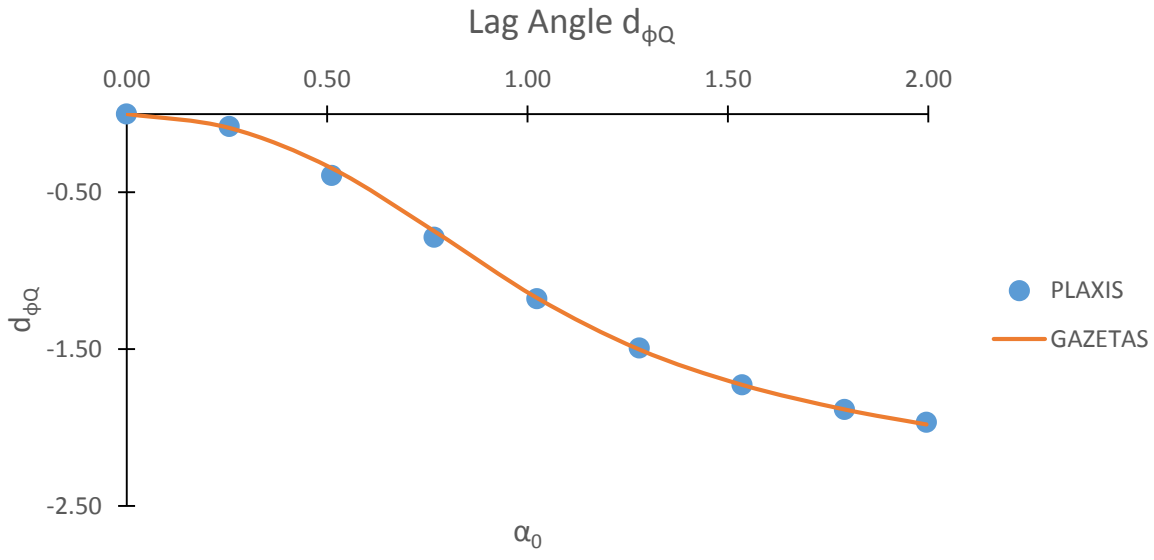

Figure 3-22: Increasing absolute value of the lag angle between the load Q(t) and the rotation angle $\phi_Q(t)$.

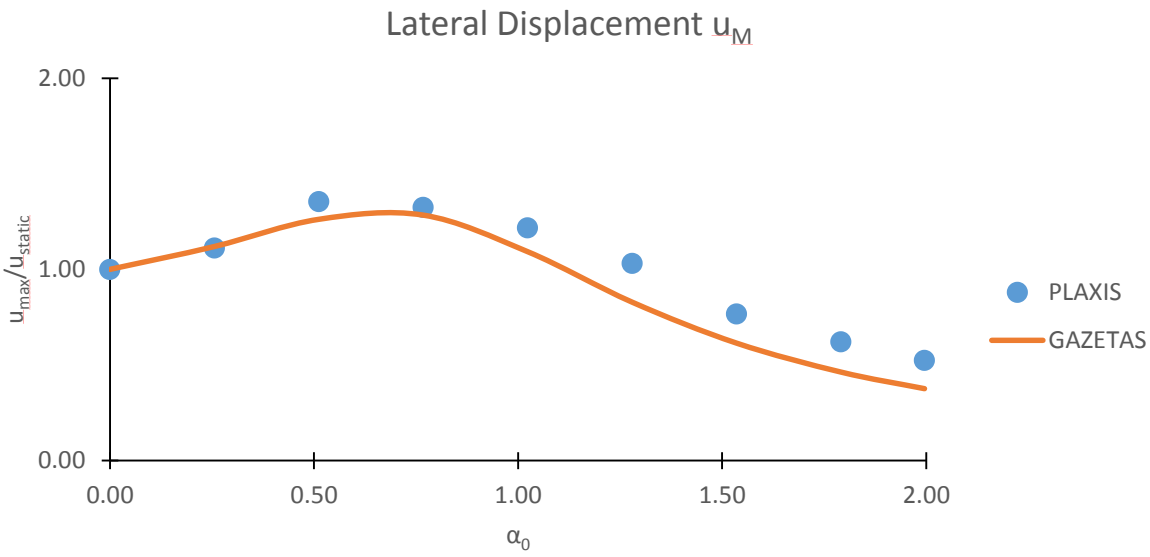

Figure 3-23: Normalized lateral maximum displacement at the center of the top of caisson resulted be lateral dynamic load: M(t)=1667sin(ωt+π/2) and Q(t)=0.

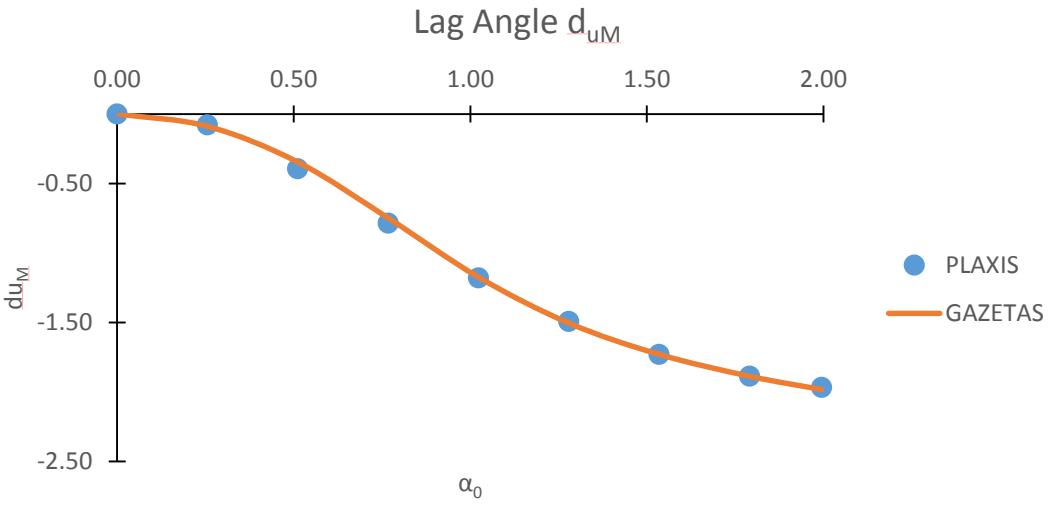

Figure 3-24: Increasing absolute value of the lag angle between the load M(t) and the lateral displacement u_M.

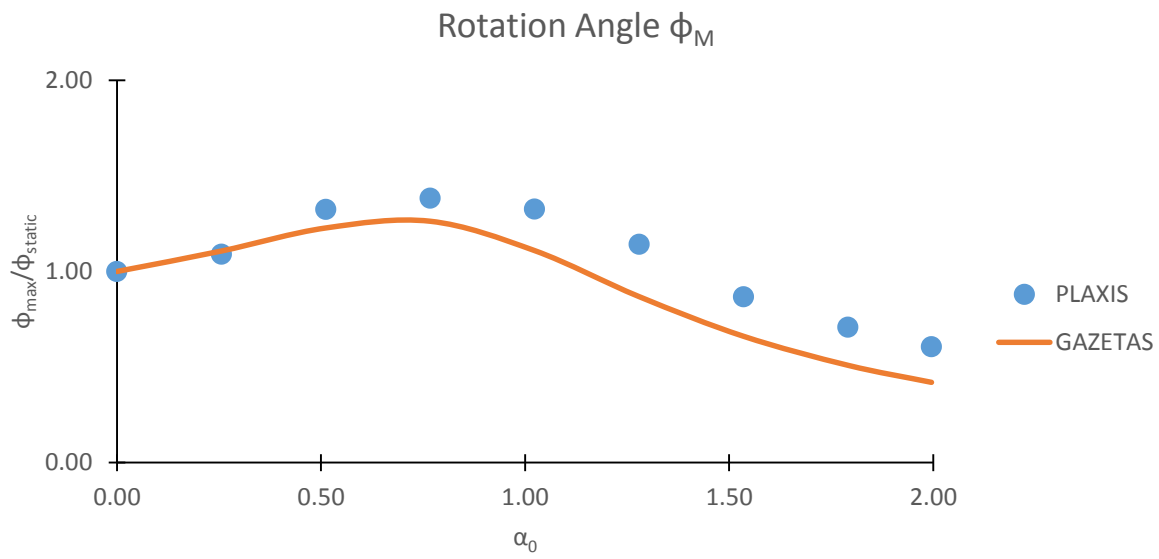

Figure 3-25: Normalized lateral maximum rotation angle of caisson resulted be lateral dynamic load: M(t)=1667sin(ωt+π/2) and Q(t)=0.

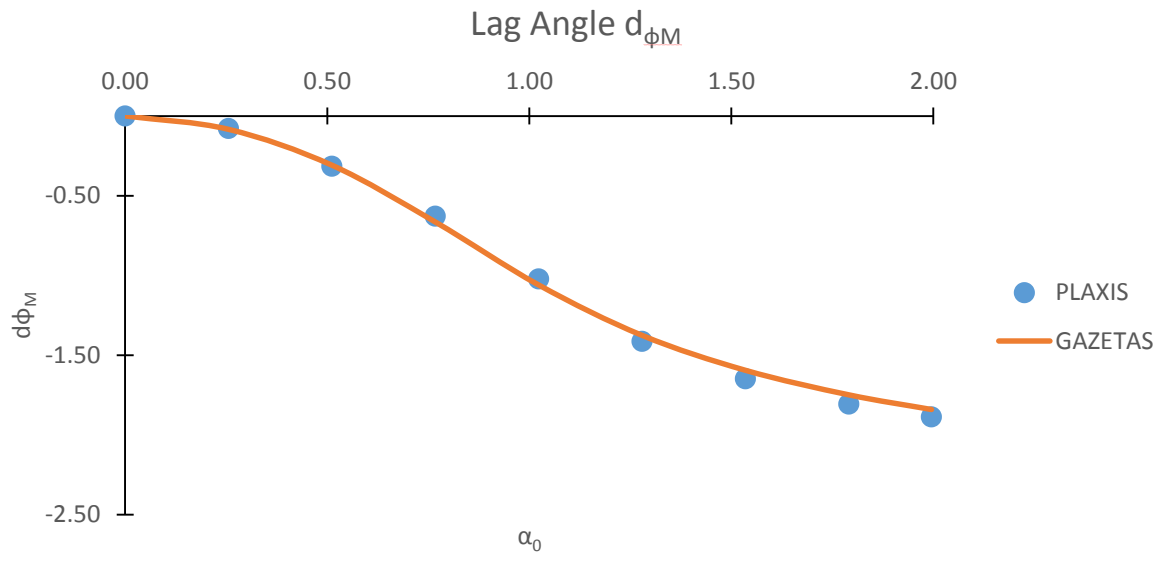

Figure 3-26: Increasing absolute value of the lag angle between the load M(t) and the rotation angle $\phi_M(t)$.

As it can be observed from the presented figures above, the numerical analyses match the simplified solutions with a very good approximation. The deviation between the response obtained from the numerical analyses and the corresponding response obtained from the analytical solutions is very small. Considering the maximum response, it can be seen that the deviation is increasing as the frequency increases. An explanation for this trend is that the numerical model is more accurate for the lower frequencies considering the element size and the domain dimensions. In general it can be concluded that the numerical analyses underestimate the response because of the smaller damping coefficients that are derived as it will be shown and explained in the following.

Another important remark that can be obtained from the results is the importance of the normalization. Although the coupling terms, rotation angle ϕ_Q due to force and lateral displacement u_M due to moment, are not equal as normal values because different amplitudes of force and moment were applied (Q=1000kN and M=1667kNm), these terms coincide when are presented in normalized charts.

As far as concerns the phase angles the remarkable fit with the analytical solutions can be seen in the figures. The deviation here is under 6% for all modes.

In the following the results of the calculated impedance are presented. First the norm of the impedance is presented with the real and imaginary part following and afterwards, the springs K_{ij} and the dashpots C_{ij} are subtracted. The relations that have been used are the following:

$$\widetilde{K}_{hh} = (K_{hh} - M_{hh}\omega^2) + i\omega C_{hh} \qquad \left|\widetilde{K}_{hh}\right| = \sqrt{(K_{hh} - M_{hh}\omega^2)^2 + (\omega C_{hh})^2}$$

$$\widetilde{K}_{hr} = (K_{hr} - M_{hr}\omega^2) + i\omega C_{hr} \qquad \left|\widetilde{K}_{hr}\right| = \sqrt{(K_{hr} - M_{hr}\omega^2)^2 + (\omega C_{hr})^2}$$

$$\widetilde{K}_{rr} = (K_{rr} - M_{rr}\omega^2) + i\omega C_{rr} \qquad \left|\widetilde{K}_{rr}\right| = \sqrt{(K_{rr} - M_{rr}\omega^2)^2 + (\omega C_{rr})^2}$$

$$\widetilde{K}_{rh} = (K_{rh} - M_{rh}\omega^2) + i\omega C_{rh} \qquad \left|\widetilde{K}_{rh}\right| = \sqrt{(K_{rh} - M_{rh}\omega^2)^2 + (\omega C_{rh})^2}$$

Where M_{ij} are the mass coefficients presented in matrix (3.13), K_{ij} are the dynamic spring coefficients and C_{ij} are the dynamic dashpot coefficients. The dynamic coefficients are frequency dependent and are functions of both caisson geometry and soil stiffness.

Table 3-8presents the results of the norms obtaining from the two methods, the dynamic analyses of PLAXIS and Gazetas formulations. A comparison between the corresponding values has been made in the last column. Figures that follow depicts these results in normalized graphs. The horizontal impedance has been normalized by EB, the rotational impedance by EB^3 and the coupling impedance by EB^2. The dimensionless frequency $\alpha_0 = \frac{\omega B}{2V_s}$ is used in all graphs.

Table 3-7: Units for each mode of impedance

$\left\|\widetilde{K}_{ij}\right\|$	units
hh	kN/m
rr	kNm
hr	kN

Table 3-8: Comparison between dynamic global impedances calculated by PLAXIS results and GAZETAS formulations. The dynamic impedances are given in kN/m.

f (Hz)	α_0	IMPEDANCE			
		$\left\|\widetilde{K}_{ij}\right\|$	PLAXIS	GAZETAS	deviation
0	0	hh	1.11E+06	9.91E+05	-12%
		rr	2.72E+08	2.98E+08	9%
		hr	-1.31E+07	-1.32E+07	1%
0.5	0.26	hh	9.09E+05	9.71E+05	-6%
		rr	2.31E+08	2.82E+08	-18%
		hr	1.10E+07	1.31E+07	-16%
1	0.51	hh	1.01E+06	1.05E+06	-3%
		rr	2.26E+08	2.85E+08	-14%
		hr	1.23E+07	1.43E+07	-21%
1.5	0.77	hh	1.59E+06	1.30E+06	22%
		rr	2.87E+08	3.23E+08	-11%
		hr	1.80E+07	1.76E+07	2%
2	1.02	hh	1.88E+06	1.74E+06	8%
		rr	3.09E+08	4.02E+08	-23%
		hr	2.05E+07	2.29E+07	-10%
2.5	1.28	hh	2.46E+06	2.34E+06	5%
		rr	3.80E+08	5.13E+08	-26%
		hr	2.63E+07	2.98E+07	-11%
3	1.54	hh	3.06E+06	3.04E+06	1%
		rr	4.68E+08	6.48E+08	-28%
		hr	3.22E+07	3.78E+07	-15%
3.5	1.79	hh	3.72E+06	3.82E+06	-3%
		rr	5.63E+08	8.00E+08	-30%
		hr	3.88E+07	4.64E+07	-16%
3.9	2	hh	4.61E+06	4.49E+06	3%
		rr	6.78E+08	9.31E+08	-27%
		hr	4.74E+07	5.37E+07	-12%

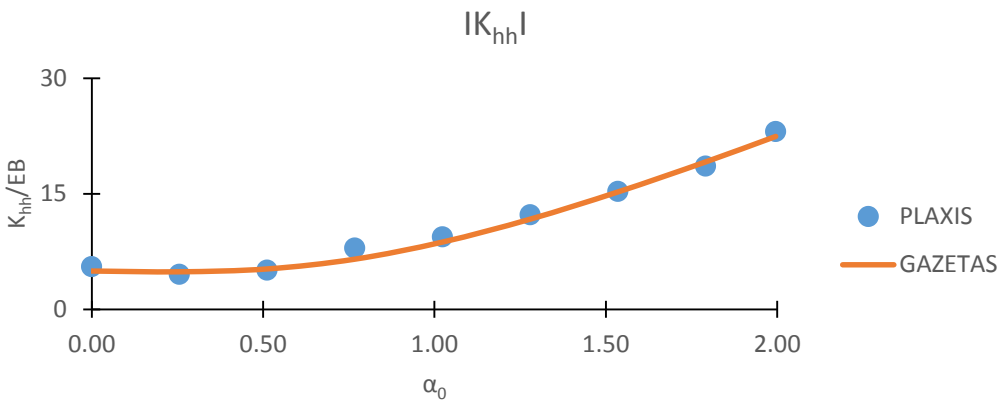

Figure 3-27: Normalized horizontal global dynamic impedance calculated by PLAXIS analyses and GAZETAS formulations.

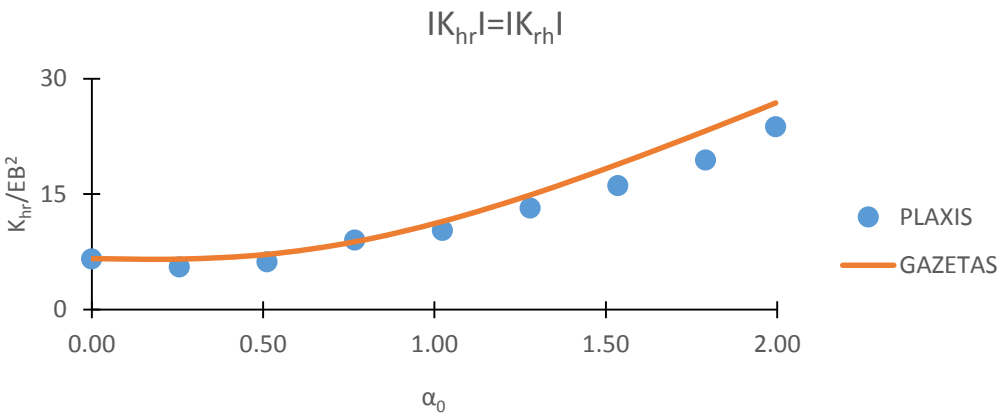

Figure 3-28: Normalized coupling horizontal-rotational global dynamic impedance calculated by PLAXIS analyses and GAZETAS formulations.

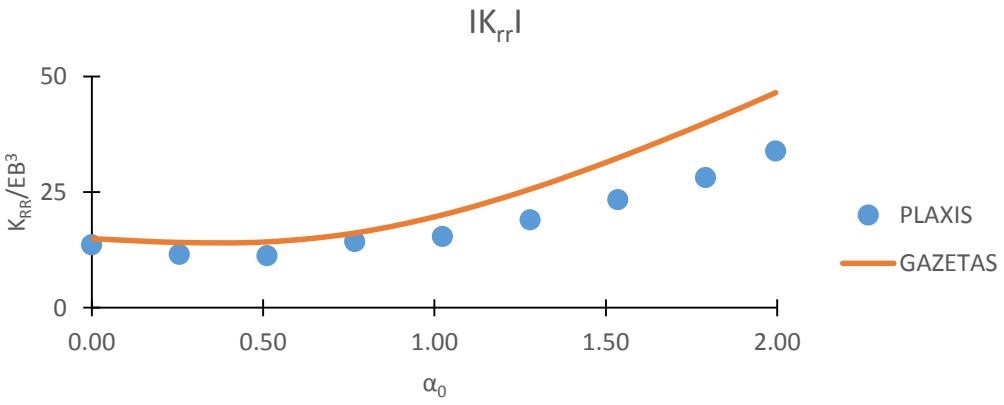

Figure 3-29: Normalized rotational global dynamic impedance calculated by PLAXIS analyses and GAZETAS formulations.

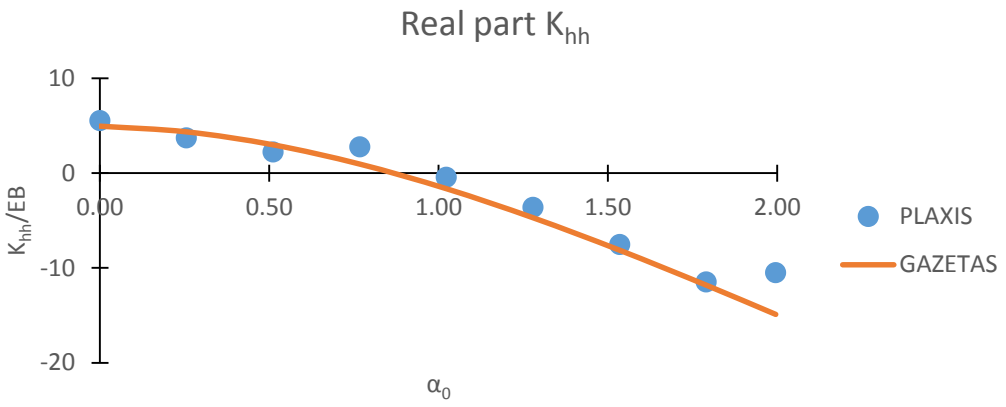

Figure 3-30: Normalized real part of the resultant horizontal impedance atop a square caisson for slenderness ratio D/B=2. Solutions derived by PLAXIS analyses and GAZETAS formulations.

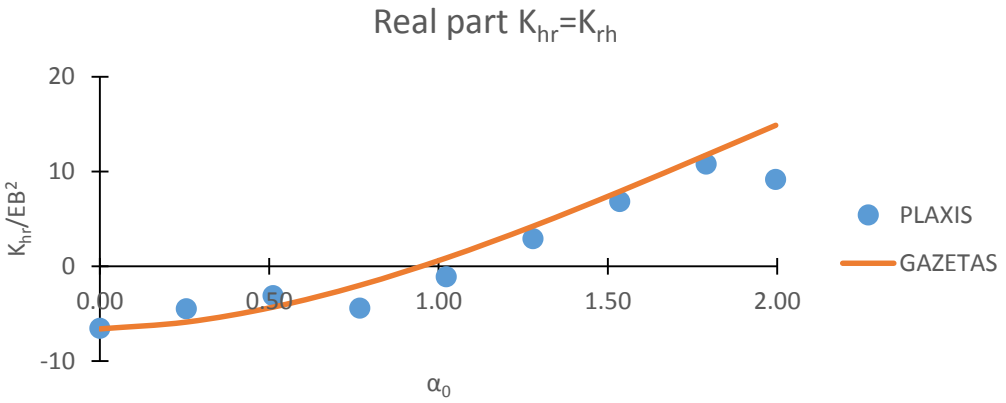

Figure 3-31: Normalized real part of the resultant cross horizontal-rotational impedance atop a square caisson for slenderness ratio D/B=2. Solutions derived by PLAXIS analyses and GAZETAS formulations.

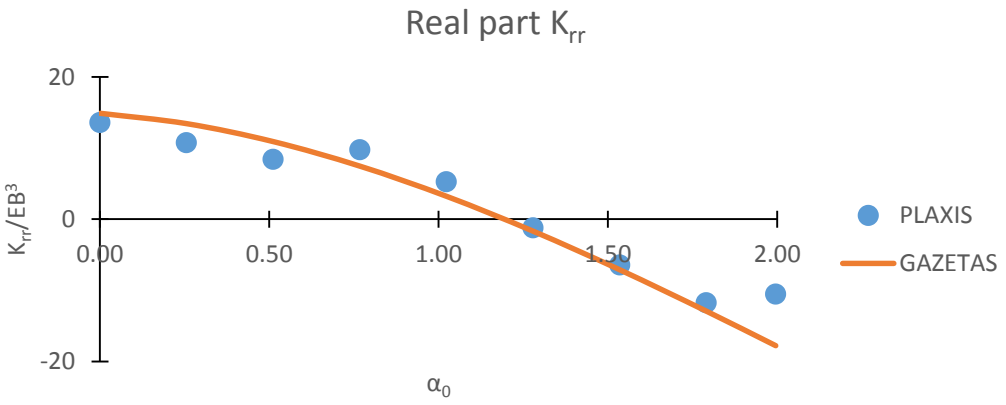

Figure 3-32: Normalized real part of the resultant rotational impedance atop a square caisson for slenderness ratio D/B=2. Solutions derived by PLAXIS analyses and GAZETAS formulations.

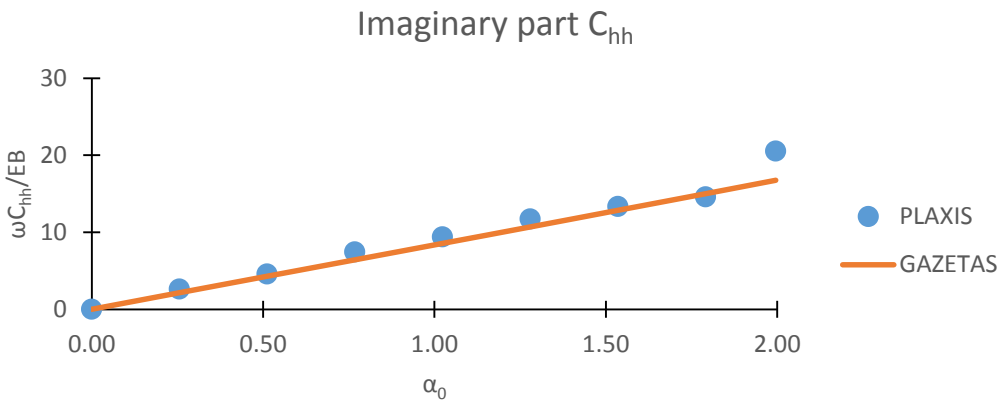

Figure 3-33: Normalized imaginary part of the resultant horizontal impedance atop a square caisson for slenderness ratio D/B=2. Solutions derived by PLAXIS analyses and GAZETAS formulations.

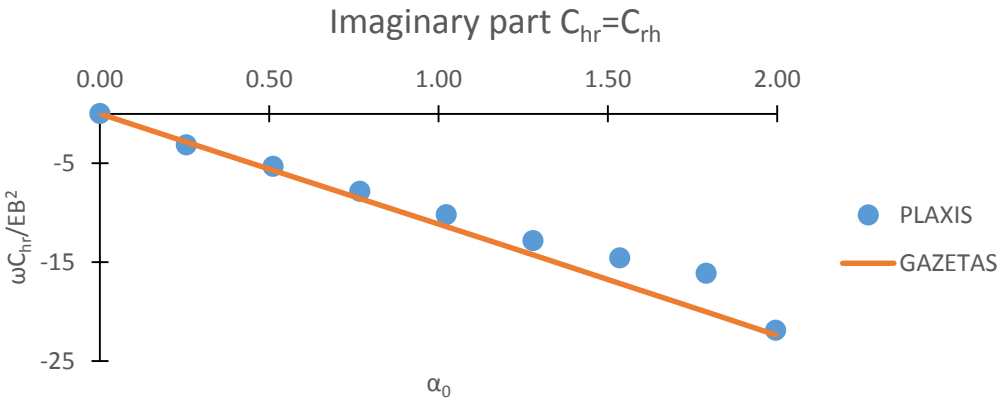

Figure 3-34: Normalized imaginary part of the resultant cross horizontal-rotational impedance atop a square caisson for slenderness ratio D/B=2. Solutions derived by PLAXIS analyses and GAZETAS formulations.

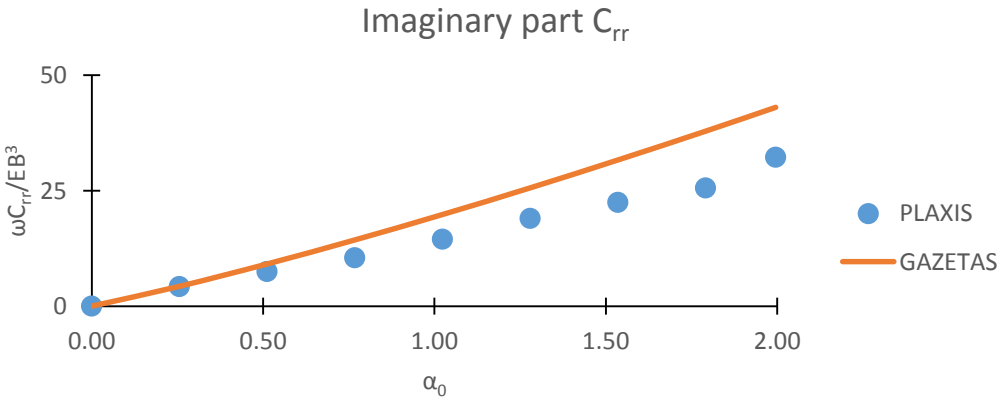

Figure 3-35: Normalized imaginary part of the resultant rotational impedance atop a square caisson for slenderness ratio D/B=2. Solutions derived by PLAXIS analyses and GAZETAS formulations.

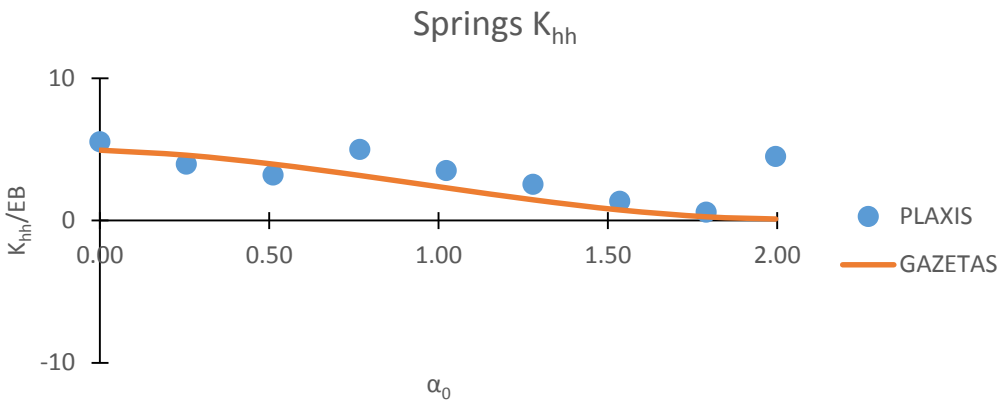

Figure 3-36: Normalized coefficients of the resultant horizontal stiffness atop a square caisson for slenderness ratio D/B=2. Solutions derived by PLAXIS analyses and GAZETAS formulations.

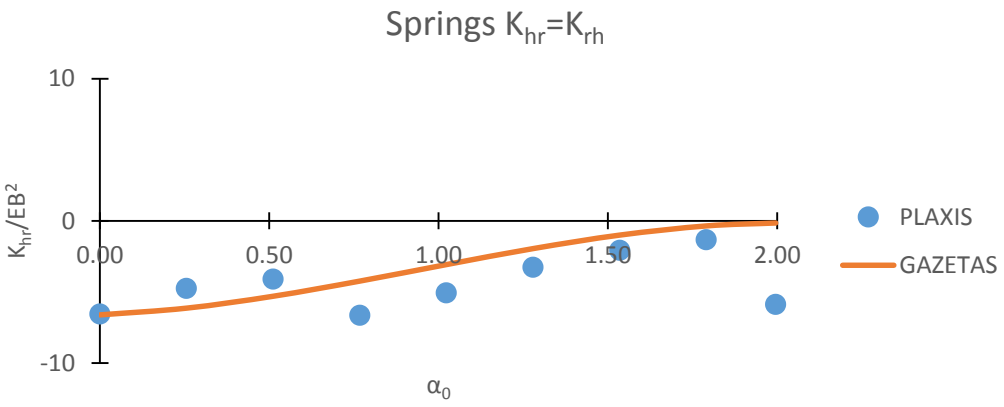

Figure 3-37: Normalized coefficients of the resultant coupling stiffness atop a square caisson for slenderness ratio D/B=2. Solutions derived by PLAXIS analyses and GAZETAS formulations.

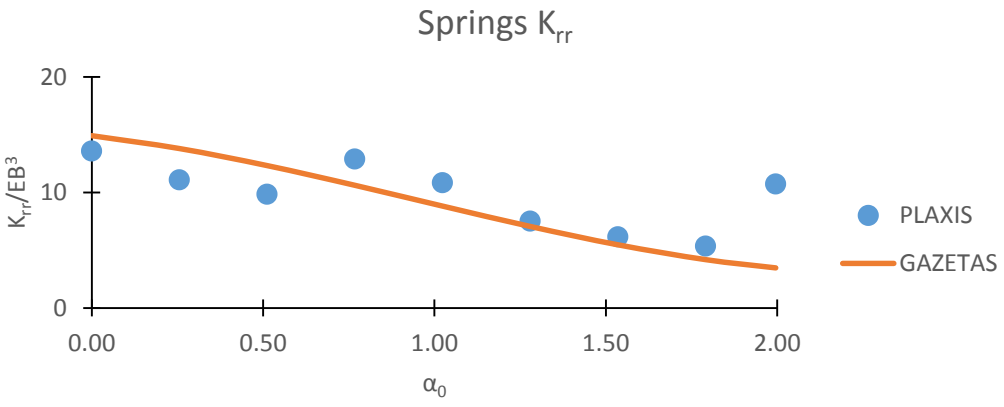

Figure 3-38: Normalized coefficients of the resultant rotational stiffness atop a square caisson for slenderness ratio D/B=2. Solutions derived by PLAXIS analyses and GAZETAS formulations.

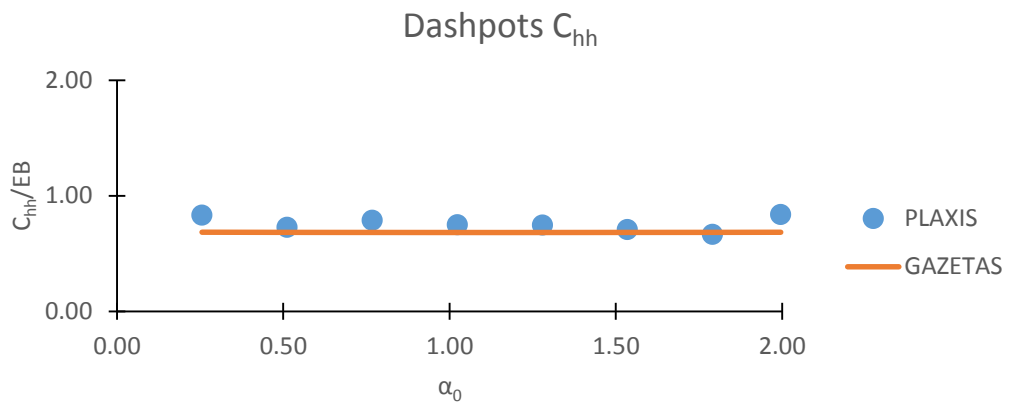

Figure 3-39: Normalized coefficients of the resultant horizontal damping atop a square caisson for slenderness ratio D/B=2. Solutions derived by PLAXIS analyses and GAZETAS formulations.

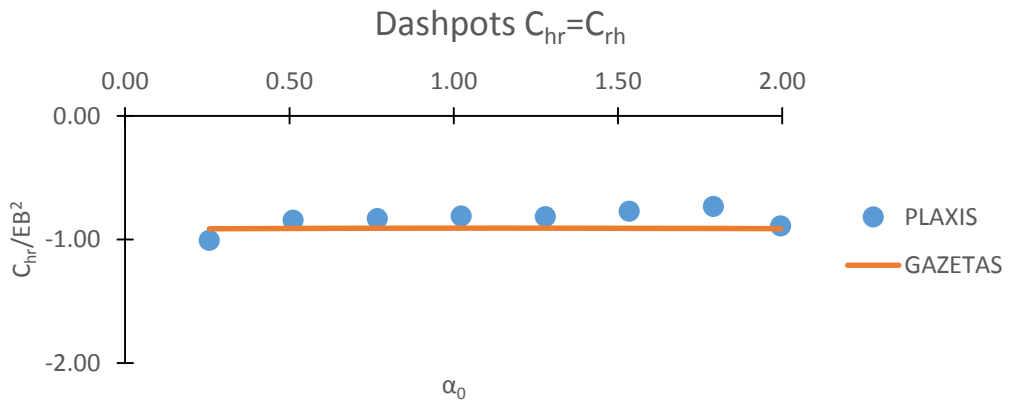

Figure 3-40: Normalized coefficients of the resultant coupling damping atop a square caisson for slenderness ratio D/B=2. Solutions derived by PLAXIS analyses and GAZETAS formulations.

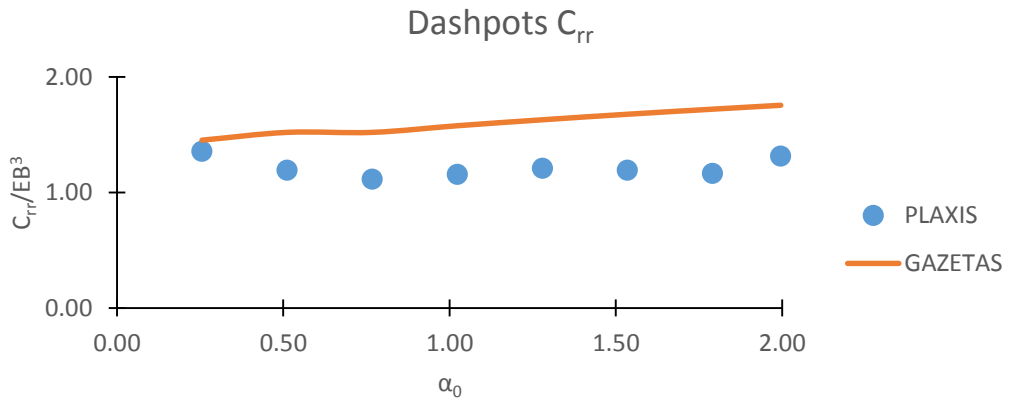

Figure 3-41: Normalized coefficients of the resultant rotational damping atop a square caisson for slenderness ratio D/B=2. Solutions derived by PLAXIS analyses and GAZETAS formulations.

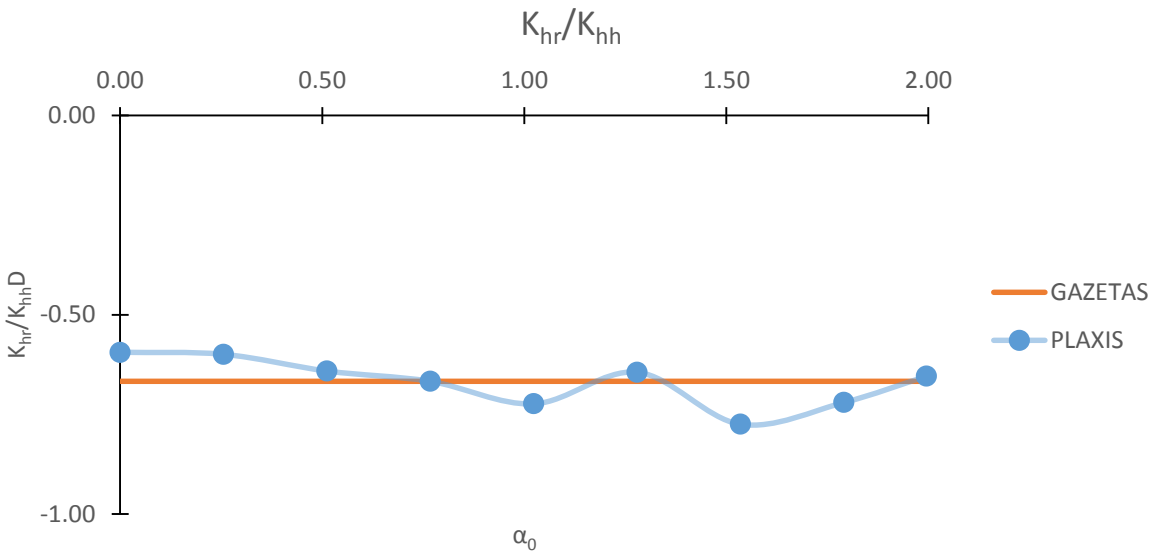

Figure 3-42: Geometric relation between the horizontal mode and the coupling mode for the stiffness, $K_{hr}/(K_{hh}D)$. Gazetas suggestion value is -0.667 and Plaxis results derive an average value of -0.669.

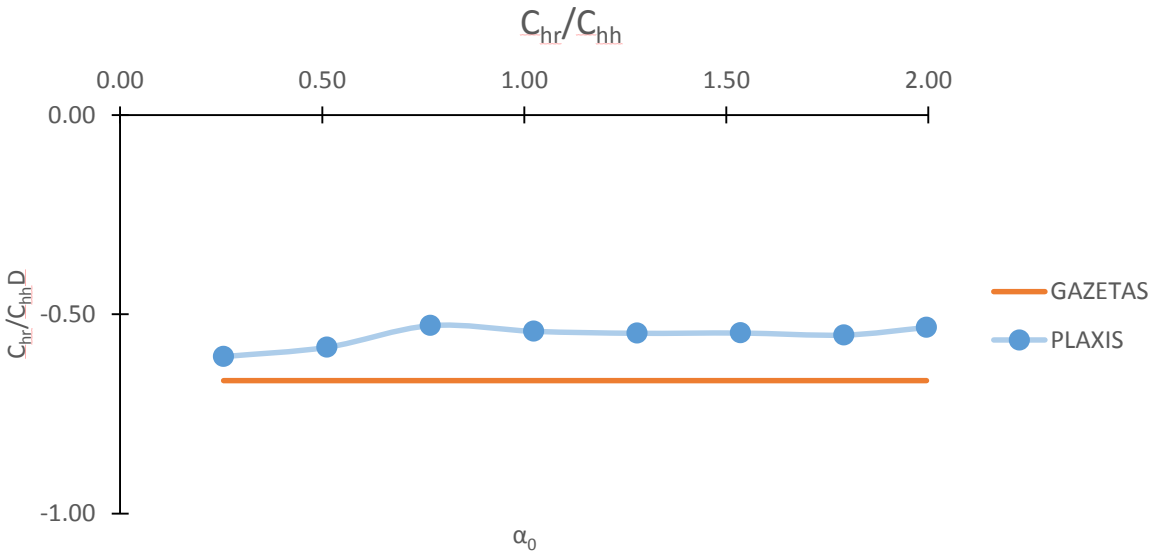

Figure 3-43: Geometric relation between the horizontal mode and the coupling mode for the dashpots, $C_{hr}/(C_{hh}D)$. Gazetas suggestion value is -0.667 and Plaxis results derive an average value of -0.555.

Some general observations that can be made from the presented results are the following. First it should be mentioned that the deviations for the norm of the impedance are the smaller comparing to its separate real and imaginary parts. This deviation is shown in Table 3-8. When subtracting from these impedances the springs and the dashpots, the deviation is increasing. Possible explanation for this is the uncertainty of the influence of the mass matrix and the corresponding mass-coefficients.

Another important observation that can be made is that the dashpots coefficients are underestimated by the numerical analyses. This leads to less maximum values of the response of the foundation as was noted before. Possible reason for this might be the uncertainty in the use of the viscous boundaries. Considering the computing of the dashpot-coefficients an alternative calculating method has been used which is described in the following chapter. The results of the two methods seem to be similar especially for the greater frequencies.

Considering the spring coefficients also another alternative method was used. The idea was to determine them independently from the dashpots by running the analyses again but without the absorbing boundaries. In this way the response of the caisson would be only due to the spring coefficients K and the mass coefficients M, as no radiation damping would be introduced (C=0) because the provided energy would remain in the system. The results of the analyses that performed in this way weren't as expected and no steady state response was obtained, probably because of the compliance of the wave reflections.

The geometric relation between the horizontal mode and the coupling mode that Gazetas formulas suggest is: $\frac{\tilde{K}_{hr}}{\tilde{K}_{hh}} = -\frac{2}{3}D = -0.667D$. The results from the finite element analyses show that this relation is totally confirmed for the stiffness where the average value of the rate is: $\frac{K_{hh}}{K_{hr}} = -0.669D$ while for the dashpots it seems that the analyses underestimate this rate, as the average value is $\frac{C_{hh}}{C_{hr}} = -0.555D$. As it was explained before this might be due to the usage of the viscous boundaries. This was the trigger to introduce Rayleigh damping as it is discussed in 3.6.4.

3.6.3 Dashpot coefficients

Dashpots coefficients represent the loss of energy due to radiation damping and material damping. The behavior of soil, meaning the constitutive model that describes it, is considered to be linear elastic in this part of the study. This fact means that no material damping is performed during the dynamic loading and dashpots coefficients represent only the radiation damping. However, despite the assumption of linear elasticity, the behavior of the caisson is described by hysteretic loops. These loops are the results of loss of energy which is only due to radiation damping and their areas represent the amount of the dissipated energy.

From the areas of these loops that are formed between the load and the response in charts Q-u, Q-ϕ and M-u, M-ϕ of each analysis, the dashpot coefficients for each mode can be calculated. By the definition of the dashpots, the areas *(DE)* of the loops are equal to the following relations:

$$DE_{Q-u} = \int_0^T (c_{hh}\dot{u} + c_{hr}\dot{\varphi})du$$

$$DE_{Q-\varphi} = \int_0^T (c_{hh}\dot{u} + c_{hr}\dot{\varphi})d\varphi$$

$$DE_{M-u} = \int_0^T (c_{rr}\dot{\varphi} + c_{rh}\dot{u})du$$

$$DE_{M-\varphi} = \int_0^T (c_{rr}\dot{\varphi} + c_{rh}\dot{u})d\varphi$$

Where c_{ij} are the dashpots coefficients for each mode, $\dot{u} = du/dt$ and $\dot{\varphi} = d\varphi/dt$, and T is the period. It should be noted here that the loop that is formed should be

taken after the first couple of cycles in order to represent the steady state response of the caisson.

For each analysis four charts are derived, two of them form loops and the other two are zero charts because of the zero corresponding driving lateral force or moment respectively.

The area of the loops has been computed graphically by dividing the area into columns. The steps have chosen to be small enough (see Figure 3-44) so the accuracy of the results to be sufficient. The equations that describe this graphical method of calculating the loop area are the following:

$$DE_{F-x} = \sum_{i=1}^{n-1} dx_i \, dF_i$$

$$dx = x_{i+1} - x_i$$

$$dF = \left(\frac{F_{i+1} + F_i}{2}\right)$$

Where F represents the load, force Q or moment M, and x represents the corresponding response, u displacement or ϕ rotation angle.

First analysis:

input: $Q(t) = 1000sin(\omega t + \pi/2)$ [kN] and $M(t) = 0$

output: $u_Q(t)$ and $\varphi_Q(t)$

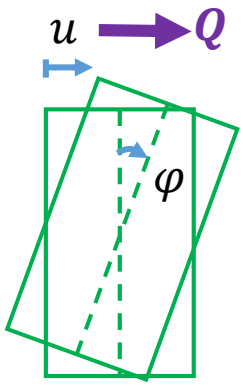

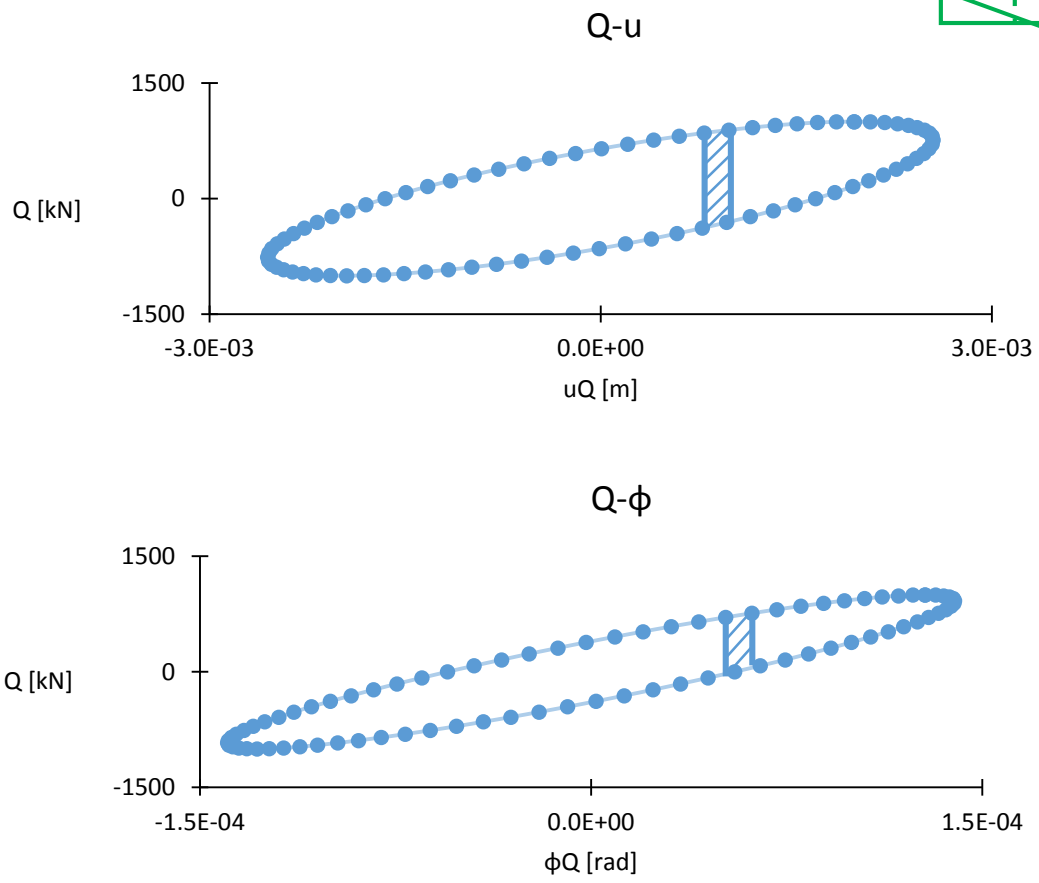

Figure 3-44: Illustration of the loops formed by the load and the response, Q-u (top) and Q-ϕ (below) from the first analysis.

From the areas of these two charts two equations are derived:

$$DE_{Q-u} = \pi\omega[u^2 c_{hh} + u\varphi \cos\delta_1 \, c_{hr}]$$

$$DE_{Q-\varphi} = \pi\omega[u\varphi \cos\delta_1 \, c_{hh} + \varphi^2 c_{hr}]$$

Where δ_1 is the phase angle between the two different modes of the response i.e. the displacement and the rotation angle.

As was mentioned before, there are another two charts (M-u) and (M-ϕ) for this analysis which correspond to the other mode of loading. However, because the driving moment M is zero for this analysis, the areas of these two loops are zero (chart M-u → DE_{M-u}=0 and chart M-ϕ→ $DE_{M-\varphi}$=0) and thus two new equations between the dashpot coefficients are derived:

$$DE_{M-u} = \pi\omega[u^2 c_{hh} + u\varphi \cos\delta_1 \, c_{hr}] = 0$$
$$DE_{M-\varphi} = \pi\omega[u\varphi \cos\delta_1 \, c_{hh} + \varphi^2 c_{hr}] = 0$$

Second analysis:

input: $M(t) = 1667sin(\omega t + \pi/2)$ [kN] and $Q(t) = 0$

output: $u_M(t)$ and $\varphi_M(t)$

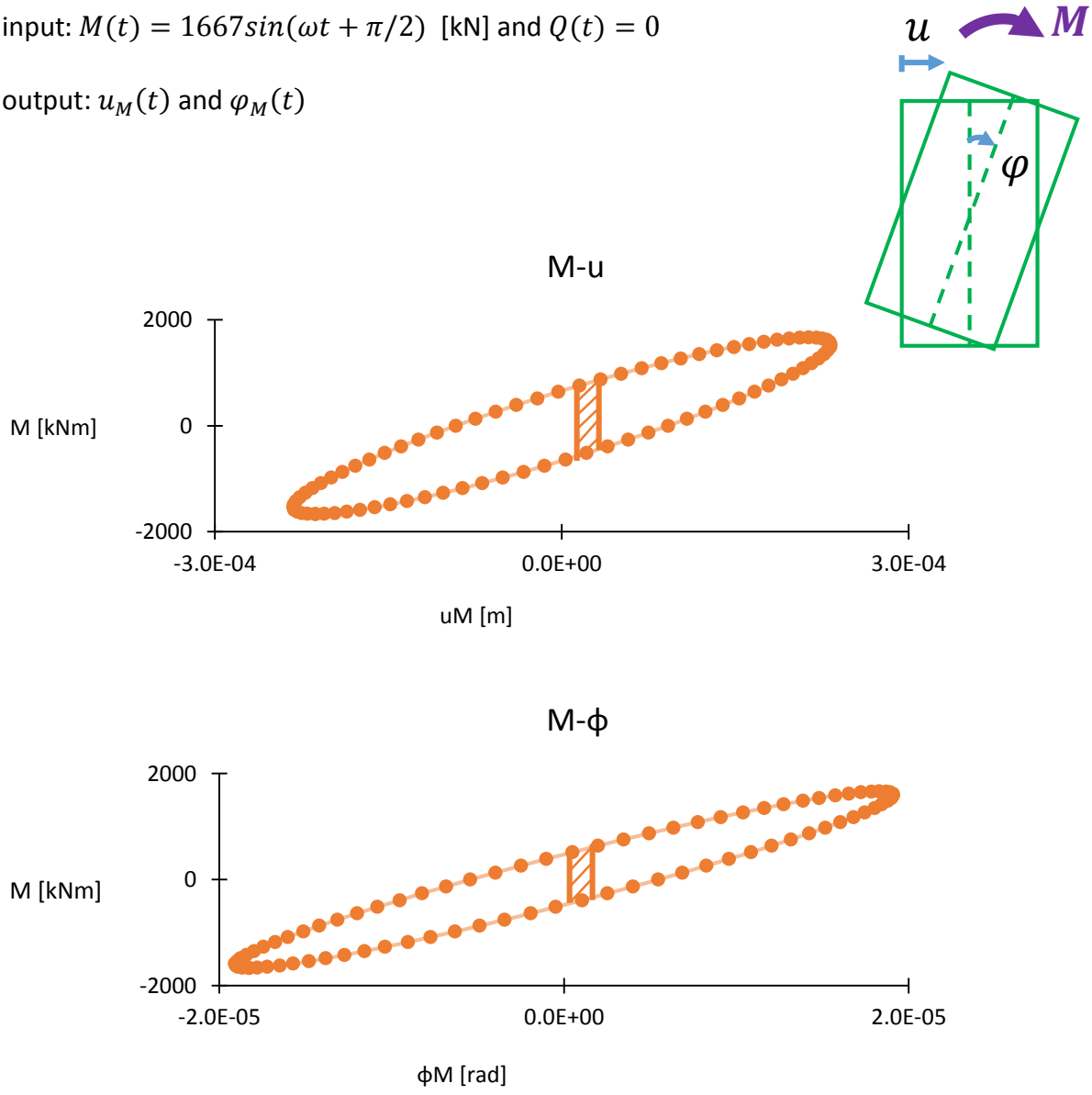

Figure 3-45: Illustration of the loops formed by the load and the response, M-u (top) and M-ϕ (below) from the second analysis.

From the areas of these two loops two equations are derived:

$$DE_{M-u} = \pi\omega[u^2 c_{hh} + u\varphi \cos\delta_2 \, c_{hr}]$$

$$DE_{M-\varphi} = \pi\omega[u\varphi \cos\delta_2 \, c_{hh} + \varphi^2 c_{hr}]$$

Where δ_2 is the phase angle between the two different modes of the response i.e. the displacement and the rotation angle.

As in the first analysis there are another two charts between the lateral force and the response, (Q-u) and (Q-ϕ) for this analysis. Because the driving force Q is zero, the areas of these two loops are zero (chart Q-u → DE_{Q-u}=0 and chart Q-ϕ→ $DE_{Q-\varphi}$=0) and thus two new equations between the dashpot coefficients are derived:

$$DE_{Q-u} = \pi\omega[u^2 c_{hh} + u\varphi \cos\delta_2 \, c_{hr}] = 0$$

$$DE_{Q-\varphi} = \pi\omega[u\varphi \cos\delta_2 \, c_{hh} + \varphi^2 c_{hr}] = 0$$

For more details about the aforementioned equations and how they have been derived the reader is referred to Appendix C.

3.6.3.1 Results

The results of the dashpots calculated by the Loop Area Method are presented in the following. The charts that follow include also the dashpots calculated by the previous methodology (complex numbers) for comparison. Some general observations and conclusions can be conducted. First of all it can be seen that the methodology of the loop area is not very accurate for the low frequencies. However as the frequency increases the values of the dashpots calculated by the two different methods tend to coincide. At the high frequencies the deviation between these values is less than 3%. It can be concluded that the loop area methodology is accurate for the high frequencies.

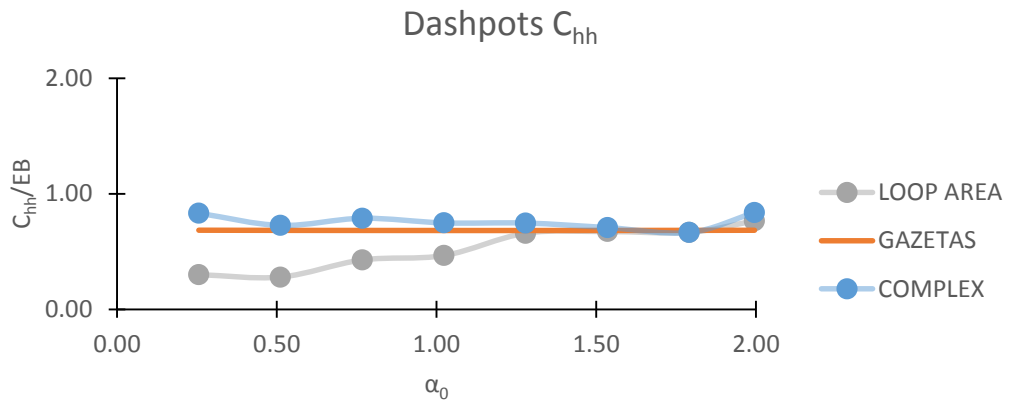

Figure 3-46: Normalized coefficients of the horizontal damping atop a square caisson for slenderness ratio D/B=2. Solutions derived by PLAXIS (loop area and complex) and GAZETAS formulations.

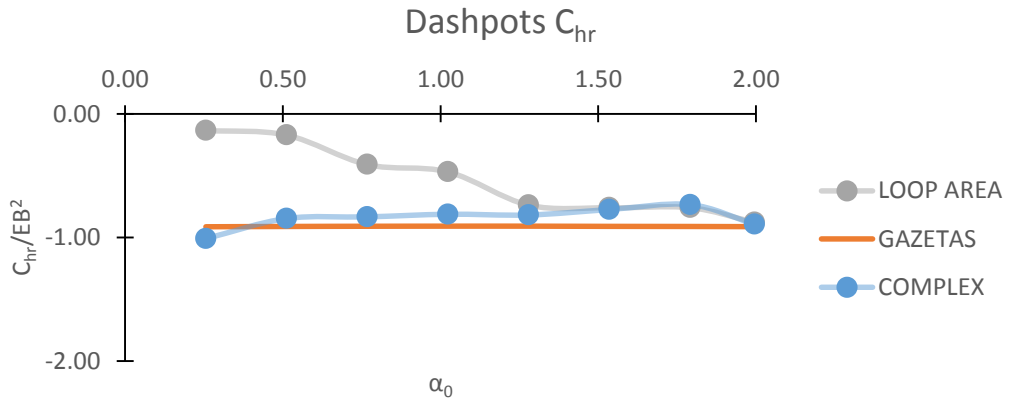

Figure 3-47: Normalized coefficients of the coupling damping atop a square caisson for slenderness ratio D/B=2. Solutions derived by PLAXIS (loop area and complex) and GAZETAS formulations.

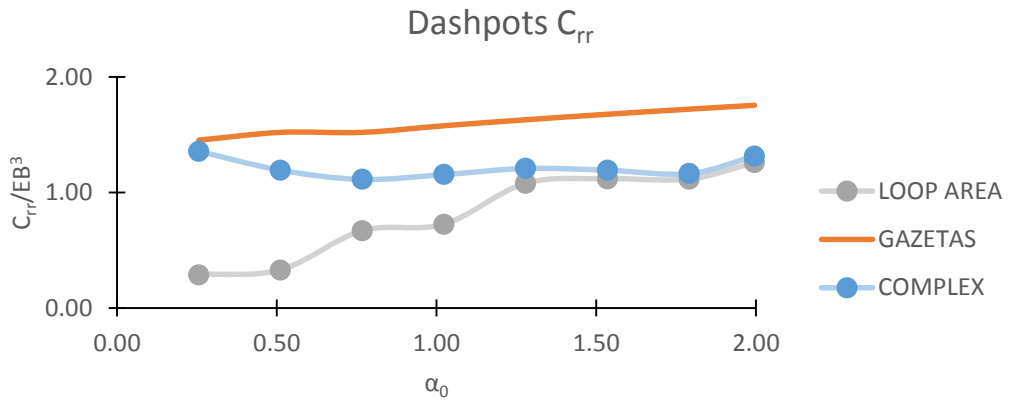

Figure 3-48: Normalized coefficients of the rotational damping atop a square caisson for slenderness ratio D/B=2. Solutions derived by PLAXIS (loop area and complex) and GAZETAS formulations.

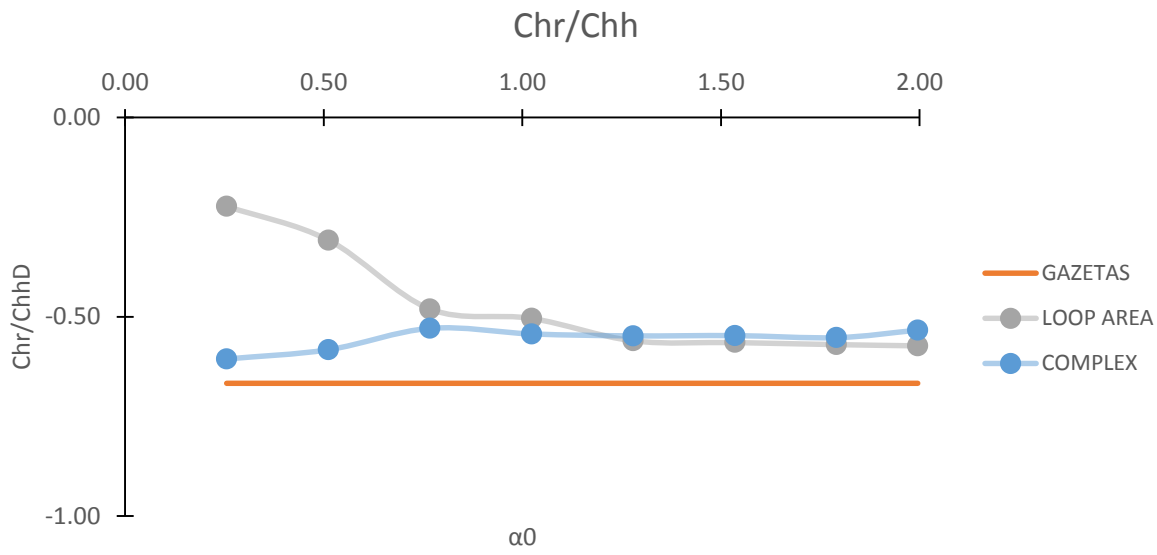

Figure 3-49: Geometric relation between the horizontal mode and the coupling mode for the dashpots, $C_{hr}/(C_{hh}D)$. Solutions derived by PLAXIS analyses by two different methodologies (loop area and complex) and GAZETAS formulations.

3.6.4 Linear elastic analyses with Rayleigh damping

Rayleigh damping is a very convenient method of representing the nonlinearities of soil in numerical analyses. The advantages of this kind of damping have been described in the literature review (2.5.4). At this part of the study all the sets of the analyses were performed again with the only difference now, adding Rayleigh damping. Linear elastic model has been used as constitutive model for both soil and caisson with same parameters as the previous analyses. Two scenarios have been investigated. In the first one 2% critical Rayleigh damping has been added and in the second one 5% critical Rayleigh damping.

It should be noted here that the dashpot coefficients calculated by Gazetas formulations do not include the soil material damping. Thus, in order the response to be comparable with Gazetas formulations, material damping has been added to the radiation damping by simply adding the corresponding material dashpot coefficient $2k\xi/\omega$, where ω is the angular frequency, k is the stiffness and ξ *is* 2% or 5% for the two scenarios. The total damping that is derived is:

$$c_{total} = c_{radiation} + \frac{2k}{\omega}\xi$$

The response of the caisson is derived by the spring coefficients, the total dashpots coefficients and the mass coefficients. The material damping is in the order of 2% or 5% thus, its influence on the response is very small as the dominant damping is the radiation damping which can exceed 40%. According to Gazetas relations the spring coefficients do not change no matter how much hysteretic damping is added. However following the methodology of calculating the springs and dashpots from the numerical analyses it can be said that Rayleigh damping has influence not only in the dashpots coefficients but also in the spring coefficients. The difference between the analyses of 2% and 5% Rayleigh damping have almost the same deviation from Gazetas relations for all the coefficients. For simplicity reasons only the graphs for Rayleigh damping 2% will be presented in the following as the 5% curves are the same but with a bit smaller values. For comparison in the charts are included the results from 0% Rayleigh for both Gazetas and PLAXIS. The dashpots coefficients that are presented for 2% Rayleigh damping are referred to the pure radiation damping as the material damping has been subtracted from the total damping in order to be comparable with the pure elastic analyses.

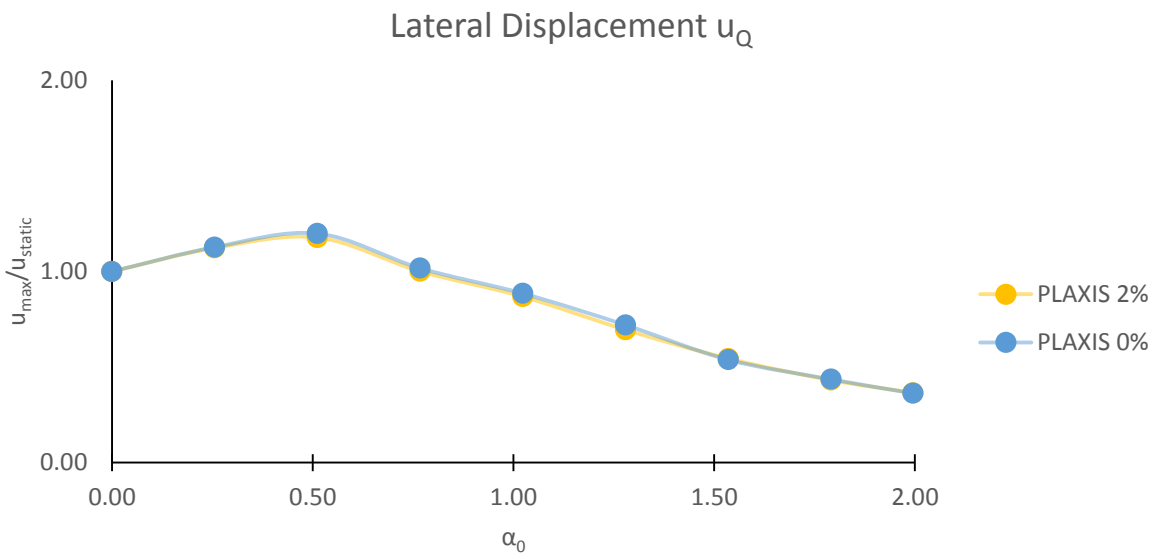

Figure 3-50: Normalized lateral maximum displacement at the center of the top of caisson resulted by lateral dynamic load: Q(t)=1000sin(ωt+π/2) and M(t)=0. Results for Rayleigh damping 0% and 2%.

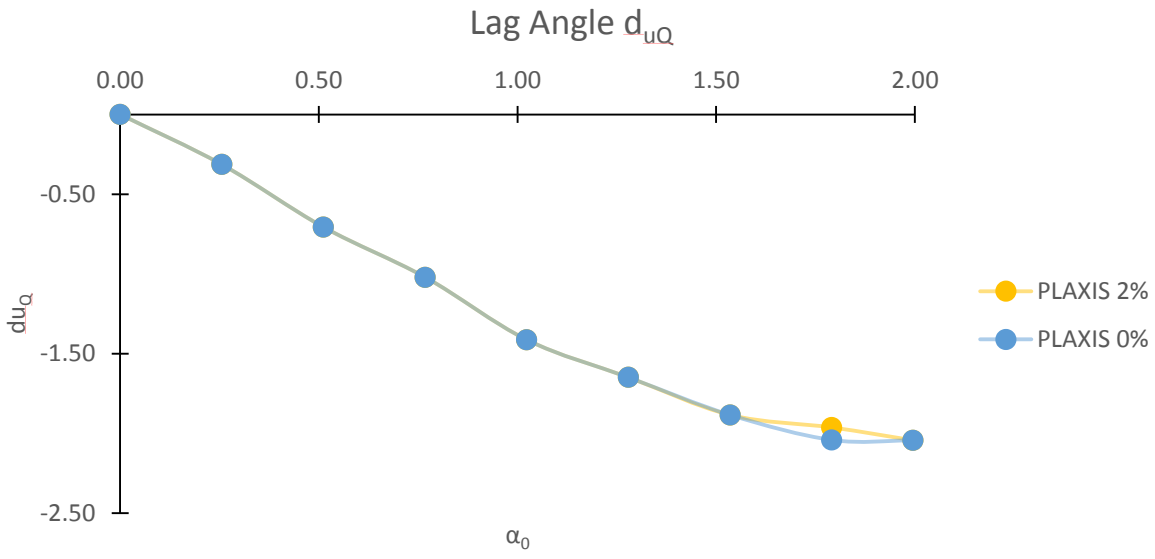

Figure 3-51: Increasing absolute value of the lag angle between the load Q(t) and the lateral displacement u_Q. Results for Rayleigh damping 0% and 2%.

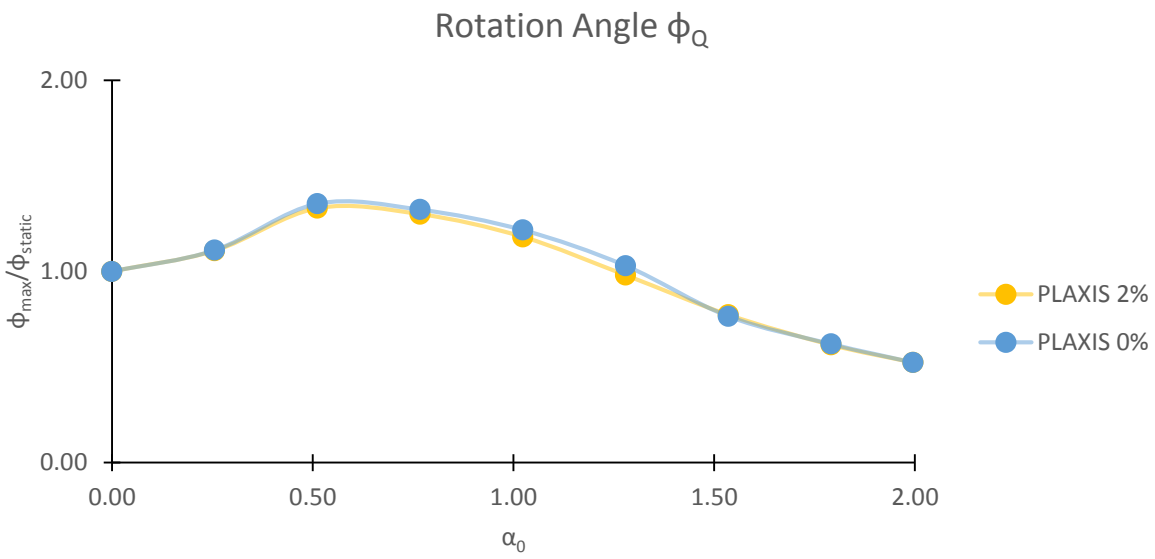

Figure 3-52: Normalized lateral maximum rotation angle of caisson resulted be lateral dynamic load: Q(t)=1000sin(ωt+π/2) and M(t)=0. Results for Rayleigh damping 0% and 2%.

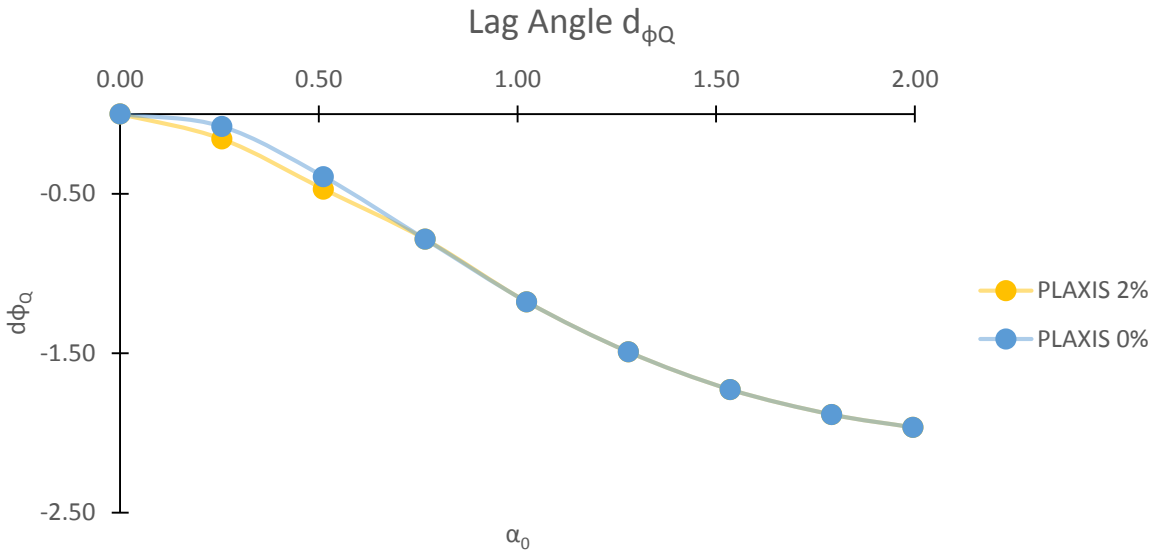

Figure 3-53: Increasing absolute value of the phase angle between the load Q(t) and the rotation angle ϕ_Q(t). Results for Rayleigh damping 0% and 2%.

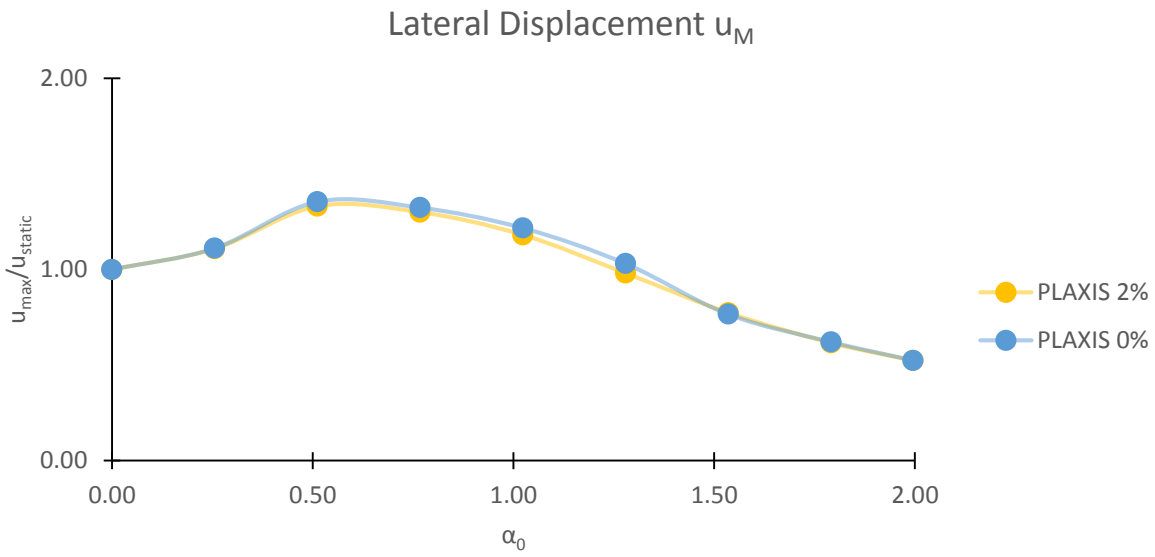

Figure 3-54: Normalized lateral maximum displacement at the center of the top of caisson resulted be lateral dynamic load: M(t)=1667sin(ωt+π/2) and Q(t)=0. Results for Rayleigh damping 0% and 2%.

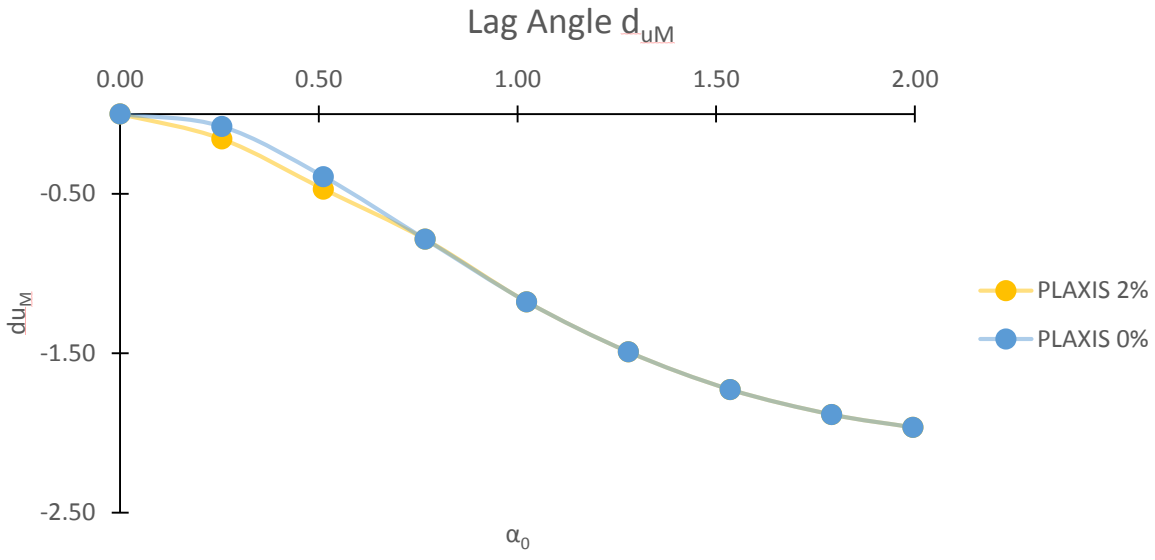

Figure 3-55: Increasing absolute value of the phase angle between the load M(t) and the lateral displacement u_M. Results for Rayleigh damping 0% and 2%.

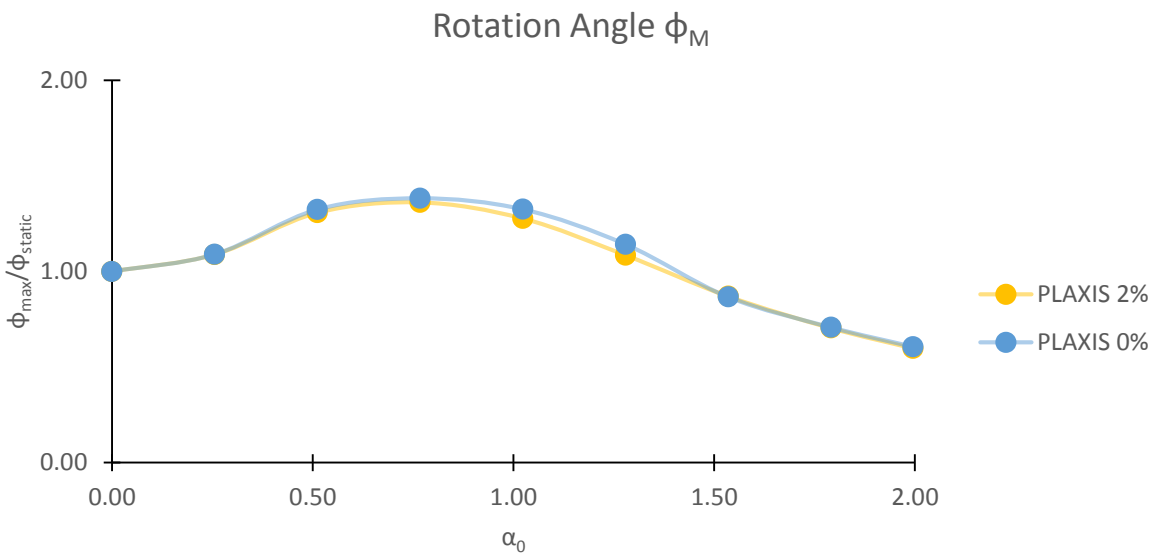

Figure 3-56: Normalized lateral maximum rotation angle of caisson resulted be lateral dynamic load: M(t)=1667sin(ωt+π/2) and Q(t)=0. Results for Rayleigh damping 0% and 2%.

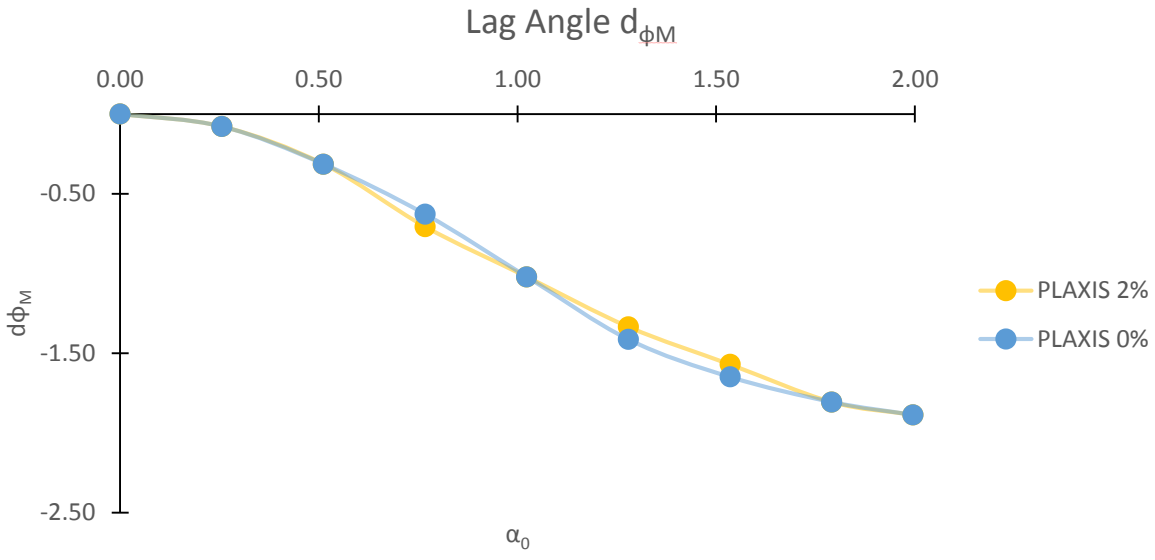

Figure 3-57: Increasing absolute value of the phase angle between the load M(t) and the rotation angle $\phi_M(t)$. Results for Rayleigh damping 0% and 2%.

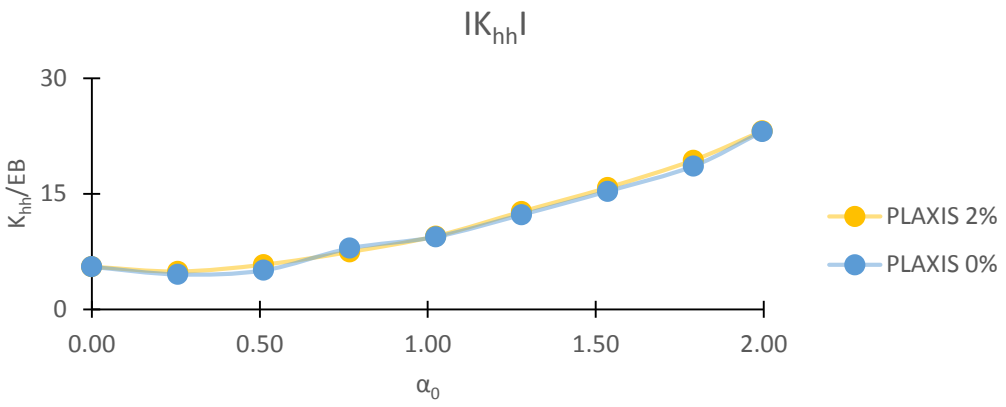

Figure 3-58: Normalized horizontal global dynamic impedance calculated by PLAXIS analyses and GAZETAS formulations. Results for Rayleigh damping 0% and 2%.

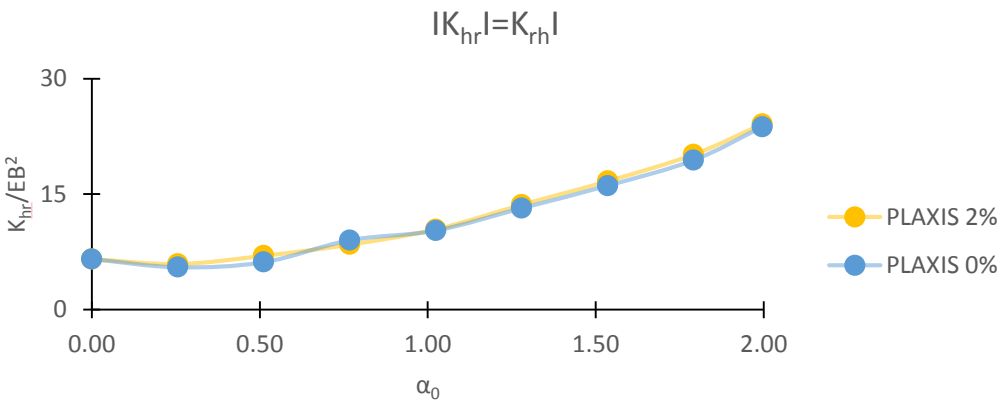

Figure 3-59: Normalized coupling horizontal-rotational global dynamic impedance calculated by PLAXIS analyses and GAZETAS formulations. Results for Rayleigh damping 0% and 2%.

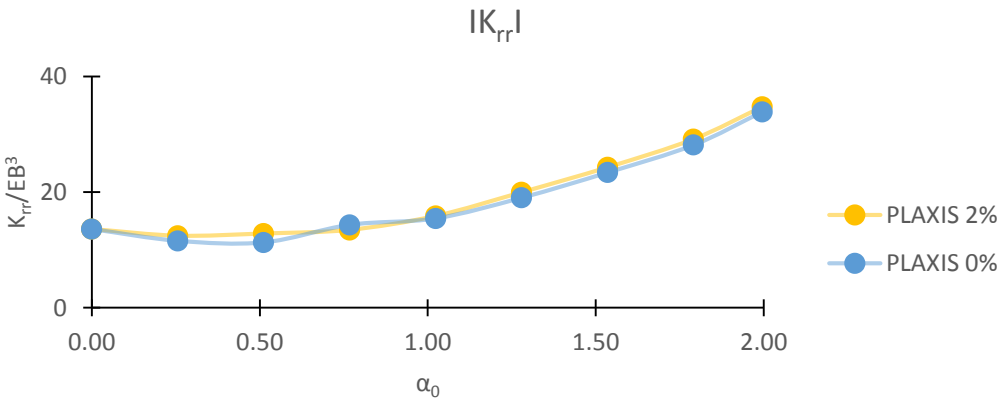

Figure 3-60: Normalized rotational global dynamic impedance calculated by PLAXIS analyses and GAZETAS formulations. Results for Rayleigh damping 0% and 2%.

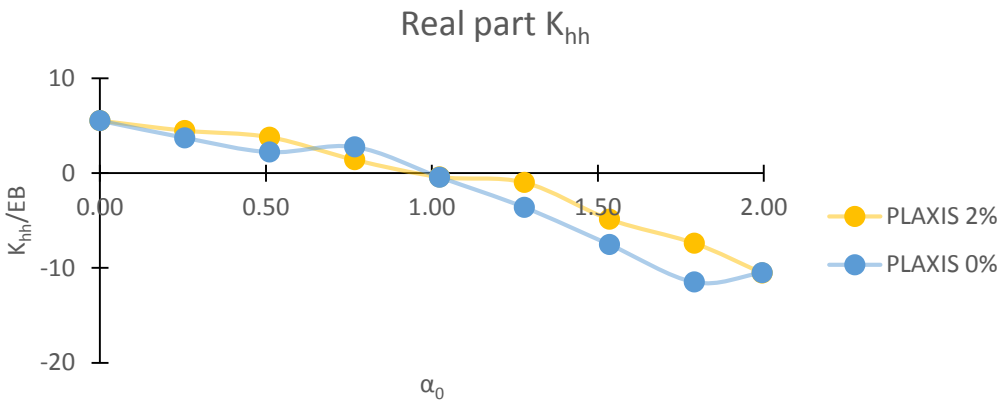

Figure 3-61: Normalized real part of the resultant horizontal impedance atop a square caisson for slenderness ratio D/B=2. Results for Rayleigh damping 0% and 2%.

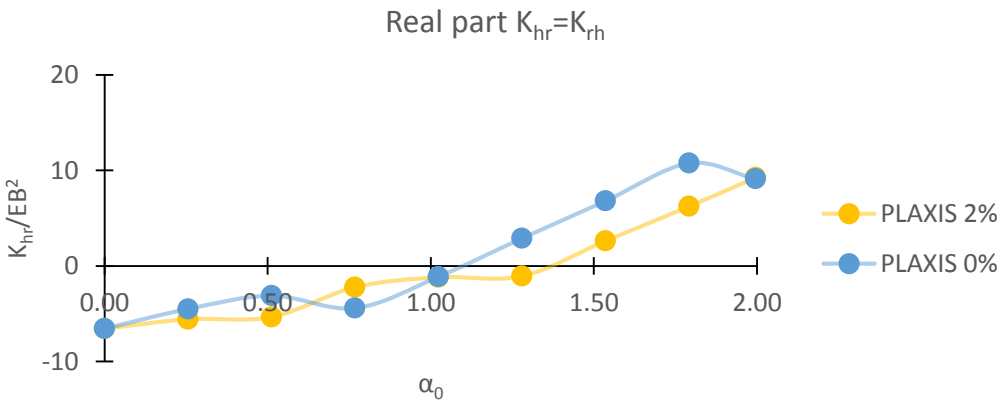

Figure 3-62: Normalized real part of the resultant cross horizontal-rotational impedance atop a square caisson for slenderness ratio D/B=2. Results for Rayleigh damping 0% and 2%.

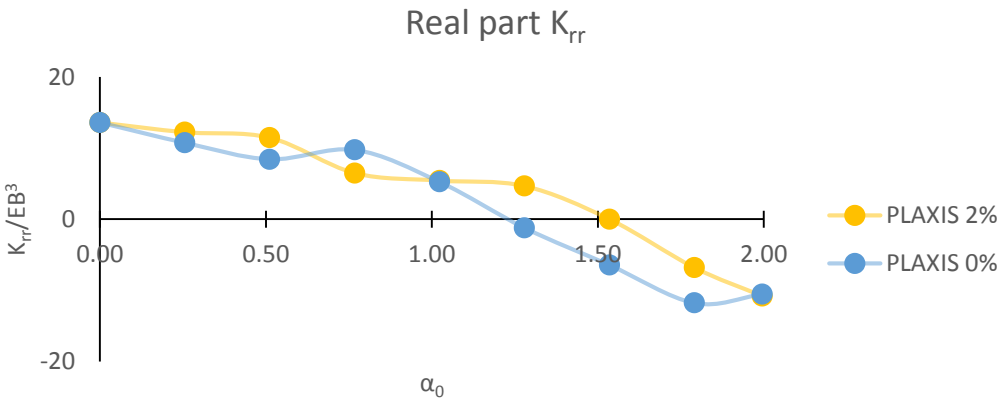

Figure 3-63: Normalized real part of the resultant rotational impedance atop a square caisson for slenderness ratio D/B=2. Results for Rayleigh damping 0% and 2%.

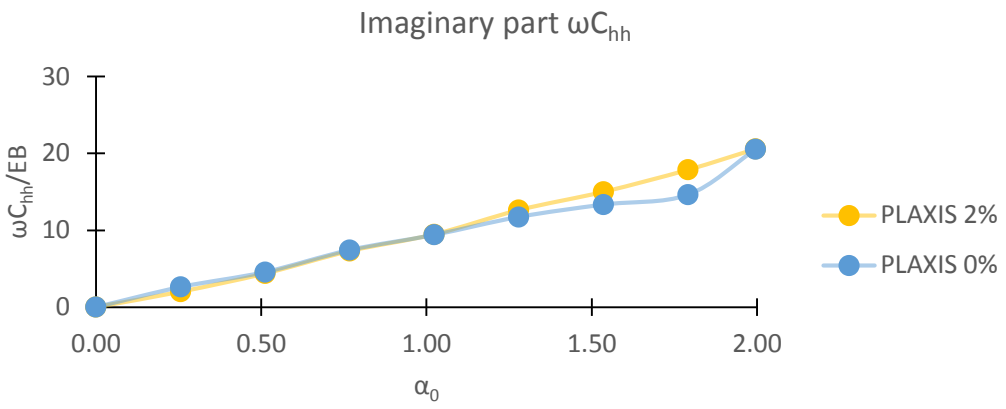

Figure 3-64: Normalized imaginary part of the resultant horizontal impedance atop a square caisson for slenderness ratio D/B=2. Results for Rayleigh damping 0% and 2%.

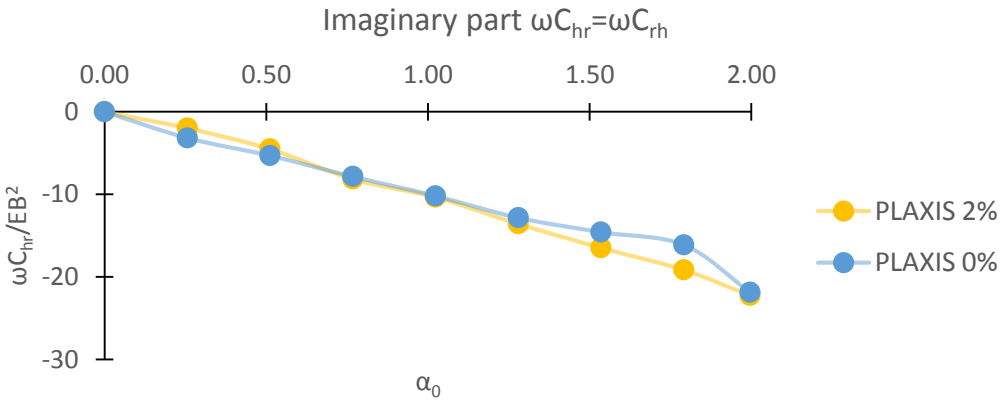

Figure 3-65: Normalized imaginary part of the resultant cross horizontal-rotational impedance atop a square caisson for slenderness ratio D/B=2. Results for Rayleigh damping 0% and 2%.

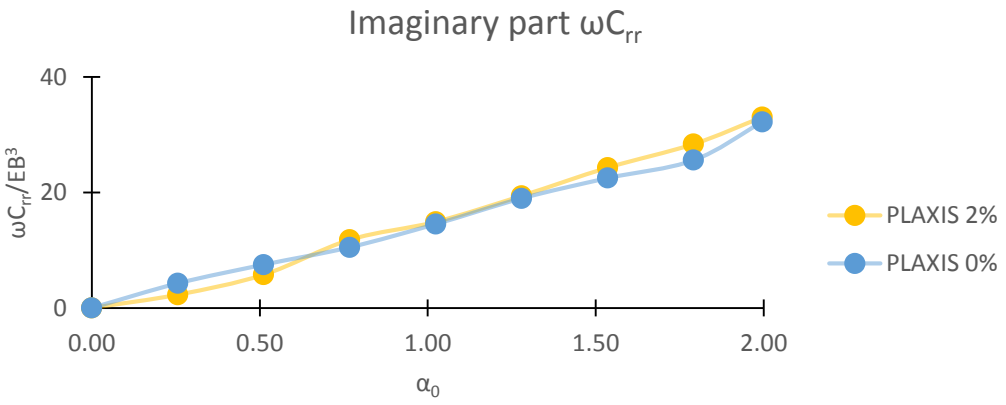

Figure 3-66: Normalized imaginary part of the resultant rotational impedance atop a square caisson for slenderness ratio D/B=2. Results for Rayleigh damping 0% and 2%.

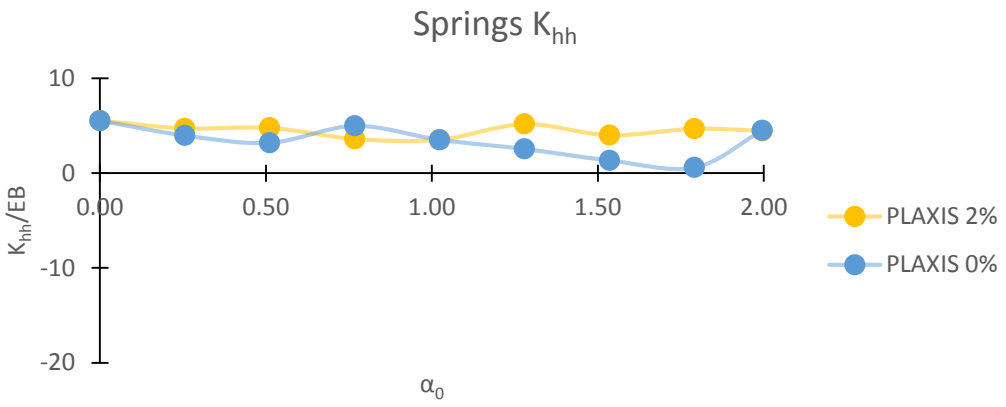

Figure 3-67: Normalized coefficients of the resultant horizontal stiffness atop a square caisson for slenderness ratio D/B=2. Results for Rayleigh damping 0% and 2%.

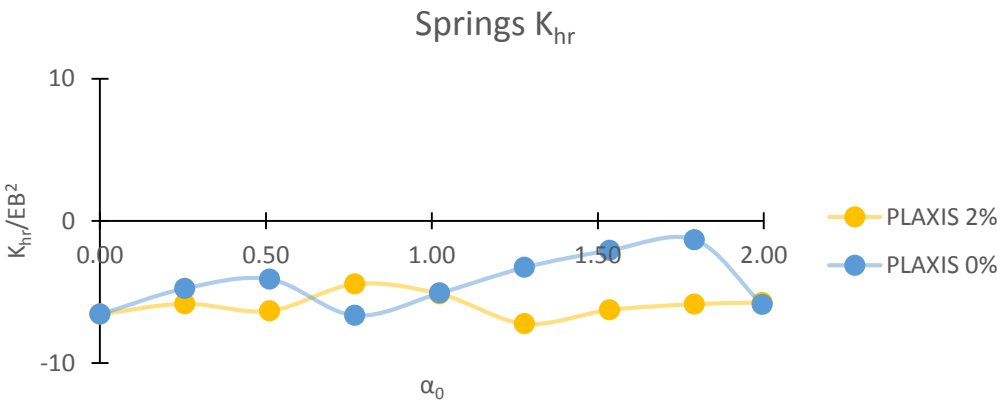

Figure 3-68: Normalized coefficients of the resultant coupling stiffness atop a square caisson for slenderness ratio D/B=2. Results for Rayleigh damping 0% and 2%.

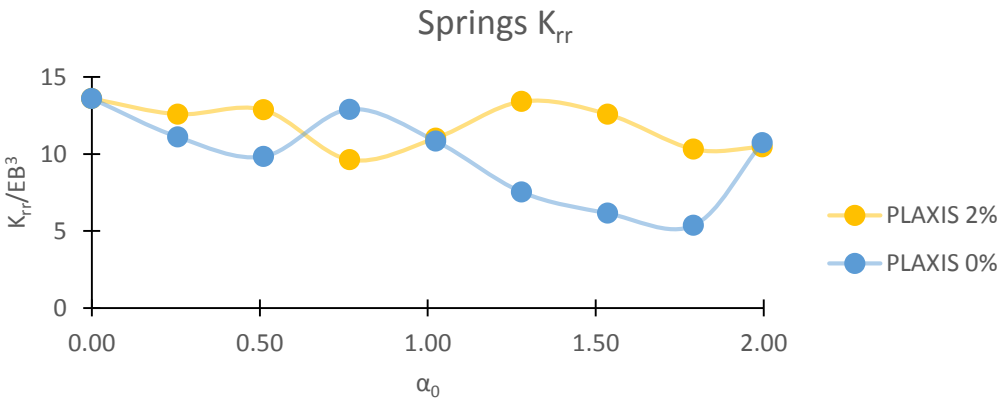

Figure 3-69: Normalized coefficients of the resultant rotational stiffness atop a square caisson for slenderness ratio D/B=2. Results for Rayleigh damping 0% and 2%.

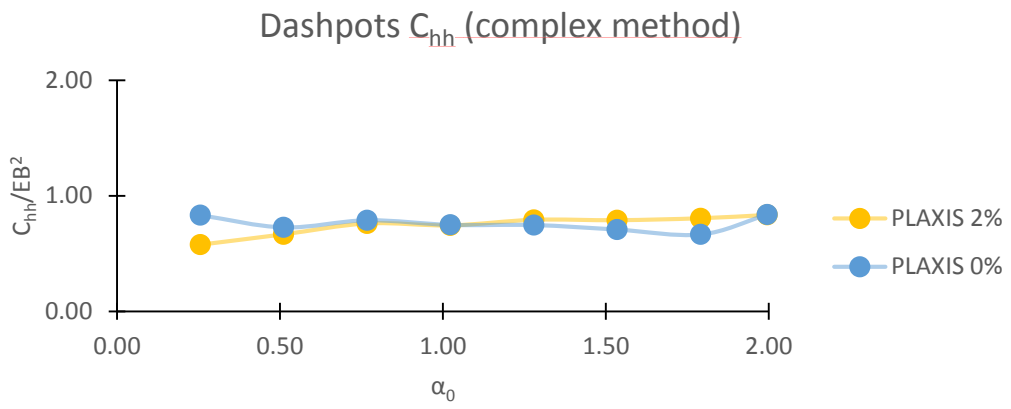

Figure 3-70: Normalized coefficients of the resultant horizontal damping atop a square caisson for slenderness ratio D/B=2. Results for Rayleigh damping 0% and 2%.

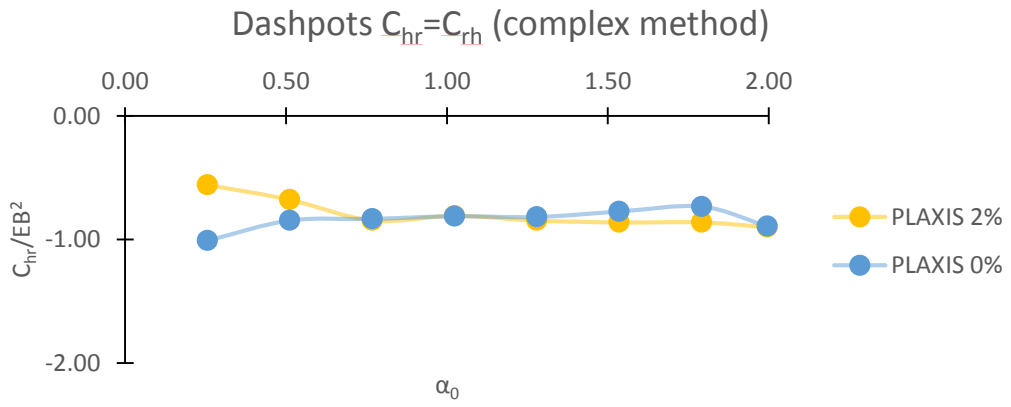

Figure 3-71: Normalized coefficients of the resultant coupling damping atop a square caisson for slenderness ratio D/B=2. Results for Rayleigh damping 0% and 2%.

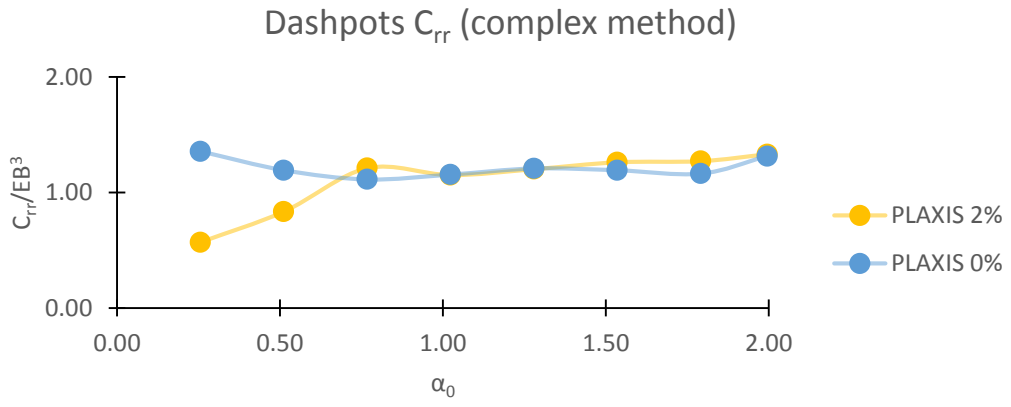

Figure 3-72: Normalized coefficients of the resultant rotational damping atop a square caisson for slenderness ratio D/B=2. Results for Rayleigh damping 0% and 2%.

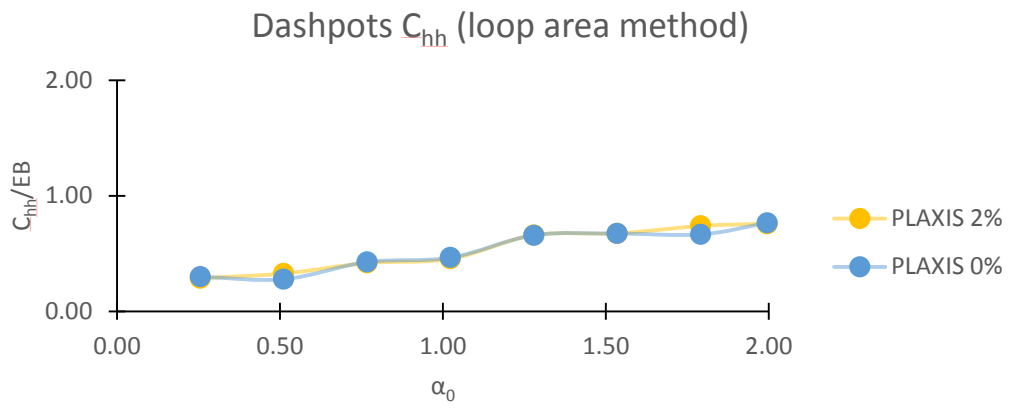

Figure 3-73: Normalized coefficients of the resultant horizontal damping atop a square caisson for slenderness ratio D/B=2. Results for Rayleigh damping 0% and 2%.

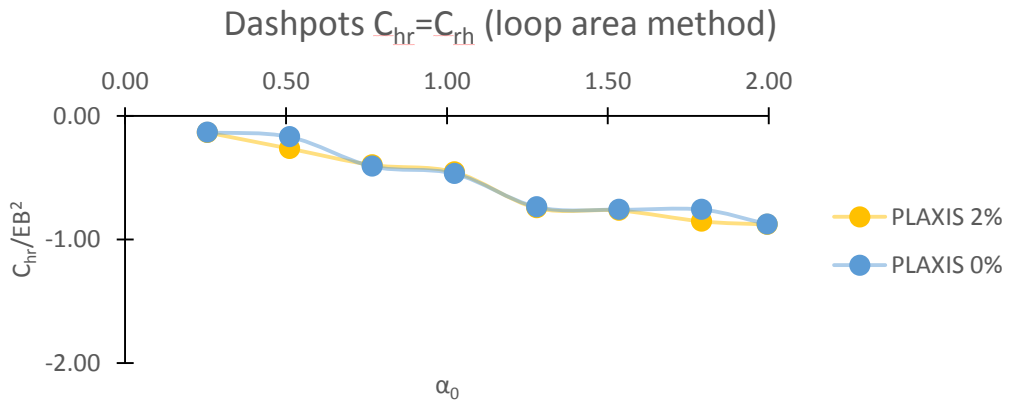

Figure 3-74: Normalized coefficients of the resultant coupling damping atop a square caisson for slenderness ratio D/B=2. Results for Rayleigh damping 0% and 2%.

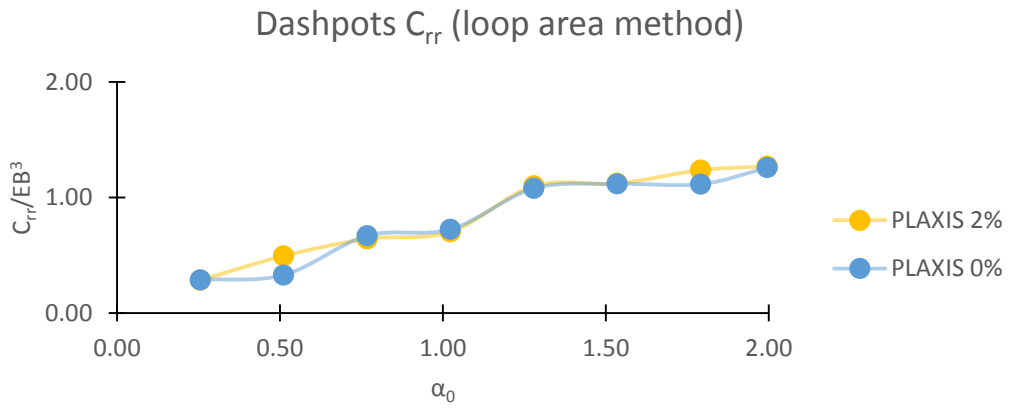

Figure 3-75: Normalized coefficients of the resultant rotational damping atop a square caisson for slenderness ratio D/B=2. Results for Rayleigh damping 0% and 2%.

4 Inelastic response

4.1 Introduction

In the previous the response of a caisson embedded in an elastic half space and subjected to dynamic loading was studied. The major limitation of that model is that soil nonlinear behavior was not taken into account, and that the caisson assumed to remain in complete contact with the surrounding soil (perfect bonding at the boundaries). These conditions can be assumed to represent reality only in the very small deformation region which for practical cases is not the case. Soil–caisson interaction involves complicated material and geometric nonlinearities such as soil inelasticity, separation (gapping) between the caisson shaft and the soil, slippage at the soil–caisson shaft interface, base uplifting, and perhaps even loss of soil strength (e.g. due to development of excess pore water pressures). Moreover, the waves emanating from the caisson periphery generate radiation damping which is strongly influenced by such nonlinearities. The general problem of a caisson embedded in cohesionless or cohesive soils and subjected to lateral loading is conceptualized in the sketch below. With strong interface and soil nonlinearities a substantially different response emerges.

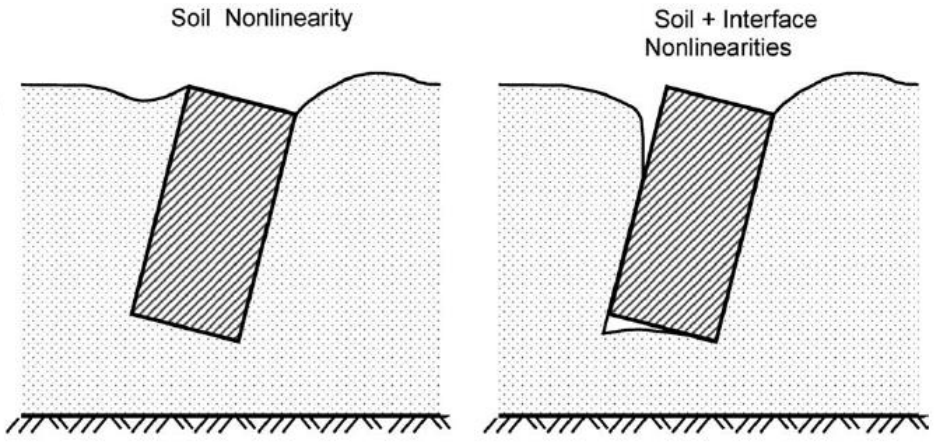

Figure 4-1: The important role of the nonlinearities on the response of a caisson. Left the illustration of the soil nonlinearity with full bonded conditions, right both soil and interface nonlinearities.

At this part of the study new numerical analyses have been performed for the same caisson (embedment ratio D/B=2) by taking into account this time the soil

nonlinearity. First full bonded conditions have been considered and afterwards the effect of the interfaces has been studied by a new set of analyses.

By taking into account the nonlinearities of the caisson the problem becomes much more complicated comparing to the elastic conditions as many more parameters play now significant role to the response of the caisson. The impedance as defined in the previous is not now applicable to the nonlinear system of the soil-structure as the coefficients are not steady for a particular frequency because more parameters influence now their values. The definition that was previously given refer now to the secant impedance of the system. The response of a nonlinear system depends not only on the frequency of the excitation but also on the magnitude of the load and the combination of the loading modes e.g. the loading ratio of the lateral force and overturning moment (h=M/Q), the applied vertical loading (V), thus the superposition cannot be applied in the nonlinear systems.

In this thesis the inelastic behavior of the caisson is studied under certain conditions and not extensively. First it should be noted that the caisson is considered to be massless. This assumption was made in order to take out the influence of the inertial forces that arise from the mass of the caisson. In this way the dynamic response would be caused only due to the soil stiffness and damping, which of course now are not steady for a specific frequency as in elastic conditions for different load levels.

The magnitude of the vertical loading changes the response as well. So at different levels of vertical loading the response of the caisson is different. The levels of the vertical loading are described by the vertical safety factor which is equal to the ultimate vertical load at failure divided by the applied vertical load, $FS_v=V/V_u$, (pure vertical loading without horizontal and rotational loading, $V\neq0$, $H=0$, $M=0$). Many times in the literature can be found as reference instead of the vertical safety factor the reversed of it which is defined as $\chi=1/FS_v$. The bigger the χ factor is more soil elements have come into the plastic area already so the response can be completely different for heavily loaded foundations (low FS_v or high χ) and lightly loaded foundations (high FS_v or low χ). In this study the reference level of the vertical loading which is described by the vertical safety factor is set to infinity, $FS_v=V_u/V=\infty$ or equally the factor $\chi=0$. In reality this would never be the case as there is always

vertical load on the caisson from the superstructure. However in practice the vertical safety factor for caissons is very big as the loading is very far away from the failure. So the assumption of χ=0 can be considered reasonable.

Secondly, the lateral force to overturning moment ratio as mentioned before plays an important role to the response. The factor h=M/Q can be considered to be the effective height of the superstructure where the lateral force is applied. In this study the effective height has been set equal to zero, h=M/Q=0. This means that the driving load is pure lateral force as no moment has been applied at the caisson.

The response of the caisson has been studied for three different levels of lateral loading. These levels are defined by the horizontal safety factor $FS_H=Q_u/Q$, where Q_u is the ultimate pure horizontal load at failure without any other kind of loading, vertical or rotational. The three levels that have been studied are for lateral force equal to 10%*Q_u, 50%*Q_u and 80%*Q_u corresponding to FS_H=10, 2 and 1.25 respectively.

4.2 Numerical model

The geometry of the numerical model that has been used is the same that derived from the sensitivity analyses that were described in 3.5. The dimensions of the domain are 9Bx9Bx4B (length x width x depth) where B is the diameter of the caisson (10m). Taking into account the symmetry of the model half of the domain needed to be analyzed. At the boundaries viscous dampers have been set in order to be able to absorb the incoming waves. The caisson is simulated by volume elements. It is either rigidly connected to the soil (“bonded” interface), which means that separation and slippage are not allowed to occur, or connected through a special contact surface that allows for realistic simulation of the response (“nonlinear” interface). The foundation is considered rigid. The ratio $E_{caisson}/E_{soil}$=5000 along with the relatively small slenderness ratios considered render the rigidity assumption safe.

4.2.1 Materials model

The constitutive model that has been used for the volume elements of the caisson is the Linear Elastic model with the same parameters that were described at the elastic analyses. The properties are given in Table 4-1. This time the unit weight of the caisson has been set equal to zero in order to extract the influence of the mass. In this way no additional vertical loading is applied at the soil due to caisson's weight. However in order to achieve a vertical safety factor of infinity a vertical static load is applied at the top of the caisson equal to the soil weight that was replaced due to the caisson's volume ($V = \gamma_{soil} B^2 D$). The reason for this load is because all the calculations have been considered at the certain level of vertical safety factor $FS_v=\infty$ as discussed before.

For the behavior of soil the Hardening Soil Small constitutive model has been used. A brief description of the model with some comments were given in 0. For more details of the model the reader is referred to (PLAXIS3D, 2012, p. Materials models). The soil represents a soft normal consolidated clay and the material parameters are given in Table 2-1. The soil profile studied herein is of a constant undrained shear strength Su = 50 kPa. The density of the soil has been set to ρ=2Mgr/m^3.

Table 4-1: Constitutive model parameters for the soil profile and the caisson

Parameter	Name	Soil	Caisson	Unit
General				
Material model	Model	HS small	Linear Elastic	
Drainage type	Type	Undrained B	Non-porous	
Unit weight	γ	20	0	kN/m3
Undrained shear strength	S_u	50	-	kN/m2
Parameters				
Young's modulus (constant)	E	-	210*10^6	kN/m2
Triaxial conditions	E_{50}	5000	-	kN/m2
Oedometer conditions	E_{oed}	10000	-	kN/m2
Unloading-Reloading conditions (cut-off)	E_{ur}	15000	-	kN/m2
Shear modulus at small deformations	G_o	25000	87.5*10^6	kN/m2
deformation at which G=0.73G_o	$\gamma_{0.7}$	6*10^-4	-	
unloading Poisson's ratio	ν	0.20	0.20	
Initial				
Lateral earth pressure coefficient	K_o	1.00	1.00	

Considering the material of the interfaces the same set of model parameters have been used. The strength is not considered to be reduced. In Plaxis one way of defining the strength of the interfaces is in relation to the strength of the surrounding soil, $S_u^{interface} = R_f S_u^{soil}$. The relative coefficient R_f has been chosen to be 1 which is a realistic value for soft clays. Except for the slippage also gapping is allowed to the interface elements, this was achieved by turning on the Tension cut-off option in the input program. In this way the elements cannot bear tensile stresses and gapping is occurred.

4.3 Bonded Interface

At this part of the study the dynamic response of the caisson is investigated for inelastic soil behavior and full contact conditions at the interfaces. First a static monotonic push over is performed in order to estimate the ultimate failure lateral load, Q_u. For three levels of load (10%, 50% and 80% of Q_u) the dynamic response is investigated for two specific frequencies (f=4Hz and f=8Hz).

4.3.1 Monotonic loading

In general, embedment increases vertical, horizontal and moment capacity as failure mechanisms are forced deeper within the soil mass. The soil mechanisms that are developed in the case of pure horizontal at the head of the caisson vary with the magnitude of the embedment ratio and the load. Gerolymos and Souliotis (2012) proposed analytical expressions for computing the ultimate bearing capacity of caissons under pure loading, either pure lateral force or pure rotational moment:

$$Q_u = BDS_u \left(\frac{D}{B}\right)^{-2.15} \left(1 + \frac{D}{B}\right)^{2.89} (1 - x)^{0.17}$$

$$M_u = 0.46B^2DS_u \left(\frac{D}{B}\right)^{-1.49} \left(1 + \frac{D}{B}\right)^{3.39} (1 - x)^{0.17}$$

As expected, the soil plastification taking place around the caisson prior to the lateral loading increases as the vertical load (χ) increases, thus reducing the system's

margins for further plastification till failure. The embedment ratio is shown to have a significant effect on the ultimate capacities and especially the moment capacity Mu. As D/B increases the soil resisting mechanisms are forced deeper into the soil mass mobilizing a greater part of it. Note also that the two capacities decline in about the same fashion with respect to FS_V.

Regarding the effect of the undrained shear strength, Souliotis and Gerolymos have shown that the ultimate capacities have a linear dependence on S_u at least in the case where it is uniformly distributed with depth. In fact, S_u is the sole indicator of the system's strength since the interface is considered bonded, and slippage or gapping may not occur.

Using the afore mentioned equation for the pure lateral loading and taking into account that the coefficient χ is equal to zero for the case studied herein the ultimate lateral force is computed as $Q_u = 53910kN$. In order to confirm this value a monotonic static push over has been carried out. The results are presented in graphs in terms of lateral force, Q, versus lateral displacement, u, and an equivalent tangent stiffness, dQ/du, versus lateral displacement, u. It should be mentioned here that this stiffness is not the stiffness in horizontal mode because of the two degrees of freedom of the system. Thus this stiffness includes except for the influence of the horizontal mode, the influence of the coupling mode between the horizontal and rotational mode. Because with one analysis where the load is imposed, the four modes of the impedance cannot be calculated as there are only two equations with four unknowns only qualitatively approximation can be conducted considering the impedance of the caisson meaning the springs and the dashpots.

As it can be seen from Figure 4-2 the system presents a continuous hardening as the load keeps increasing even at very large displacements. In order to define the failure the criterion that has been used consists of two conditions that should be satisfied simultaneously. First the tangent stiffness should be reduced to less than 1% of the initial stiffness and secondly the displacement at which failure occurs should not exceed the value of B/10=1m where B is the diameter of the caisson. B/10 is a reference value that comes out quite often in the literature as a first approximation

for the level of failure of caissons. Taking into account the above criterion the ultimate lateral load computed by the numerical analysis is $Q_u = 54017kN$ and it is reached at the lateral displacement of 0.82m. The numerical analysis as well as the analytical expression are in total agreement. In Figure 4-4 the pole of rotation of the caisson is depictured. It can be seen that the pole is located at a depth of 2D/3 where D is the embedment of the caisson.

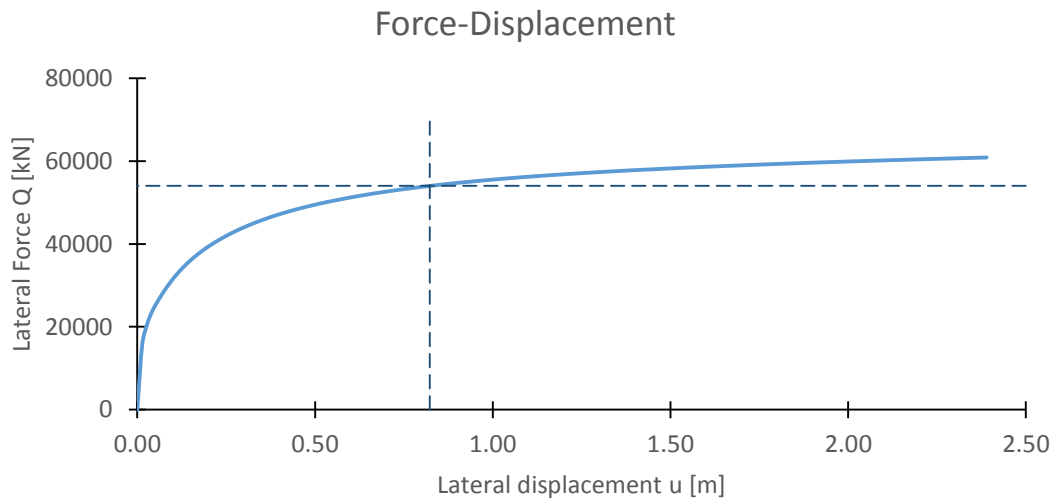

Figure 4-2: Monotonic Static push over test, graph load versus response. The dashed lines indicate the ultimate load and the displacement at which failure occurs.

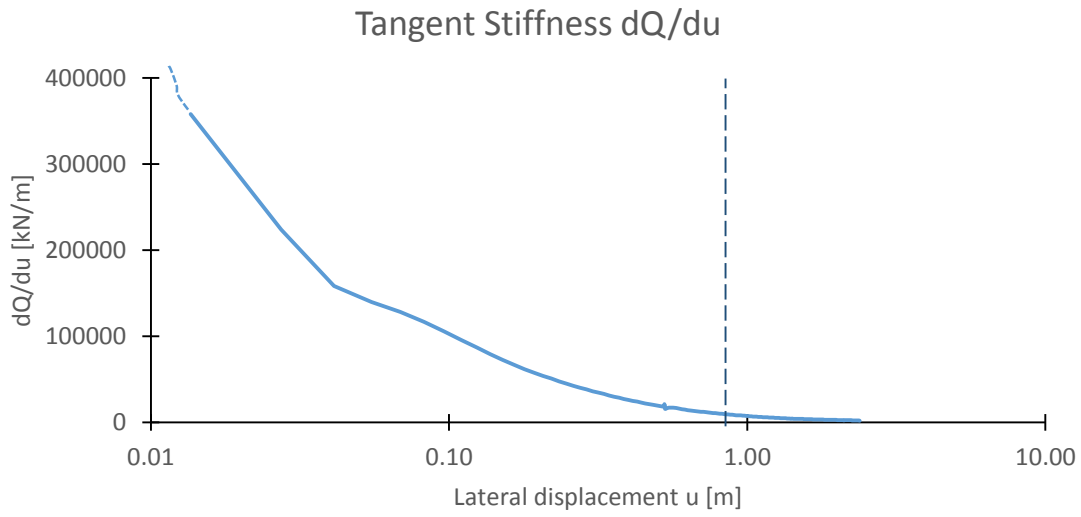

Figure 4-3: Monotonic Static push over test, graph dQ/du versus u. The dashed line indicates the displacement where failure is considered to be occurred. The initial stiffness is 1791000 kN/m and is not shown in the figure.

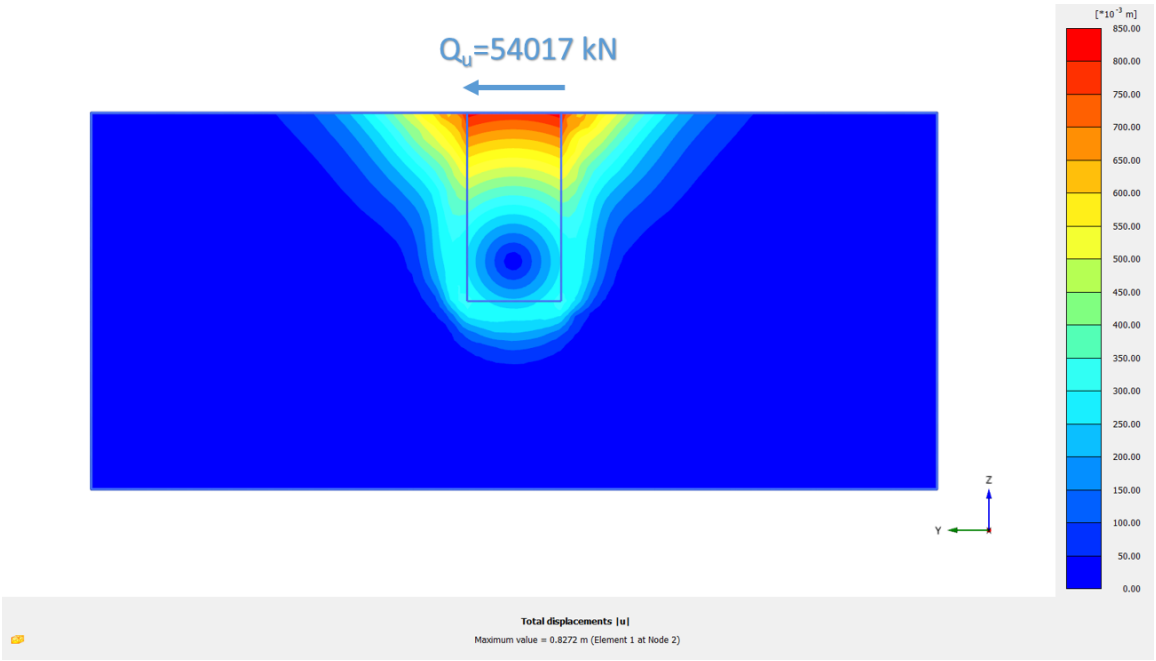

Figure 4-4: Illustration of the total absolute displacements of the caisson due to pure lateral loading. It can be seen that the pole of rotation of the caisson is located about at depth 2D/3.

4.3.2 Dynamic loading

At this part the caisson is studied under dynamic loading at two specific frequencies. The frequencies that have been chosen are 4Hz and 8Hz because as it was concluded from the elastic analyses the Loop Area Method is more accurate for the greater frequencies. For each frequency three dynamic calculations have been performed with three different amplitudes, namely 10%, 50% and 80% of the ultimate lateral load Q_u. It should be mentioned here that because the Hardening Soil with small strain stiffness soil model even though it follows a G-γ reduction curve, it works with an elastic unloading-reloading part, which means that no accumulation of plastic strains is occurred, only in the first cycle permanent deformation takes place and afterwards a steady state response is achieved. Thus, the oscillation is not around the point where displacement is zero (as in elastic analyses) but around a permanent displacement value. This value is very low for the 10% of Q_u amplitude because as it will be seen in the following the behavior is nearly elastic for this level of load while for the greater amplitudes of 50% and 80% of Q_u where the stiffness has been reduced more, the permanent deformation of the initial cycle increases.

In Figure 4-5 and Figure 4-6 the dynamic loops that have formed from the three levels of loading are presented for the small and the big frequency respectively. In the vertical axis the load has been normalized with the ultimate lateral load at failure (Q_u) while in the horizontal axis the displacements have been normalized with the failure displacement (u_f) meaning the displacement at which in monotonic loading Q_u is achieved. As it can be seen from each figure the loops are located in different places because of the permanent deformation of the initial loading as it was explained before. Comparing the same load level for the two frequencies it can be concluded that as the frequency arises the response becomes stiffer for the same load level. The center of the loop for the lowest load level is oriented almost at zero for both frequencies which means that the behavior of the system is almost elastic. Moreover it can be seen that the loops are rotating as the load level increases for the small frequency while for the greater frequency this rotation is very limited. As the loops are turning the difference between the displacements at which the maximum force is occurred, and the maximum displacement of the response, becomes greater. The area of the loops represent the dissipated energy of the system. There are two reasons that energy dissipates, except for the energy dissipated due to radiation of the system, energy dissipates also due to the material damping of the soil elements that is caused by the inelastic soil model that has been adapted. The loops from the dynamic calculations represent the total damping of the system. More details about the dampings and their meaning are described in the following.

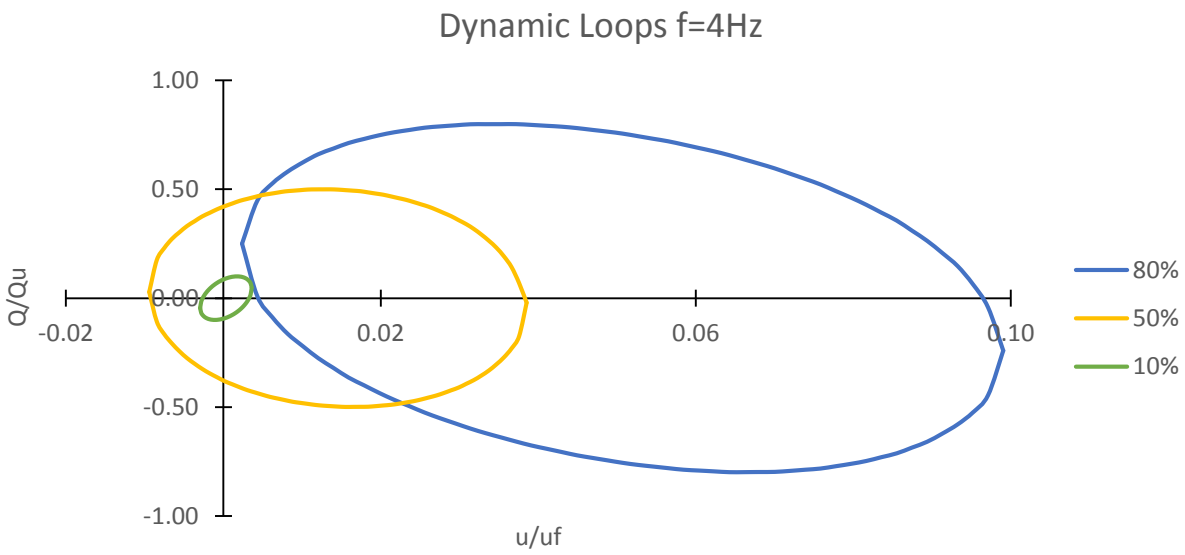

Figure 4-5: Loops of the dynamic analyses with frequency f=4Hz for the three levels of loading, namely 10%, 50% and 80% of the ultimate load Q_u.

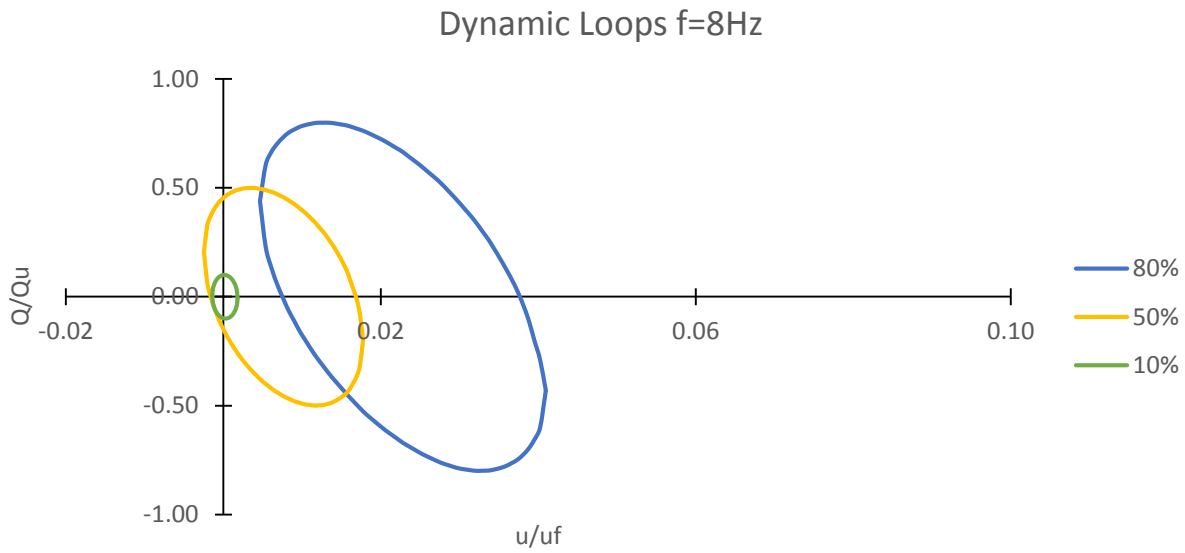

Figure 4-6: Loops of the dynamic analyses with frequency f=8Hz for the three levels of loading, namely 10 %, 50% and 80% of the ultimate load Qu.

4.3.3 Cyclic loading

In order to distinguish the material damping from the total damping cyclic static pushovers needed to be performed in such way that the amplitude of the displacements of the dynamic loops for each load level would be compatible with the

corresponding dynamic analyses. In this way the material damping can be calculated from the cyclic loops that are formed and then can be subtracted from the total damping of the dynamic loops. In Figure 4-7 the cyclic loops are presented. The normalization has been performed with the same way as for the dynamic loops.

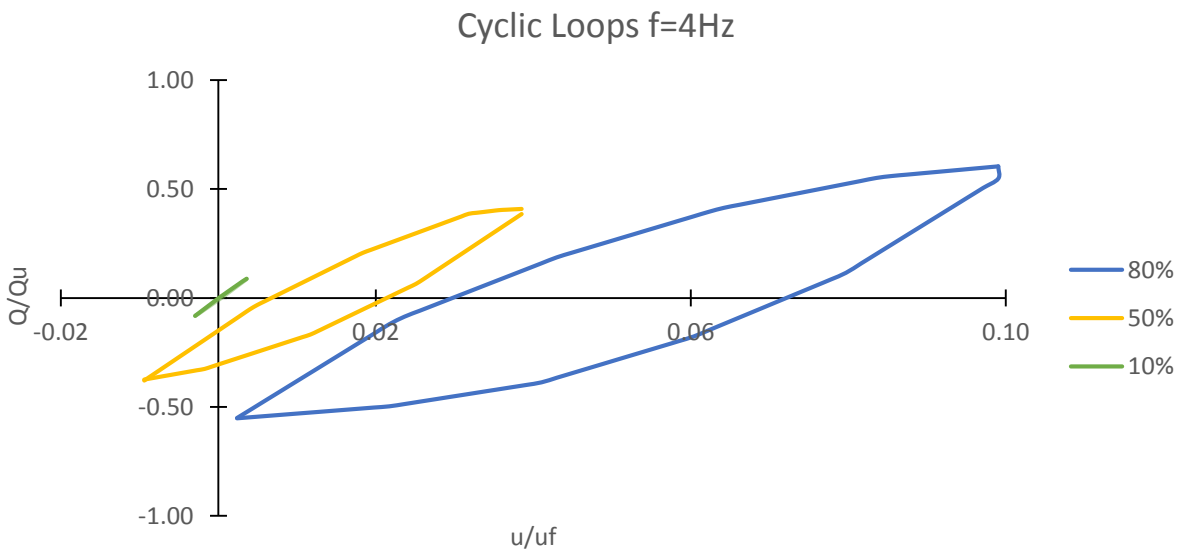

Figure 4-7: Loops of the cyclic analyses for the three levels of loading, namely 10%, 50% and 80% of the ultimate load Qu corresponding to the small frequency f=4Hz.

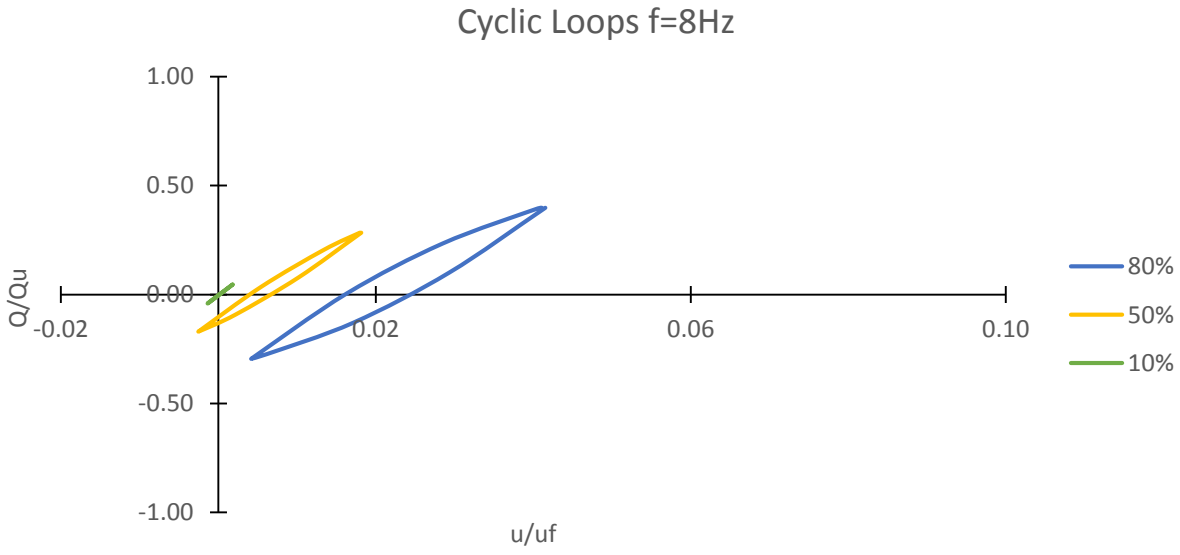

Figure 4-8: Loops of the cyclic analyses for the three levels of loading, namely 10%, 50% and 80% of the ultimate load Qu corresponding to the greater frequency f=8Hz.

It can be seen that for the lowest level of load the loop that is formed is very small, this is another way of concluding that at this level the behavior is almost elastic. As the load level increases the area of the corresponding loop increases too, depicturing in this way the bigger influence of the material damping. Because the cyclic loading is performed under static conditions, the maximum force is achieved at the same place where the maximum displacement is occurred. The reason for this is the absence of the radiation damping.

Comparing the small with the large frequency it can be seen that for each load level the lower frequency presents much more material damping as the loops that are formed are quite bigger. This is because the permanent deformation at which the oscillation occurs is greater for the lower frequency so in static conditions more load is needed in order this displacement to be reached.

In order to quantify the damping that is occurred due to the cycling loading a damping ratio is defined by the ratio of the energy that dissipates to the maximum elastic energy that is stored in the system as the figure below shows.

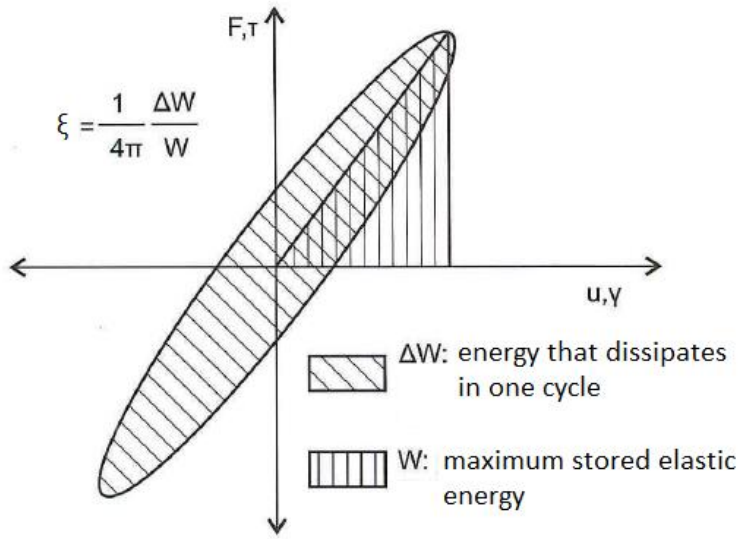

Figure 4-9: Definition of the damping ratio.

It must be noted here that the damping ratio that has been computed from the loops that are formed in the graphs load-response is not the pure corresponding damping ratio in horizontal mode as it also includes the coupling mode (horizontal-rotational)

due to the second degree of freedom of the caisson. Thus this damping ratio is only an expression of the dissipated energy of the soil-structure system.

The areas of the loop (ΔW) have been computed with the column method while the maximum stored elastic energy has been computed according to the following formula: $W = \frac{1}{2} Q_{max} u_{max}$. In cyclic static loading the maximum load is achieved at the same time that the maximum displacement is reached due to the absence of tha radiation damping. In the following Table the damping ratio, $\xi_{cyclic} = 4\pi \frac{\Delta w}{W_{max}}$, for the cyclic loops for both frequencies is presented. As it can be seen by comparing the corresponding damping ratios of the same load level for the two frequencies, the lower frequency presents greater ratios for the same reasons that were explained before.

Table 4-2: Damping ratios for cycling static loading for the case of bonded interfaces.

Load Level	10%	50%	80%
Damping Ratio	ξ	ξ	ξ
CYCLIC (f=4Hz)	2%	15%	23%
CYCLIC (f=8Hz)	1%	5%	9%

4.3.4 Radiation damping

In order to calculate the radiation damping, the material damping of the cyclic analyses must be subtracted from the total damping of the dynamic analyses. To make the results more accurate linear interpolation has been made with the use of special mathematic software for the densification of the points that form the loops. For each loop 100 points have been computed. This action was necessary as in Plaxis the number of the steps of the process is generated automatically and thus different number of points formed the dynamic loops from the cyclic loops.

As has been mentioned before the area of the dynamic loop represents the total damping of the system which includes both the material and the radiation damping. Subtracting the area of the cyclic loops from the area of the dynamic loops, the area

of the radiation loops is derived. In order to quantify the damping of the system a dashpot coefficient is defined according to the following relation:

$$DE_{Q-u} = \int_0^T C\dot{u}\, du \rightarrow C = \frac{DE_{Q-u}}{\pi\omega u_{max}^2}$$

It must be noted here again that this damping coefficient is not the pure corresponding damping ratio in horizontal mode as it also includes the coupling mode (horizontal-rotational) due to the second degree of freedom of the caisson. Thus this damping coefficient is only a generalized expression of the dissipated energy of the soil-structure system. The areas of the loop (ΔW) have been computed with the column method.

In the following Tables the computed areas of the loops as well as the corresponding damping coefficients for each kind of loop are presented for both frequencies. It can be clearly seen that the area of the dynamic loops is a sum of the area of the cyclic loops and the area of the radiation loops. An important conclusion that can be conducted here is that although the material damping ratio is increased as the load level increases (see Table 4-2) the corresponding radiation damping coefficient decreases. However, the decrease of the radiation damping is greater than the increase of the cyclic damping causing eventually the total dynamic damping coefficient to be reduced. A general conclusion that can be said is that the total damping coefficient is reduced for a specific frequency as the soil becomes more and more plastic. The meaning of this reduction of the dashpot coefficient is that the wave is not transferred to the whole domain. The figures that follow illustrate clearly this fact.

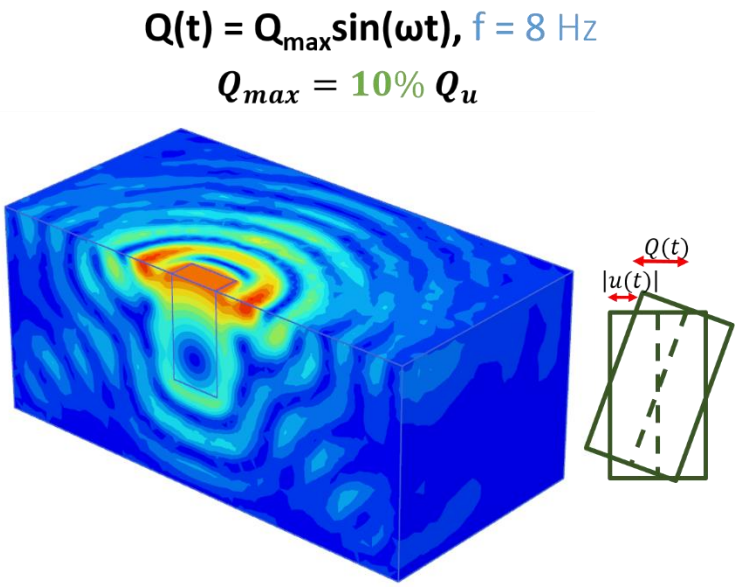

Figure 4-10: Absolute values of displacements due to dynamic loading. The low amplitude of loading indicates elastic conditions. The waves propagate to the whole domain as the soil elements have not be plastified extensively.

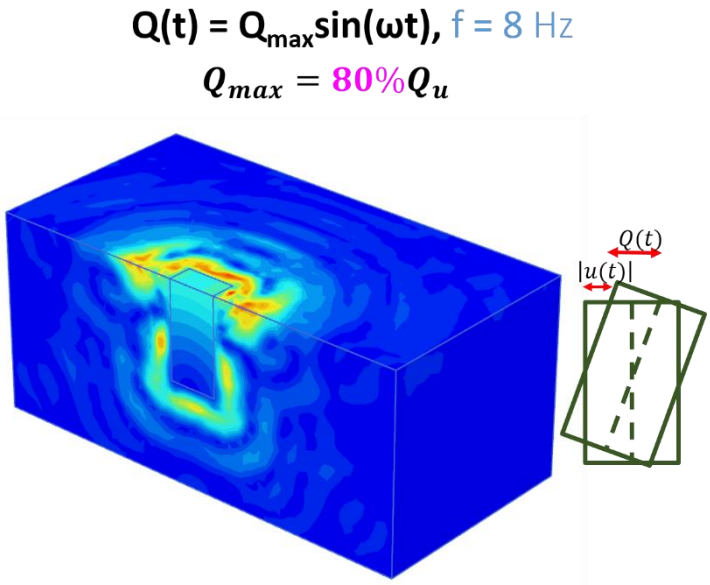

Figure 4-11: Absolute values of displacements due to dynamic loading. The high amplitude of loading indicates inelastic conditions. The waves propagate mainly at the region of the plastified soil indicating a low dashpot coefficient.

Table 4-3: Computed areas and damping coefficients for each kind of loops for the frequency of 4Hz and 8Hz.

Frequency f=4Hz

Load Level	10%	50%	80%
Loop Area [kN*m]	ΔW	ΔW	ΔW
DYNAMIC	41.29	1666.39	5139.62
CYCLIC	1.36	384.60	1660.64
RADIATION	39.93	1281.78	3478.99

Frequency f=4Hz

Load Level	10%	50%	80%
Damping Coefficient	C	C	C
DYNAMIC	7.41E+04	5.57E+04	4.22E+04
RADIATION	7.17E+04	4.28E+04	2.86E+04

Frequency f=8Hz

Load Level	10%	50%	80%
Loop Area [kN*m]	ΔW	ΔW	ΔW
DYNAMIC	22.28	645.46	1690.49
CYCLIC	0.14	34.12	143.67
RADIATION	22.13	611.34	1546.82

Frequency f=8Hz

Load Level	10%	50%	80%
Damping Coefficient	C	C	C
DYNAMIC	8.37E+04	6.06E+04	4.92E+04
RADIATION	8.31E+04	5.74E+04	4.50E+04

For the visualization of the radiation loops the cyclic loops need to be rotated in such way that their maximum displacement will match the maximum displacement of the dynamic loops. This rotation is necessary to be done in order the radiation loops that are formed after the subtraction of the cyclic loops from the dynamic loops to be horizontal. The figures that follow include all kinds of loops for all load levels and for both frequencies.

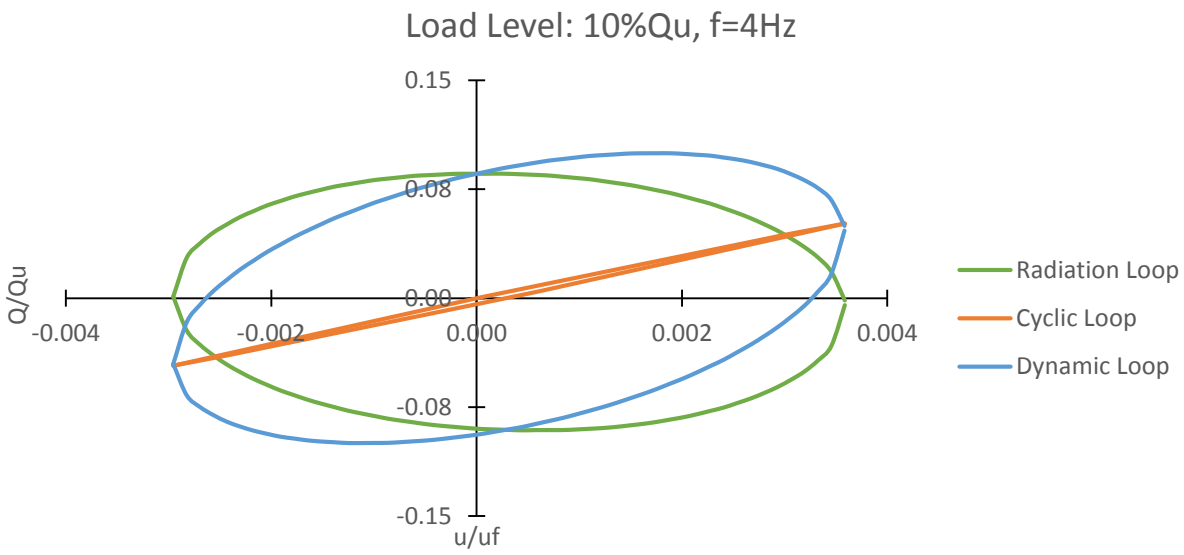

Figure 4-12: The three loops for the load level of 10% of Q_u for frequency f=4Hz. The radiation loop is formed from the difference between the dynamic loop and the cyclic loop.

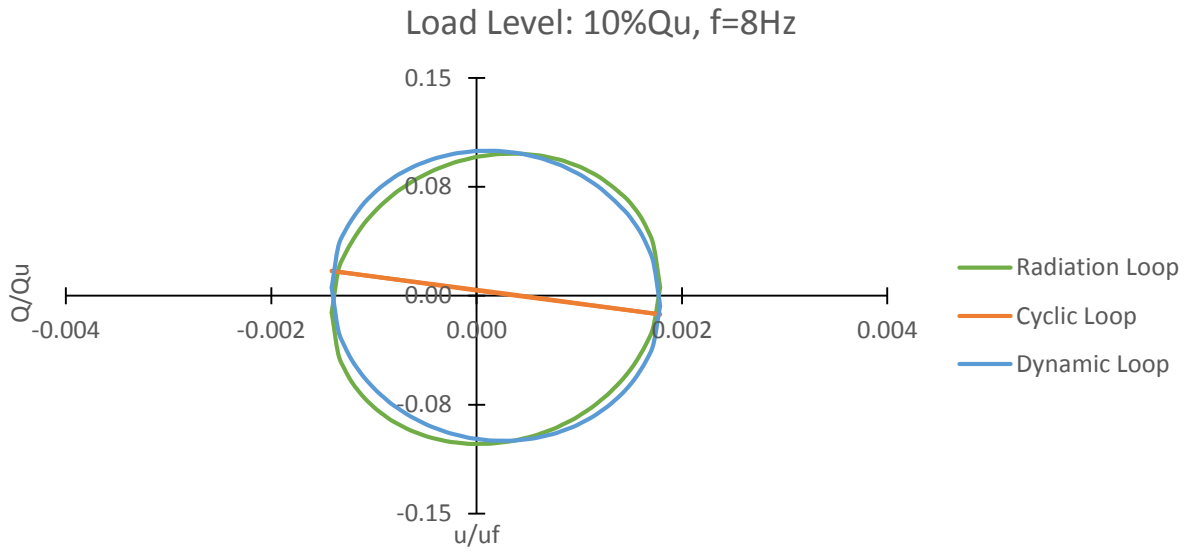

Figure 4-13: The three loops for the load level of 10% of Qu for frequency f=8Hz. The radiation loop is formed from the difference between the dynamic loop and the cyclic loop.

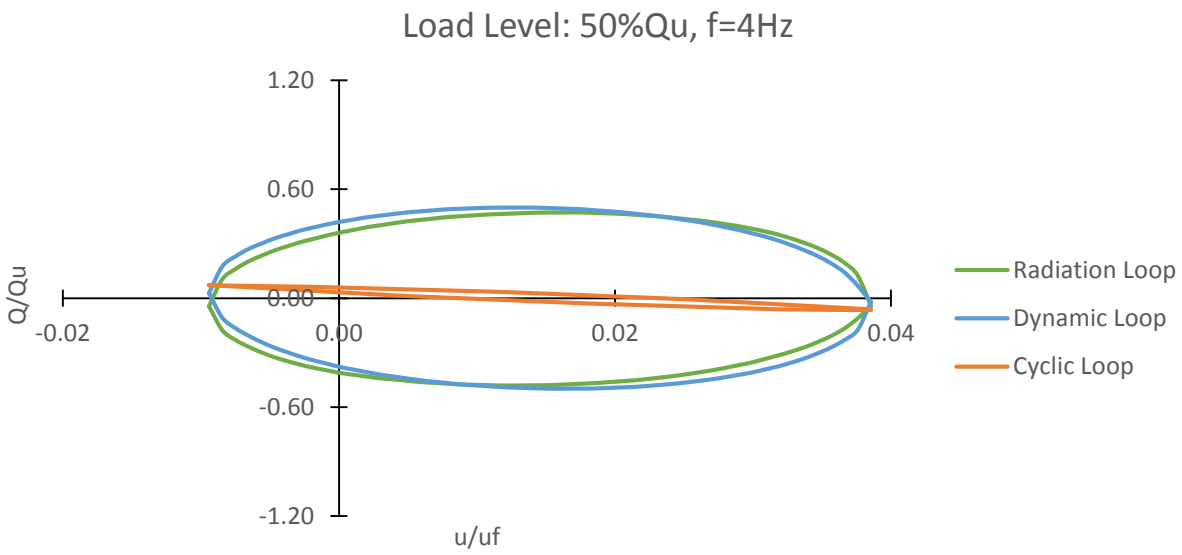

Figure 4-14: The three loops for the load level of 50% of Qu for frequency f=4Hz. The radiation loop is formed from the difference between the dynamic loop and the cyclic loop.

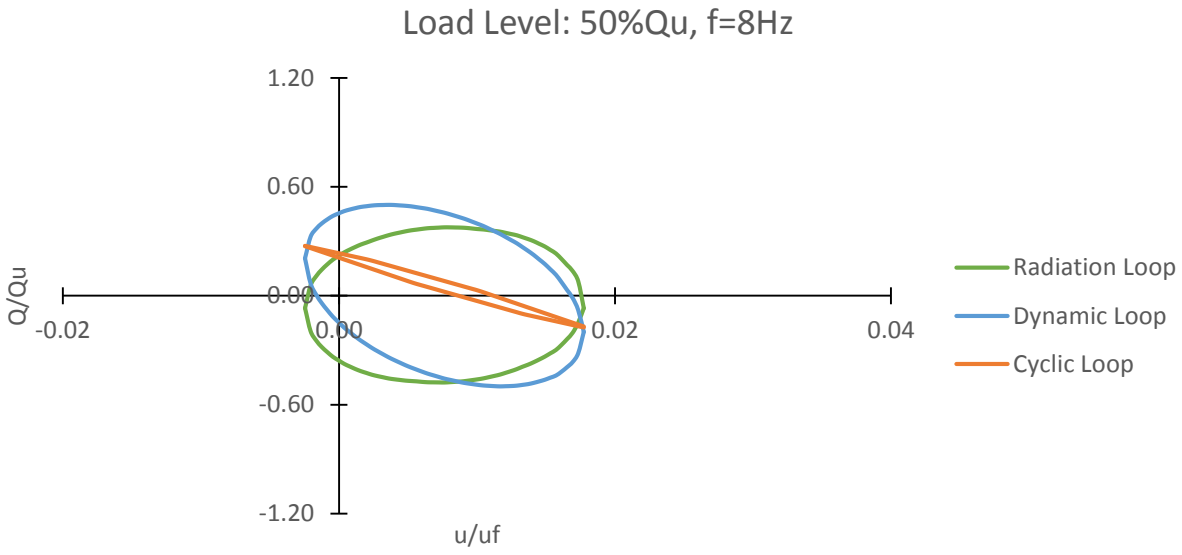

Figure 4-15: The three loops for the load level of 50% of Qu for frequency f=8Hz.. The radiation loop is formed from the difference between the dynamic loop and the cyclic loop.

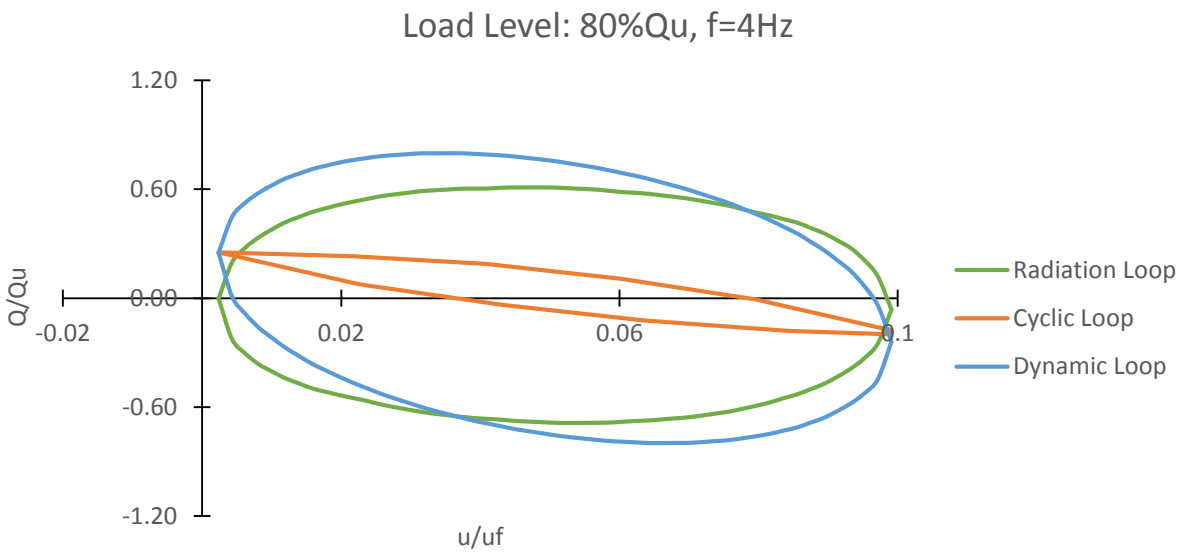

Figure 4-16: The three loops for the load level of 80% of Qu for frequency f=4Hz. The radiation loop is formed from the difference between the dynamic loop and the cyclic loop.

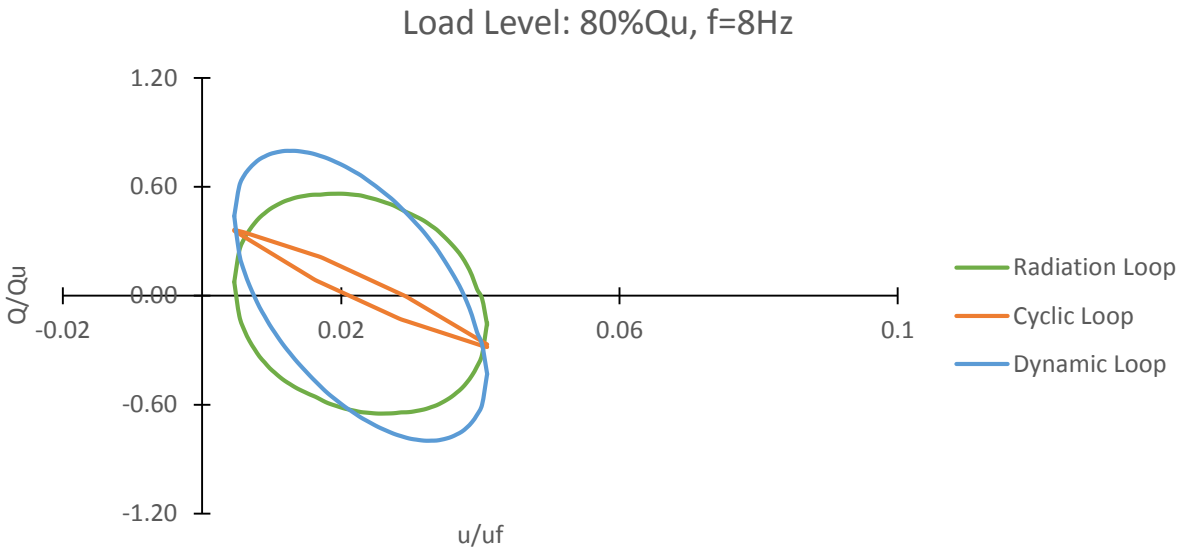

Figure 4-17: The three loops for the load level of 80% of Qu for frequency f=8Hz. The radiation loop is formed from the difference between the dynamic loop and the cyclic loop.

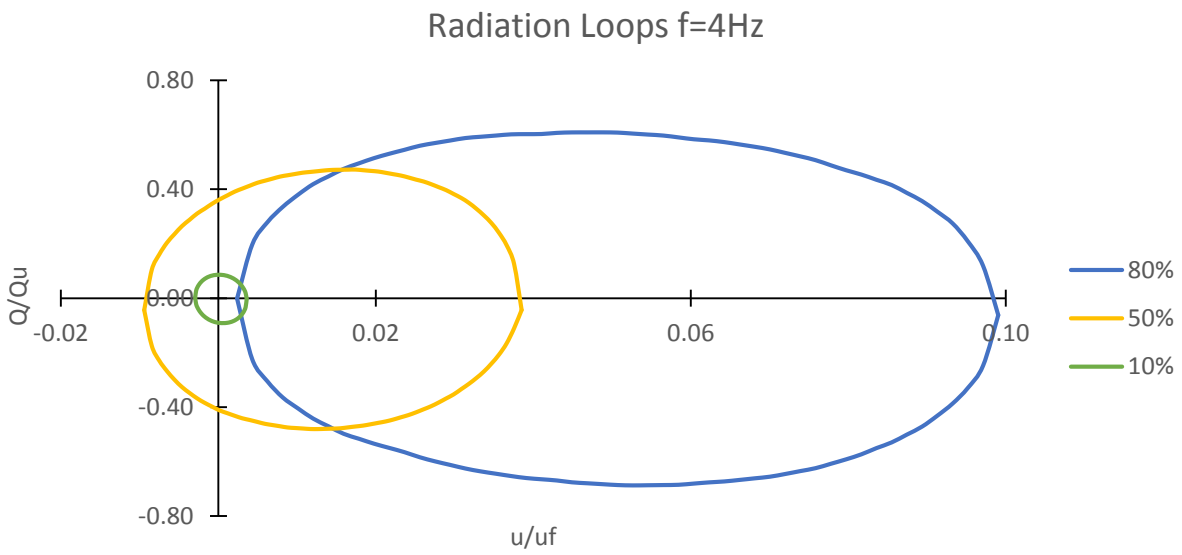

Figure 4-18: Loops that represent the radiation damping for the three levels of loading, namely 10%, 50% and 80% of the ultimate load Qu for the frequency 4Hz.

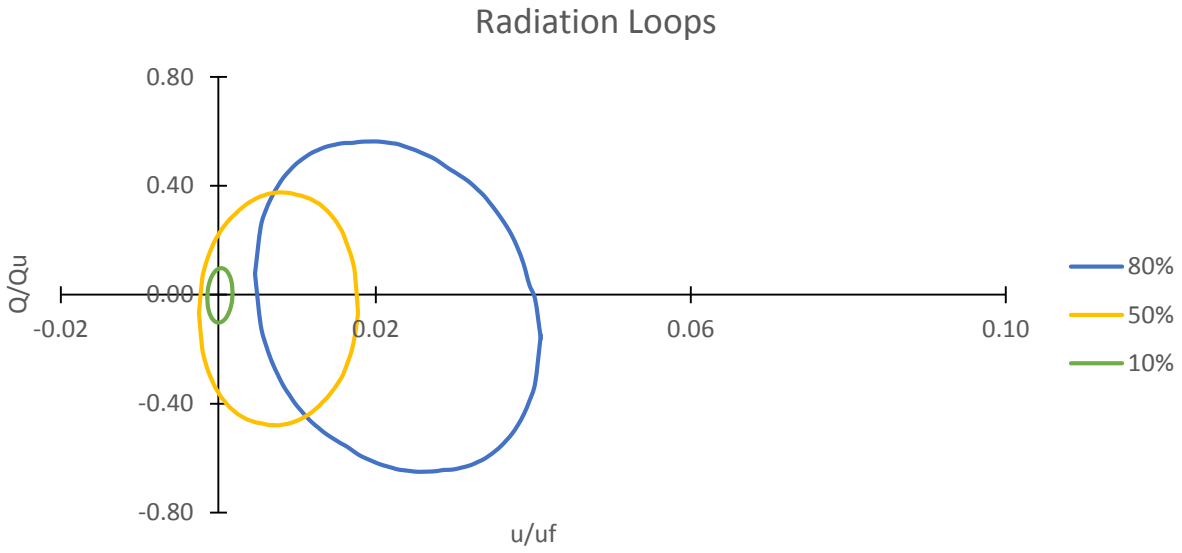

Figure 4-19: Loops that represent the radiation damping for the three levels of loading, namely 10%, 50% and 80% of the ultimate load Qu for the frequency 8Hz.

As it can be seen from the figures above the dynamic loops that are formed become greater as the load level increases. The area of the loops represents the dissipated energy. The bigger the load is the more energy the system gets and consewuently

more energy is dissipated comparing to the lower load levels for the same frequency. However, by the increase of the areas of the loops it cannot be concluded that the damping is increased. This can be concluded by the dashpot coefficient C. As it can be seen from Table 4-3 for a specific frequency as the load level increases the computed dashpot coefficient becomes smaller or equivalently as the soil becomes more and more plastic C reduces. This fact can be explained by the physical meaning of the dashpot coefficient. The dashpot coefficient C, represents the amount of the soil elements that participate to the transmission of the waves. As the soil becomes more and more plastic the wave "sees" more and more surfaces at which it reflects. Another reason that C is reducing is because the velocities of the waves decrease as the soil plastifies.

For the elastic region of a square plan foundation it is known from the literature that as the frequency increases, the dashpot coefficient presents a trend to increase until the value of $C_h = \rho V_s A$. However for a plain strain analysis the dashpot coefficient in elastic region presents opposite behavior, meaning reductive trend but until the same asymptote value. Comparing the dashpots coefficients for each load level it can be observed that the increment of C due to the rise of frequency is getting higher (14%, 25%, 36% respectively for the low load level till the high load level) as the soil gets more into the plastic area. Comparing the areas of each load level for the two frequencies it can be clearly seen that for the small frequency the dissipated energy which is represented by the area of the loop is much bigger.

4.4 Comparison between inelastic and elastic analyses

At this part of the thesis, the aim is to compare the inelastic analyses with elastic analyses. A new set of elastic analyses have been performed where the constitutive model for the soil has been selected to be the Linear Elastic model. The Poisson's ratio has been chosen to be the same as the inelastic analyses (v=0.2) while considering the shear modulus G investigation has been performed in such way that for each load level the corresponding dynamic elastic loop would match the inelastic dynamic loop in terms of horizontal maximum and minimum displacements. No

additional damping, in terms of Rayleigh damping, has been included to the elastic analyses as in the inelastic analyses that were described before.

The shear moduli that were eventually selected for both frequencies are presented in the following Table. As it can be seen the reduction of the initial shear modulus G_0 that needed to be chosen in order to take the same magnitude of amplitudes for the response, is very close to the reduction of the load for each load level for both frequencies.

Table 4-4: Reduction of the initial shear modulus for the elastic analyses for the two frequencies.

Shear modulus G [kN/m2] for f=4Hz

Load Level	10%	50%	80%
inelastic analyses (Go)	25000	25000	25000
elastic analyses (G)	22500	10000	5000
reduction	10%	60%	80%

Shear modulus G [kN/m2] for f=8Hz

Load Level	10%	50%	80%
inelastic analyses (Go)	25000	25000	25000
elastic analyses (G)	21500	12000	7500
reduction	14%	52%	70%

Some general comments that should be mentioned for the elastic analyses are described here. First the cyclic loops because of the absence of the material damping become now straight lines. As a consequence of this the radiation loop that comes from the subtraction of this line from the dynamic loop is only the rotation of the loop without any change at the area at all. This is something that is expected from the elastic analyses as the area of the dynamic loop is a representation of the dissipated energy of the system only due to the radiation as the material damping is zero. As the figure below shows, the radiation loop that is derived becomes horizontal.

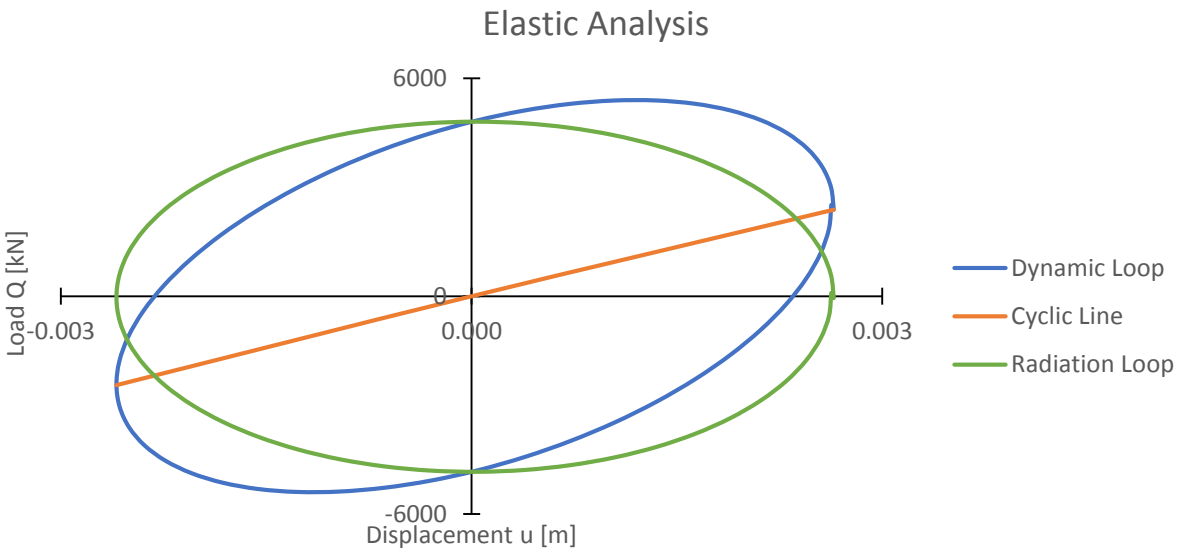

Figure 4-20: Loops derived from the elastic analysis. The radiation loop has the same area as the dynamic loop and is horizontal.

Another difference that should be mentioned between the elastic and inelastic analyses is the location of the steady state response. For the inelastic analysis, as has been described in the previous, the steady state response is reached at a certain level of permanent deformation. This level increases as the load magnitude increases and causes the maximum and minimum values of the displacement to vary. The reason for this permanent deformation is the initial cycle at which plastic deformations occur. However for the elastic analyses the steady state response is reached without any permanent deformation and thus the center of the loops that are derived is located at zero. In order to compare the elastic dynamic loops with the corresponding inelastic the latter have been relocated in such way that their center would match with zero as well. In the figures that follow the permanent deformation that is reached due to the inelastic soil model and can be observed. The deviation from the elastic response increases as the load level rises.

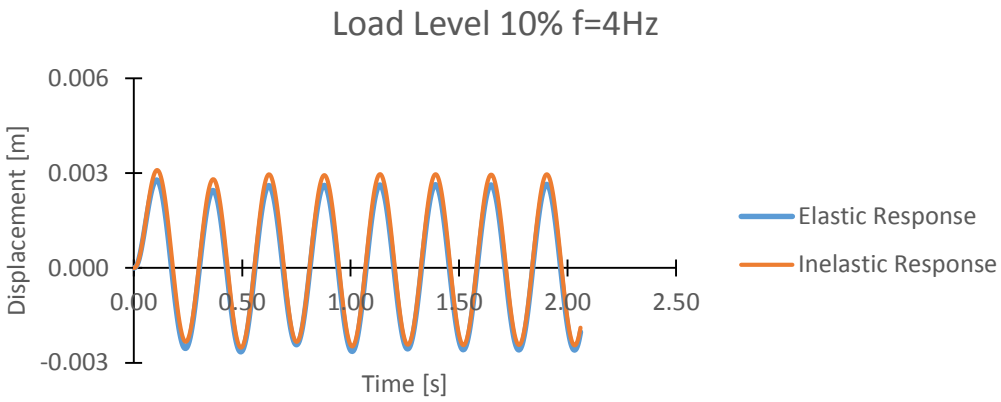

Figure 4-21: Lateral response of the caisson at load level 10% for the elastic and inelastic analyses.

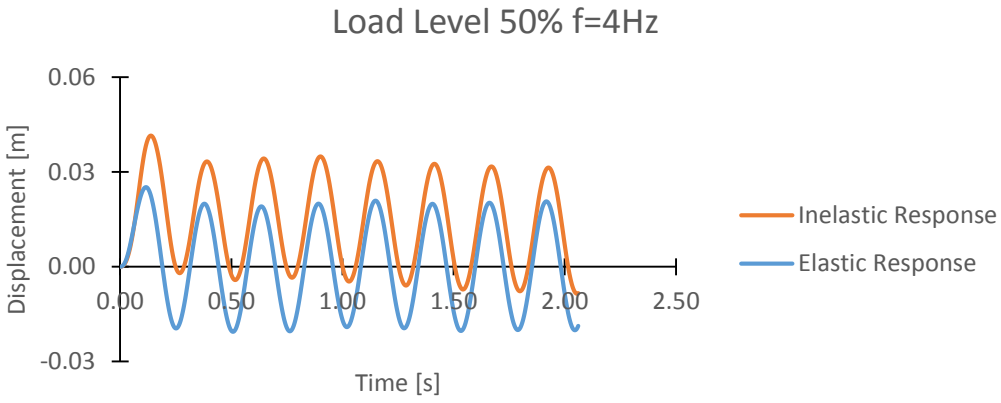

Figure 4-22: Lateral response of the caisson at load level 50% for the elastic and inelastic analyses

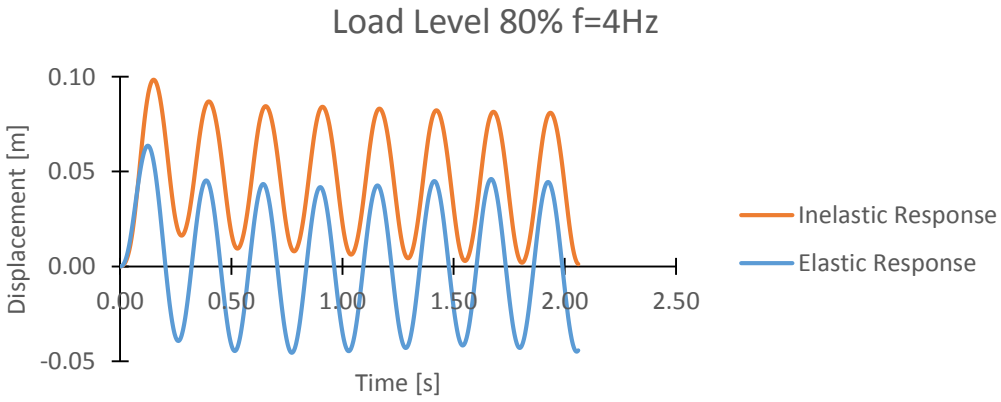

Figure 4-23: Lateral response of the caisson at load level 80% for the elastic and inelastic analyses.

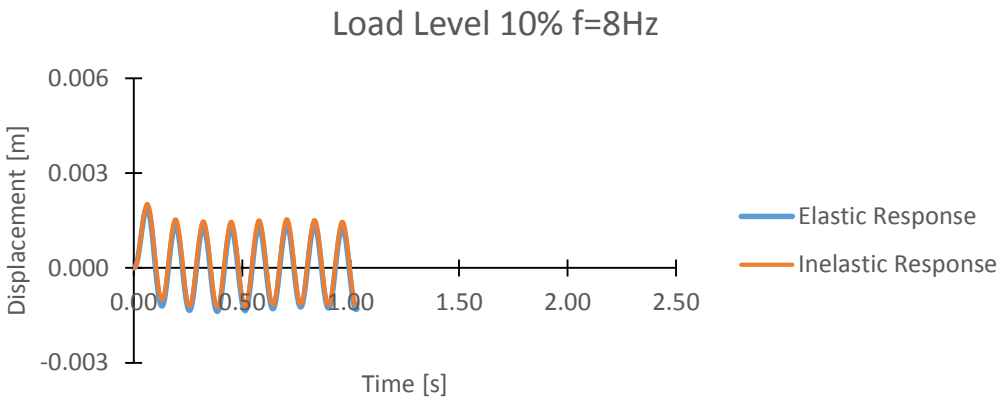

Figure 4-24: Lateral response of the caisson at load level 10% for the elastic and inelastic analyses.

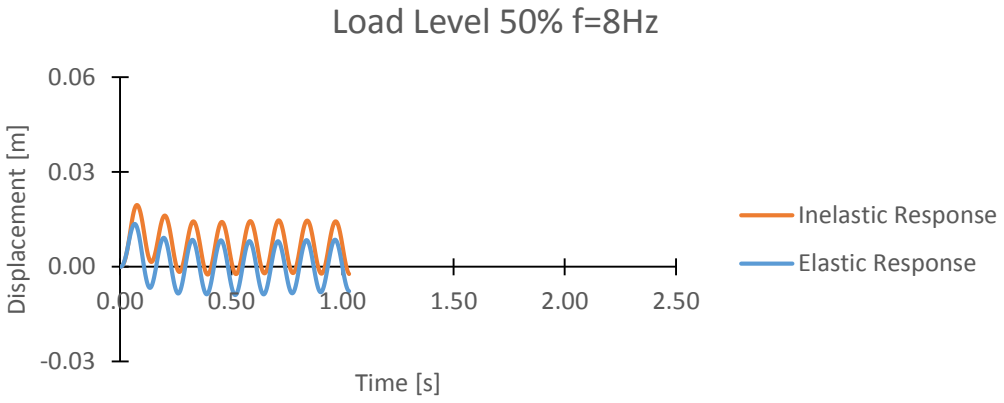

Figure 4-25: Lateral response of the caisson at load level 50% for the elastic and inelastic analyses

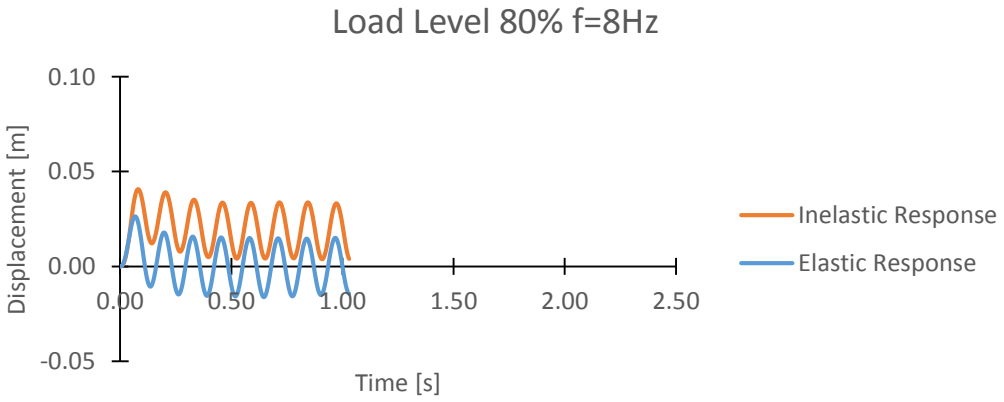

Figure 4-26: Lateral response of the caisson at load level 80% for the elastic and inelastic analyses.

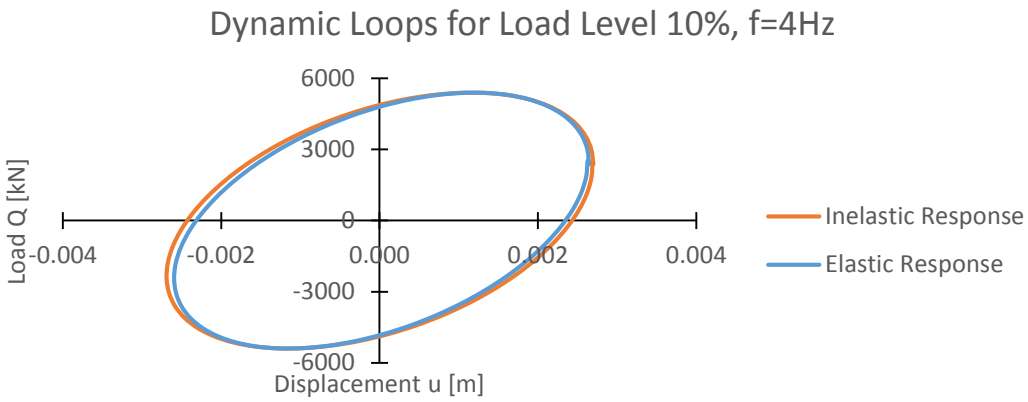

Figure 4-27: Comparison between the dynamic loops for the inelastic response and the elastic response with a reduced shear modulus, reduction 10%G_o, for f=4Hz.

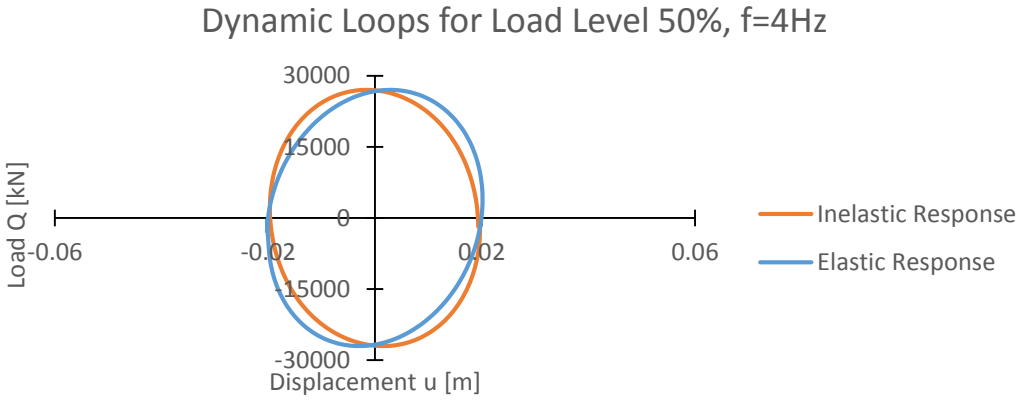

Figure 4-28: Comparison between the dynamic loops for the inelastic response and the elastic response with a reduced shear modulus, reduction 60% G_o, for f=4Hz.

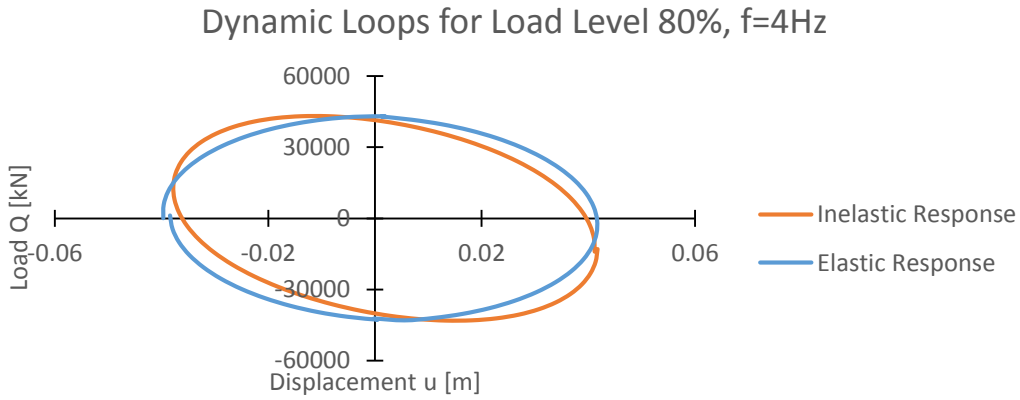

Figure 4-29: Comparison between the dynamic loops for the inelastic response and the elastic response with a reduced shear modulus, reduction 80% G_o, for f=4Hz.

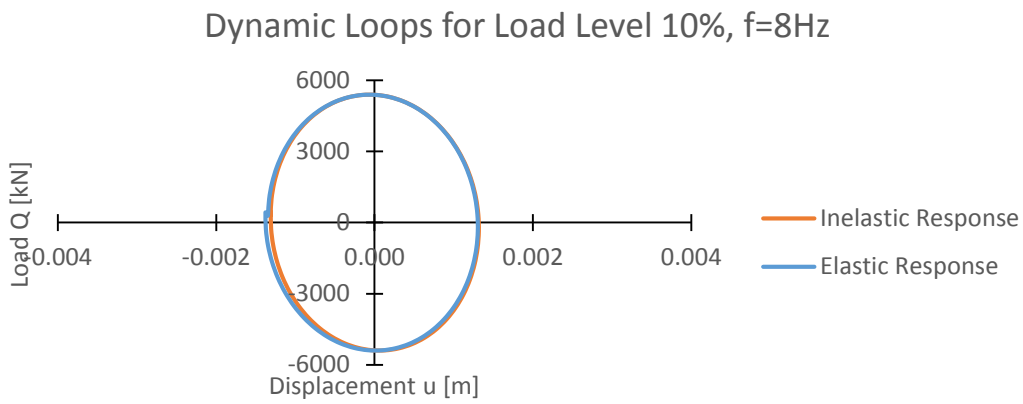

Figure 4-30: Comparison between the dynamic loops for the inelastic response and the elastic response with a reduced shear modulus, reduction 14% G_o, for f=8Hz.

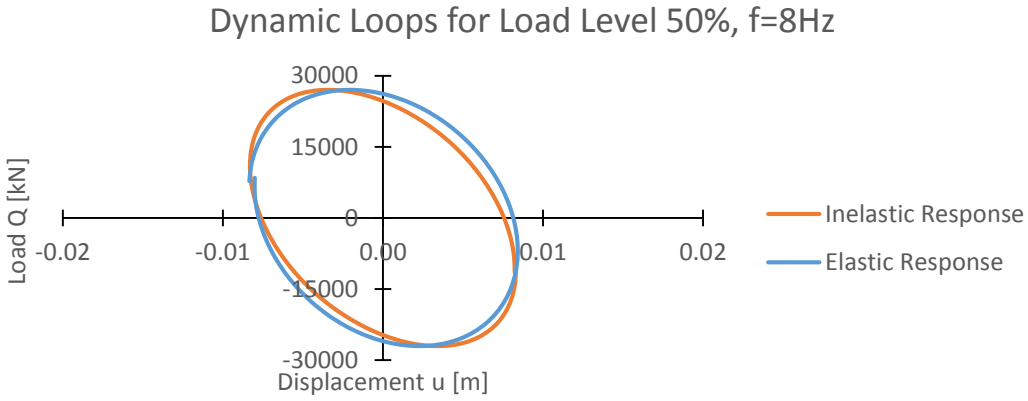

Figure 4-31: Comparison between the dynamic loops for the inelastic response and the elastic response with a reduced shear modulus, reduction 14% G_o, for f=8Hz.

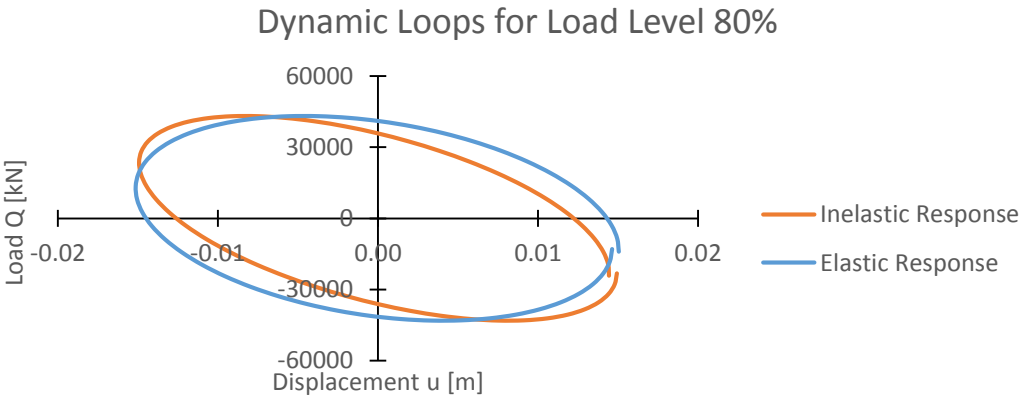

Figure 4-32: Comparison between the dynamic loops for the inelastic response and the elastic response with a reduced shear modulus, reduction 70% G_o, for f=8Hz.

Table 4-5: Areas of the dynamic loops for each kind of analysis

Frequency f=4Hz

Load Level	10%	50%	80%
Loop Area [kN*m]	ΔW	ΔW	ΔW
ELASTIC	39.5	1690.4	5368.6
INELASTIC	41.3	1666.4	5139.6
deviation	-4%	1%	4%

Frequency f=8Hz

Load Level	10%	50%	80%
Loop Area [kN*m]	ΔW	ΔW	ΔW
ELASTIC	22.5	679.7	1934.5
INELASTIC	22.3	645.5	1690.5
deviation	1%	5%	13%

As the above Tables show the deviation of the areas of the loops is very small. The loops present a slightly different shape. This difference increases as the load level increases. For the smallest load level it can be seen that the dynamic loops match almost identically. This is due to the fact that for the low load level the behavior at the inelastic analysis is almost elastic as has been explained in the previous.

4.5 Nonlinear Interface

The bonded interface does not represent the real soil-structure interaction behavior where slippage and gapping are very likely to occur, especially for magnitudes of load where inelastic response is expected, i.e. greater deformations. At this part, the same procedure as in the bonded interface part was followed with the only difference now that interface elements have been introduced at the base of the caisson as well as the sidewalls of it. The data material set is described in 4.2.1.

First a static monotonic push over is performed in order to estimate the ultimate failure lateral load, Q_u and then for three levels of load (10%, 50% and 80% Q_u) the dynamic response is investigated for the small frequency (f=4Hz).

4.5.1 Monotonic loading

As there are no analytical expressions for the ultimate load at failure for the case of the nonlinear interface, the failure was considered to be achieved at the same value of the displacement (u_f) where the failure occurred for the bonded interface. The load (Q_u= 39260kN) at which this displacement was reached was 27% smaller than the corresponding load of the bonded interface. As it was expected the introduction of the interfaces reduced the load at failure. In the figures that follow the monotonic push over test is depictured in load-displacement (Q-u) terms and in an equivalent tangent stiffness (dQ/du-u) terms. In Figure 4-35 the gap that is occurred at the sidewall of the caisson can be clearly observed. Moreover the rotation pole is located about at the same depth (2D/3) as in the bonded interface analysis.

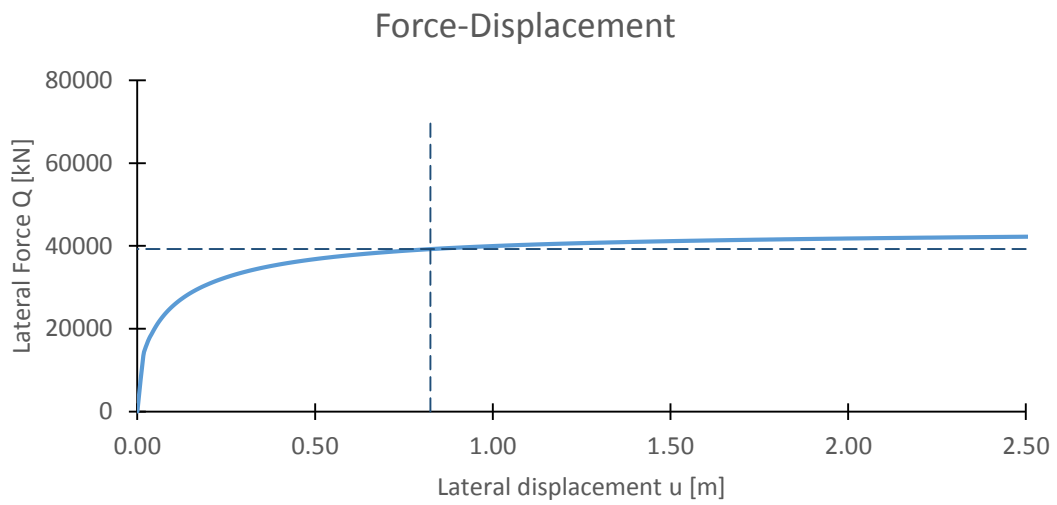

Figure 4-33: Monotonic Static push over test, graph load versus response. The dashed lines indicate the ultimate load and the displacement at which failure is considered.

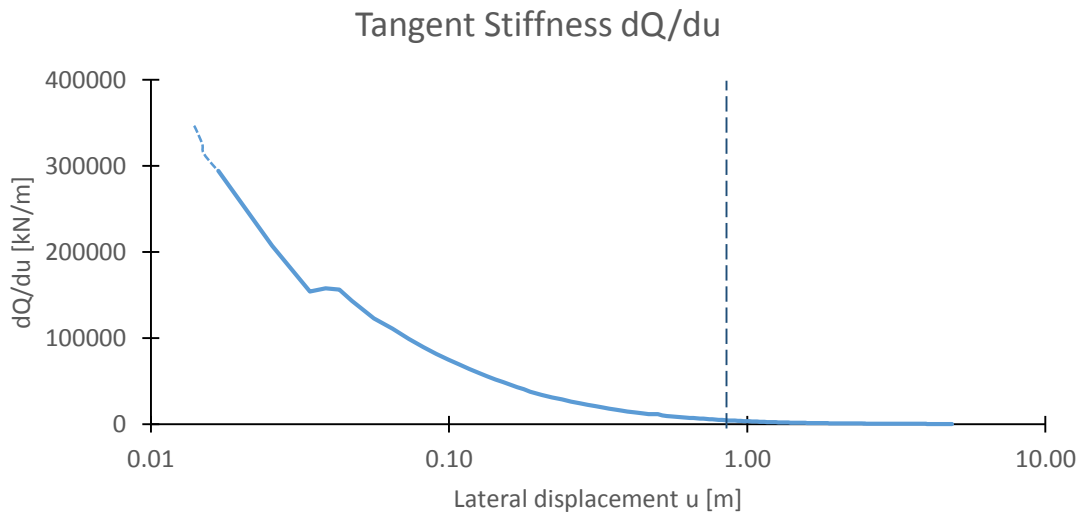

Figure 4-34: Monotonic Static push over test, graph dQ/du versus u. The dashed line indicates the displacement where failure is considered to be occurred.

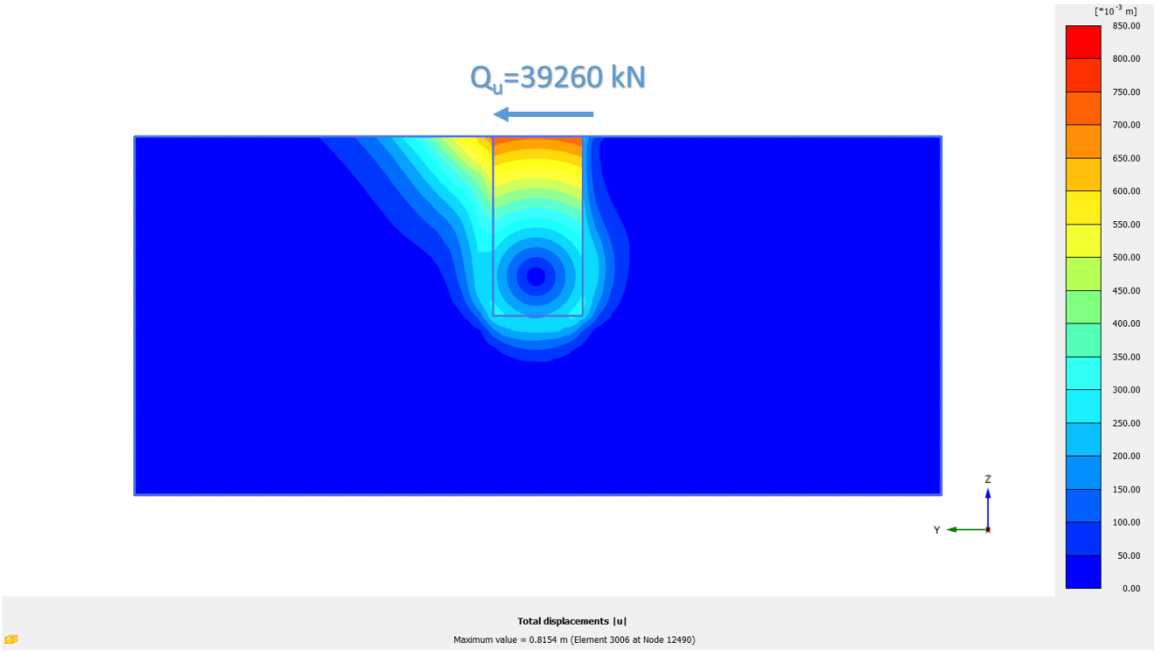

Figure 4-35: Illustration of the total absolute displacements of the caisson due to pure lateral loading. The gapping can be observed at the right side of the caisson. The pole of rotation of the caisson is located at the depth of 2D/3, same as in bonded interface analysis.

4.5.2 Dynamic loading

Following the same procedure as in the bonded interface analyses the results for the nonlinear interfaces are presented in the following. In order to make comparisons between the nonlinear interfaces and the bonded interfaces both resulting loops have been included in the graphs. The dynamic loops that are formed from the nonlinear analyses seem to be located almost at the same place as the ones formed from the bonded interface analyses. The main difference that can be observed is the clockwise rotation of the loops. The introduction of nonlinear interface elements at the caisson influence the shape of the dynamic loops. As the load level increases the dynamic loops tend to become horizontal.

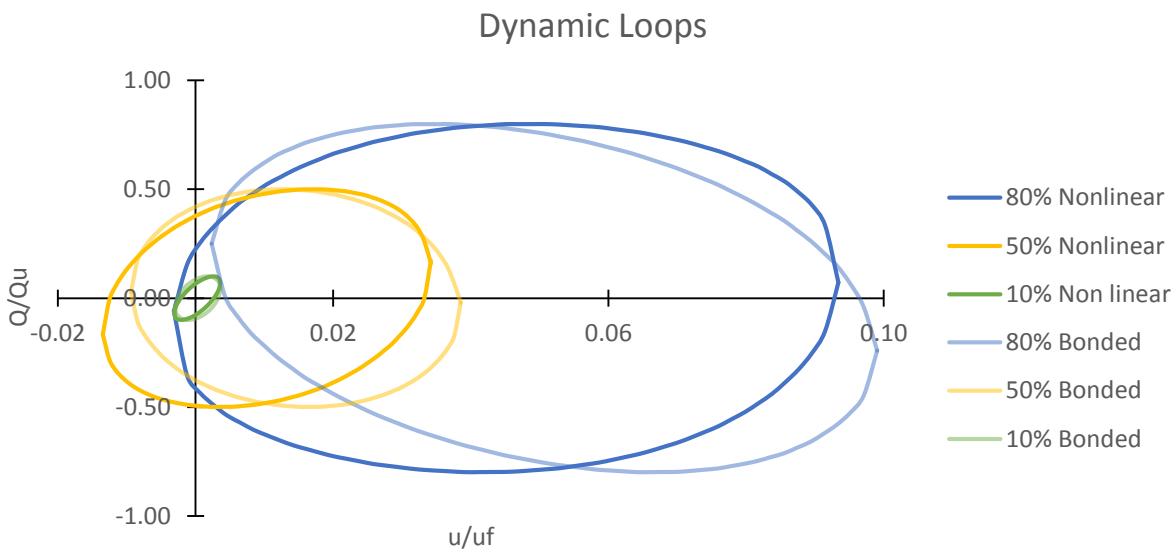

Figure 4-36: Loops formed from the dynamic analyses for the three load levels. The light colors indicate the results where the interface is considered to be bonded with the surrounding soil while the solid lines indicate the nonlinear interfaces where slippage and gapping are allowed.

4.5.3 Cyclic loading

In order to calculate the radiation loops, cyclic static push overs needed to be performed. The cyclic loading was chosen to be in such way that the maximum response of the dynamic loops would be achieved. In this way the loops are compatible. As it can be observed from Figure 4-38 below the shape of the cyclic loops for the nonlinear analyses and the bonded analyses is almost the same. The shape of the cyclic loops for the case that slippage and gapping have occurred at the interfaces is completely different than the shape of the loops of the full contact conditions as Figure 4-37 reveals. However this is not the case here as the shape of the loops is identical. The most possible reason for this is because gapping has not achieved in great depths as the magnitude of the deformations is very small. As it can be seen very close maximum and minimum values of the displacement are achieved for both scenarios. For the bonded interfaces these values are slightly greater so the material damping ratio is expected to be a bit greater in this case as Table 4-6 reveals in comparison with Table 4-2.

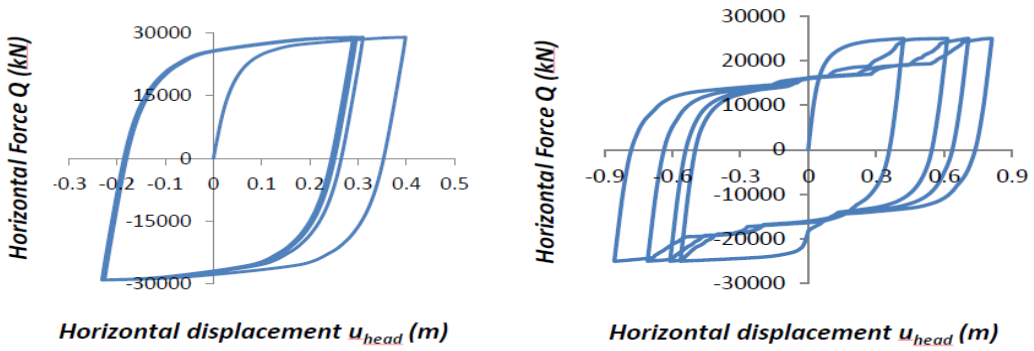

Figure 4-37: Cyclic loops for the case of light loaded caisson with embedment ratio (D/B=3). Left the case of full contact conditions, right the case of nonlinear Coulomb interfaces that allow gapping and sliding, (after Karapiperis (2012)).

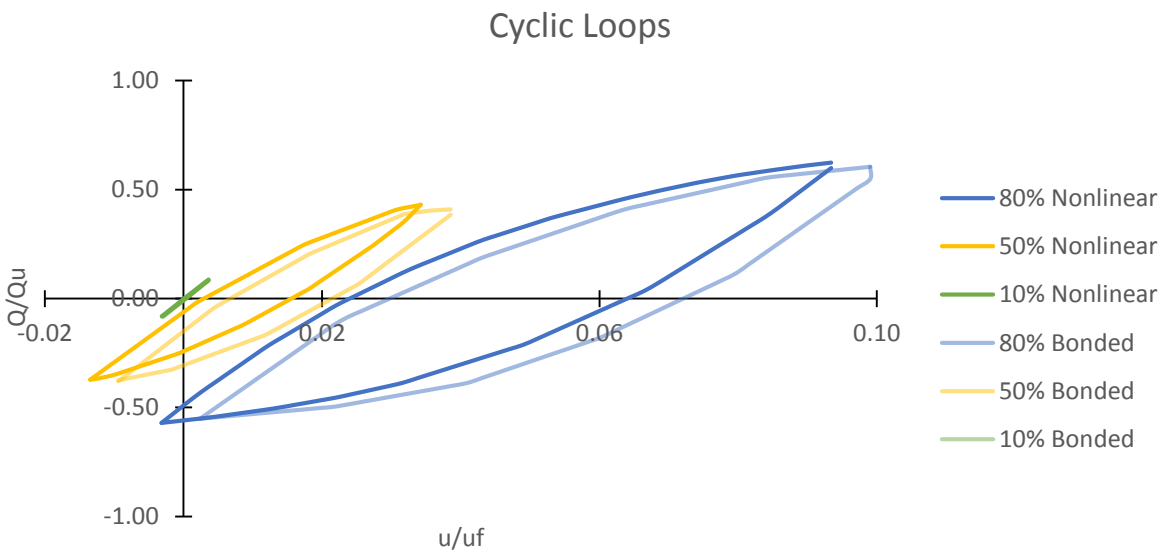

Figure 4-38: Loops formed from the cyclic analyses for the three load levels. The light colors indicate the results where the interface is considered to be bonded with the surrounding soil while the solid lines indicate the nonlinear interfaces where slippage and gapping are allowed.

Table 4-6: Damping ratios for cycling lstatic oading for the case of the nonlinear interfaces.

Load Level	10%	50%	80%
Damping Ratio	ξ	ξ	ξ
CYCLIC (f=4Hz)	2%	12%	20%

4.5.4 Radiation damping

Following the same procedure as in bonded interfaces the radiation damping is computed. Radiation loops can be computed by subtracting the cyclic loops from the dynamic loops after the rotation of the cyclic loops in such way that would match with the maximum and minimum displacements of the dynamic loops.. Again here linear interpolation has been performed in order to compute the loops (area and shape) more accurately. 100 points have been calculated for each kind of loops.

Considering the dashpots coefficients, Table 4-7 shows that the same trend as in bonded interfaces is followed. The dashpot reduces as the load level increases and the soil becomes more plastic.

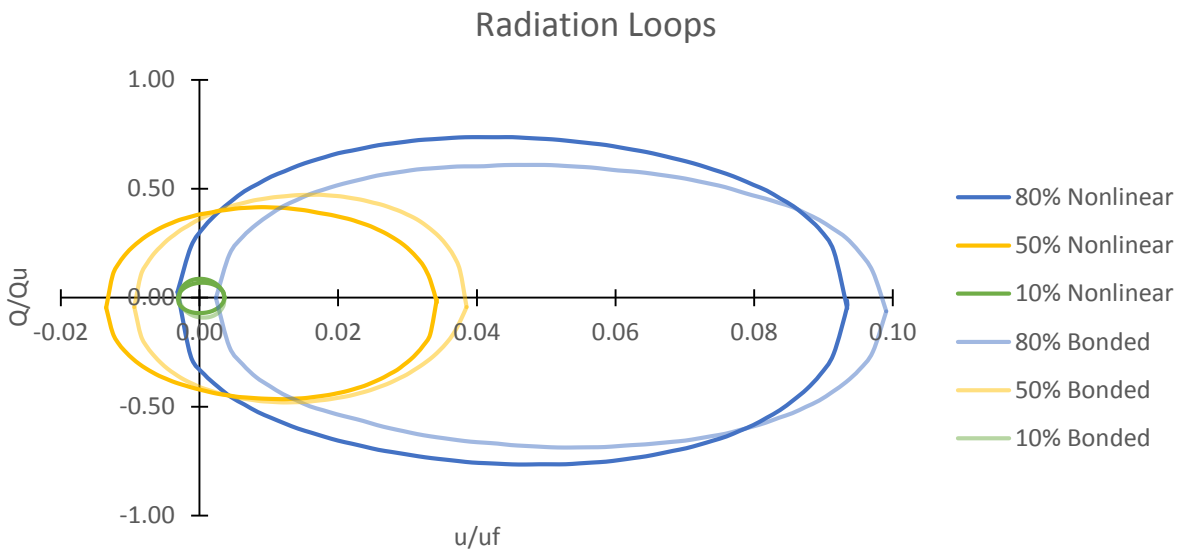

Figure 4-39: Loops that represent the radiation damping for the three levels of loading. The light colors indicate the results where the interface is considered to be bonded with the surrounding soil while the solid lines indicate the nonlinear interfaces where slippage and gapping are allowed.

Table 4-7: Areas and damping ratios for each kind of loops.

Load Level	10%	50%	80%
Loop Area [kN/m]	ΔW	ΔW	ΔW
DYNAMIC	24.5	1170.9	3989.8
CYCLIC	0.9	232.6	1129.4
RADIATION	23.6	938.3	2860.4

Load Level	10%	50%	80%
Damping Coefficient	C	C	C
DYNAMIC	4.14E+04	3.94E+04	3.27E+04
RADIATION	3.99E+04	3.15E+04	2.35E+04

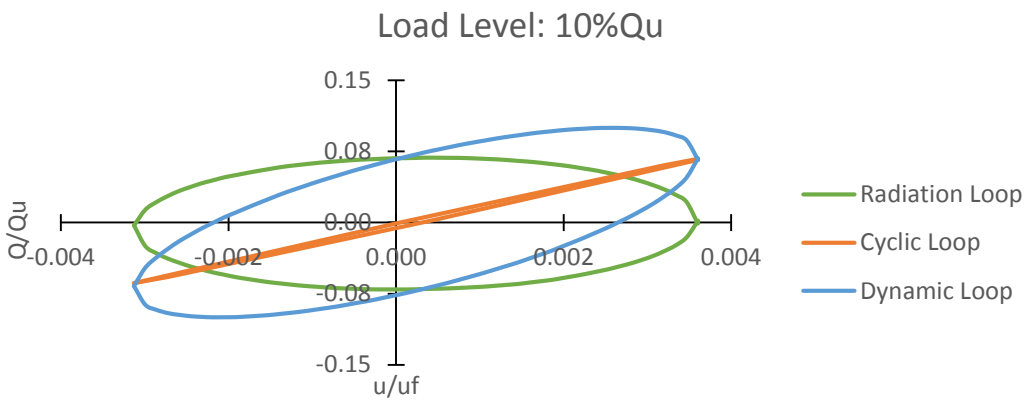

Figure 4-40: The three loops for the load level of 10% of Qu for the nonlinear interfaces.

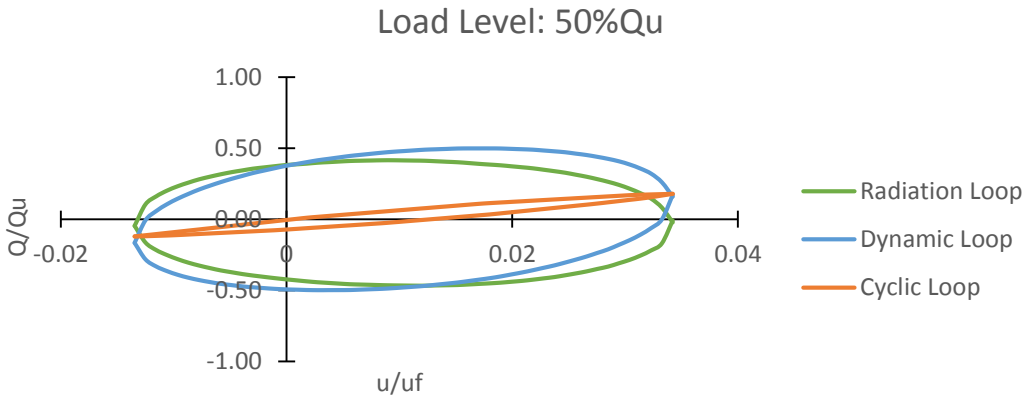

Figure 4-41: The three loops for the load level of 50% of Qu for the nonlinear interfaces.

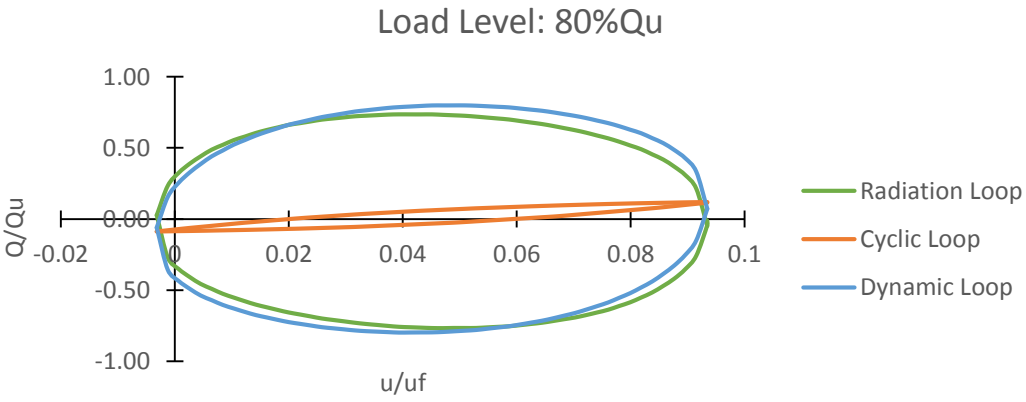

Figure 4-42: The three loops for the load level of 80% of Qu for the nonlinear interfaces.

5 Winkler approach

A different approach for the caisson's behavior is performed at this section. Until now the caisson has been considered to be a full rigid body that interacts with the surrounding soil under elastic or inelastic conditions. Now a Winkler type method is followed to describe the caisson's response. It is considered that the caisson is divided into horizontal plains along its depth. Each of these plains can be considered to be under plain strain conditions. The sum of the resistance of the surrounding soil of all the plains represents the resistance of the sidewall of the caisson. In the Winkler method the soil at each plain can be replaced by a set of pairs of horizontal and rotational springs and dashpots. The resistance of the base is different than the resistance of the sidewall so different springs and dashpots are needed to be applied at the base and the sidewall. In total four types of springs and dashpots for the analysis of inertially and kinematically loaded caissons are needed as Figure 5-1 depicts.

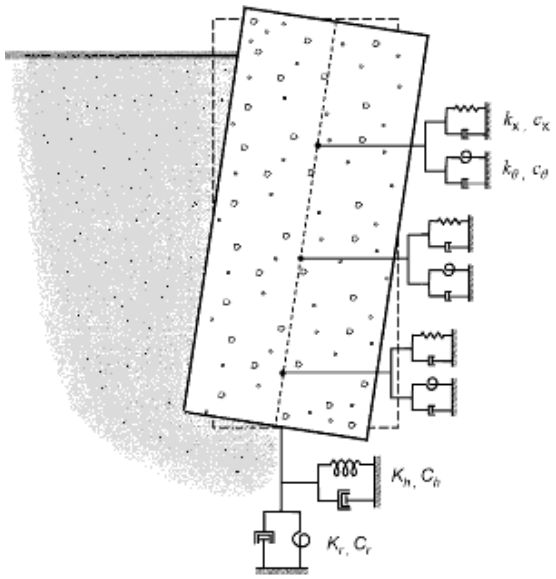

Figure 5-1: The Winkler approach for the behavior of the caisson. Four types of springs and dashpots are needed for the analysis of inertially and kinematically loaded caissons.

At this part of the thesis numerical analyses have been performed in order to evaluate the behavior of the horizontal plain. The dynamic lateral loading of the plain is investigated by forming the stiffness-displacement (K-u) and damping-

displacement (C-u) curves for each different frequency. Important conclusions are made by the physical meaning of these curves while frequency-dependent relations are developed for their description. For the Winkler model some suggestions are made for the mathematical analog that consists of different types of elements (springs, dashpots, mass) that are frequency independent but with the proper connection provide frequency dependent behavior. An attempt is made to calibrate these horizontal springs and dashpots coefficients of the sidewall of the caisson for both elastic and inelastic conditions by following the physics of the problem.

5.1 Plain Strain numerical analyses

For the plain strain analyses a section of one meter width of the previous caisson has been studied. The side of the caisson is B=10 meters while the lateral boundaries have been set to a distance 4B far away from the caisson.

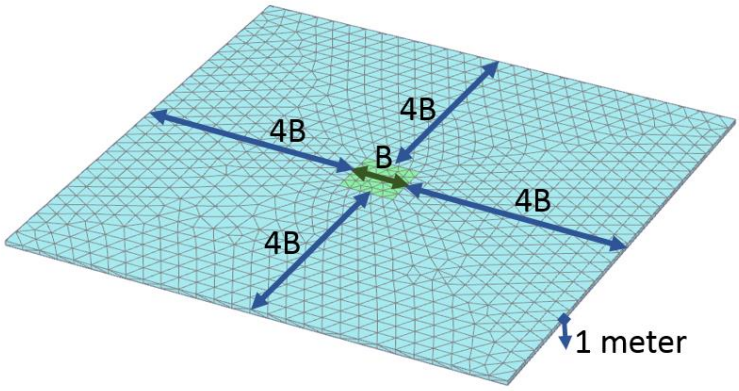

Figure 5-2: Numerical model for the plain strain analyses. The deformation at the vertical direction is not allowed.

The constitutive model that has been used is the Hardening Soil small and the parameters that have been selected are the same as in the previous analyses and are given in Table 4-1. It must be noted here that the caisson is massless. This section of the caisson has been studied for lateral static and dynamic loading under drained and undrained conditions and for bonded interfaces as well as nonlinear interfaces between the soil and the caisson.

In order to simulate the undrained conditions the Poisson's ratio has been set automatically to a value very close to 0.50 as the undrained Method B has been adapted. For the drained conditions the Poisson's ratio has been set to 0.20. The strength of the soil for both conditions is defined as the undrained shear strength (S_u=50 kPa).

5.1.1 Static lateral Push over

First static push overs were performed. Defining the failure as the moment when the tangent stiffness becomes less than 1% of the initial stiffness the strength of the plain found to be $13.6S_uB$ for the bonded case and $13.3S_uB$ for the nonlinear case. These normalized values where verified by additional pushovers that performed for a different caisson with width, B=5m. For circular in plan view caissons, as discussed before the strength can reach till $12S_uB$. The slightly greater strength that derived from the numerical analyses can be attributed to the different shape (square instead of circle) of the foundation as well as to the fineness of the numerical mesh.

5.1.2 Dynamic loading

For the dynamic loading of the inelastic behavior of the plain strain problem, six different frequencies were investigated. For each frequency different load levels were applied in order to form the stiffness-displacement and dashpot-displacement curves. The plain strain problem involves only one degree of freedom in the direction of lateral load. Thus the dynamic impedance can be defined immediately as the ratio between the applied force and the resulting displacement. Working with complex numbers the real part of this ratio corresponds to the stiffness or spring as the caisson is massless, and the imaginary part divided by the angular frequency, w, corresponds to the dashpot coefficient. Graphically from the dynamic loops that are formed between the force and the displacement, the spring coefficient can be calculated as the ratio between the force at the moment when the maximum displacement is achieved, and the maximum displacement. The dashpot coefficient, which includes both the radiation and the material damping in the case of inelastic

conditions, can be calculated from the area of the loop as has been explained extensively in the previous. The ratio between the maximum force and the maximum displacement corresponds to the norm of the impedance. From the loop that is formed between the force and the velocity these values can be verified. The ratio between the force at the moment when the maximum velocity is achieved and the maximum velocity, the dashpot coefficient can be calculated. Also, the maximum force divided by the maximum velocity times the angular frequency, gives the norm of the impedance. The following figures illustrate the aforementioned definitions.

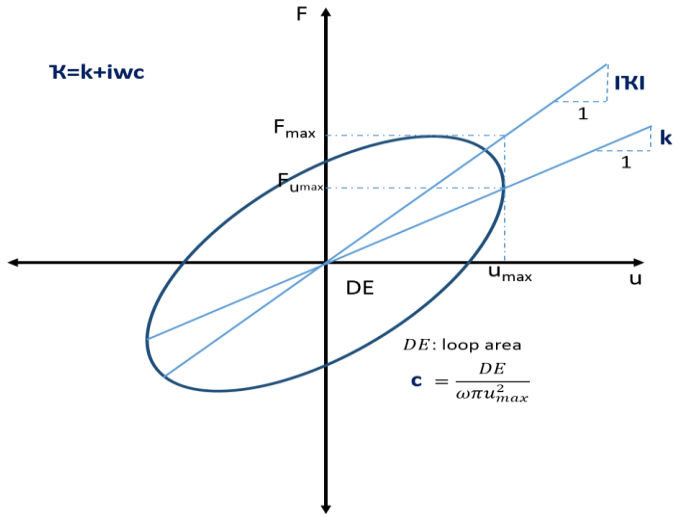

Figure 5-3: Schematic dynamic loop between the applied force and the resulting displacement.

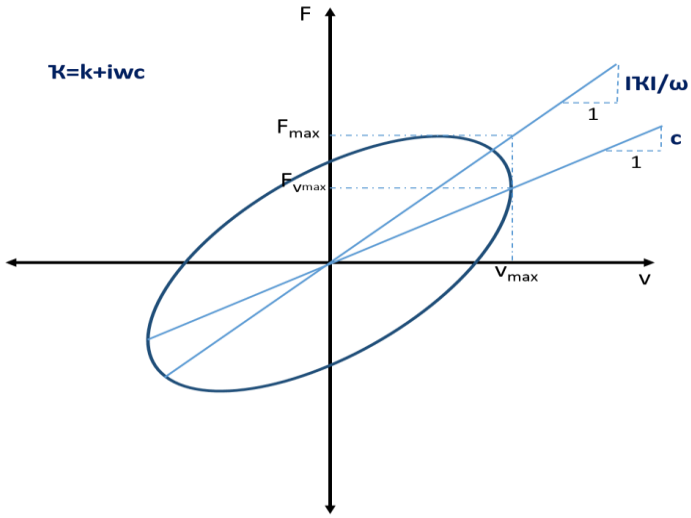

Figure 5-4: Schematic dynamic loop between the applied force and the resulting velocity.

» Bonded Interface

» Nonlinear interface

v = 0.20

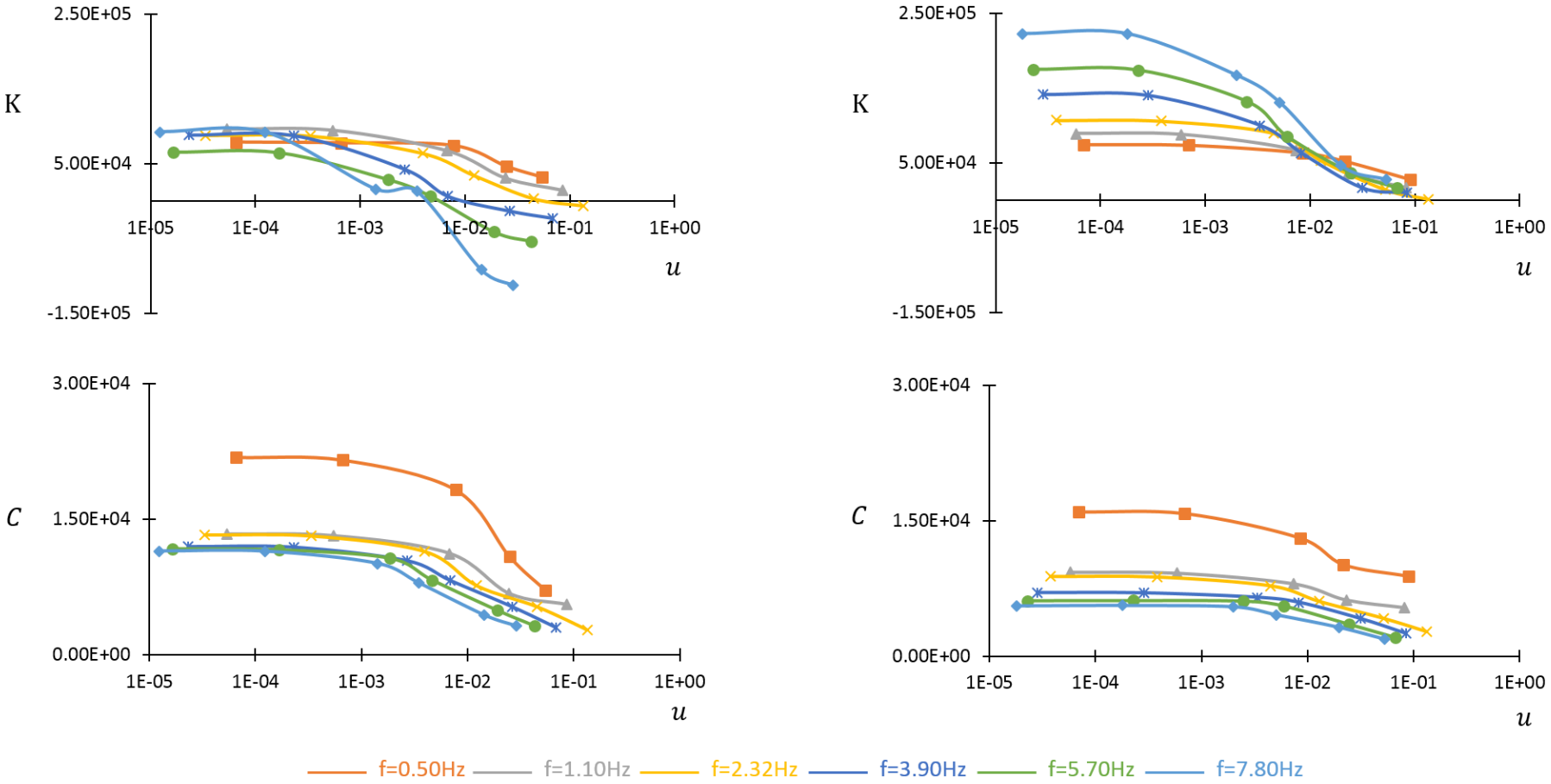

» Bonded Interface v = 0.20

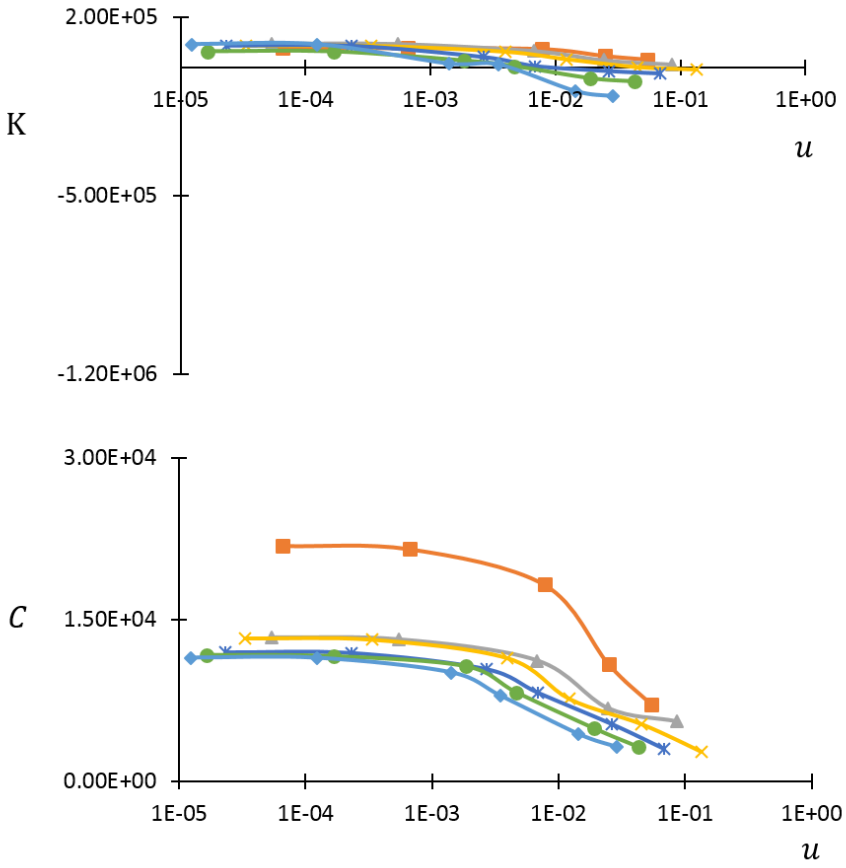

» Bonded Interface v = 0.50

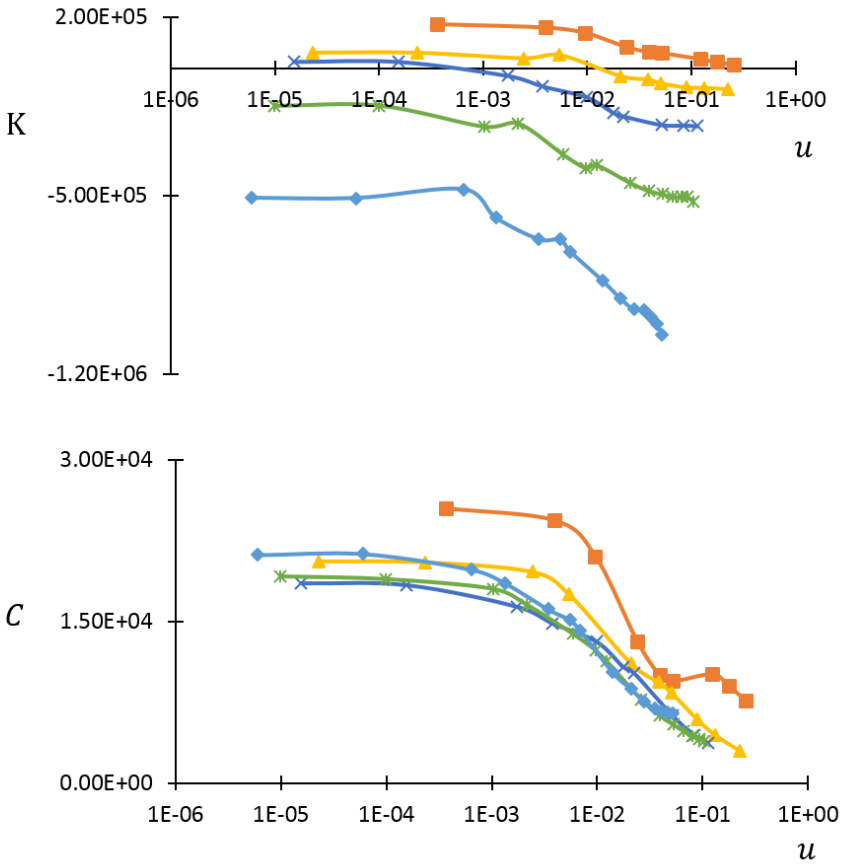

f=0.50Hz f=1.10Hz f=2.32Hz f=3.90Hz f=5.70Hz f=7.80Hz

5.1.4 Discussion and conclusions

Some very important conclusions can be conducted by the graphs that presented in the previous pages. First of all it should be noted that for the drained conditions (v=0.20) and the bonded interface the stiffness K remains almost the same for each frequency at the small deformations region. This is something that was expected as the conditions at this region can be considered elastic and as it is already known from the literature, for the case of the lateral loading of a plain strain foundation problem the stiffness remains independent of the frequency in the elastic conditions. However this is not true for the case of the nonlinear interfaces. As it can be seen, as the frequency increases the elastic stiffness at the small deformations region increases too. It should be denoted that for the lowest frequency, which is nearest to the static conditions, the difference between the bonded curve and the nonlinear curve is very small.

For all frequencies and for all cases the stiffness decrease as the deformations increase. Of course as the soil plastifies the resistance of the soil reduces. This resistance is being represented by the stiffness, K. One important difference between the K-u curves for the bonded and nonlinear interfaces is that the former curves take negative values as the frequencies increase and the deformations increase while the nonlinear curves remain at the positive side. This is something that can be explained easily if someone considers that for the case of the bonded interfaces there is no gap between the caisson and the soil so as the load level increases and consequently the deformations increase, a time lag between the applied oscillation of the caisson and the oscillation of the soil elements is being created thus when the caisson is moving through one direction the soil from the opposite side pushes the caisson and etc. This condition cannot happen for the case of the nonlinear interfaces because gapping is occurred so there is no interaction of the opposite side of the moving caisson.

Considering the dashpots it can be observed that for both cases, bonded and nonlinear interfaces for the drained conditions, the behavior is quite similar. At the small deformations region, the elastic dashpot decrease as the frequency increase with a decreasing tempo and tends to reach one specific value as the frequency

increase. This value is not random. As it will be explained later it is the value that comes from the theory of the one dimensional wave propagation. For the case of the nonlinear interface this value is smaller because of the gap that is occurred and so the one side does not participate to the propagation of the wave that is formed from the oscillation.

As far as concerns the numerical analyses for the case of the undrained conditions (v=0.50), it should be mentioned that the problem becomes much more sensitive to the boundaries of the model because of the wave velocity of the P-waves that becomes infinite. The animations that were created from the analyses revealed that the viscous boundaries do not work properly as the waves found to partially reflect at the boundaries. This is something that was not presented in the drained conditions.

Comparing the bonded interface for the drained conditions and the undrained conditions it can be observed that for the case of the undrained conditions the stiffness becomes negative already for the elastic region for the greater frequencies. This is also something that is not new to the literature for the case of the lateral dynamic loading of a plain strain problem under undrained conditions. As the load level increase for each frequency the stiffness becomes smaller or in the case of the negative area becomes more negative. Considering the dashpots the same behavior is presented. The damping reduces as the soil plastifies for every frequency.

The wave cannot be transferred through the plastified area as the figure below reveals. Something else that should be observed from this figure is that for the case of the great load level (80%Q_u) the color of the caisson is different than the color of the surrounding soil. This fact reveals the time lag between the oscillation of the caisson and the soil indicating in this way the negative stiffness. As it can be seen this is not true for the case of the low load level where elastic conditions can be considered. The colors of the caisson and the surrounding soil are the same, a fact that indicates positive stiffness.

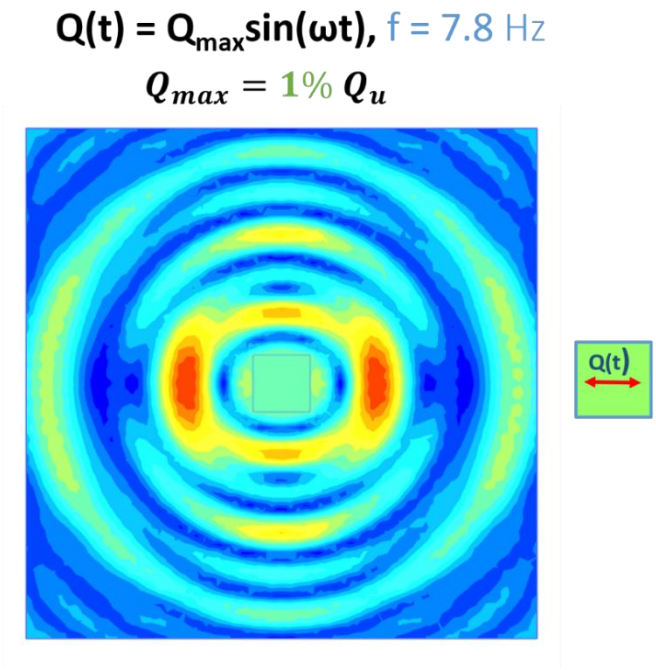

Figure 5-5: Absolute displacements due to dynamic low loading for the case of bonded interfaces under drained conditions at the steady state. Because of the low amplitude of the load and consequently the low deformations, the conditions can be considered to be elastic. The waves propagate to the whole domain.

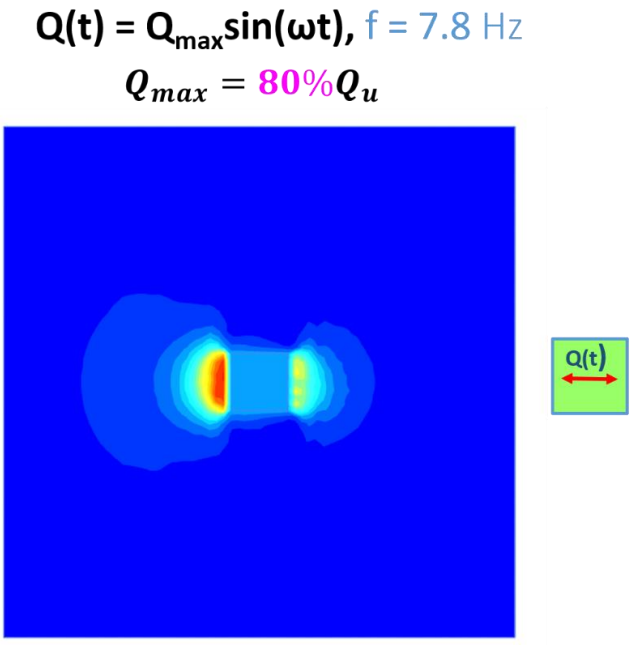

Figure 5-6: Absolute displacements due to dynamic high loading for the case of bonded interfaces under drained conditions at the steady state. Because of the high amplitude of the load the soil plastifies and the conditions are inelastic. There is a permanent deformation at the direction of the first half cycle (left at the picture). The different color between the caisson and the soil indicate the negative stiffness.

5.2 Development of relations for the K-u and C-u curves

In order to quantify the behavior of the caisson relations that describe the curves that presented before have been developed. First the curves were normalized with the elastic values, K_{max} or C_{max}, (values at the smallest deformation) for both the springs and the dashpots. The relations that can describe these curves found to have the following form:

$$\frac{K}{K_{max}} = x_5 \frac{x_1}{x_1 + x_2 \left(\frac{u}{x_3}\right)^{x_4}} + (1 - x_5)$$

and

$$\frac{C}{C_{max}} = x_5 \frac{x_1}{x_1 + x_2 \left(\frac{u}{x_3}\right)^{x_4}}$$

Of course for each equation the coefficients x_i are different for the stiffness and the dashpot. These coefficients are frequency dependent. Their calibration was made by curve fitting using advanced genetic algorithms and the optimization was achieved using special software (MATLAB). It should be noted here that the last term in the first equation has been added in order the stiffness K to be able to get negative values. This term is not necessary for the dashpots because the dashpot tends to zero as the displacement increase and cannot take negative values. In the following charts the coefficients and their equations are presented for the case of the bonded interfaces under drained conditions.

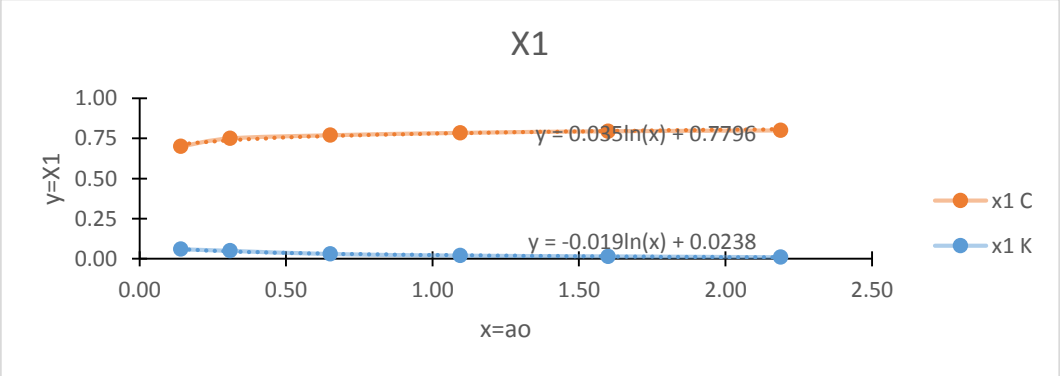

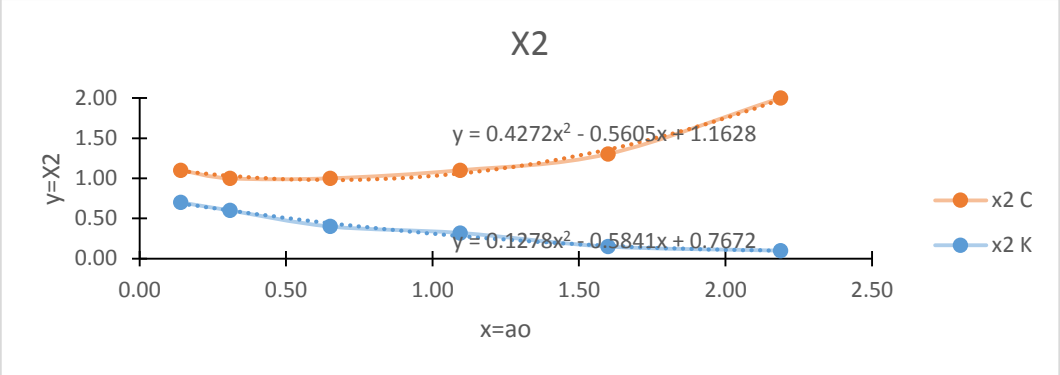

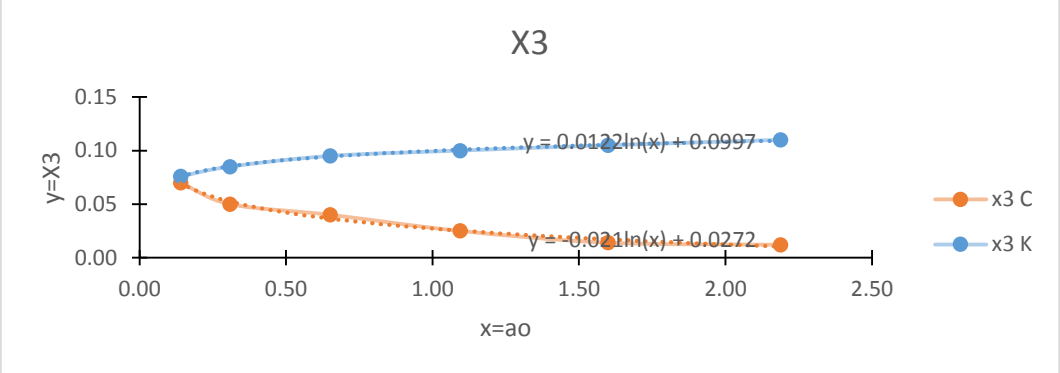

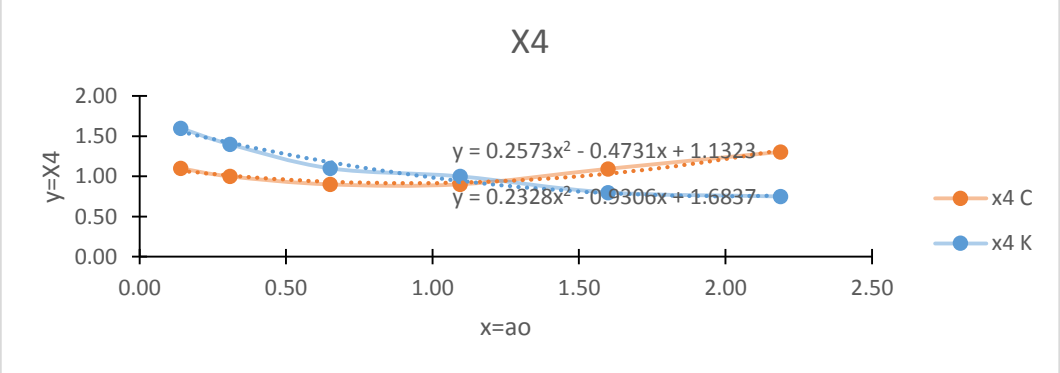

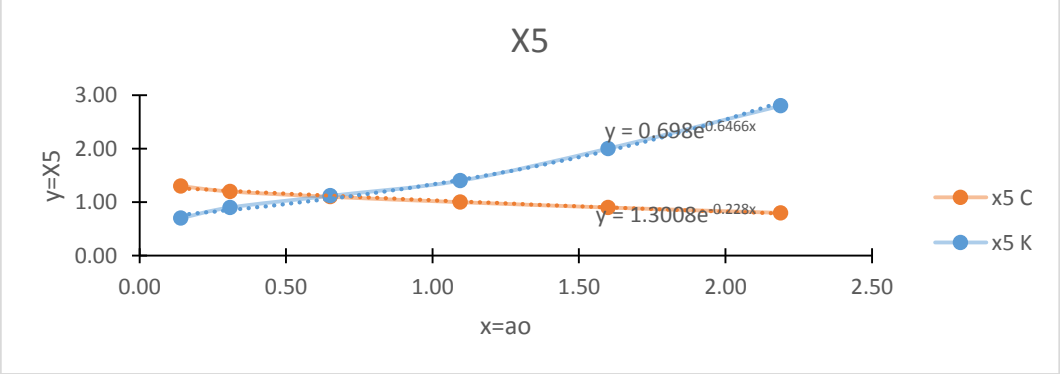

Figure 5-7: Frequency dependent coefficients Xi that are included in the developed relations for the stiffness K and the dashpot C. The x axis shows the dimensionless frequency a_0.

5.3 Proposed model

After understanding the mechanisms of the plain strain problem, an attempt has been made to develop a proper mathematical model using the Winkler approach for the drained conditions. One of the advantages of such a model is of course the minimum computational effort that it needs. A Winkler model is expected to give the same results with the numerical analyses only after a few seconds and not several minutes or hours as the finite element programs need. Moreover and most importantly such models can easily adapted to structural codes and represent the real soil. In the suggested mathematical model frequency independent elements of springs, dashpots and masses are connected properly in order to achieve the desirable frequency dependent inelastic behavior. In the following the process of the work until the final solution is described. The reader is recommended to read the following process with reference to Figure 5-76.

First restriction is the static inelastic behavior. The solution of one simple linear spring is not correct as the relation that it gives between the force and the displacement is linear something that it is not realistic. In order to achieve real inelastic static response a nonlinear spring needs to be adapted. For the description of the nonlinear spring the BWGG law was adapted. The reaction of the nonlinear spring, K_2, is given by the simple following equations. For more details about the mathematical description of BWGG the reader is referred to (Gerolymos & Gazetas, 2006) and (Gerolymos, 2002).

$$\mathrm{F} = \mathrm{K}_2\mathrm{u} = F_y\zeta, \quad F_y = ultimate\ resistance$$

$$d\zeta = \frac{1}{u_y}\left[(1-|\zeta|^n)\left(0.5 - 0.5sign\left(du\, d\zeta\right)\right)\right] du$$

After having fixed the static behavior next step is to fit the behavior in dynamic loading. Of course it is already known that damping is occurred in dynamic analyses and that dashpots are proper mathematical tools to describe it. The case of adding a dashpot in series to the inelastic spring would not be correct as the model will not work in static loading because the load would not be able to be transferred through

the dashpot because of the zero velocity that describes the static conditions. Consequently, the dashpot needs to be added in parallel to the inelastic spring.

It is known, and validated by the previous numerical analyses, that in elastic drained conditions the dynamic lateral loading of a plain strain problem gives the same spring for every frequency. However considering the dashpots in elastic conditions it is known that there is a constantly decreasing rate as the frequencies increase. The asymptote value of the dashpots comes from the one dimensional propagation of waves' theory and more details are given in the following. The model with the nonlinear spring and the dashpot in parallel is not able to describe this elastic curve for the dashpots. In order to achieve the decreasing curve it found that another pair of a spring and a dashpot connected in parallel needed to be added to the model. In this way the model is able to describe except for the static loading also the dynamic loading in elastic conditions.

Next step is to make the model to be able to describe the inelastic dynamic behavior. As we saw from the numerical analyses the stiffness of each frequency is reducing as the displacements increase and is also able to take negative values. The dashpot found also to have similar behavior as it reduces with the increase of the displacement but it remains at the positive side and tends to zero as the load level rise. The model with the two pairs of springs and dashpots connected in parallel is able to describe the decrease for each frequency of the stiffness. This is due to the first nonlinear spring. However it cannot make the stiffness to go to the negative side. Considering the dashpots, the model is not able to describe the reductive curves as the dashpots for each frequency remains almost steady with the increase of the displacement. In order to fix these two conditions it found that a special element of mass needed to be added to the model. The mass element that is added, is called "gyro" mass and is frequency independent. It is defined as a unit system that generates a reaction force due to the relative acceleration of the nodes between the gyro mass is placed. Adding a gyro mass at the nearest-to-the-foundation pair of the nonlinear spring and dashpot makes the model to be able to fit not only the static and the elastic dynamic behavior but also the dynamic inelastic behavior.

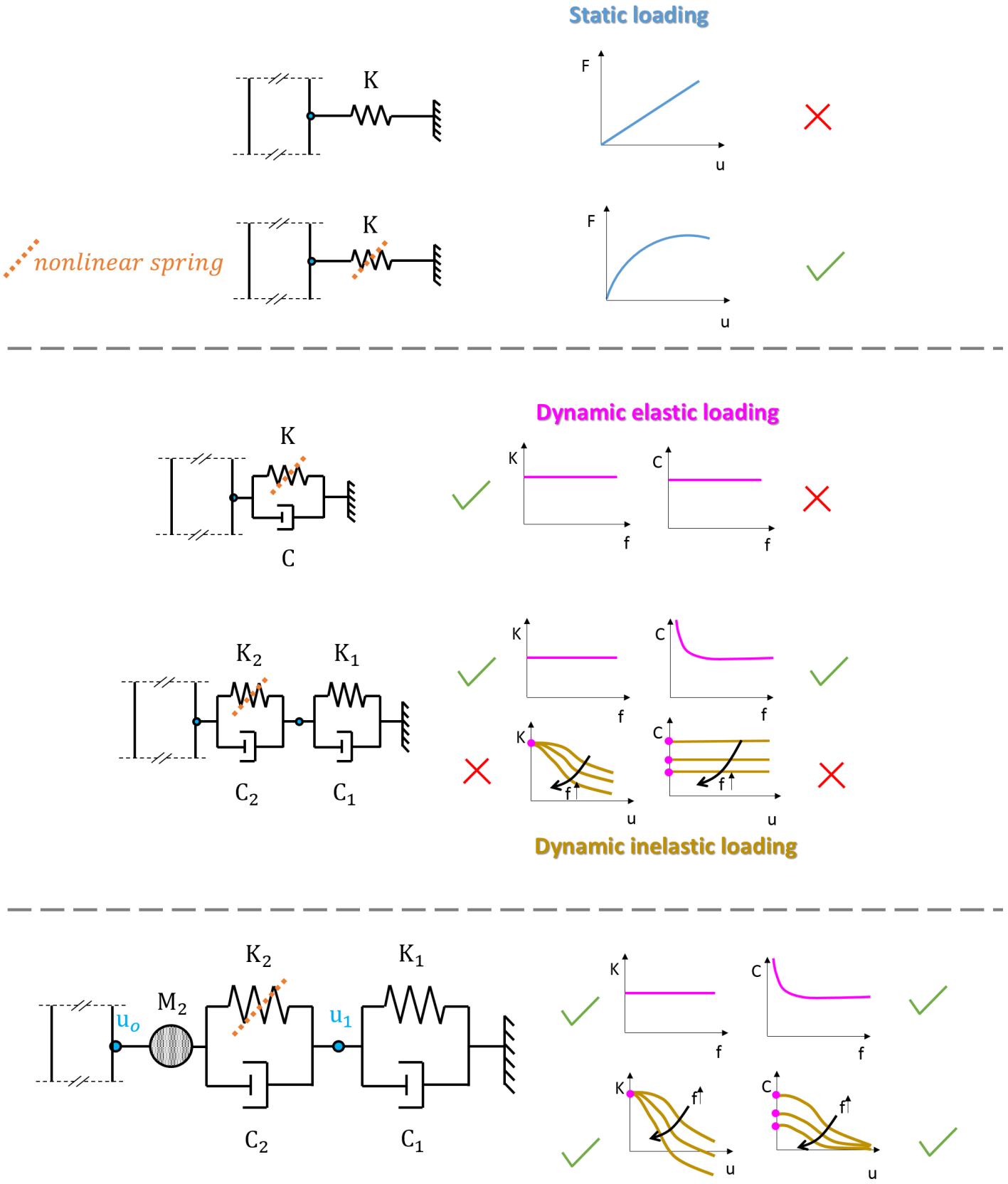

Figure 5-8: Process of concluding to the suggested Winkler model. The yellow dashed line indicate the nonlinear spring. At the charts the blue color indicate static conditions, the pink color the elastic dynamic condition and the yellow color the inelastic dynamic conditions.

5.3.1 Calibration of the coefficients of the model

The calibration of the coefficients of the suggested model was made in such way that the model would fit the numerical results. However some general principles that derive from the physics of the model were followed and are given below. The global stiffness and the global dashpot of the suggested model for the elastic conditions are given by the following relations:

$$K_h^{square} = Re\left(\frac{\widetilde{K}_1\widetilde{K}_2}{\widetilde{K}_1 + \widetilde{K}_2}\right)$$

and

$$C_h^{square} = \frac{Im\left(\frac{\widetilde{K}_1\widetilde{K}_2}{\widetilde{K}_1 + \widetilde{K}_2}\right)}{w}$$

The caisson that has been studied until now is square in plan view with side length B. Following the theory from the plain strain analysis we can assume that the square plan section consists simplified by four different strips. Applying a lateral force in the plain with direction parallel to one of the sides, two of the four strips are loaded horizontally while the other two are loaded vertically.

$$Square\ plan = 2 * vertical\ strips + 2 * horizontal\ strips$$

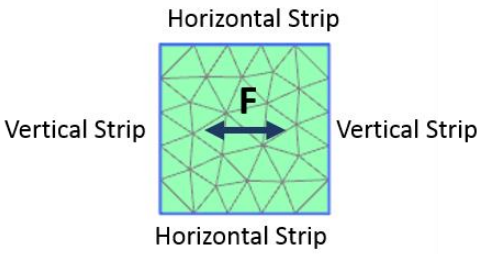

Figure 5-9: The square plan plain strain problem consists of four strips. For lateral loading, two vertical strips and two horizontal.

With this simplifying assumption the static stiffness of the surrounding soil can be calculated as the sum of the stiffnesses of these strips. The most common elastic relations (Gazetas) for vertically and horizontally loaded strips are given below. G is the shear modulus, v is the Poisson's ratio and E_s is the modulus of elasticity.

$$K_v^{strip} = \frac{1.2G}{1-v} = \frac{1.2E_s}{(1-v)2(1+v)}$$

$$K_h^{strip} = \frac{2.1G}{2-v} = \frac{2.1E_s}{(2-v)2(1+v)}$$

Subsequently the initial static global stiffness of the square section is given by:

$$K_h^{square} = 2K_v^{strip} + 2K_h^{strip} = 2\frac{1.2(2-v) + 2.1(1-v)}{(1-v)(2-v)}G$$

This formula corresponds to the initial elastic stiffness for static conditions for the plain strain for full bonded conditions meaning that no gapping or slippage is allowed to occur. In case of nonlinear interfaces between the caisson's section and the soil because of the fact that gapping is occurred at the very beginning of the lateral loading the vertical strip at the opposite direction of the load does not contribute to the resistance. Thus, the stiffness reduces to:

$K_h^{square} = 1K_v^{strip} + 2K_h^{strip}$, in the case of nonlinear interfaces.

Considering the dynamic stiffness (Gerolymos & Gazetas, 2006) have estimated that the lateral stiffness of the distributed horizontal springs is constant and equal to $k_h = 2.18\left(\frac{D}{B}\right)^{-0.13} E_s$. Taking into account that the section of the caisson is studied under plain strain conditions (so D equals to infinity), the dynamic stiffness for elastic conditions for the case that is studied herein should be also constant and equal to the initial elastic stiffness as given above.

Considering the global dashpot coefficient, following the same procedure we can assume that the waves generated at the foundation-soil interface can propagate from the four sides each of which is a strip. Shear loading produces primarily shear waves which propagate with the S-wave velocity, V_s. On the other hand, vertical loading produces compression-extension as well as shear deformations, thereby the selection of an appropriate wave velocity is not so obvious. Gazetas and Dobry have suggested the use of Lysmer's analog wave velocity defined as $V_{La} = \frac{3.4}{\pi(1-v)}V_s$.

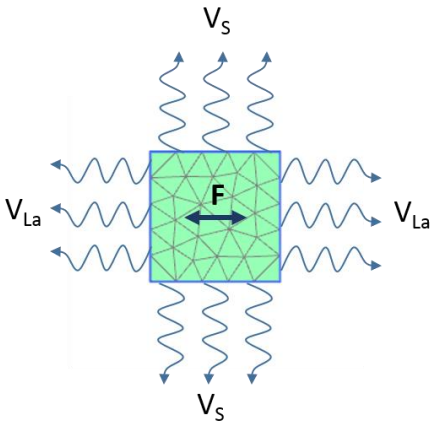

Figure 5-10: Simplified approximation for the propagation of waves from the four strips that consist the plain strain problem.

Taking into account the fact that as the frequency arises all the dashpot coefficients despite the shape of the foundation or the direction of the loading tend to the one dimensional value: $C = \rho V A_b$ where ρ is the density of the soil, A_b is the area of the perpendicular surface on which the wave is induced, V is either the S-wave velocity or the Lysmer's analog as explained before. At very high frequency factors (or very small wavelengths) waves propagate only in the vertical direction perpendicular to the plane of the source. This one-dimensionality of the travelling waves suggests that the global dashpot coefficient will tend asymptotically to this value.

$$C_{\alpha o \to \infty} = \rho V A_b$$

For very high frequencies and vertically loaded strips or horizontally loaded strips the dashpot coefficients is given as:

$$C_v^{strip} = \rho V_{La} A_b$$

$$C_h^{strip} = \rho V_s A_b$$

Subsequently for the square plan plain strain problem the asymptotic value is:

$$C_h^{square} = 2C_v^{strip} + 2C_h^{strip} = \rho B(2V_{La} + 2V_s)$$

Considering the case that nonlinearities are taken into account at the interfaces between the soil and the foundation the dashpot coefficient is given by:

$$C_h^{square} = 1C_v^{strip} + 2C_h^{strip} = \rho B(V_{La} + 2V_s)$$

Furthermore (Gazetas, 1987) have shown using a simple cone model for radiation damping of the plain strain problem that the radiation dashpot coefficient can be readily obtained from the following equation:

$$C = \rho V A_b Re\left[-i\frac{H_1^{(2)}(a_o)}{H_0^{(2)}(a_o)}\right]$$

In which Re[·] denotes the real part and A_b=B is the area (per unit length) of the foundation and $H_1^{(2)}, H_0^{(2)}$ denote the complex-valued second kind Hanklel functions of first and zero order, respectively. It is evident that for the strip $C \geq \rho V A_b$ and that the exact value of C depends on frequency.

All the above relations are referred to the small deformations (elastic conditions) and can be used as constraints mainly for the calibration of the distributed horizontal springs and dashpots of the caisson (K1,K2,C1,C2). Considering inelastic conditions where the shear modulus is reduced and subsequently the wave velocities decrease too, there are not much information in the literature that can be used for the calibration of the springs and the dashpots, thus only the numerical analyses that performed in order to study qualitatively the inelastic problem for drained and undrained conditions as well as for bonded and nonlinear interfaces were used for the calibration of the coefficients.

As far as concerns the ultimate resistance of the shaft under static conditions the theoretical value Fy for cylindrical foundations ranges between $6S_uB$ and $12S_uB$. The lowest value is approximately the plasticity solution for the bearing capacity of a surface footing and the highest value of a deeply embedded footing with rough footing-soil interface. For square foundations these values are expected to be a bit higher, a fact that was verified with the numerical analyses as it was shown in the previous.

Considering the mass element, the calibration was made in such way that the results would fit the results of the numerical analyses. For the mathematical description of the model the reader is referred to Appendix D.

5.3.2 Results

In the following figure qualitatively comparisons are made between the proposed Winkler model and the numerical analyses for one frequency (5.70Hz) and different levels of loading. The results are very satisfactory.

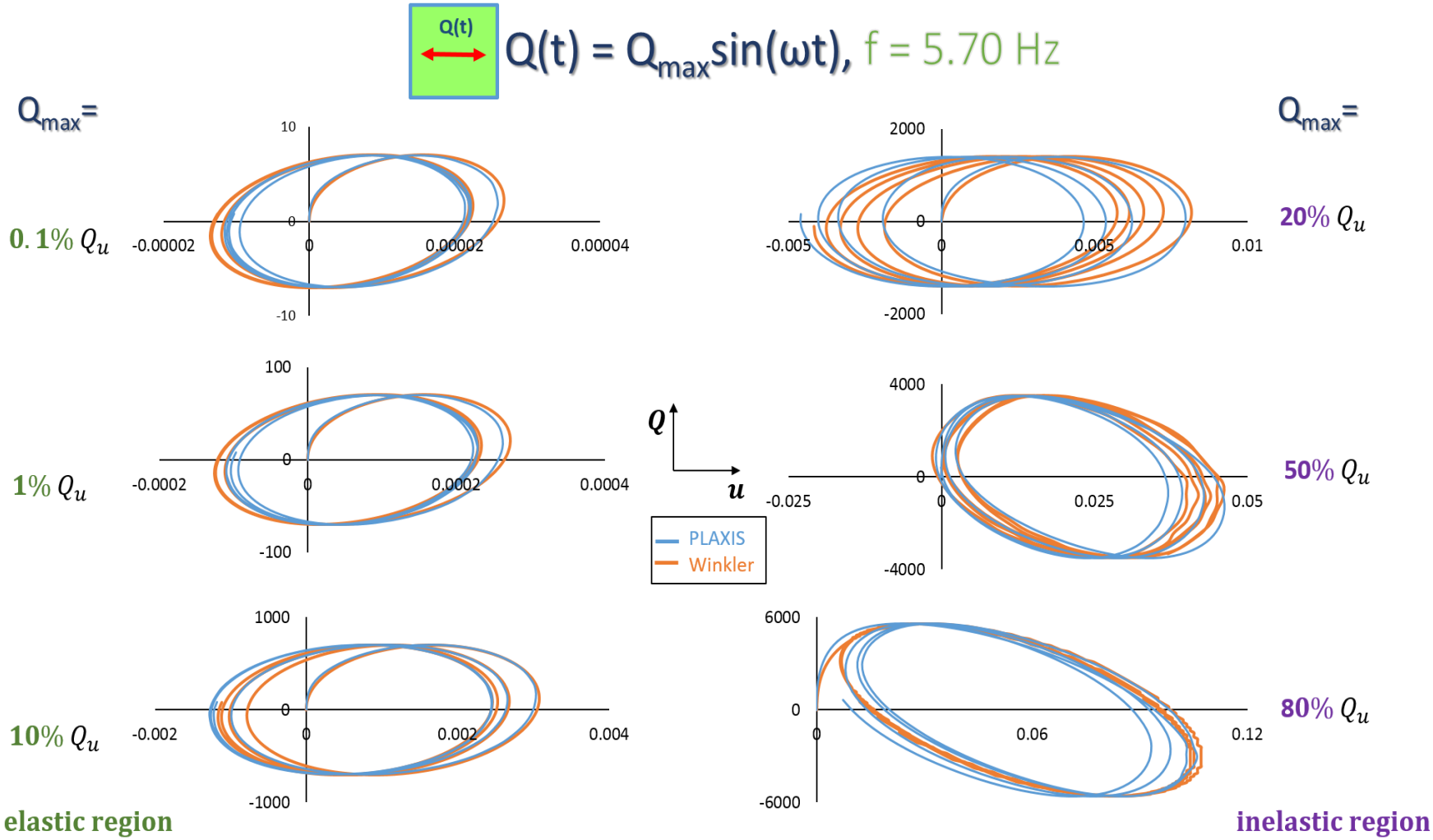

Figure 4-4 : Comparison between the Winkler model and the numerical analyses for one frequency and different levels of amplitude of the loading under drained conditions and for the case of bonded interfaces. Until 10% of the ultimate load the behavior can considered to be elastic while above this value the behavior becomes inelastic.

6 Case study: Suction caisson

6.1 Description of field tests

At this part of the thesis a real case study is compared with numerical results of Finite Element analyses using PLAXIS 3D. A set of tests of caisson foundations in clay at the Bothkennar test site has been conducted and analyzed by (Houlsby, et al., 2005). The tests are relevant to the design of foundations for offshore wind turbines, in the form of either monopod or tetrapod foundations. This type of caissons is called "suction" caissons and they were subjected to intermediate scale experiments. The rigid caisson that has been studied till far in this study is quite different in behavior from the suction caissons that has been tested at the Bothkennar site. A brief description of the new type of caissons follows below.

Suction caissons are large cylindrical structures, open at the base. During installation they cut a small distance into the seabed under their own weight, but are then installed to their full depth (with the caisson lid flush with the seabed) by pumping out the water that is trapped within the caisson (see Figure 6-1). They can be installed in either clays or sands. The use of suction caisson foundations as an alternative kind of foundation is getting more and more famous. They are widely used as anchors for floating structures, and have also been used offshore as foundations for a small number of fixed platforms. The principal advantage for the offshore wind application is that the caissons can be installed rapidly, using relatively inexpensive equipment.

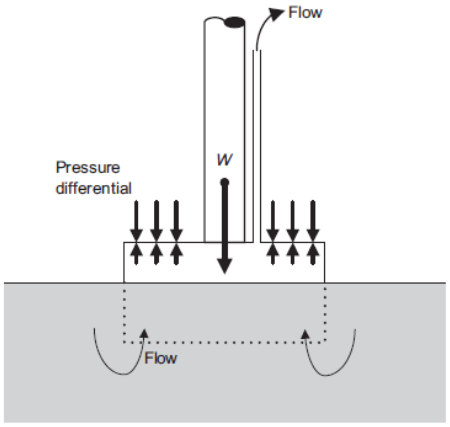

Figure 6-1: Installation of a suction caisson and its installation.

Considering the field experiments, two main structural configurations using caissons have been tested, either a ‘monopod’ consisting of a single large caisson (typically 20–25 m in diameter for a modern large turbine structure), or a ‘tetrapod’ in which the load is transferred through a truss structure to four smaller caissons. For the monopod the most important load on the foundation is the overturning moment. In the case of the tetrapod the moment loading is carried principally by ‘push–pull’ action by opposing footings, and it is the variation of vertical load (and in particular the possibility of tension on a footing) that is most important. The part of the experiments that concerns this thesis is the dynamic records for the monopod.

The caisson that represented the monopod was subjected, among others, to cyclic moment loading under dynamic conditions. The caisson that constructed for the experiments was fabricated from mild steel. Its diameter was 3.0 meters and the length of the skirt was 1.5 meters resulting an embedment ratio of 2, the same ratio as the rigid caisson that was studied till far. The thickness of the wall was 8.0mm. It should be mentioned that the lid of the caisson was stiffened by I-sections.

Figure 6-2: The 3 meters diameter suction caisson that was subjected to dynamic loading in the field.

Small-amplitude cyclic horizontal loads were applied at the top of a frame (4.23 m above the lid of the caisson) by means of a machine (SEMV), operating at 10 Hz, at which frequency the amplitude of the applied load was 5.0 kN. These loads are intended to be representative primarily of wave loads experienced by a prototype

structure. Undrained conditions were assumed. The undrained shear strength at the base of the caisson is S_u=14.4 kPa and the bulk density of the clay at relevant depths is estimated as 1680 kg/m^3.

Figure 6-3 shows the record of the applied moment against time. The test starts at an offset moment of approximately 16.6 kNm. The amplitude of loading builds up steadily with the frequency, with a minor fluctuation at about 7 Hz. After the 15th second the frequency remains steady at 10Hz causing a steady state response of the caisson. Figure 6-4 shows the resulting moment–rotation response. When the steady state response is achieved the dynamic loop becomes stable. The purpose of the numerical analyses that follow is to capture this dynamic loop at the steady state. Thus, the applied moment profile for the numerical analyses, as it will be discussed below, includes only the last part of the profile that was used in the dynamic experiment where the frequency is steady at f=10Hz and the dynamic loop is stable.

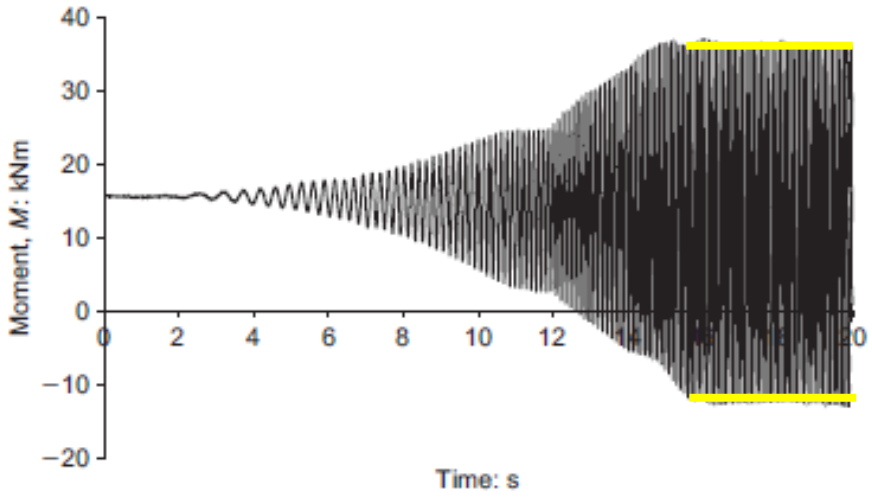

Figure 6-3: Applied moment against time. The frequency becomes 10Hz and remains steady after the 15th second.

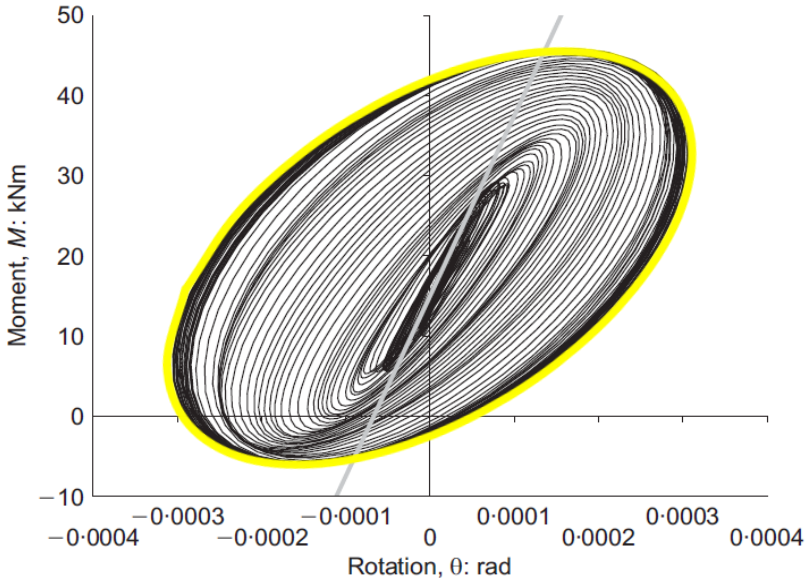

Figure 6-4: Full moment-rotation response of the caisson. The yellow line indicates the steady state dynamic loop for f=10Hz.

6.2 Numerical model

The geometry of the numerical domain has been chosen following the previous sensitivity analyses that concerned the rigid caisson that was studied before and were extended even more. Thus, the lateral boundaries have been set to a distance of 5D (D=3 meters: diameter of the caisson) from the center of the caisson and the lower boundary to a distance of 5D from the center of the lid of the caisson. Proper care has also been taken for the fineness of the mesh.

The suction caisson was simulated by plate elements. The diameter of the lid has been set to 3 meters while its thickness has been chosen to be big enough (1.5 meters) in order to behave as rigid body, so the model would capture the fact that the lid of the caisson in the experiment was stiffened by I-sections. The depth of the skirt has been set to 1.5 meters and its thickness to 8mm, values exact same as in the experiment. The material of the caisson is steel so the moduli of elasticity for all the plate elements has been chosen to be E_{steel}=210 GPa.

In order to apply the moment loading to the caisson, following the same procedure as in the real experiment, a beam in the center of the lid of the caisson has been added. At the top of the beam a lateral point load was applied, $F = F_{max}\sin(\omega t)$, where ω=2πf (f=10Hz) transmitting in this way a rotational moment at the lid of the caisson $M = Fh$,where h is the height of the beam. The beam was set to 4.23 meters high and its properties were chosen in such way (A=1 meter, E_{steel}=210 GPa) that it would behave rigid, so no P-δ effects would take place. It should be mentioned here that the thickness of the plates and the area (A) of the beam have no physical meaning, these parameters have effect only on the stiffness of the corresponding elements.

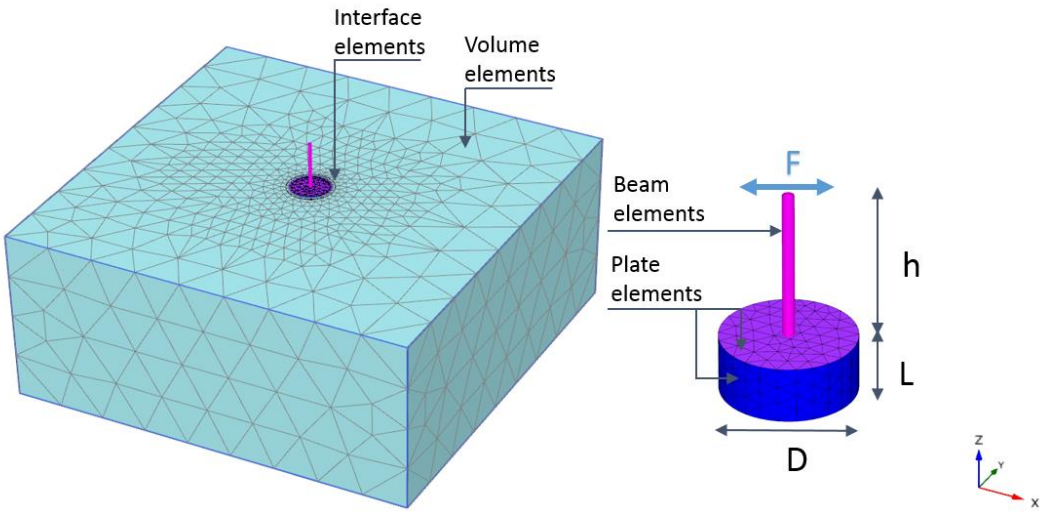

Figure 6-5: Numerical simulation of the suction caisson: D=3 meters, L=1.50 meters, h=4.23 meters.

The soil has been simulated with volume elements. The constitutive model that has been chosen to represent the behavior of the real soil is the Hardening Soil small model. The parameters of the constitutive model that were chosen are discussed in the following section where comparisons are made with the suggested parameters from (Houlsby, et al., 2005). Moreover, in order to represent the real conditions of the field tests, interface elements both outside of the skirt as well as inside of the skirt have been introduced. The material parameters of these elements are the same as the soil elements. The parameter that represents the strength of the interface

elements has been set to R_{inter}=1. This means that the interfaces have the same strength as the surrounding soil. However for the interface elements, in contrast to the soil elements, the tension cut off option has been activated in order to allow gapping to occur.

6.3 Comparison and conclusions

The suction caisson is a type of embedded foundations, thus normally proper care should be taken to the cross-coupling between the moment and the horizontal loading. (Houlsby, et al., 2005) although recognizing the importance of the embedment, they use a preliminary analysis based on factors for surface footings. For surface foundations, the rocking impedance can be defined directly as $\widetilde{K}_r = \frac{M}{\tilde{\theta}}$ where M is the moment loading and θ is the rotation angle. The rocking impedance is a complex number where the real part represents the stiffness and the inertial effects, and the imaginary part the damping. As it is mentioned in the report of the experiments, the principal effect of ignoring the footing embedment is that the stiffness coefficients may be underestimated by a factor that may be in the region of 1.5, but depending on the assumptions about interactions on the side of the caisson, and the variation of stiffness with depth. This factor as the numerical analyses revealed and is presented in the following is 1.90.

Following the methodology for the surface footings the rocking stiffness is given by: $k = \frac{8GR^3}{3(1-v)}$ where G is the shear modulus and v is Poisson's ratio. The tests have been considered to be under undrained conditions so the Poisson's ratio is half (v=0.50). In the report it is given that $\frac{k_0}{k_{50}} = 10$ where k_o is the initial stiffness corresponding to a value of G_0=14000 kPa and G_{50}=1400 kPa or equally E_{50}=4200 kPa. Moreover in the report is given the reduction curve of the secant shear modulus in relation to the rotation angle [log(Δθ)-G curve]. Taking into account that the rotation of the caisson is of course approximately proportional to the shear strain amplitude in the soil, the shear strain where the initial shear modulus has been reduced to 70% of the initial value can be estimated as $\gamma_{0.7}=6*10^{-4}$.

The aforementioned values have been adapted for the parameters of the Hardening Soil small model. Taking into account that the clay is considered to be quite soft the rest parameters of the model can be estimated according to the following relations: $1.25E_{oed} = E_{50}$ and $E_{ur} = 3E_{50}$.

The analyses that were performed with the aforementioned parameters revealed that in order the dynamic loop to capture the maximum displacements Rayleigh damping in the order of 22% needed to be added. This amount of Rayleigh damping is unrealistic however. The loops that derived from this set of material parameters for 0% Rayleigh damping and 22% Rayleigh damping are given in the following figures.

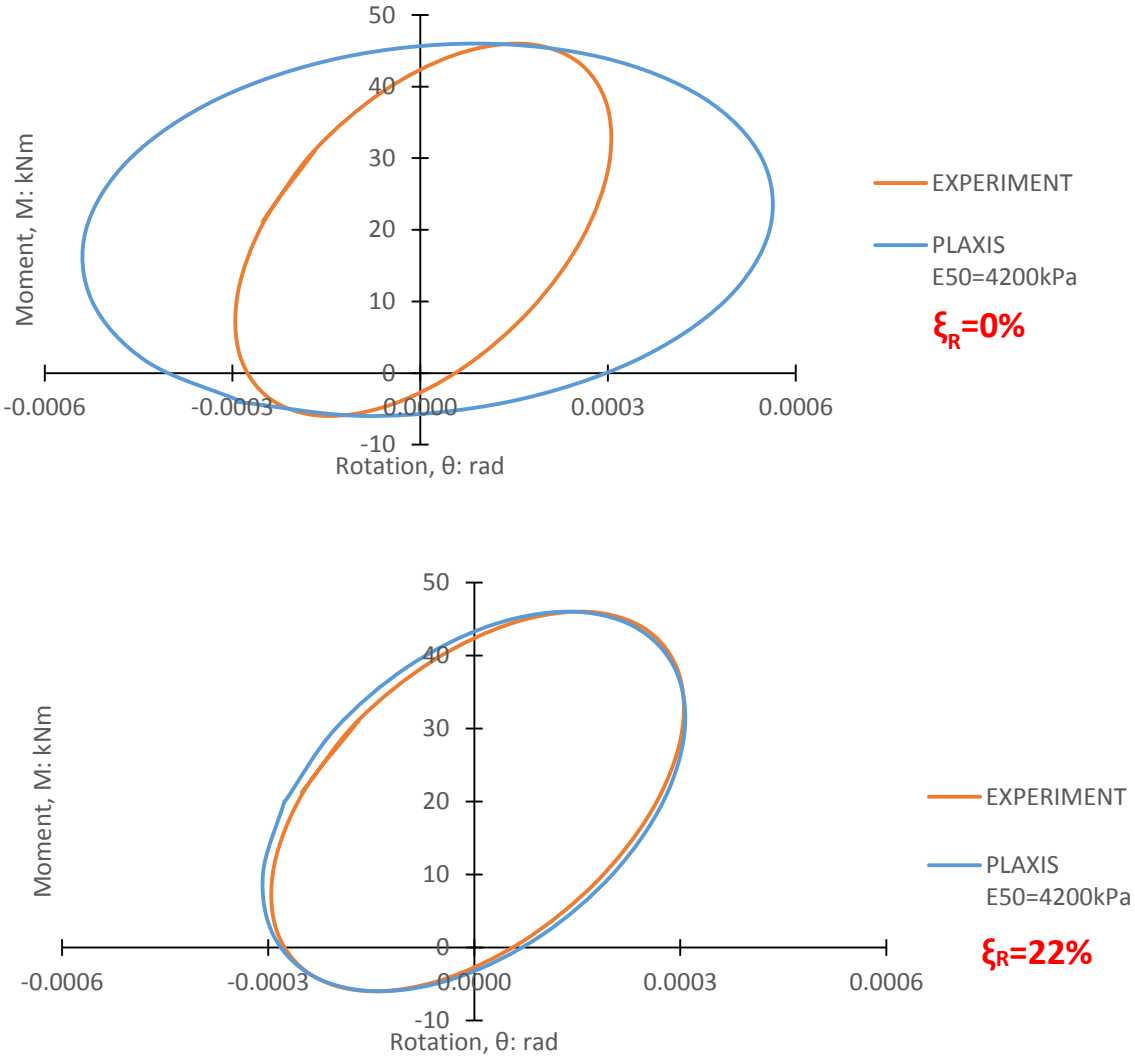

Figure 6-6: Dynamic loops for the steady state response at the frequency of 10Hz. The analyses with Plaxis have been performed with the parameters that have been calculated from the surface footing approximation. 22% Rayleigh damping is needed to be added in order the maximum rotation angles to match.

From the areas of the loops the dashpot coefficient can be estimated as $C = \frac{DW}{\pi \theta_{max}^2 \omega}$ where DW is the area of the loop, θ_{max} is the amplitude of the rotation angle and ω is the rotational frequency (ω=2πf). The two loops that are depictured in the figure below have the same frequency and almost the same amplitude of the rotation angle. The areas of the loops deviate less than 1%, thus the dashpot coefficients are almost the same.

Taking into account that 22% Rayleigh damping is considered unrealistic a new set of analyses were performed where the secant stiffness E_{50} was changed in such way that the dynamic loop from the numerical analysis would match the dynamic loop from the experimental data. Subsequently the shear strain $\gamma_{0.7}$ has also been changed. Rayleigh damping in the order of 2% was added in these analyses. Since E_{50} is changed, E_{oed} and E_{ur} are also changed according to the relations that were given before. The initial shear modulus G_0 has remained the same as before (G_0=14MPa).

The value of the E_{50} that eventually was selected to match the dynamic loops is E_{50}=9200 kPa and the shear strain parameter is $\gamma_{0.7}=1*10^{-4}$. This values reveals that the stiffness was underestimated by a factor of 56%. This underestimation is something that was expected as was mentioned before because of the simplified assumption that the caisson behaves as surface foundation. It can be seen that this assumption is not correct and leads to soil parameters that can be half of the real ones. In the following picture the dynamic loop that has derived from the numerical analysis where E_{50} has chosen to be almost twice the suggested one, and Rayleigh damping has been selected to be 2%, is compared with the dynamic loop that has derived from the experiment. As it can be seen in the figure that follows the fit is quite satisfactory.

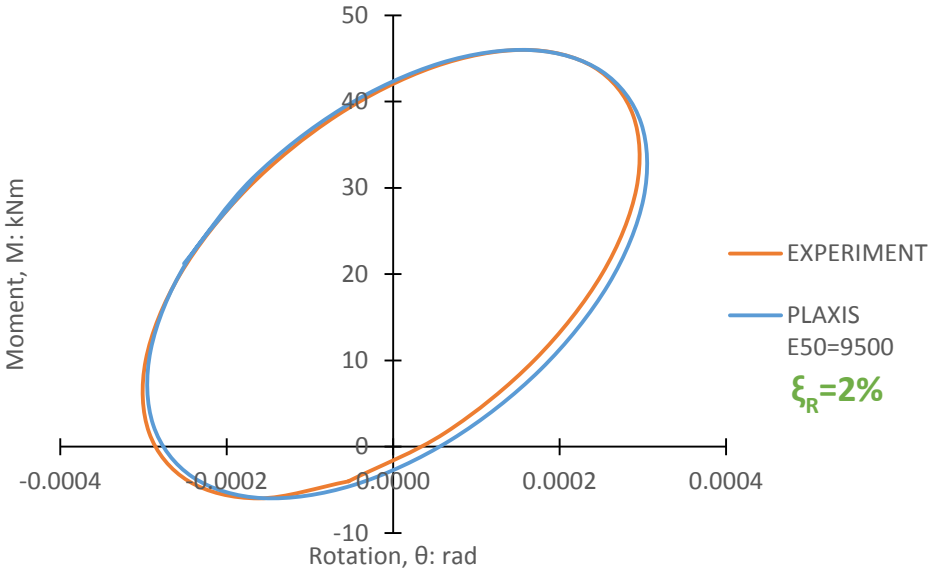

Figure 6-7: Dynamic loop for the steady state response at the frequency of 10Hz. The analysis with Plaxis has been performed with the secant E_{50} from the surface footing approximation multiplied by a factor of 1.90. 5% Rayleigh damping has been added.

A general conclusion that can be conducted from this part is the significance that the embedment can have. The simplified assumption that the suction caisson can behave as a surface footing can lead to underestimated moduli. This underestimation cannot be ignored as it can reach the factor of 2.

Moreover it can be seen how an advanced materials' model such as the Hardening Soil small can capture the real behavior of a foundation including the interaction between the soil and the caisson.

7 General conclusions and future work

7.1 General conclusions

This thesis dealt with the response of caisson foundations resting on a uniform undrained and drained clay profile and subjected to lateral static monotonic and dynamic loading under elastic and inelastic conditions. After developing appropriate Finite Element models for the soil-foundation system, numerous analyses were carried out that served the purposes of this work.

The first aim was to optimize the numerical model in terms of the maximum element size (Δl) of the mesh and the domain dimensions. The sensitivity analysis that was performed lead to the conclusion that the maximum size of the finite elements of the model needs to satisfy the following inequality in relation to the wavelength (λ) of the input signal: $\Delta l \leq \frac{\lambda}{4}$.The reason that the denominator is smaller than the guiding from the literature value, 8, is because the volume elements implemented in Plaxis are 10-node tetrahedral elements while the guiding value has derived from linear elements. Hence lower value of k was expected to be resulted because tetrahedral elements interpolate more nodes than linear elements.

Considering the domain dimensions of the numerical model sensitivity analyses both for the width and the depth of the model were performed. The optimum width of the domain resulted to be $4.5D$, where D is the depth of the caisson while the optimum depth of the domain resulted to be $4B$, where B is the width of the caisson. Values greater than those make the model inefficient by computational view and have a very small improvement in the accuracy of the results. Values smaller than the proposed are not suggested as they would lead to inaccurate results due to the greater influence of the boundaries of the numerical model.

The second aim was to evaluate the elastic response of the caisson under dynamic loading and investigate the influence of each component of the dynamic impedance, namely the stiffness which is represented by springs and the damping which is represented by dashpots. The fact that the case of the caisson consists of two degrees of freedom makes the problem complicated because except for the normal

horizontal and rotational modes, a coupling mode is introduced. The complex dynamic impedance was computed from the numerical analyses (complex method) and from analytical expressions, their results were compared. The reverse problem of computing the impedance from the numerical analyses seemed to be very sensitive to the time step of the analyses. Although the deviation for the corresponding response, namely the displacement and the rotation, remained at low levels the corresponding deviation for each separate coefficient of the impedance was increased considerably. However the trend of the results from the numerical analyses and the analytical expressions was the same.

Considering the damping a second method, which was named Loop Area Method, was used for the computation of the dashpot coefficients of each mode. This method is based on the definition of the dashpots and the areas of the loops that are formed between the load, force or moment, and the response, displacement or rotation. The results of this method lead to the conclusion that the two different methods, namely the Complex Method and the Loop Area Method, match only for the greater frequencies. For the smaller frequencies the latter method found to be inappropriate for the calculation of the dashpots.

Moreover the effect of the Rayleigh damping was investigated. 2% and 5% Rayleigh damping were introduced to the elastic analyses. The results that came up revealed only a very small influence on the response, the amplitude of which as was expected was slightly reduced. The influence seemed to be greater for the impedance coefficients, a fact that revealed the great sensitivity that the reverse calculation problem presents. One important conclusion that was made is that the Rayleigh damping has influence not only on the dashpots coefficients as it was expected but also on the spring coefficients. However this influence is very small for the selected ratios of Rayleigh damping.

Following the elastic behavior of the caisson the more realistic case of the inelastic caisson under dynamic loading was investigated forming the third aim of this thesis. The evaluation was limited to two specific frequencies for three different load levels under pure horizontal excitation, without moment or vertical loading. The load levels were defined as a percentage of the ultimate horizontal load at failure (10%, 50% and

80%). The response was evaluated qualitatively in terms of the lateral force – lateral displacement terms. Comparisons were performed between the case of full contact conditions considering the interfaces of the soil-structure (bonded interface) and the more realistic case of the nonlinear interfaces where sliding and gapping were allowed to be occurred. Moreover comparisons were performed between the inelastic analyses and equivalent elastic analyses where the initial shear modulus was properly reduced. The conclusions that can be conducted from this part are summarized in the following.

For the case of the inelastic behavior with bonded interfaces, the ultimate resistance in static loading that was derived from the numerical analysis confirmed the analytical relation that exist in the literature as the deviation was negligible. Considering the loops that formed from the dynamic calculations seemed to be different for the three load levels. As was expected the area of the loops increased as the load level increased. Moreover, the loops present a clockwise rotation with increasing loading and their center was moving towards the direction of the first half cycle of loading due to the plastification of the soil. The static cyclic loops seemed to have realistic shape with the lowest load level being very close to the elastic behavior. The dashpots coefficients of the dynamic analyses that derived presented a reductive trend as the load level increased, a fact that means that the total damping (material and radiation) is reducing as the soil plastifies although the material damping is increasing. These conclusions were made for both the two tested frequencies.

Considering the comparison between the inelastic and elastic analyses, it revealed that in order to match the amplitude of the inelastic analyses a reduced shear modulus needed to be applied. The reduction of the stiffness was about at the same level of the reduction of load level for both frequencies. However this observation cannot be generalized. The dynamic loops that formed seemed to be very similar with the corresponding inelastic dynamic loops, especially for the case of the lowest load level. There was not significant change in the areas of the loops. However, the main difference between the inelastic and elastic analyses was that the steady state loops of the inelastic analyses did not have their center at the initial center of the

caisson but at a permanent displacement which was increasing as the load level was increased, as it was explained before. With the elastic analyses this transfer of the dynamic loop could not be achieved.

Considering the case of the nonlinear interfaces, the ultimate load in static monotonic loading found to be smaller than for the case of the bonded interfaces of the tested caisson. The dynamic loops that formed showed a smaller clockwise rotation comparing to the corresponding loops of the bonded interface, a fact that reveals greater stiffness. The static cyclic loops did not show any difference from the corresponding cyclic loops with bonded interfaces.

Furthermore, another Winkler type approach was attempted for the dynamic inelastic behavior of the caisson. The caisson was divided into several horizontal plains and the dynamic behavior of one of these plains was investigated in horizontal static and dynamic loading under plain strain conditions. Important observations and conclusions were made by the formation of stiffness-displacement (K-u) and dashpot-displacement (C-u) curves. Drained and undrained conditions were considered as well as bonded and nonlinear interfaces.

For the case of drained conditions and bonded interfaces the numerical analyses revealed that in the elastic region the horizontal spring remains steady for all frequencies while the horizontal dashpot presents a reductive trend that tends asymptotically to the value of the one dimensional wave propagation theory as the frequency increase. This was something that was expected. For each frequency the stiffness reduces as the displacements increase (more soil elements into the inelastic region) and takes negative values for the greater frequencies. This negative stiffness means time lag between the oscillation of the caisson and the oscillation of the soil elements. For the case of the nonlinear interfaces the stiffness is not able to take negative values. Considering the dashpots it was observed that for both cases, bonded and nonlinear interfaces, as the load increases, the dashpots decrease and tend to zero for each frequency. Nonlinear interfaces as expected showed lower values for the dashpot comparing to the bonded interface due to the gap that occurred and consequently the non-participation of the one side. As far as concerns the undrained conditions the numerical analyses revealed that waves were partially

reflecting at the boundaries. The horizontal stiffness presented negative values already at the elastic region for the greater frequencies, something that it is not new to the literature. The dashpots showed the same trend as for the drained conditions however the quantitatively evaluation cannot be considered trustworthy due to the reflection of the waves.

Utilizing the numerical results a Winkler type model was suggested considering the horizontal mode of the shaft of the caisson. The proposed connection of different springs (nonlinear and elastic), dashpots and masses presented to be able to represent the inelastic behavior for different load levels and frequencies.

The final aim of this thesis was to compare the numerical simulation of a suction caisson with a real case study. The comparison revealed the significance that embedment can have. Ignoring the embedment of a suction caisson can lead to underestimation of the stiffness by a factor that can reach more than 2. Thus, the approach of a suction caisson as a surface foundation is not suggested.

7.2 Suggestions for future work

The problem of the dynamic excitation of embedded foundations is very extensive. Because of the time limitation of a diploma thesis an extensive research is not allowed. In order to evaluate the dynamic response of caissons from different aspects in the following some recommendations are presented for future work.

Considering the elastic analyses, parametric investigation in terms of different aspects of the problem of caisson could be performed. The embedment ratio and the shape of the plan are some suggestions for the geometry of the caisson. For the soil profile parametric investigation could be performed for the Poisson's ratio and the density of the soil. The latter has great influence on the damping of the soil and it would be very interesting to investigate its influence on the dashpots. Most importantly research should also be conducted for the case of non-uniform/layered soil profiles since this type constitutes he majority of the profiles in practice.

Considering the inelastic analyses a more extensive research is suggested. In order to generalize the conclusions of this thesis. A greater range of frequencies needs to be applied in order to find out the influence of the frequency on the case of the inelastic behavior of embedded foundations. This is a very difficult problem that represent the real seismic problems where the range of frequencies vary. Moreover the dynamic response should be evaluated in the more realistic case of combined loading (M, Q, N) except for the pure horizontal load that was studied herein. The inelastic behavior was studied for three different load levels, in future it would be very interesting to extent this study to greater levels and investigate whether the ultimate static loading can be exceeded under dynamic conditions. Future work should also focus more on the effects that the nonlinear interfaces have on the response of the caisson.

As far as concerns the proposed Winkler model, it would be very interesting and useful for the design to extend the research on the calibration of its parameters. The meaning of each component and the physics behind the whole model can lead to a theory that would make the calibration of the coefficients easy and practical.

8 Appendices

A. Gazetas elastodynamic formulations

In this project the caisson that is being studied is rectangular and fully embedded. This means that B=L and D=d. With these observations the formulae can simplified.

First the geometrical parameters can be modified as following:

$A_b = B^2$

$h = \frac{d}{2}$

$I_b = \frac{1}{12}B^4$

$A_w = 4BD$

$A_{w,s} = A_{w,ce} = 2BD$

$J_{ws} = \frac{2}{3}BD\left[\left(\frac{B}{2}\right)^2 + D^2\right]$

$J_{wce} = \frac{2}{3}BD^3$

Consequently the formulae can be simplified to the following:

- For the horizontal axis the dynamic impedance is:

$$\widetilde{\boldsymbol{K_{hh}}} = k_{hh} + i\omega c_{hh}$$

where the dynamic stiffness is:

$k_{hh} = k_{h,static}^{emb}\chi_{emb}$

$$k_{h,static}^{emb} \approx \frac{9GB}{2-v}\left(1 + 0.15\sqrt{\frac{2D}{B}}\right)\left[1 + 1.58\left(\frac{D}{B}\right)^{2.4}\right]$$

The coefficient χ_{emb} is a dynamic stiffness coefficient presented in chart form (Figure 6-8) in terms of D/B and d/B as a function of the dimensionless

parameter $\alpha_0=\omega B/(2V_s)$. In the case of fully embedded caisson (d=D), curve fitting gives χ_{emb} in the following form:

$$\chi_{emb} \approx 1 + \alpha_0 \left(\frac{D}{B}\right)\left\{\left[0.08 - 0.0074\left(\frac{D}{B}\right)\right]\alpha_0^2 - \left[0.31 - 0.0416\left(\frac{D}{B}\right)\right]\alpha_0 - 0.0442\left(\frac{D}{B}\right) + 0.14\right\}$$

and the horizontal dashpot coefficient is:

$$c_{hh} = \rho V_s B^2 c_{surf} + \rho V_s BD + \rho V_{La} BD$$

c_{surf}: obtained from Graph d

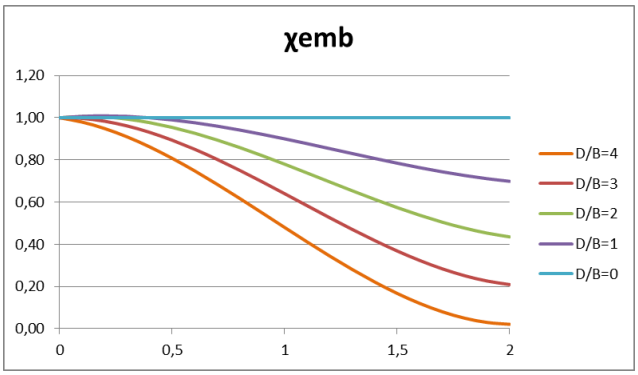

Figure 8-1: Graph χ_{emb} for square plan caisson (L/B=1) for various ratios of embedment (D/B)

- For the dynamic coupled swaying-rocking complex impedance:

$$\widetilde{K_{hr}} = k_{hr} + i\omega c_{hr}$$

$$\widetilde{K_{rh}} = k_{rh} + i\omega c_{rh}$$

The approximate formulae remain the same:

$$k_{hr} = k_{rh} \approx \frac{1}{3} d k_{hh}$$

and

$$c_{hr} = c_{rh} \approx \frac{1}{3} d c_{hh}$$

- For the dynamic rocking impedance the complex form is:

$$\widetilde{K_{rr}} = k_{rr} + i\omega c_{rr}$$

where the dynamic stiffness is:

$$k_{rr} = \frac{3.6GB^3}{1-v}\left[1 + 0.92\left(\frac{2D}{B}\right)^{0.6}\right]\left[1.5 + \left(\frac{2D}{B}\right)^{1.9}\right](1 - 0.30\alpha_0)$$

and the rocking dashpot coefficient is:

$$c_{rr} = \frac{1}{12}B^4\rho V_{La}c_{surf} + \frac{1}{12}BD^3\rho V_{La}c_{emb} + \frac{1}{12}BD(B^2 + D^2)\rho V_s c_{emb} + \frac{1}{3}B^3D\rho V_s c_{emb}$$

c_{surf}: obtained from Graph f

$$c_{emb} \approx 0.25 + 0.65\sqrt{\alpha_0}\left(\frac{2D}{B}\right)^{-0.25}$$

From all these formulae the dynamic impedances for each mode are calculated for every frequency and are compared with the corresponding results of PLAXIS.

B. Coordinate transformation of impedance and mass matrix

When the coordinate system of reference differs a coordinate transformation should be applied in each matrix (Forces, Impedance, and Displacement). Gazetas formulations refer to the base of the caisson while in the numerical analyses of PLAXIS the reference has been taken on the top of the caisson. The transformation follows the procedure that is described below.

The relation between the displacement at the base (u_b) and the displacement at the top (u_t) is:

$$u_b = u_t - \varphi D$$

Considering the forces referred to the base of the caisson and the top of the relation is:

$$Q_{BASE} = Q_{TOP}$$

$$M_{BASE} = M_{TOP} + Q_{TOP} D$$

Applying the dynamic equilibrium the following equations should be equal:

$$[F]_{TOP} = [K]_{TOP}[X]_{TOP}$$

$$[F]_{BASE} = [K]_{BASE}[X]_{BASE}$$

Elaborating the matrices the following equations are derived:

$$Q_{BASE} = \; Q_{TOP} = {K_{hh}}^{BASE} u_b \; + \; {K_{hr}}^{BASE} \varphi = \; {K_{hh}}^{BASE} (u_t - \varphi D) + \; {K_{hr}}^{BASE} \varphi$$
$$= {K_{hh}}^{BASE} u_t \; + ({K_{hh}}^{BASE} - D{K_{hr}}^{BASE}) \varphi$$

$$Q_{TOP} = \; {K_{hh}}^{TOP} u_t \; + \; {K_{hr}}^{TOP} \varphi$$

Thus the relation between the impedance referred at the top and at the base is the following:

$${K_{hh}}^{TOP} u_t \; + \; {K_{hr}}^{TOP} \varphi = {K_{hh}}^{BASE} u_t \; + \left({K_{hh}}^{BASE} - D{K_{hr}}^{BASE}\right) \varphi$$

With the same procedure considering the moment the equations that are derived are:

$$M_{BASE} = M_{TOP} + Q_{TOP}D = {K_{rh}}^{BASE}u_b + {K_{rr}}^{BASE}\varphi = {K_{rh}}^{BASE}(u_t - \varphi D) + {K_{rr}}^{BASE}\varphi = {K_{rh}}^{BASE}u_t + \left({K_{rr}}^{BASE} - D{K_{rh}}^{BASE}\right)\varphi$$

$$M_{TOP} = {K_{rh}}^{TOP}u_t + {K_{rr}}^{TOP}\varphi$$

$$M_{TOP} = M_{BASE} - Q_{TOP}D = {K_{rh}}^{BASE}u_t + \left({K_{rr}}^{BASE} - D{K_{rh}}^{BASE}\right)\varphi - \left[{K_{hh}}^{BASE}u_t + \left({K_{rh}}^{BASE} - D{K_{hh}}^{BASE}\right)\varphi\right]D = \left({K_{rh}}^{BASE} - D{K_{hh}}^{BASE}\right)u_t + \left({K_{rr}}^{BASE} - 2D{K_{rh}}^{BASE} + D^2{K_{hh}}^{BASE}\right)\varphi$$

Thus the relation between the impedance referred at the top and at the base is the following:

$${K_{rh}}^{TOP}u_t + {K_{rr}}^{TOP}\varphi = \left({K_{rh}}^{BASE} - D{K_{hh}}^{BASE}\right)u_t + \left({K_{rr}}^{BASE} - 2D{K_{rh}}^{BASE} + D^2{K_{hh}}^{BASE}\right)\varphi$$

In a more elegant way the previous equations can be written in matrix form. In this way the coordinate transformation is given by the following matrix.

$$\widetilde{K_{TOP}} = \begin{bmatrix} \widetilde{K_{hh}} & \widetilde{K_{hr}} - D\widetilde{K_{hh}} \\ \widetilde{K_{rh}} - D\widetilde{K_{hh}} & \widetilde{K_{rr}} - 2D\widetilde{K_{hr}} + D^2\widetilde{K_{hh}} \end{bmatrix}$$

where D is the depth of embedment and $\widetilde{K_{ij}}$ are the impedances referred at the base.

In this way the corresponding transformation matrix that is derived is:

$$A = \begin{bmatrix} 1 & -D \\ 0 & 1 \end{bmatrix}$$

$$\widetilde{K_{TOP}} = A^T\widetilde{K_{BASE}}A$$

The same procedure is followed for the mass matrix. Thus the corresponding mass matrix with reference the top of the caisson is derived from the mass matrix that is referred at the base:

$$M_{base} = \begin{bmatrix} m & m\frac{D}{2} \\ m\frac{D}{2} & (J_c + m\frac{D^2}{4}) \end{bmatrix}$$

Where m: mass, D: depth of embedment, J_c: mass moment of inertia about the center of gravity $J_c = \frac{1}{12}m(B^2 + D^2)$

$$M_{top} = A^T M_{base} A$$

$$M_{top} = \begin{bmatrix} m & -m\frac{D}{2} \\ -m\frac{D}{2} & (J_c + m\frac{D^2}{4}) \end{bmatrix}$$

C. Loop area method

The equations that are used in order to calculate the dashpots coefficients by the area of the loops that are formed in the charts between load (Q or M) and response (u or ϕ) have derived according to the following process. Ana extended description is made for one of the two analyses, Q(t)≠0 and M(t)=0.

$$DE_{Q-u} = \int_0^T (c_{hh}\dot{u} + c_{hr}\dot{\varphi})du$$

Where

DE_{Q-u}: the area of the loop calculated by the graph Q-u

$u(t) = u\sin(\omega t - d_u)$: the lateral displacement of the reference point

$\varphi(t) = \varphi\sin(\omega t - d_\varphi)$: the rotation angle of the reference point

$\dot{u} = \frac{du}{dt}$: the lateral velocity of the reference point

$\dot{\varphi} = \frac{d\varphi}{dt}$: the angular velocity of the reference point

u, φ are the maximum values of the response of the caisson and d_u, d_φ are the phase angle due to the time lag between the load and the displacement or the load and the rotation angle respectively.

$$DE_{Q-u} = \int_0^T (c_{hh}\dot{u} + c_{hr}\dot{\varphi})du = \int_0^T (c_{hh}\dot{u} + c_{hr}\dot{\varphi})\dot{u}dt = \int_0^T (c_{hh}\dot{u}^2 + c_{hr}\dot{\varphi}\dot{u})dt$$

$$= \int_0^T [c_{hh}(\omega u)^2 cos^2(\omega t + d_u)$$

$$+ c_{hr}\omega^2 u\varphi\cos(\omega t + d_u)\cos(\omega t + d_\varphi)]dt$$

$$= c_{hh}(\omega u)^2 \int_0^T cos^2(\omega t + d_u)dt$$

$$+ c_{hr}\omega^2 u\varphi \int_0^T \cos(\omega t + d_u)\cos(\omega t + d_\varphi)dt$$

$$= c_{hh}(\omega u)^2 \frac{T}{2} + c_{hr}\omega^2 u\varphi \frac{T}{2}\cos(d_u - d_\varphi)$$

Taking into account that $\omega = \frac{2\pi}{T}$ the equation that is derived is:

$$DE_{Q-u} = \pi\omega[u^2 c_{hh} + u\varphi \cos(d_u - d_\varphi)\, c_{hr}]$$

Following the same procedure for the graph Q-ϕ the equation that is derived is:

$$DE_{Q-\varphi} = \int_0^T (c_{hh}\dot{u} + c_{hr}\dot{\varphi})d\varphi$$

$$DE_{Q-\varphi} = \pi\omega[u\varphi \cos(d_u - d_\varphi)\, c_{hh} + \varphi^2 c_{hr}]$$

The areas of the graphs M-u and M-ϕ are zero. So the corresponding equations are:

$$DE_{M-u} = \int_0^T (c_{rr}\dot{\varphi} + c_{rh}\dot{u})du$$

$$0 = \pi\omega[u^2 c_{hh} + u\varphi \cos(d_u - d_\varphi)\, c_{hr}]$$

and

$$DE_{M-\varphi} = \int_0^T (c_{rr}\dot{\varphi} + c_{rh}\dot{u})d\varphi$$

$$0 = \pi\omega[u\varphi \cos(d_u - d_\varphi)\, c_{hh} + \varphi^2 c_{hr}]$$

The aforementioned four equations have been derived from the one analysis where Q(t)≠0 and M(t)=0. From the second analysis where M(t)≠0 and Q(t)=0 four more equations are derived. Of course here the corresponding maximum response u,ϕ are different than the previous analysis.

$$0 = \pi\omega[u^2 c_{hh} + u\varphi \cos(d_u - d_\varphi)\, c_{hr}]$$

$$0 = \pi\omega[u\varphi \cos(d_u - d_\varphi)\, c_{hh} + \varphi^2 c_{hr}]$$

$$DE_{M-u} = \pi\omega[u^2 c_{hh} + u\varphi \cos(d_u - d_\varphi)\, c_{hr}]$$

$$DE_{M-\varphi} = \pi\omega[u\varphi \cos(d_u - d_\varphi)\, c_{hh} + \varphi^2 c_{hr}]$$

D. Mathematical description of the proposed Winkler model

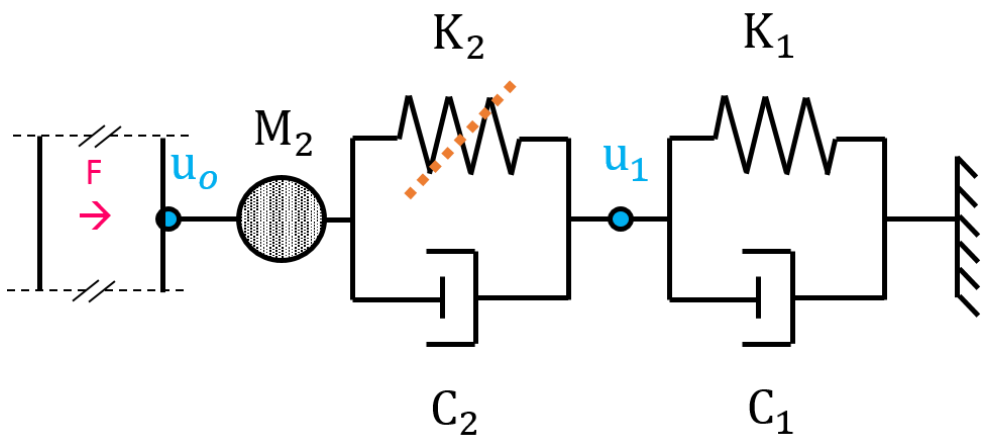

Figure 8-2: Schematically illustration of the proposed Winkler model.

The model works by taking as input data the load $F=F_{max}\sin(\omega t)$ and giving as output data the displacement u0(t) or the opposite way around. In the following description it is used as input data the load F(t) and as output the displacements u0(t).

The model needs as input parameters the following coefficients: K1, K2=Fy/uy, C1, C2, M2 and Dt (a very low value is suggested). Considering the nonlinear spring K2 the BWGG law needs as input parameters the following: Fy (=6-12S_uB) and n (a very low value is suggested for the fit of the numerical results). The mathematical description is the following:

$$\text{matrix}(u0) := \text{for } i \in 0..10000$$

$$u1_0 \leftarrow 0$$

$$u1_1 \leftarrow 0$$

$$u0_0 \leftarrow 0$$

$$u0_1 \leftarrow 0$$

$$z_0 \leftarrow 0$$

$$u1_{i+2} \leftarrow \frac{Dt}{C1}\cdot\left(F_i - K1\cdot u1_{i+1}\right) + u1_{i+1}$$

$$u0_{i+2} \leftarrow \frac{Dt^2}{M2}\cdot\left(F_i - Fy\cdot z_i\right) - \frac{Dt\cdot C2}{M2}\cdot\left[\left(u0_{i+1} - u0_i\right) - \left(u1_{i+1} - u1_i\right)\right] + 2\cdot u0_{i+1} - u0_i + u1_{i+2} - 2\cdot u1_{i+1} + u1_i$$

$$z_{i+1} \leftarrow z_i + \frac{\left[\left(u0_{i+1} - u1_{i+1}\right) - \left(u0_i - u1_i\right)\right]}{uy}\cdot\left[1 - \left(\left|z_i\right|\right)^n\left[\frac{1}{2} + \frac{1}{2}\cdot\text{sign}\left[\left[\left(u0_{i+1} - u1_{i+1}\right) - \left(u0_i - u1_i\right)\right]\cdot z_i\right]\right]\right]$$

9 Bibliography

Abbiss, C., 1986. The effects of damping on the interpretation of geophysical measurements.

Alpan, 1970. Geotechnical properties of soils. *Earth Science Review.*

Aviles, J. & Perez-Rocha, L., 1998. "Effects of foundation embedment during building–soil interaction",. *Earthquake Engineering and Structural Dynamics, 27 (12), 1523–1540.*

Bolton, M. & Wilson, J., 1990. Soil stiffness and damping.

Bringreve, R., Kappert, M. & Bonnier, P., 2007. Hysteretic damping in a small strain stiffness model. *Proc.NUMOG.*

Celebi, M., 2000. Radiation samping observed from seismic responses of buildings. *12WCEE.*

Das, B., 1995. Fundamentals of soil dynamics. *Elsevier.*

Davidson, H., 1982. *Laterally loaded drilled pier research,* Pensylvania: Gai Consultans, Inc.: Electric Power Research Institute.

Dobry, R. & Gazetas, G., 1986. Dynamic response of arbitary shaped foundations. *J Geotech Eng , ASCE,* 112(2), pp. 109-135.

Fotopoulou, M., Konstantopoulos, P., Gazetas, G. & Tassoulas, J., 1989. Rocking damping of arbitarily-shaped embedded foundations. *J Geotech Eng ASCE,* Issue 115, pp. 473-489.

Gadre, A. & Dobry, R., 1998. Lateral cyclic loading centrifuge tests on square embedded footing. *J Geotech Geoenviron Eng ASCE,* Issue 124, pp. 1128-1138.

Gazetas, G., 1982. Vibrational characteristics of soil deposits with variable wave velocity. *International Journal for noumerical and analytical methods in geomechanics,* Volume 6.

Gazetas, G., 1983. Analysis of machine foundation vibrations: state of the art. *Soil Dyn Earthquake Eng,* Volume 2, pp. 2-42.

Gazetas, G., 1987. Simple Physical Methods for Foundation Impedance. In: E. A. Science, ed. *Dynamic Behavior of Foundations and Burried Structures.* s.l.:s.n.

Gazetas, G., 1991. Foundation Vibrations. *Foundation Engineering Handbook*.

Gazetas, G. & Apostolou, M., 2004. Nonlinear soil–structure interaction: foundation uplift and soil yielding. *odorovska M., Celebi M., editors, Proceedings of the 3rd US–Japan workshop on soil–structure interaction, USGS, Menlo Park, CA.*

Gazetas, G. & Tassoulas, J., 1987. Horizontal damping of arbitarily embedded foundations. *J. Geotech Eng ASCE,* Issue 113, pp. 458-475.

Gazetas, G. & Tassoulas, J., 1987. Horizontal stiffness of arbitarily shaped embedded foundations. *J. Geotech Eng ASCE,* Issue 113, pp. 440-457.

Gerolymos, N., 2002. *Constitutive model for the static and dynamic response of soil, pile-soil interaction and caisson-soil interaction..* PhD thesis ed. Athens: NTUA.

Gerolymos, N. & Gazetas, G., 2006. Development of Winkler model for static and dynamic response of caisson foundations with soil and interface nonlinearities. *ELSEVIER.*

Gerolymos, N. & Gazetas, G., 2006. Winkler model for lateral response of rigid caisson foundations in linear soil. *Soil Dynamics and Earthquake Engineering,* Volume 26, pp. 347-361.

Hardin & Black, 1969. Closure to vibration modulus of normally consolidated clays. *Proc.ASCE: Journal of soil mechanics and foundations division,* pp. 1531-1537.

Hardin & Drnevich, 1972. Shear modulus and damping in soil. *Proc.ASCE: Journal of the soil mechanics and foundation divisions,* pp. 1531-1537.

Houlsby, T., Kelly, R. B., Huxtable, J. & Byrne, B. W., 2005. Field trials of suction caissons in clay for offshore wind turbine foundations. *Geotechnique,* Volume 5, pp. 287-296.

Iwasaki, T., Tatsuoka, F. & Takagi, Y., 1978. Shear moduli of sands under cyclic torsional shear loading.

Kausel, E. & Roesset, J., 1975. Dynamic stiffness of circular foundations. *J Eng Mech Div ASCE,* Volume 6, pp. 770-785.

Kausel, E. & Rosset, J., 1975. Dynamic stiffness of circular foundations. *J. eng Mech Div, ASCE,* Volume 101(6), pp. 110-85.

Kramer, S., 1996. *Geotechnical Earthquake Engineering.* s.l.:s.n.

Kuhlemeyer, R. & Lysmer, J., 1973. Finite element method accuracy for wave propagation problems. *J. Soil Mech. And Foundations,* Volume Div. ASCE, 99(SM5), pp. 421-427.

Luco, L., 1974. Impedance functions for a rigid foundations on a layered medium. *Nud Eng Des,* Issue 31, pp. 204-217.

Lysmer, J. & Kuhlmeyer, R., 1969. Finite dynamic model for infinite media.

Mylonakis, G., 2001. Elastodynamic model for large diameter end bearing shafts. *Soil Found,* 3(41), pp. 31-44.

Ostadan, F., Deng, N. & Roesset, M., 2004. *Estimating Total System Damping for Soil-Structure Interaction Systems.* s.l., s.n.

Pitilakis, K. D., 2010. *Geotechnical Earthquake Engineering.* s.l.:s.n.

PLAXIS3D, 2012. *Material Models.* Delft, The Netherlands: Plaxis b.v..

PLAXIS3D, 2012. *Scientific Manual.* Delft, The Netherlands: Plaxis b.v..

Potts, D. M. & Zdravkovic, L., 1999. *Finite element analysis in geotechnical engineering, theory.* s.l.:s.n.

Varun, 2006. *A simplified model for lateral response of caisson foundations,* s.l.: s.n.

Varun, Assimaki, D. & Gazetas, G., 2009. A simplified model for lateral response of large diameter caisson foundations - Linear elastic formulation. *Soil Dynamics and Earthquake Engineering,* 29(2), pp. 268-291.

Wong, H. & Luco, J., 1985. Tables of impedance functions for square foundation on layered media. *Soil Dyn Earthquake Eng,* Volume 4, pp. 64-68.